TECHNISCHE UNIVERSITÄT MÜNCHEN
Lehrstuhl für Raumfahrttechnik

Thermal Constrained Traverse Planning at Lunar Poles

Dipl.-Ing. Univ. Matthias Killian

Vollständiger Abdruck der von der Fakultät für Maschinenwesen der Technischen Universität München zur Erlangung des akademischen Grades eines

Doktor-Ingenieurs (Dr.-Ing.)

genehmigten Dissertation.

Vorsitzender:		Prof. Wolfgang Polifke, Ph. D.
Prüfer der Dissertation:	1.	Prof. Dr. rer.nat. Dr. h.c. Ulrich Walter
	2.	Prof. Dr.-Ing. Thomas Sattelmayer
	3.	Prof. Dr.-Ing. Markus Czupalla Fachhochschule Aachen

Die Dissertation wurde am 12.11.2019 bei der Technischen Universität München eingereicht und durch die Fakultät für Maschinenwesen am 23.06.2020 angenommen.

Acknowledgements

At first, I want to thank all of the LRT staff for the pleasant, cooperative, and productive atmosphere and endless discussions about the right method to brew coffee.

This thesis would not have been possible with the previous work done by Philipp Hager, who I am deeply thankful for providing the initial code of TherMoS, introducing me to the Moon and for fruitful discussions at the beginning of this thesis.

Claas Olthoff was always open minded and ready to help when it came to programming in MATLAB®. Even more important his social support in private activities.

Matthias Tebbe and Philipp Reiß, thank you for all the fruitful discussions about work and non-work related topics. There are so many things to do out there.

I want to thank Prof. Markus Czupalla for giving me the possibility to work in the field of thermal engineering and for always giving honest feedback and including new suggestions at the same time.

Prof. Walter, thank you for the trust that you put in the work of all your PhD students, including mine. The freedom and autonomy that I was allowed during my work helped to take important steps in my personal development.

Last but not least, I want to thank my family who always supported me at all activities. A special thank you goes to my wife Claudia who had to endure all the mood changes, doubts, and that come as a side effect of writing such a thesis.

Abstract

In the near future, solar-powered rovers are expected to explore the poles of the Moon. Research will focus in particular on the Moon's south pole. This thesis deals with the automatic planning of optimal traverses on the lunar surface for solar-powered rovers under consideration of their energy state. In addition to the illumination of the rover, the heat exchange with its environment via radiation is also determined, which is a novel supplement to existing approaches. Due to the almost perpendicular angle of incidence of the Sun at the poles, a terrain model as precise as possible is required to realistically simulate the illumination and thus also the temperatures on the lunar surface.

A simulation method called Thermal Moon Simulator (TherMoS) previously developed at the Chair of Astronautics has been further improved in order to precisely simulate the conditions at the south pole of the Moon. This concerns on the one hand an improved terrain model and on the other hand the thermal model of the Moon, including the calculation of the illumination as well as the heat exchange including the solving algorithm of the thermal model. Validation of the updated model with measured temperatures at the south pole shows a Pearson correlation coefficient of 0.955. In addition, a component for optimising traverses between two points was introduced that takes into account the overall energy state of the rover. The optimisation is based on the classical approach A*, which is implemented in a modified form. This means that although the algorithm no longer finds the optimal solution, it converges quickly and can handle a dynamic environment. Nevertheless, the algorithm still finds very good solutions that are close to the optimum in quality. The name of the updated simulation method developed in the context of this work is Thermal Moon Simulator for Exploration (TherMoS-X).

Many design options for rovers include the use of solar energy. For this reason, an exemplary model of a rover that uses incoming solar radiation as energy source was implemented in this thesis. Excess energy can be stored in a rechargeable battery. The model takes into account the power consumption of different consumers to determine the total energy demand. This includes a computer, the power required for driving, communication and a heating element.

Traverse optimisation was carried out in two scientifically interesting regions near the south pole. The investigated areas are about 30 km by 30 km in size and consist of 62,000 triangles and ten times as many thermal nodes. The results show that in both scenarios a rechargeable battery is required to find a traverse that is navigable under the boundary conditions and to bridge shadow phases. In both cases, the traverse with the lowest battery capacity differs significantly from the ones that result from optimisation with the classic approach A* neglecting the energy state of the rover. Depending on the region, the distances are only slightly longer, but have a significantly different shape and the required battery capacity is 70 W h or 100 W h. Furthermore, there is a pronounced correlation between the solar radiation along the traverse and the state of charge of the battery.

As a conclusion, the additional consideration of a thermal model calculating the energy state during optimisation increases the accuracy of the planning and in some cases significantly different traverses are required to reach the target with a certain battery capacity.

Zusammenfassung

In naher Zukunft werden voraussichtlich solarbetriebene Rover die Pole des Mondes erkunden. Dabei steht besonders der Südpol des Mondes im Fokus der Forschung. Diese Arbeit beschäftigt sich mit der automatischen Planung von optimalen Routen auf der Oberfläche des Mondes für solarbetriebene Rover unter Berücksichtigung ihres Energiezustands. Dabei wird neben der Beleuchtung des Rovers auch der Wärmeaustausch über Strahlung mit seiner Umgebung ermittelt, was eine neuartige Ergänzung zu bestehenden Ansätzen darstellt. Aufgrund des nahezu senkrechten Einfallswinkels der Sonne an den Polen ist ein möglichst präzises Geländemodell erforderlich, um die Beleuchtung und damit auch die Temperaturen auf der Mondoberfläche realistisch zu simulieren.

Eine bereits am Lehrstuhl für Raumfahrttechnik entwickelte Simulationsmethode mit dem Namen Thermal Moon Simulator (TherMoS) wurde weiter verbessert, um die Bedingungen am Südpol des Mondes präzise simulieren zu können. Dies betrifft zum einen ein verbessertes Geländemodell und zum anderen das Thermalmodell des Mondes, darunter die Berechnung der Beleuchtung sowie des Wärmeaustausches inklusive dem Lösealgorithmus des Thermalmodels. Die Validierung des aktualisierten Modells mit gemessen Temperaturen am Südpol zeigt einen Korrelationskoeffizienten nach Pearson von 0,955. Zusätzlich wurde eine Komponente zur Optimierung von Routen zwischen zwei Punkten eingeführt, die den gesamten Energiezustandes des Rovers berücksichtigt. Die Optimierung beruht auf dem klassischen Ansatz A*, der abgeändert implementiert ist. Dadurch findet der Algorithmus zwar nicht mehr die optimale Lösung, konvergiert dafür aber schnell und kann mit einer dynamischen Umgebung umgehen. Dennoch findet der Algorithmus immer noch sehr gute Lösungen, die in der Qualität nahe dem Optimum sind. Der Name der im Rahmen dieser Arbeit entstandenen, aktualisierten Simulationsmethode lautet Thermal Moon Simulator for Exploration (TherMoS-X).

Viele Designentwürfe für Rover sehen die Verwendung von Solarenergie vor. Deswegen wurde in dieser Arbeit ein beispielhaftes Modell eines Rovers eingebaut, das eingehende Sonnenstrahlung als Energiequelle nutzt. Überschüssige Energie kann in einer wieder aufladbaren Batterie gespeichert werden. Das Modell berücksichtigt die Leistungsaufnahme von verschiedenen Verbrauchern, um den gesamten Energiebedarf zu ermitteln. Dazu gehört ein Computer, die erforderliche Leistung für den Antrieb, Kommunikation und ein Heizelement.

Eine Optimierung von Traversen wurde an zwei wissenschaftlich interessanten Gegenden in der Nähe des Südpols durchgeführt. Die untersuchten Gebiete sind ca. 30 km mal 30 km groß und bestehen aus knapp 62.000 Dreiecken und zehnmal so vielen Thermalknoten. Dabei zeigt sich, dass in beiden Szenarien eine wieder aufladbare Batterie notwendig ist, um überhaupt eine unter den Randbedingungen fahrbare Traverse zu finden und Schattenphasen zu überbrücken. In beiden Fällen unterscheidet sich die Traverse mit der geringsten Batteriekapazität deutlich von der, die eine Optimierung ohne Berücksichtigung des Energiezustandes des Rovers mit dem klassischen Ansatz A* ergibt. Je nach Gebiet sind die Strecken nur unwesentlich länger, weisen jedoch eine deutlich andere Form auf und die erforderliche Batteriekapazität liegt bei 70 W h bzw. 100 W h. Ferner zeigt sich eine ausgeprägte Korrelation zwischen der Sonneneinstrahlung entlang der Traverse und dem Ladezustand der Batterie.

Als Fazit bleibt festzuhalten, dass die zusätzliche Berücksichtigung eins Thermalmodells zur Berechnung des Energiezustandes während der Optimierung die Genauigkeit der Planung erhöht und zum Teil deutlich abweichende Traversen erforderlich sind, um mit einer bestimmten Batteriekapazität ans Ziel zu gelangen.

Contents

Abbreviations

ACO	Ant Colony Optimisation
CNSA	China National Space Administration
DEM	Digital Elevation Model
DTE	Direct To Earth
DTM	Digital Terrain Model
DynamicSWS-FP	Dynamic Strictly Weak Superior function Fixed Point problem
ESA	European Space Agency
FEM	Finite-Element Method
FDM	Finite-Difference Method
FVM	Finite-Volume Method
GA	Genetic Algorithm
GER	Global Exploration Roadmap
ISECG	International Space Exploration Coordination Group
ISRO	Indian Space Research Organisation
JAXA	Japanese Aerospace Exploration Agency
LOLA	Lunar Orbiter Laser Altimeter
LPM	Lumped Parameter Method
LRO	Lunar Reconnaissance Orbiter
LVP	Lunar Volatiles Prospector
MER	Mars Exploration Rover
MGCM	Mars General Circulation Model
MLI	Multi-Layer insulation
MOLA	Mars Orbiter Laser Altimeter
MRO	Mars Reconnaissance Orbiter
MSL	Mars Science Laboratory
NA	Neural network
NAC	Near Angle Camera
NASA	National Aeronautics and Space Administration
PROSPECT	Package for Resource Observation and in-Situ Prospecting for Exploration, Commercial exploitation and Transportation
PDS	Planetary Data System
PSR	Permanently Shadowed region
RHU	Radioisotope Heating Unit
ROI	Region Of Interest
RP	Resource Prospector
SA	Simulated Annealing
SELENE	SELenological and ENgineering Explorer
SLDEM	LOLA Digital Elevation Model Coregistered with SELENE Data
TEMPEST	TEmporal Mission Planner for the Exploration of Shadowed Terrain
TherMoS	Thermal Moon Simulator
TherMoS-X	Thermal Moon Simulator for Exploration
TUB	Technische Universität Berlin
TUM	Technical University of Munich
VIPER	Volatiles Investigating Polar Exploration Rover
WAC	Wide Angle Camera
WEB	War Electronic Box

Symbols

Symbol	*SI unit*	*Description*
α	[-]	Solar absorptivity
α	[°]	Slope angle
ε	[-]	Emissivity
η	[-]	Exponent of sinkage
λ	[m]	wavelength
ρ	[kg m^{-3}]	Density
σ	[W m^{-2} K^{-4}]	Stefan Boltzmann Constant
χ	[-]	Radiative conductivity parameter
A	[m^{2}]	Area
b	[cm]	Smaller dimension of loading area
$B(\lambda,T)$	[W sr^{-1} m^{-3}]	Planck function
c	[m]	Cost between two nodes
c_p	[J kg^{-1} K^{-1}]	Specific heat capacity
C	[J K^{-1}]	Capacitor
d	[m]	Distance
d_E	[m]	Euclidian distance
D	[m]	Diameter
e	[-]	Eccentricity
f	[m]	Evaluation function
g	[m s^{-2}]	Gravity acceleration
g	[m]	Cost value
F	[-]	View factor
h	[m]	Heuristic value
H	[m]	Scale factor
k	[W m^{-1} K^{-1}]	Thermal conductivity
k_c	[N cm^{-2}]	Cohesive modulus of soil deformation
k_φ	[N cm^{-3}]	Frictional modulus
K	[W K^{-1}]	Conductor
n	[-]	amount
t	[s]	Time
T	[K]	Temperature
q	[W m^{-2}]	Heat flux
P	[W]	Power
$\dot{Q}$	[W]	Heat
R	[W K^{-4}]	Radiation exchange factor
R	[m]	Radius
V	[m^{3}]	Volume
v	[m s^{-1}]	Speed
W	[W]	Load
z	[m]	Depth

1 Introduction

1.1 Motivation

Over the last two decades, exploration of the Moon gained importance in the programs of space agencies all around the world as well as to private companies after a decline in its exploration with the termination of the Apollo program in the early 1970s. While space agencies focus to increase our scientific knowledge of the Moon, private companies further try to fulfil different business models such as mining the Moon or bringing space tourist there.

Exploration of the Moon experienced a renaissance in the 1990s with remote sensing instruments orbiting the Moon and sending back an enormous amount of valuable scientific data to Earth. The first orbiter of this renewed interest was Clementine launched in 1994, which provided the first complete look at the Moon. A decade later, instruments mapped the elevation profile of the Moon globally with laser altimeters on board the Japanese spacecraft Kaguya, also known as SELenological and ENgineering Explorer (SELENE), launched in 2007 and ended in 2009. In addition, NASA launched its Lunar Reconnaissance Orbiter (LRO) in 2009. It is still operational and is equipped with a laser altimeter with the name Lunar Orbiter Laser Altimeter (LOLA). Additional instruments on LRO provide even more data in various fields of science. LRO can conduct infrared measurements of the surface with its instrument Diviner Lunar Radiometer Experiment (DLRE). For visual inspection, it also carries a wide angle camera (WAC) and two near angle cameras (NAC). With the help of data from LRO, it became evident that the Moon still contains water trapped as ice on and underneath the surface (Hayne et al. 2015; Li et al. 2018). Nevertheless, remote sensing data has to be bolstered by in-situ measurements on the lunar surface. In preparation for missions to polar regions, lunar landers followed, some of them even carrying small rovers, which enable measurements at different locations. With the mission Chang'e 3, the China National Space Administration (CNSA) placed successfully a lander including a rover, named Yutu, on the surface of the Moon in 2013 in north-western Mare Imbrium (44.12° N, 19.51° W) (Li et al. 2015). It has a mass of about 140 kg and it travelled 114 m (Li et al. 2015) on the surface. In January 2019, its successor mission Chang'e 4 reached the South Pole-Aitken basin and landed in Von Kármán crater at 49.03° S, 174.16° E. As it was the backup system of Chang'e 3, the architecture and technological systems are similar. The rover Yutu 2 exceeded the travelled distance of Yutu already after three lunar days with a total distance of 163 m (Di et al. 2019). The Indian mission Chandrayaan-2 followed in July and its lander was supposed to touch down between craters Manzinus C (69.95° S, 21.6° E) and Simpelius N (71.37° S, 23.96° E) (Padma 2019), but unfortunately crashed. It carried a rover with a mass of 27 kg (ISRO 2019) planned for an operational time of 14 days and a maximum reach of 500 m. These most recent missions prove the importance of robotic exploration and the scientific interest in the south polar region of the Moon.

Consequently, the next steps include longer mission scenarios for rovers as well as returning astronauts to the Moon. In the focus of nearly all missions in the near term is the lunar south pole. On the one hand, because many locations exist there with nearly persistent solar illumination, on the other hand because there are also permanently shadowed regions close by. It is expected that water ice and volatiles are mainly trapped at those locations. Furthermore, the presumably oldest basin on the Moon and the largest impact in our solar system, the South Pole Aitken basin, is also located close to the south pole representing a scientific target of high priority. Rovers are going to conduct exploration of polar regions on the Moon first without assistance of astronauts. They will be required to travel longer distances in order to collect scientific data at different locations around the landing site. A favourable power system for such traverses consists of solar cells and a rechargeable battery. The latter allows for high power values, which can be provided constantly in the best case without any hazardous components on board such as a radioisotope thermal generator. The low solar elevation angles at the lunar poles allow nearly ideal illumination of solar cells if they are mounted perpendicular to the surface. However, low solar elevation angles are also the cause of long shadows and the rover has to be able to cope with driving through shaded regions. Here, the rechargeable battery provides the required power. In addition, if a rover shall drive into a permanently shadowed region (PSR) where coldest temperatures on the surface of the Moon occur, a battery becomes mandatory, but its operation in this cold environment poses additional challenges. Automatic traverse planning and optimisation of such rover systems can assists planning activities as well as mission operation.

One push towards peaceful exploration of our solar system was the foundation of the International Space Exploration Coordination Group (ISECG) in the year 2006. Currently, 15 space agencies are part of it to coordinate and collaborate in order to produce a vision of exploration of our solar system including also private enterprises. They released the Global Exploration Roadmap (GER) in a third revision in 2018 (ISECG 2018), which services as a reference for future exploration targets.

NASA is currently implementing a new strategy for lunar exploration with the name Artemis. It aims to land humans at the south pole by 2024 and to establish human presence at the Moon by 2028 (NASA 2019a). A former potential mission with the name Resource Prospector (RP) which was intentionally planned to launch in 2019 (Andrews et al. 2014) has been cancelled. Two requirements of the missions are defined. “RP shall land at a lunar polar region to enable prospecting for volatiles” and “RP shall be capable of obtaining knowledge about the lunar surface and subsurface volatiles and materials” (Andrews et al. 2014). Technical information on the planned rover system is sparse, but it is mentioned that operation on the lunar surface is short and that the rover relies on solar power. Recent information indicates that engineering work done on RP is transferred to the new project Volatiles Investigating Polar Exploration Rover (VIPER) within Artemis. VIPER will roam several miles during its planned life-time of 100 days near the south pole and launch supposedly in December 2022 (NASA 2019b). It shall map the presence of water in the region where humans shall land by 2024.

Future plans of the European Space Agency (ESA) to explore the Moon focus on return of humans in international collaboration and on providing scientific instrumentation on landers and rovers. The Package for Resource Observation and in-Situ Prospecting for Exploration, Commercial exploitation and Transportation (PROSPECT) is an instrument package “which will support the extraction and analysis of lunar surface and subsurface samples as well as acquisition of data from additional environmental sensors” (Trautner et al. 2018). PROPSECT will be part of the Russian lander Luna-27 scheduled to land at the south pole in 2023. Furthermore, ESA is currently preparing a mission campaign that shall prepare future human missions by sending robotic systems to the Moon first (ESA 2019). Still, ESA is actively looking at polar landing sites, which are of scientific interest. Some studies also include rover activities and traverses, but published information is sparse.

As already mentioned, China has two operational landers on the surface of the Moon by the time of writing this thesis. Their future exploration program foresees a launch of Chang’e 5 in early 2020, which shall land in the northern part of Oceanus Procellarum and return regolith samples to Earth. After that, CNSA focusses on the south pole of the Moon with the successor missions Chang’e 6 and Chang’e 7. They aim for returning samples from the south pole and also conduct scientific investigations there (Li et al. 2019).

India’s next lunar mission is not scheduled yet. After their only partially successful mission Chandrayaan-2, they team up with Japan in order to aim for a mission in 2024 with the preliminary name Lunar Polar Exploration (The Times of India 2019). A sample return is in discussion but besides that, no information is available.

The Japan Aerospace Exploration Agency (JAXA) itself is studying a mission with the name SELENE-R (Hoshino et al. 2017). It shall land in a polar region for investigation of lunar volatiles such as water ice. Additionally to its main purpose of researching resource prospecting for future mission, also scientific observations shall be part of it. SELENE-R consists of a lander and a rover, which has mass of up to 350 kg. They aim for a high precision landing in the polar region with an accuracy of 100 m and deploy its rover there. No further details are given on the rover design except that lithium-ion batteries allow access to dark and cold areas. Images of the rover show solar cells placed perpendicular to the lunar surface on the top of the rover.

The Russian space agency Roscosmos has quite ambitious goals for the lunar exploration but information is sparse and previously targeted launch dates have been delayed several times. Starting with the mission Luna-25, Roscosmos wants to send five spacecraft successively (one orbiter and four lander) to the Moon in the next years (Litvak 2016). Again, the south pole is the prime target for scientific investigations. Two of their four landers are going to carry a rover for exploration of the vicinity of the lander. Mission goals also include returning regolith samples to the Earth.

Private companies show an increased interest in the exploration of the Moon as well. The private non-profit organisation SPACEIL recently wanted to land the spacecraft Beresheet on the Moon. However, their attempt sadly failed during landing approach in April 2019 (The Planetary Society 2019).

The privately funded company ispace developed a small rover with the name Sorato as part of their mission Hakuto. Their latest flight model has a mass of only 3.8 kg and has a power consumption of 13 W. A simple and cheap production is a priority because they aim to produce dozens of it. Solar cells on the sidewalls of the rover provide power and the overall design enables operation during a lunar day at latitudes between 28° and 38°. (Acierno 2017; Walker J. 2017). There exist more private companies on the global market, which currently develop small rovers, but technical information is sparse.

Private companies are now also offering transportation to the Moon. One example is the Company Astrobotic Technology, Inc., which offers transport capabilities to lunar orbit, to the lunar surface, and even mobility on the lunar surface. It is going to send 14 payloads from NASA to the lunar surface by 2021 (Astrobotic Technology 2019a, 2019b).

1.2 State of the Art

This chapter covers two research fields that are important in order to enhance planning of rover traverses at the lunar poles. Most recent research on traverse optimisation of rovers at the lunar poles is presented in the following chapter. In the last chapter, the latest best fitting thermal models of lunar surface are discussed with respect to the dynamic simulation of the energy state of a rover along a traverse.

1.2.1 Traverse Planning for Rovers

Traverse planning is usually a highly manual process (for example Potts et al. (2015)) where an optimisation process that considers the mobility system supports planning activities. Recent research puts a lot of effort into automatic calculation of the optimal traverse but there is not one solution to the problem fitting all possible mission configurations and technological constraints. Planning of traverses for rovers depends highly on the mission needs and the design of the rover. It can make a significant difference if a short-term mission of a couple of days has to be planned or a mission lasting a couple of months or even years. The main objective of traverse planning of missions is to achieve all relevant science goals within technological boundaries. Sometimes, this includes dedicated locations to be visited (Killian and Fisackerly 2017; Speyerer et al. 2016), at other times scientific goals are only described by their features without giving a precise location which gives mission planners some degree of freedom (Elphic et al. 2017; Potts et al. 2015; Steenstra et al. 2016). Then, it could still be decided during mission operation where exactly these goals can be achieved. The meaning of traverse planning is to ensure that all goals can be achieved while fulfilling technological constraints of the exploration system such as temperature limits, power limits, mass limits, communication limits, and more. On top of that, traverse planning can provide means of reaching mission goals of secondary order if available resources exceed previous calculations. For example, it might be possible to prolong mission time with the help of sophisticated traverse planning or to extend the covered area of exploration. With that, more data of science instruments can be collected.

There are several tools for supporting traverse planning and many of them are mission specific whilst others are part of bigger software packages used and developed by agencies for different missions. Furthermore, a distinction is necessary between mission planning activities including scheduling of operation and traverse planning along waypoints only. In this thesis, the focus lies on improving the traverse planning process between two points, which shall give guidance in mission planning in the future. The following chapter shall give an overview of current state of the art in traverse planning for future mission studies related to operation scenarios at lunar poles. Common to all is the ability to account for maximum slopes along the traverse that the rover system can cope with. Consideration of other constraints differs from publication to publication and they are outlined in the description hereafter. Publications are only considered if they have at least a proper illumination assessment implemented in their planning algorithm. At the vicinity of poles of the Moon, it is mandatory to consider insolation along a traverse for planning if the Sun is the main energy source for the rover system. Due to high angles of solar incidence, prolong shadows exist which have a big influence on the temperature of the surface of the Moon as well as on the rover itself including possible energy harvesting by solar cells. Hence, more sophisticated traverse optimisation is needed with additional components to be considered than locomotion aspects only. Most publications focusing on science goals along their traverse treat illumination conditions with strong simplifications such as average illumination over one year (Allender et al. 2019; Potts et al. 2015).

The mission Resource Prospector from NASA aimed to land a rover to a polar site on the Moon (Andrews et al. 2014). Unfortunately, it has been cancelled in April 2018. By that time, researchers already published conference papers and journal articles about potential landing sites as well as potential traverses at specific locations (Elphic et al. 2017; Heldmann et al. 2016). Both publications use different tools for deriving an optimal traverse but they need the same input parameters such as solar illumination, a terrain map with slopes, calculation of communication possibility, and stereo imagery from LRO NACs. Elphic et al. (2017) present two landing sites at the south pole (crater Nobile at 85.194° S, 35.436° E, crater Shoemaker at 87.185° S, 59.921° E) and two landing sites at the north pole (crater Erlanger at 87.19° N, 29.119° E, crater Hermite-A at 87.436° N, 49.039° E). They show an exemplary traverse but without giving further details. They also mention that a tool is needed that is able to support with predictive calculations in real-time so that the operator can base decisions on that during mission operation. This tool shall also handle time-varying constraints, i.e. solar illumination and communication, in combination with static constraints, i.e. terrain slope map.

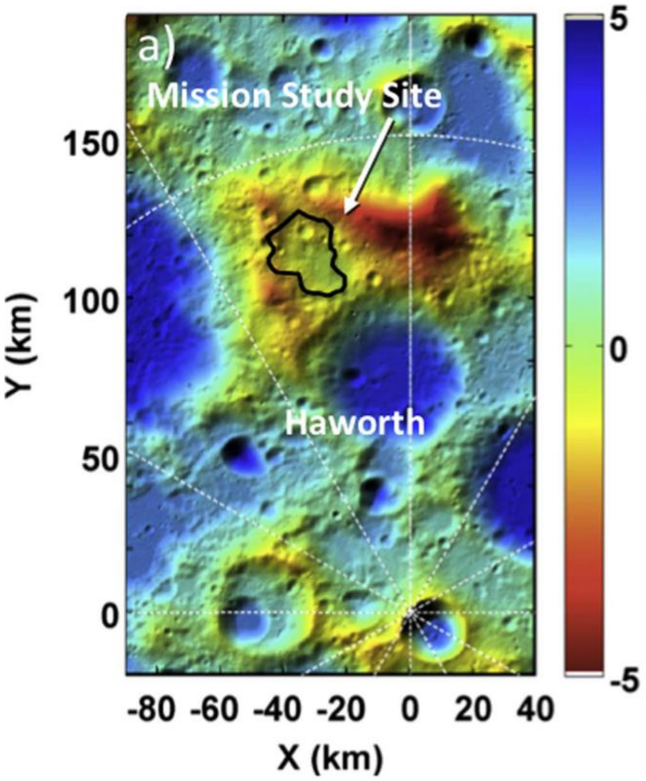

Figure 1: Mission study site for Resource Prospector. Colour scheme refers to height above reference sphere [km]. Image source: (Heldmann et al. 2016)

Heldmann et al. (2016) describe traverse options at a specific landing site north of Haworth crater, which Figure 1 shows in a crop of the south pole map. Their tool set allows for consideration of the same set of constraints as in Elphic et al. (2017). They describe mission goals for Resource Prospector with the minimum goal of making measurements at two locations at least 100 m apart. “Full success requires measurements from two locations on the Moon separated by at least 1000 m surface and subsurface measurements (where subsurface measurements are specifically obtained with a drill for sample collection), measurements in and a sample acquired from a shadowed area, and demonstration of ISRU. Stretch goals include making subsurface measurements (with an auger) in at least eight locations across 1000 m (point-to-point) distance, making subsurface measurements (sample and processing) at least four locations across a 1000 m point-to-point distance, and providing geologic context.” (Heldmann et al. 2016). Based on these success criteria, they developed a traverse plan fulfilling all of them. The final traverse is about 5 km long and it takes the rover 140 h and 19 min to finish it. Figure 2 highlights the traverse in a series of simulated illumination at the site. Sun reaches the rover all the time except for its trips into PSRs because its power system consists of solar cells, which require nearly permanent illumination. Heldmann et al. (2016) mapped the entire traverse manually under time varying constraints with a constant rover speed of 0.02 m s^{-1} checking at each time step whether constraints are met. As this is a time consuming process, they state that “the RP mission would benefit from an automated cross-check of the traverse plan against all known constraints and/or inputs” (Heldmann et al. 2016). Furthermore, with automation of the planning process it could be possible to maximise the time available for science operation on the surface of the Moon.

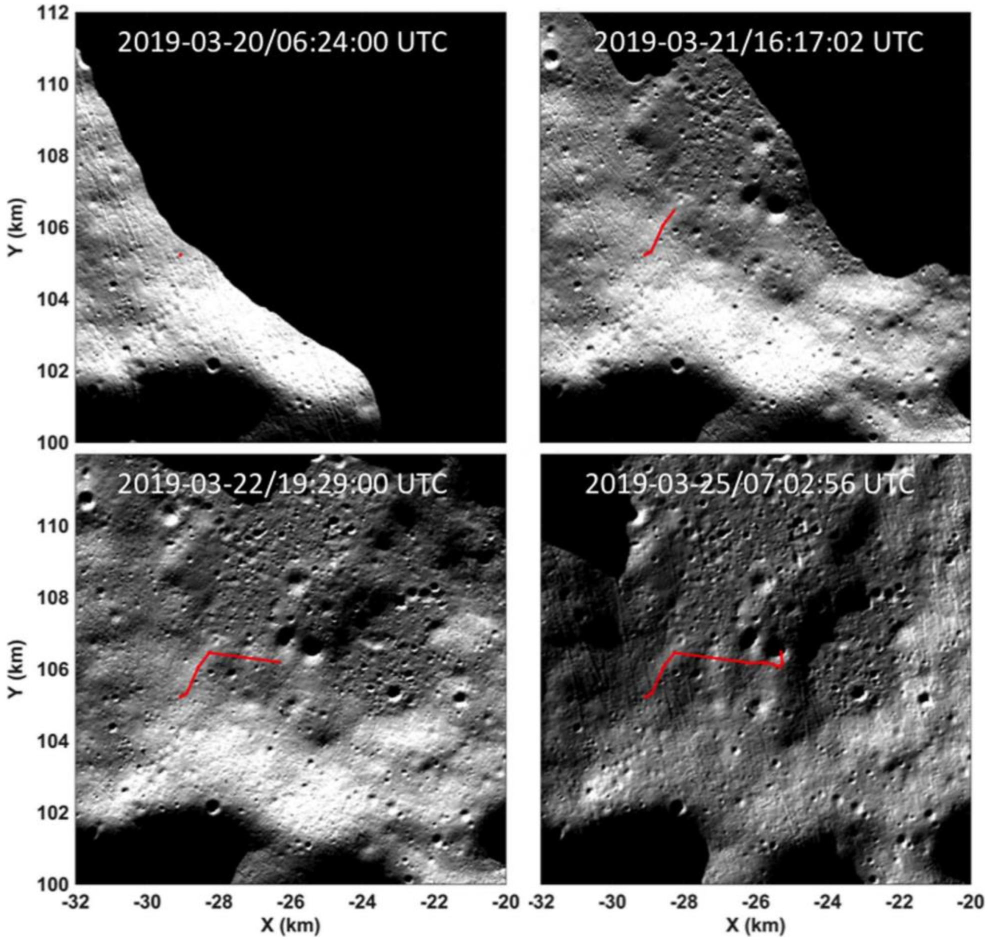

Figure 2: Series of time steps demonstrating a potential traverse of Resource Prospector at landing site immediately north of crater Haworth. Image source: (Heldmann et al. 2016)

Bresina et al. (2017) extended capabilities of the tool chain used by Heldmann et al. (2016) with automatic processes. They use an approach that performs optimisation “within a space of minimum-time paths, which is determined via the reachability analysis” (Bresina et al. 2017) due to high computational demand if global search space was used. Still, the user of their tool has to aid traverse planning with additional manual input. This includes specification of period of time for which reachability on the surface of the Moon is calculated as well as defining a landing site and a start date for surface operation. Output of the tool is a map highlighting all points on the terrain that the rover can reach within the defined period if it drives with constant speed. It is also possible to overlay information on this map such as an ice stability map. After manually choosing a station point, the tool calculates a reachability map from the marked point and the user can select the next station point. This process is repeated until the mission ends. An example of a manually selected station point is highlighted in Figure 3. After definition of all station points, the tool calculates automatically the optimal traverse along those points taking account of the order of station points. Traverse planning in this case is a semi-automated process, because the user has to intervene stepwise in between calculations. Example here is also resource prospector mission of NASA. They mention in the section future work that consideration of energy should be implemented in traverse planning.

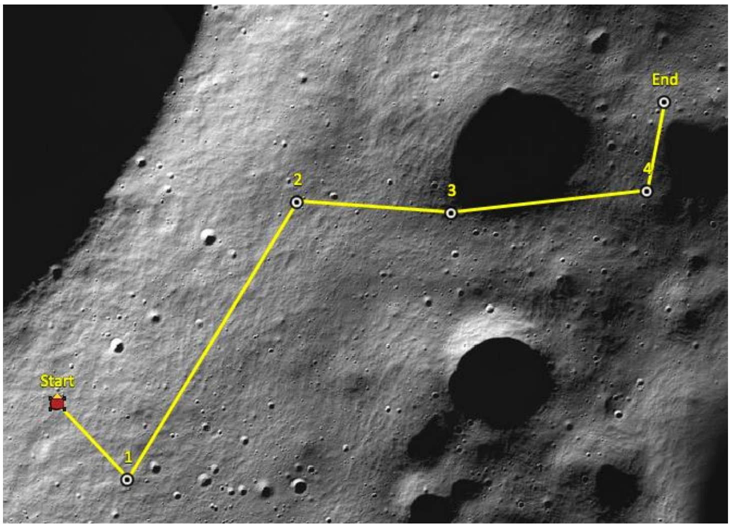

Figure 3: Example definition of six stations of mission RP. Image source: (Bresina et al. 2017)

Otten et al. (2015) present an automated process at other locations at the lunar poles. They do not look for traverses for a specific mission but in a general manner. In their publication, they present a planning tool that considers dynamic illumination and terrain slopes, lacking the ability for consideration of communication constraints. Their intention is to prove that sun-synchronous traverses exist at the vicinity of lunar poles along which the rover receives direct sun light all the time. They present two traverses fulfilling this condition, one close to Malapert crater and one close to Shackleton crater. An approach with the name connected component analysis was used in order to create three-dimensional maps of terrain nodes that are connected by time and are always sun lit. Those maps are then searched by their optimisation algorithm adapted from A* for finding the shortest traverse with the rover always being sun lit. A* is a widespread heuristic optimisation algorithm and chapter 2.1 gives a detailed description about it. The tool chain of Otten et al. (2015) evolved further and the constraint of direct-to-Earth (DTE) communication is now considered additionally. “A 74-Earth-day route near Nobile Crater on the Lunar South Pole serves as a proof of concept that there exist multi-month routes that satisfy hard constraints on both sunlight and DTE communication simultaneously, assuming the topographic maps used to generate predictive models are sufficiently accurate” (Otten 2018). Figure 4 shows this traverse in a series of four frames overlain with colours from constraints maps. This traverse has a total length of about 63.5 km and was optimised with the A* approach in two iterations. First, an A* search on a lower resolution grid of 80 m per pixel finds a traverse with minimum distance along a certain number of manually chosen waypoints. Second, A* search on the fine mesh with 20 m per pixel and the previously calculated traverse as waypoints defines the final traverse. The digital elevation model used in his optimisation is a product from Geosciences Node of NASA's Planetary Data System (PDS) derived by measurements of LRO DLRE. In his outlook for future work, he emphasises that the thermal state is important for planning and should be implemented as additional state in the planning process. Solar illumination is provided as map with assuming illumination of the rover at ground level.

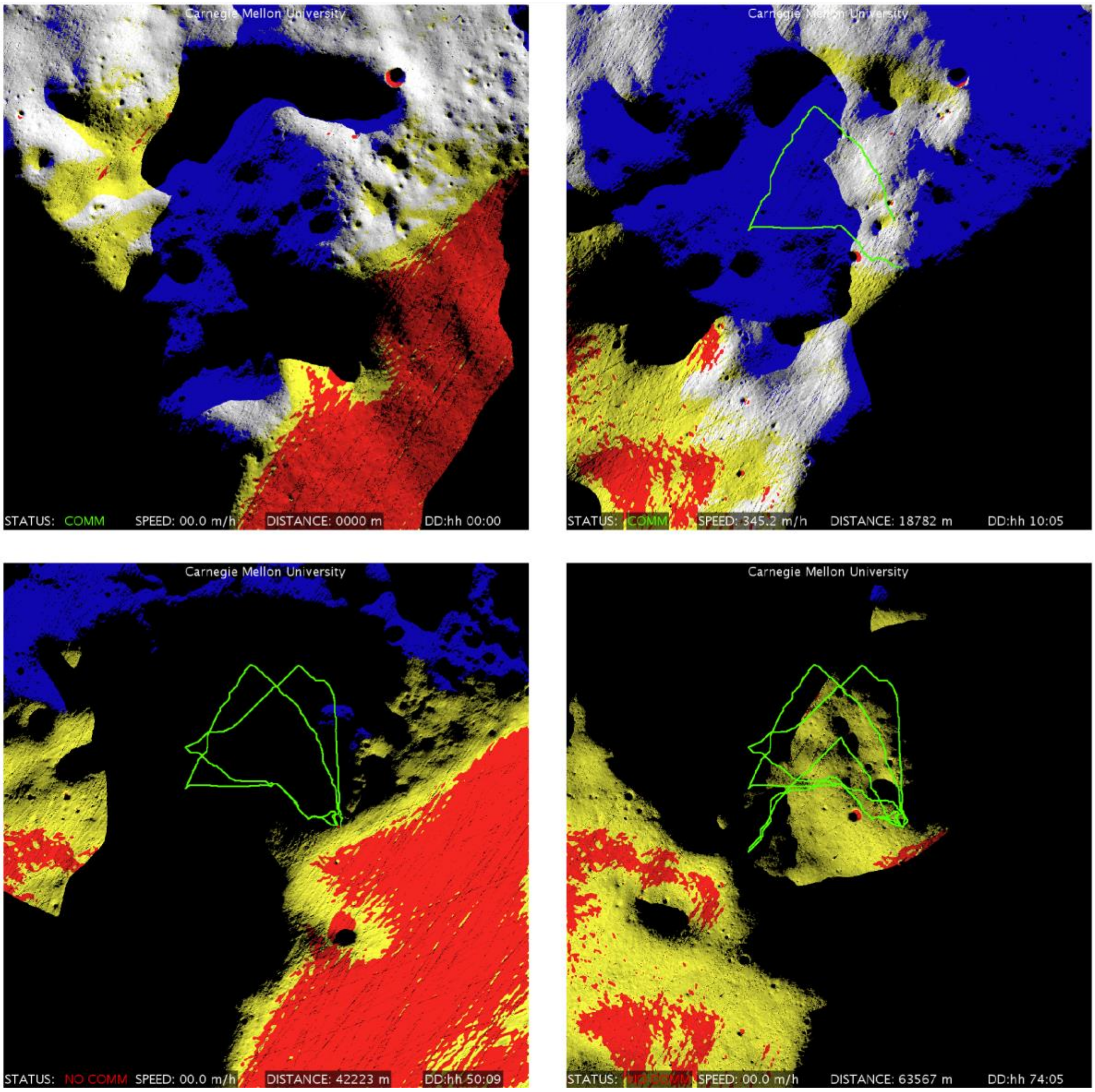

Figure 4: Traverse along rim of crater Nobile. It is a prolonged solar-powered traverse spanning 74 Earth days. Colour is as follows: white = sunlight and communication, yellow = sunlight only, blue = communication only, black = neither sunlight nor communication, red = slope steeper than 20 degrees. Times are 0, 10, 50, and 74 Earth days from left to right and top to bottom. Image source: (Otten 2018)

Speyerer et al. (2016) published an article describing traverse optimisation at the south pole with incorporation of an advanced digital terrain model (DTM). In this DTM, elevation data from orbital measurements is co-registered with stereo image information. This resolves issues of improper aligned tracks of elevation data within the terrain data as can be found in terrain models used in literature (Bresina et al. 2017; Heldmann et al. 2016; Otten et al. 2015; Otten 2018). The tool from Speyerer with the name R-traverse can also consider illumination as a spatiotemporal constraint if required. Figure 5 shows the investigated region at the rim of Shackleton crater and the connecting ridge towards de Gerlach crater within which seven stations can be visited by the rover. Simulation and optimisation time cover the entire year of 2021. They allowed the rover to drive as long as it receives direct illumination at 2 m above ground, stopping as soon as illumination vanishes. An empirical model for the power need during driving which also considers a dependency on slope is part of the optimisation process Top speed of the rover is set to 0.0083 m s^{-1} (30 m h^{-1}) leading to a total distance of the traverse of 22.11 km. During the whole time, the eclipse lasting longest is about 101 h and the rover receives direct illumination for 94.43 % of the time. Doubling the speed of the rover did not alter results in a meaningful way. The Optimisation algorithm is based on A* with adding the option to remain at the same location instead of moving to a neighbouring node. It allows finding the traverse with the lowest energy consumption between station points.

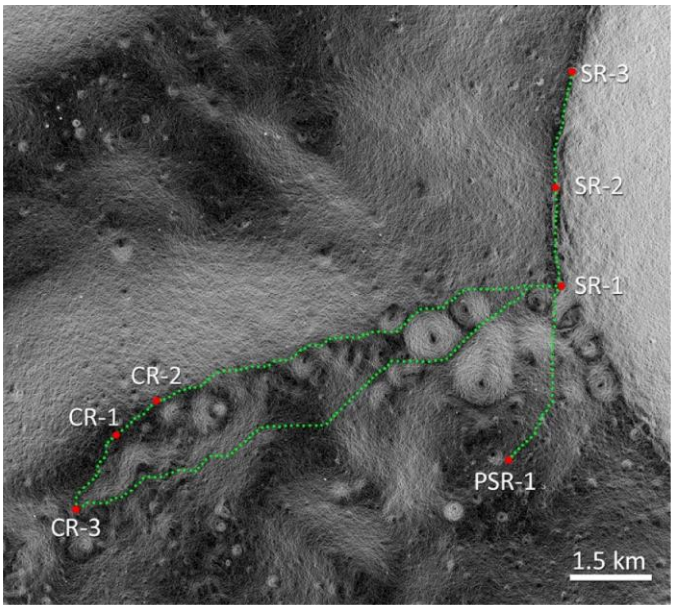

Figure 5: Optimal traverses on a NAC/LOLA slope map. Image source: (Speyerer et al. 2016)

In 2013, Wu and Ju presented a mission integrated method for path planning including simulation of energy demand. This publication is not about traverse optimisation only but about mission timeline optimisation including traverse optimisation. However, they give no explanation how calculation of a thermal model is conducted. They calculate a value of T dependant on the angle of solar cell area, the heading angle of the rover, and the angle towards sun. T can have a value of either 0 (task is not performable) or 1 (task is performable) at each time step and Wu and Ju (2013) state that “the value of $T(\alpha,\beta,\theta)$ needs to be computed under thermal control demand, and it is not the main job of this paper.” No further information about thermal control is given and it is not clear whether heat exchange with the surface of the environment is considered in their approach. They also use A* for optimisation of the traverse where energy is calculated in the cost function. Their process ensures that the energy stored within the battery is always within its permitted range. Results of their traverse planning process includes the dynamic evolution of energy stored within the rover and a mission timeline where pre-selected tasks are performed by the rover whilst their optimisation tool fills the time gaps between those tasks.

Another mission planning tool was developed by Tompkins (2005) and is called TEmporal Mission Planner for the Exploration of Shadowed Terrain (TEMPEST). It was designed to include all relevant features of mission planning for rover operation on a planetary body. This encompasses a terrain model, illumination, a rover model including power state, communication availability and many more. Optimisation is done by what he calls an incremental search engine based on D*. In two examples, Tompkins shows that TEMPEST can optimise battery power generation of a solar powered rover with spatiotemporal lighting variation. Those examples refer to experiments carried out at sites on Earth only. An application for planning activities on the Moon is mentioned in this publication but no example is shown. Furthermore, no thermal model of a rover is considered in this publication but in theory, it should be possible to implement it in his code.

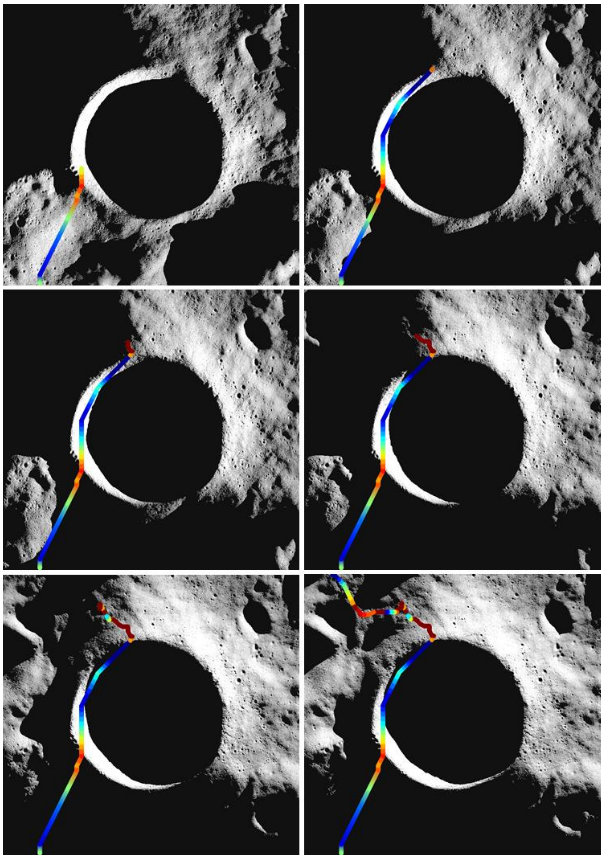

Figure 6: Traverse optimised with a hierarchical planner based on A*. Image source: (Cunningham et al. 2014)

Cunningham et al. (2014) published an article describing a hierarchical planner based on A* for application to activities at the lunar poles. They aim for integrating thermal and power state of a solar powered rover in their optimisation algorithm. Just as Otten (2018), they include a sophisticated terrain model and illumination conditions at their investigated side at the south pole but the thermal model of the rover is simple and does not interact with the lunar surface. They model a radiator plate on top of the rover, which defines the temperature of the entire rover by applying a heat capacity, absorbed solar power, internal power, and emitted infrared radiation on this radiator. The surface of the Moon is not thermally modelled. Figure 6 highlights an example of an optimised traverse coloured with the energy of the rover along the traverse. As a finding, they state that “it was difficult to tune the thermal model to produce interesting results” (Cunningham et al. 2014), probably due to neglecting the infrared environment of the surface of the Moon or their implementation of a the thermal model is too prohibiting. In an update of their optimisation algorithm, Cunningham et al. (2017) discard the thermal state of the rover entirely. They focus on improving performance of their algorithm and extend its capabilities to cover direct communication to Earth. Energy state of the rover is still tracked and simulated but without a thermal model. With a pre-computed heuristic map, they achieve faster performance. In combination with temporally compressing graphs (i.e. maps), they speed up calculation time even further. The optimisation algorithm from their previous publication remains unchanged with only minor performance adjustments added.

There are additional publications available which describe how optimisation after spatiotemporal constraints can work but none of them includes a dynamic thermal environment for the planning process (Fink 2008; Fink et al. 2015; Johnson et al. 2009).

To sum it up, there are already tools or approaches published, which can handle dynamic illumination conditions at the lunar poles, and some of them even the energy state with two of them include a simple thermal model. One commonality between all optimisation algorithms is that they can handle slope limits of the terrain as a boundary condition, which is necessary due to the rough nature of the terrain on the Moon. However, no publication incorporates a thermal model of the Moon during optimisation neither a sophisticated thermal model of a rover that interacts with the thermal environment of the lunar surface.

Especially the interaction of a thermal model of the rover with its environment is difficult to achieve during optimisation.

1.2.2 Thermal Models of the Moon

Thermal models of the Moon have a long history dating back to the early 20th century. Only the most important evolution of those models is presented in this chapter concluding with implementations of the most current models. Over the last two decades, there seemed to be a consensus on a generally used model, which is accurate enough even though in-situ thermo-physical data of the lunar surface was only available through the data collected during the Apollo program. Literature refers to that as “the two-layer model”. However, with missing information on the real composition of the lunar surface at different locations, this model has some uncertainties. Its main purpose is to predict temperatures on the surface of the Moon with a geophysical meaningful model. It shall provide information about the composition of the soil, the history of the Moon, the formation of the Moon, and the location where volatiles on the surface could exist. Accuracy of thermal models became better with time as more remote sensing data were available with scientific improving the existing temperature and terrain data with a wider coverage and results.

As already mentioned, current models such as the two-layer model share the common approach of having an insulating less dense top layer with only view millimetres in thickness and a thicker more dense bottom layer underneath up to a depth of two meters. Thermo-physical properties differ in both layers.

Two types of models are used for scientific purpose. This is on the one hand a thermal equilibrium model where no ray tracing is required and on the other hand a heat diffusion model in combination with ray tracing for heat transfer by radiation. Both models fulfil different requirements. While calculation of the thermal equilibrium model is much faster than the heat diffusion model, it cannot be used for all kind of simulations. There are occurrences during a lunar day (one lunation) where conditions on the surface of the Moon are not in thermal equilibrium, for example at sunrise and sunset and during a lunar night (Bandfield et al. 2015). Consequently, this type of model produces erroneous results at those dynamic conditions, which occur more often at the poles due to high solar angle of incidence.

The following paragraph gives a brief overview of the history of models. First thermal models of the Moon appeared in 1930 (Pettit and Nicholson 1930), followed by the late 1940s to 1960s (Jaeger 1953; Jaeger and Harper 1950; Krotikov, V. D., and Shchuko, O. B. 1963; Linsky 1966; Wesselink 1948; Winter 1967; Winter and Saari 1969) either having a homogenous layer of regolith or several layers. Models of that kind are not considered in further publications because they did not produce results as accurate as models with two or more layers. The first model that suggested the presence of a two-layer composition of the surface was developed by Piddington and Minnett (1949). However, at that time no accurate measurements of the temperature of the Moon or of physical properties of regolith were available in order to improve their model.

Models were refined with the Apollo program of NASA in the 1970s as returned samples of lunar regolith could be examined in laboratories and in-situ measurements close to landing sites on the Moon became available. It also became evident that the suggested temperature dependent conductivity of regolith exists (Cremers and Birkebak 1971; Horai et al. 1970; Horai and Fujii 1972; Krotikov, V. D., and Shchuko, O. B. 1963; Linsky 1966; Menzel 1969) and also that its heat capacity is a function of temperature (Robie et al. 1970). With this new information the most up to date model at that time was developed by Cremers et al. (1971).

After two decades without any major update to thermal models of the Moon, Vasavada et al. (1999) established the two-layer model based on Mitchell et al. (1972) and heat capacity derived by Ledlow et al. (1992) with incorporation of heat diffusion which became the standard of today’s models. Vasavada et al. (1999) analysed the possibility of stable polar ice deposits on Mercury and the Moon by simulating near-surface temperatures. In their model, both layers are separated by a sharp boundary in density as well as in thermal conductivity.

Paige et al. (2010b) took this model in order to simulate temperatures at the poles of the Moon with terrain model from derived by data from the Kaguya mission. They had to slightly modify some constants of Vasavada’ s model in order to match measured temperatures from the LRO DLRE instrument to their results of local midday and midnight temperatures. For years, these two publications (Paige et al. 2010b; Vasavada et al. 1999) were the standard approach for simulating temperatures at the poles of the Moon.

Further improvements were made by Vasavada et al. (2012b) by removing the sharp boundary between both layers based on best model fit parameters to Diviner measurements at equatorial regions. This affects thermo-physical properties of the regolith, thermal conductivity, and density as well as the angle dependent value of albedo.

Hager (2013) also made use of the two-layer model in order to simulate dynamic heat loads for moving objects on the surface of the Moon. His aim was to identify dynamic heat loads in order to assess possibilities for thermal design options without using static worst cases. This could be used for evaluation of emerging technologies and help in their design process (Hager et al. 2014; Hager et al. 2015b; Hager et al. 2015a). He mainly used values from Vasavada et al. (1999) for modelling purpose in combination with a self-written ray tracing algorithm.

The latest update on the two-layer model comes from Hayne et al. (2017). They used measurements from Diviner in order to slightly improve the model from Vasavada et al. (2012b) trying to determine global regolith thermo-physical properties between -±70 N. The resulting parameters deviate only slightly from previous values and they do not change the nature of the modelling approach. As this is the most up to date thermal model of the lunar surface at the point of writing the thesis, it was implemented in TherMoS-X as presented in this thesis. Chapter 3.1.2 gives a detailed description of this model.

Currently, other studies implemented and made use of the two-layer model as well. They use either values from Vasavada et al. (2012b) (Gläser and Gläser 2019) or from Hayne et al. (2017) (Warren et al. 2019). However, the size of terrain in their simulation differs drastically. While Gläser uses terrain data separated by 180 m and an overall area of 60 km by 60 km, Warren modelled the terrain with a resolution of 230 m in one case but considered terrain size of only 9 km by 9 km for shading effects. They both focus on simulating ice stability maps in order to answer scientific questions and to find most promising sites for exploration. Both compared simulation results with measurements from DLRE instrument, but Warren shows only results for a rough terrain with a resolution of 2 km per pixel. Hence, measurements and simulation data are averaged over the terrain making it hard to draw proper conclusions from that comparison. The focus of their model lies on implementing the angle dependency of thermos-optical properties of regolith. Results from Gläser are shown in Figure 7. Model temperatures show a good agreement with measurements from DLRE with a Pearson correlation coefficient of 0.944.

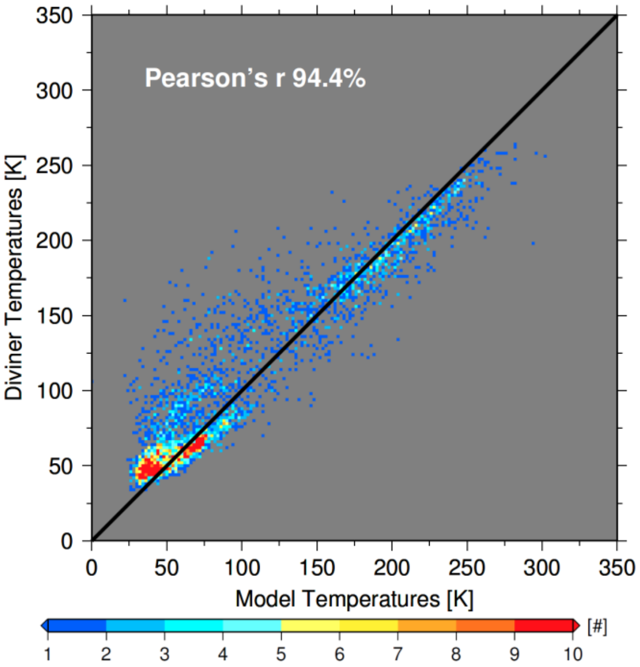

Figure 7: Temperature comparison of modelled and measured temperature data at south pole. Image source: (Gläser and Gläser 2019)

Another possibility to simulate temperatures on the Moon is the thermal equilibrium model. Here, the temperature of the surface is represented by an equilibrium of incoming and outgoing radiation. As the name suggest, it works only if the surface is in thermal equilibrium, which is not the case during lunar night, at sunrise and sunset. Hence, it works only for equatorial regions up to latitudes of about 70°, but it has the advantage of fast computation. For some scientific questions this is sufficient as used by Bandfield et al. (2015) in order to estimate the surface roughness based on measurements or to determine distribution of H_2O/OH^- (Bandfield et al. 2016; Wöhler et al. 2017). This kind of model is not explained in detail here due to its limitation of simulating the dynamic thermal behaviour of the surface of the Moon outside the equilibrium state, which, as described before, is required at the lunar poles.

As a conclusion, a thermal model that shall accurately represent conditions at the lunar poles throughout a lunation has to use the two-layer assumption of regolith and to consider solar heat radiation as well as infrared heat transfer between surface elements. Furthermore, additional improvements on thermal modelling of the surface of the Moon seems only feasible by gaining more knowledge about the composition of lunar regolith by conducting in-situ measurements at different locations on the Moon. Also, rock abundance has an effect on the temperature and needs further research (Hayne et al. 2017). Table 1 gives an overview of the current models and their implementation.

Table 1: Summary of most recent thermal models and current implementations

Author	Simulation approach for insolation	Year	Comments
Gläser et al.	Horizon method, solar angle calculated	2019	Based on Vasavada et al. (2012b)
Warren et al.	Not given	2018	Based on Hayne et al. (2017)
Hayne et al.	Solar angle calculated	2017	Update of Vasavada et al. (2012b)
Wöhler et al.	Solar angle calculated	2017	Equilibrium model
Bandfield et al.	Solar angle calculated	2016	Equilibrium model
Hager	Ray tracing	2013	Based on Vasavada et al. (1999)
Vasavada et al.	Solar angle calculated	2012	Update of Vasavada et al. (1999)
Paige et al.	Ray tracing	2010	Based on Vasavada et al. (1999)
Vasavada et al.	Solar angle calculated	1999	Two-layer model

1.3 Research Gaps

Literature review in chapter 1.2 revealed that up to now, traverse planning is often a labour-intensive, manual process if all systems of a rover shall be considered. Conditions at the lunar poles call for automatic planning processes with consideration of elements relevant to traverse planning. For best results, this includes a sophisticated thermal model of the Moon with realistic illumination conditions, terrain model, and an implementation of the rover state, which covers energy and thermal state. None of the publications described in the previous chapter cover all of them at the same time. Standard traverse planning incorporates the terrain itself with slopes that are either traversable or not and power demand or velocity of the rover depends on the slope. More sophisticated traverse planners factor in illumination conditions on the rover and can even find continuously sun-lit traverses. The most advanced traverse planners consider the energy state of a solar powered rover but they do not simulate thermal behaviour of the rover moving on the lunar surface and exchanging heat with its environment.

This thesis intends to implement the energy state of a rover system, which also depends on the thermal environment into traverse planning for operation at the lunar poles. Results of optimising potential traversers at the lunar south pole will identify benefits of this approach. It will help to extend mission coverage on the surface.

The following research gaps were identified through literature review.

1. The overall energy state of a rover defines whether it can successfully operate because it considers all domains and subsystems, for example thermal, power for driving, power management, power for communication etc. If a successful implementation of the aforementioned aspects is realised, precise traverse planning will be made possible and new insights into important factors influencing traverses at the lunar poles will be generated.
2. A proper implementation of the thermal environment of a rover operating at the lunar poles is mandatory. A sophisticated thermal model of the surface of the Moon provides the environment but the treatment of heat transfer between environment and rover during optimisation requires further research.
3. The implementation of the energy state of the rover into an optimisation algorithm is crucial. Dynamic environment as well as dynamic behaviour of the rover system has to be considered by the algorithm. Several algorithms could be identified during literature review but research is needed on necessary modifications. The outcome has to be an algorithm that can conduct an optimisation in a dynamic environment.
4. After addressing the above stated research gaps, the achieved results with the novel approach call for a general evaluation of the approach with respect to the current state of the art. This will answer the question when the consideration of the energy state including thermal simulation during traverse optimisation provides benefits to missions.

1.4 Scope of this Thesis

The primary objective of this thesis is to implement the energy state of a solar powered rover into traverse planning process and determine possible benefits for missions to the lunar poles. It is clearly outlined in the previous chapter that this part is not covered by any of the existing approaches and that the main novelty of the presented work is the implementation of a comprehensive thermal model of both, the Moon and the rover. This new approach could support a mission at an early stage where only few technological details of the rover system are defined. It would be possible to assess different landing sites of scientific interest and the accessibility by a rover taking into account more aspects of mission planning and operations than previously possible.

1.4.1 Objectives

The main research question, whether an implementation of the energy state of a rover in traverse optimisation of a mission to the poles of the Moon is beneficial, is a primary objective. This cannot be reached without covering another primary objective, an accurate thermal model of the surface of the Moon.

Primary objectives are postulated as follows:

1. Demonstrate benefits of traverse optimisation considering the energy state for operation of solar-powered rovers at lunar poles.
2. Implement the most current thermal model of the surface of the Moon and assess its suitability at the lunar poles.

In order to achieve those primary goals, fulfilling supplementary objectives in a stepwise procedure is a suitable approach. Some of them are highlighted in the following paragraph to give the reader an overview of necessary tasks that were performed within this thesis.

The most recent thermal model for simulation of temperatures of the surface of the Moon has to be implemented and its capability to predict temperatures at the lunar poles has to be critically assessed. Because the Sun rises only to low elevation angles at the poles due to the characteristics of the orbit of the Moon, a rugged topography with high variation in local height at the lunar poles creates long shadows and a precise digital terrain model is required. There is a need to define the size and the resolution of the scene in order to simulate thermal conditions properly at the investigated location. In addition, available computational power and the duration of the simulation period have to be considered here. An optimisation algorithm needs to be identified and adapted for automatic creation of traverses of a rover. This rover system has also to be defined and implemented in order to simulate its energy state. Only solar powered rovers, which generate their power by converting solar radiation into electricity, are considered in this thesis. Finally, traverses with a specific rover system have to be computed in realistic scenarios. Those scenarios have also to be defined first.

By accomplishing the mentioned objectives, it is eventually possible to estimate benefits of considering the energy state of a rover including a thermal model during traverse planning. This could be potential energy savings, proper sizing of battery capacity, prolonged mission time for more scientific return and more.

1.4.2 Approach

In a nutshell, the approach was to improve an already existing simulation tool (TherMoS) so that simulation and traverse optimisation at the lunar poles became possible. The name of this extended software tool is TherMoS-X. Two assumptions were made and applied throughout the entire thesis.

The first assumption was that it is acceptable to examine only locations at the south pole. This is justified by the fact that the topography is more rugged and the extreme values in height above the reference sphere of the Moon are much higher than at the north pole. As a result, the local horizon at locations at the south pole can be further away which leads to larger scenes to be modelled for proper illumination conditions. Hence, if the simulation tool performs well at locations near the south pole, it will also perform well at locations near the north pole. Chapter 2.3.3 gives more details about conditions at the lunar poles in general. Furthermore, most currently planned missions aim to land near the south pole, which bolsters this assumption.

The second assumption refers to optimisation itself. It is not required to find the absolute optimum for a traverse (e.g. based on slope, illumination, Earth visibility, and energy state of the rover) in order to produce meaningful results on the topic of this thesis. Instead, also a near-optimal traverse between two points is considered adequate as long as the energy state of the rover – the major constraint of a mission – remains within its limits. Even though algorithms exist, which allow finding the absolute optimum of a traverse, the computational demand strongly increases with the number of variables rendering optimisation within an acceptable time frame impractical.

In order to derive an optimal solution to a problem it is necessary to define clearly the property that shall be optimised. In the case of traverse planning this is often the shortest or the fastest traverse possible. From a mission perspective, many different parameters might be more important such as best scientific return, lowest stress on the thermal system of the rover, most benign charging conditions on the battery, best communication possibilities, and many more. Optimisation in this thesis focused on the shortest traverse possible to achieve with constant speed of the rover under technological constraints of the rover system. Consequently, the result is also the fastest traverse possible. Technological constraints include temperature limits of the internal of the rover, battery capacity, power demand for driving, maximum slope the rover can drive along, power demand for communication, and power demand for heating.

The implementation of the thermal model of the Moon and the optimisation algorithm were written in MATLAB® and Nvidia® Optix®, which is based on the programming language C++. A simulation tool for dynamic simulation of the surface of the Moon including moving objects on the surface was previously developed at the Chair of Astronautics at TUM (Hager 2013) with the name TherMoS. However, the tool itself was not able to optimise traverses and to simulate temperatures of the surface of the Moon at the lunar poles due to several reasons outlined in chapter 4.1. Major updates were necessary on the thermal model in order to simulate lunar poles properly and the ray tracing code needed a major revision. This also affected the digital elevation model (DEM) as the previously implemented topography from LRO data was not accurate enough for local simulation of the temperature.

The implemented updates were verified in several steps culminating in a comparison of simulated temperatures with measured temperatures from LRO DLRE. With a simulation tool capable of handling polar conditions, the optimisation was then also implemented in MATLAB®.

Chapter 1 of this thesis covers an intensive research of the state of the art for traverse planning at lunar poles and thermal models of the surface of the Moon. Chapter 2 explains fundamentals needed for an implementation of traverse optimisation, which are potential planning algorithms, conditions at the lunar poles, and thermal modelling. The thermal model of the Moon and the model of the rover are presented in chapter 3 with validation of the Moon model at the south pole. Chapter 4 describes the updates necessary for TherMoS, their implementations, and additional tools. Furthermore, the optimisation algorithm is outlined in this chapter. Chapter 5 presents analysis cases near the south pole and their results. As this approach might also be useful for missions to Mars, its applicability for that is evaluated in chapter 6. Finally, an assessment of the topic of this thesis based on results is given in chapter 7.

2 Fundamentals

2.1 Planning Algorithms

A wide variety of different techniques in order to derive optimal and nearly optimal traverses between two points has been discussed in countless publications. This chapter gives an overview of the most common ones used for global traverse planning. Furthermore, a definition of an optimum is necessary. Amongst others, this can be the shortest distance, the least energetic costs, the fastest traverse, and the least inclined traverse. Most common is the definition of an optimum as the shortest or fastest traverse. It is also possible to combine different characteristics and implement them with different weightings. It is also possible to state additional boundary conditions, which render certain areas as not traversable. Algorithms used in traverse planning are usually based on techniques from robot path planning. The classic path planning problem is to find a collision free path from a start point to a goal point while moving within a given subset of points. Figure 8 gives an overview of a classification of approaches for robot path planning and for more information about optimisation methods the reader can refer to (Koubaa et al. 2018). The term path planning refers to any kind of robot motion such as driving, moving a robotic arm, turning, and similar kind, whilst traverse planning refers to finding a connecting path, which a rover can drive between two points or along points.

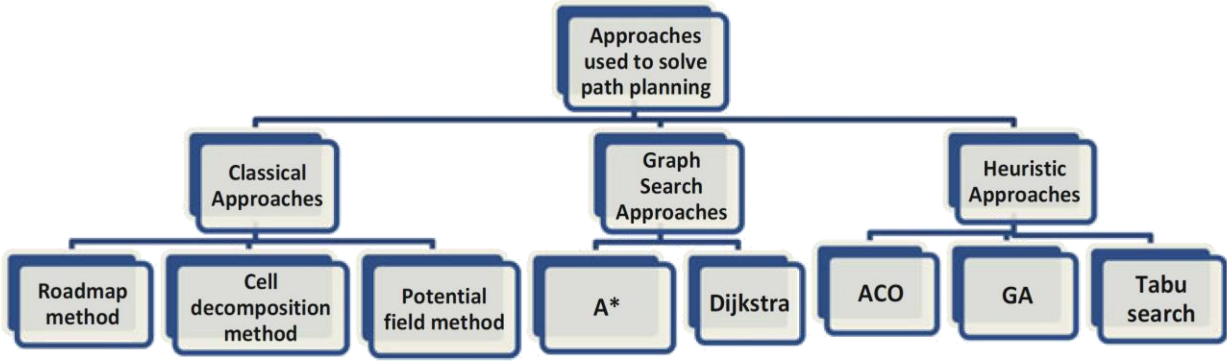

Figure 8: Path planning categories of different approaches Image source (Koubaa et al. 2018)

The classification of approaches contains three main elements, namely classical approaches, graph search approaches, and heuristic approaches. Classical methods refer to general approaches developed at the early stage of tackling robot path planning such as roadmap, cell decomposition, and potential field. They are all based on global path planning meaning that the robot has knowledge of its environment in form of a map prior to planning. However, classic approaches can become computational expensive and in some cases lead to infeasible paths or get stuck in local minimum. There are techniques to overcome those drawbacks but in general, classical approaches are not used in traverse planning of exploration rovers.

Heuristic approaches are a recent development in robot path planning. They are not able to find reliably the optimum but solutions coming close to it. All of them share two commonalities, a randomness in altering paths to find better solutions and a heuristic to probabilistic decision making on how to continue the search. Commonly known approaches are for example genetic algorithm (GA), simulated annealing (SA), neural network (NA), and ant colony optimisation (ACO). The main drawback of heuristic approaches is that there is no guarantee that they find the optimal solution. This is the main reason why they are not discussed further in this thesis.

Graph search approaches are well spread and established since the beginning of the computer age. The most well-known graph search algorithm in rover path planning is A* and it is also one of the most efficient ones (Koubaa et al. 2018). As shown in chapter 1.2.1, most recent publications discussing optimisation of traverses near lunar poles make use of algorithms based on the A* approach. This chapter describes this class of optimisation algorithms in detail. Dijkstra (1959) described an algorithm that finds the path with lowest costs connecting two nodes. However, this algorithm becomes inefficient with large amount of nodes aligned in a mesh. The so-called A* approach is an improvement of Dijkstra' s algorithm leading the search direction of it with a heuristic (Hart et al. 1968). It helps the algorithm to investigate nodes next, which will most likely lead to the final path with lowest costs. This speeds up the calculation time while still being able to find the optimum traverse defined in a cost function. The A* algorithm defines an evaluation function which estimates the costs of a traverse from start point S to a goal point G passing through point N. Equation (1) defines the evaluation function.

$$f(N) = g(N) + h(N) \tag{1}$$

The real costs from start point S to the current point N are in g(N) and h(N) is the heuristic estimation of minimal costs to reach the goal point G from the current point N. The heuristic must not overestimate real costs to the goal point and it has to fulfil the criterion defined in equation (2) stating that costs to reach G from point N has to be less than real costs to travel to next node including heuristic to reach G from next point N'.

$$h(N) \leq c(N, N') + h(N') \tag{2}$$

The real costs to travel from point N to next point N' are calculated with the function c(N,N'). This cost function has to be defined during the implementation of A*. Often the Euclidian distance is used for the heuristic and the real distance is then incorporated in function c(N,N'). The Euclidian distance d_E between two points p and q in 3-D space can be calculated with equation (3).

$$d_E(p, q) = \sqrt{(p_1 - q_1)^2 + (p_2 - q_2)^2 + (p_3 - q_3)^2} \tag{3}$$

A* operates with two lists which define the behaviour of the algorithm for the next step. One list is the open list, which contains nodes due to investigation. The other list is the closed list containing nodes, which have already been investigated. An example is given in Figure 9 with which the operating principle of A* can be explained. The algorithm finds the route with the lowest evaluation function from start node S to goal node G. The heuristic h in order to reach the goal node from any node is depicted on the right side of each node. The real costs c in order to travel along any edge to the connected node is written on the right side of the connecting line.

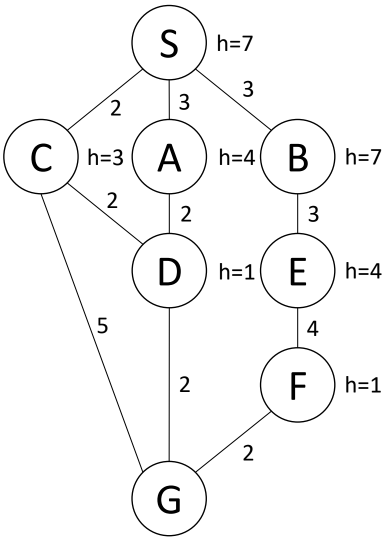

Figure 9: A* example node graph

The algorithm starts with both lists being empty. At the first step, the start node is added to the open list. After that, all nodes that are connected to the start node are inserted into the open list. In this example these are C, A, and B. The start node S is added to the closed list. The next node for investigation is C, as it has the lowest value of costs plus its heuristic value. The open lists gets update with nodes D and G, as they can be reached from node C. Now, node C moves to the closed list and node D is due to investigation as it has the lowest evaluation value. No additional node is reachable from D, but costs of G are updated in the open list. A* transfers D to the close list and in the last step, the goal node G is finally selected as the node with lowest evaluation value within the open list. If this is the case, then A* finishes as the goal node is reached. A representation of A* in pseudocode can be found in Figure 12. Table 2 lists the above-mentioned steps of A* for a better overview of the open and closed list.

Table 2: Behaviour of open and closed list of A* example

Step	Current node	Open list	Closed list
1	S	C (2+3), A (3+4), B (3+7)	
2	C	A (3+4), B (3+7), D (4+1), G (7+0)	S
3	D	A (3+4), B (3+7), G (6+0)	S, C
4	G	A (3+4), B (3+7)	S, C, D

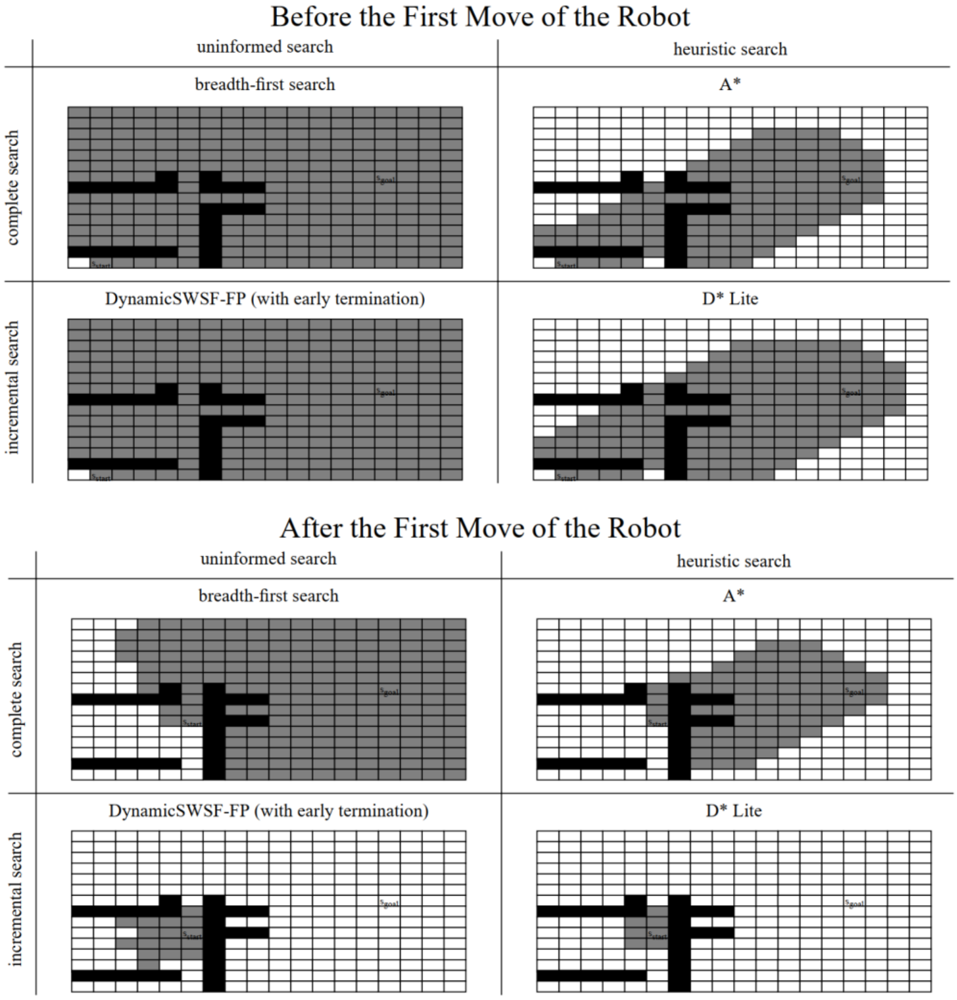

Figure 10: Grid schematic showing investigated nodes of different optimisation approaches. Image source: (Koenig and Likhachev 2002b)

The example in the paragraph above refers to a graph search tree which is usually not the kind used by traverse planning. Here it is common to have a map represented by a 2-D grid of nodes. Figure 10 depicts a gridded map with obstacles. It also shows how nodes are expanded by different optimisation algorithms in order to derive their solution of the traverse. The rover is allowed to move diagonally from one node to another, resulting in eight potential neighbouring nodes as highlighted in Figure 11 a. In this case, nodes are placed at the centre of a square within the grid of Figure 10.

The advantage of A* is that it finds the global optimum and with a suitable heuristic it converges fast as well. However, in huge grids, its performance decreases drastically. One extreme example comes from Koubaa et al. (2018) who also describe their implementation of A* as pseudocode shown in Figure 12. With a grid of 100 nodes by 100 nodes, A* takes about 114 µs to execute. With a grid 400 times as big (2000 nodes by 2000 nodes), A* needs more than 296 E6 µs in order to find the shortest path. Therefore, an increase of the grid size of 400 times leads to an increase of the computational time of a factor of 2.597 E6. Even worse is the huge demand in memory of the A* approach. Large amount of nodes are not manageable anymore by it. Consequently, A* is usually not an approach utilised by on-board computers on rovers due to this. Another drawback is that re-planning of a path is inefficient because it always starts from scratch and cannot benefit from previous optimisation. Re-planning might be necessary if costs to travel to another node change with time for example due to the appearance of a moving obstacle or a change on boundary conditions or an updated map. This has been addressed in different publications and mitigation strategies lead to further developments of A* (Koenig and Likhachev 2002a, 2002b, 2002c; Stentz 1994; Stentz and Anthony 2002). Two of them are also included in Figure 10, namely D* Lite (Koenig and Likhachev 2002a) and dynamic strictly weak superior function fixed point problem (DynamicsSWSF-FP) (Ramalingam and Reps 1996). They all aim for a faster and more efficient re-planning if new information is available for the map. In Figure 10 D* Lite is the most efficient one in terms of performance as well as in terms of nodes the have to be re-examined after implementation of new information on the map.

All of the above mention methods operate on a grid of nodes and do not find the real optimal path due to allowed movements of the rover as depicted in Figure 11 a. In order to travel from node S to the next best neighbour, only movements separated by 45° are allowed as indicated in Figure 11 a. A further development with the name field D* (Ferguson and Stentz 2006) which the Mars exploration rovers (MER) used (Carsten et al. 2007) overcomes this drawback by also allowing movements crossing an edge at any position as Figure 11 c indicates. This is realised by moving the grid nodes from the centre of the squares to the edge points of those squares. Linear interpolation can then be used at any position of an edge connecting two potential neighbours in order to calculate the real costs of traveling.

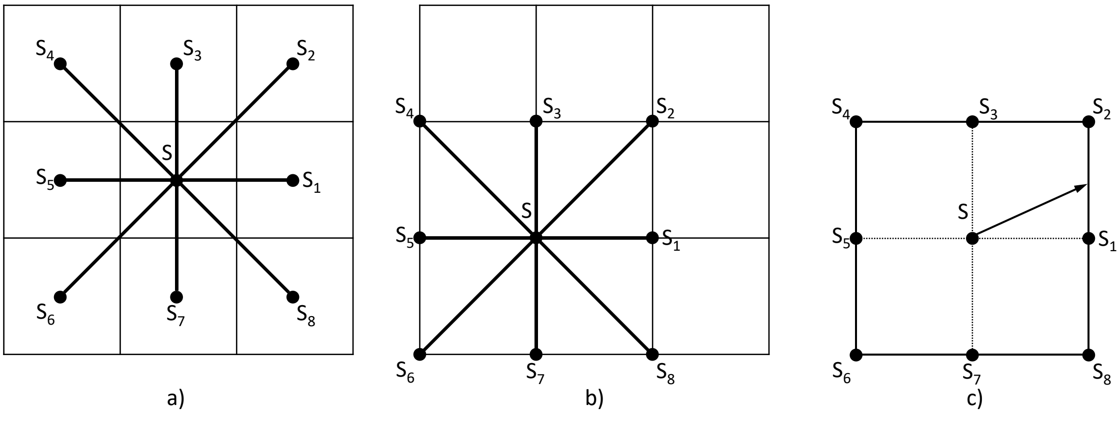

Figure 11: Standard grid and allowed movements in A* (a), in Field D* (b), and optimal path from node S (c). Image source: (Ferguson and Stentz 2006)

Other variants and further developments can be found in publications. For the purpose of this thesis understanding of the A* approach is sufficient as this is the main algorithm found in literature for global optimisation of exploration rovers operating on other planetary bodies.

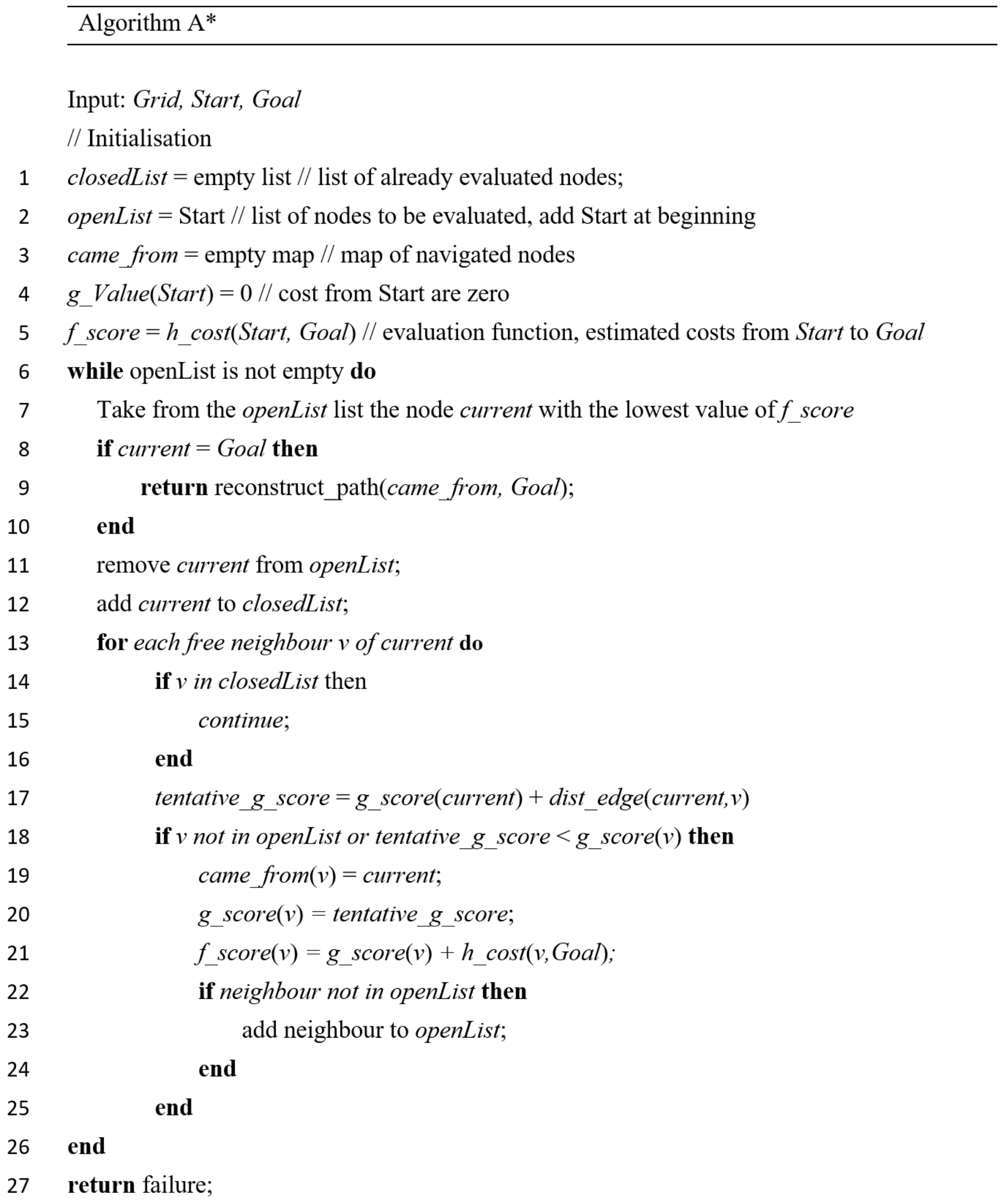

```
Algorithm A*

Input: Grid, Start, Goal
// Initialisation
closedList = empty list // list of already evaluated nodes;
openList = Start // list of nodes to be evaluated, add Start at beginning
came_from = empty map // map of navigated nodes
g_Value(Start) = 0 // cost from Start are zero
f_score = h_cost(Start, Goal) // evaluation function, estimated costs from Start to Goal
while openList is not empty do
    Take from the openList list the node current with the lowest value of f_score
    if current = Goal then
        return reconstruct_path(came_from, Goal);
    end
    remove current from openList;
    add current to closedList;
    for each free neighbour v of current do
        if v in closedList then
            continue;
        end
        tentative_g_score = g_score(current) + dist_edge(current,v)
        if v not in openList or tentative_g_score < g_score(v) then
            came_from(v) = current;
            g_score(v) = tentative_g_score;
            f_score(v) = g_score(v) + h_cost(v,Goal);
            if neighbour not in openList then
                add neighbour to openList;
            end
        end
end
return failure;
```

Figure 12: A* algorithm pseudocode. Image source: (Koubaa et al. 2018)

In order to conclude this chapter, Table 3 gives an overview of some of the main path planning algorithms. Additional comments are provided for a quick overview. For planning processes in this thesis, only algorithms, which are able to find the optimum, are considered and investigated in detail. From those, only A* or a derivative of it seems to match criteria important for this thesis as it can handle additional boundary conditions easily. The implementation of A* within TherMoS-X is presented in chapter 4.3.

Table 3: Overview of optimisation algorithms for traverse planning

Algorithm	Finds optimum	Comment
A*	Yes	High memory demand for large problems, can be slow
Cell decomposition	Yes	Can produce infeasible results (Šeda 2007)
Potential field	Yes	Might get stuck in local minimum
D* Lite	Yes	Faster re-planning than A*
Roadmap	Yes	Not efficient on grids
Genetic algorithm	No	
Simulated annealing	No	
Polynomial	No	Approaches optimum with few iterations
Random tree	No	

2.2 Thermal Modelling

Numerical models can be solved in many ways. Most commonly used are the finite-element-method (FEM), finite-difference-method (FDM), and finite-volume-method (FVM). However, in the field of thermal engineering for spacecraft, another approach is used more often. It is the so-called lumped parameter method (LPM), which is based on FVM. Detail description of this method and on thermodynamics in general can be found in literature (Gilmore 2002-©2003; Incropera 2007; Polifke 2009).

With LPM, one divides the system to be modelled into several nodes. Each node represent a volumetric part of the real system and is placed at the centre of this part where also all its mass is lumped to. An aluminium bar for example can be modelled as one node only with its entire mass bundled at this node in the centre. On LPM, a node has two properties, namely temperature and thermal capacity. It is then possible to calculate temperatures of each node depending on the connection of nodes within the thermal model. In the frame of this thesis, nodes can be connected by conduction and thermal radiation. An implementation of convection will be possible in the future, if it has to be considered in a prospective mission scenario. Eventually, there exists a thermal network representing the real system as Figure 13 exemplary depicts. In this case, seven nodes represent the thermal behaviour of a system. Nodes are connected either by conduction (K_{ij}) or by radiation (R_{ij}).

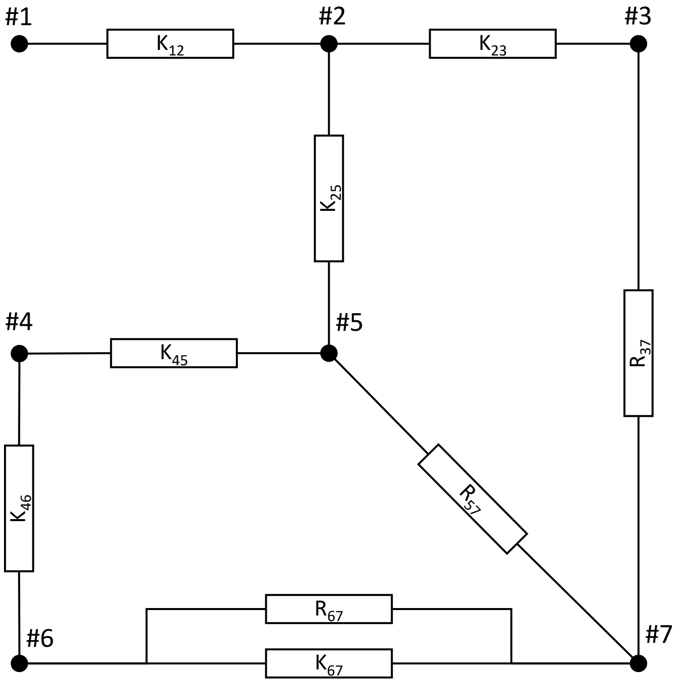

Figure 13: Example of thermal network with lumped parameter method

Each node in the thermal model is treated as a capacitor C and its thermal capacity assigned to it as defined in equation (4).

$$C = \rho \cdot c_p \cdot V \tag{4}$$

Density ρ, specific heat c_p and the volume V of the node are needed as input in order to calculate its thermal capacity.

Connection between nodes can either be of a linear type or depend on the fourth power. Equation (5) describes a connection between nodes i and j by conduction, which has a linear dependency.

$$\dot{Q}_{ij} = K_{ij}(T_i - T_j) \tag{5}$$

The transferred heat $\dot{Q}_{\mathrm{ij}}$ depends on the conductor K_{ij} and the difference in temperature of connected nodes. A conductor in general is calculated with its geometry and one thermo-physical value as described in equation (6)

$$K = \frac{k \cdot A}{d} \tag{6}$$

A denotes the cross sectional area of the geometry, d is the distance between both nodes, and k is the thermal conductivity in of the material. Determination of a conductor can be straight forward, for example if it is within a homogenous body, or it can be more challenging and several conductors have to be calculated and summed up. Here, it can either be a serial or parallel coupling just as is the case for electric resistors. Because a conductor is exactly the inverse of a resistor, its values have to be inversed.

$$K_{ij} = K_{i,n} + K_{i,n+1} + \cdots \tag{7}$$

Equation (7) describes a parallel coupling of conductors. The final value that connects node i and j is the sum of all parallel conductors n.

$$\frac{1}{K_{ij}} = \frac{1}{K_{i,n}} + \frac{1}{K_{n,n+1}} + \cdots \tag{8}$$

Equation (8) describes a serial combination of conductors. The inverse value of conductor is the sum of inverse of all conductors in series.

Heat transfer by radiation between two nodes is non-linear and depends on the fourth power of their temperatures. As for heat transfer by conduction, a factor can be defined which describes the connection between both nodes as equation (9) describes.

$$\dot{Q}_{ij} = R_{ij}\left(T_i^4 - T_j^4\right) \tag{9}$$

The radiation exchange factor R_{ij} is either defined as in equation (10) with a view factor for surfaces with diffuse thermo-optical properties or is directly derived by ray tracing. If surfaces have also or only specular thermo-optical properties, R_{ij} is usually most efficiently determined by ray tracing.

$$R_{ij} = \sigma \cdot \alpha_j \cdot \varepsilon_i \cdot A_i \cdot F_{ij} \tag{10}$$

In equation (10), σ is the Stefan-Boltzmann constant with a value of $\sigma = 5.6704\text{e-}08\ \mathrm{W\ m^{-2}\ K^{-4}}$, α is the absorptivity of the receiving node in infrared range, ε the emissivity of the transmitting node in infrared range, A_i the area of the transmitting node and F_{ij} the view factor from the transmitting to the receiving node.

With all connections between nodes known, one can calculate the temperature of each node within the network dependent on time with a differential equation (11). An internal heat source $\dot{Q}_\mathrm{i}$ can be considered additionally, if it exists. A positive heat flow in equation (11) means incoming energy on the node, hence indices of i and j have to be switched for input of temperatures in order to derive the correct sign of the heat flow and the change in temperature.

$$C_i \frac{dT_i}{dt} = \sum_{j \neq i} K_{ij}\left(T_j - T_i\right) + \sum_{j \neq i} R_{ij}\left(T_j^4 - T_i^4\right) + \dot{Q}_i \tag{11}$$

2.3 The Moon

The Moon is Earth's natural satellite and is bound to Earth for about 4.6 billion years. Its origin is still unknown, even though profound models and indications suggest that it formed after a huge body impacted on Earth. Focus in this thesis lies on exploration of the lunar south pole. For understanding the environment at the poles it is necessary to explain the orbit of the Moon because it defines illumination conditions on the surface. After describing the environment in a global context, emphasis is put on the environment of the poles describing the polar terrain and its implication on exploration mission.

2.3.1 Orbit

The geometric position of the Moon within the Earth-Sun system and its rotational axis are depicted in Figure 14. The orbital plane of the Moon is inclined by 5.145° against the ecliptic and the spin axis of the Moon is inclined by 6.683° against its orbital plane. As a consequence, the lunar equator is inclined by 1.54° against the ecliptic in contrast to Earth, which has a tilt of 23.44°. That implies that the maximum solar elevation possible for a location directly at one of the poles is also only 1.54° in contrast to Earth's poles, where maximum elevation of 23.44° is possible. The precession cycle of the spin axis lasts about 18.6 years. A sidereal month takes about 27.321 days and a draconic month about 27.212 days whilst a synodic day takes about 29.53 days to complete. Hence, a lunar day is much longer than one day on Earth which leads to three thermal environments: daytime, night time, and polar (Paige et al. 2010a). Solar heat flux dominates daytime, whilst no solar radiation reaches the lunar surface during night. In polar regions, the terrain in combination with the position of the Sun dictates which regions are illuminated.

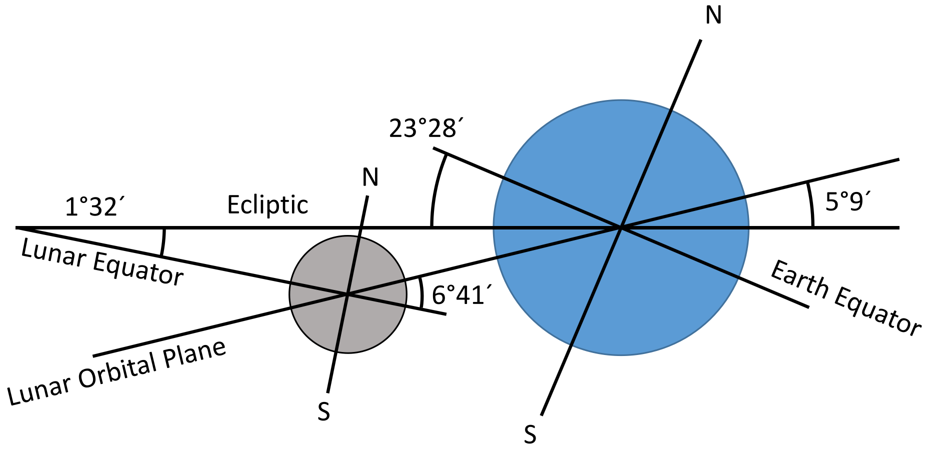

Figure 14: Geometric description of the Earth-Moon-Sun system. Reproduced from (Mutch 1972)

2.3.2 Environment

The environment on the Moon is characterised by radiation dominant effects due to the very thin atmosphere which varies between 1.3 10^{-12} mbar and 1.3 10^{-14} mbar (Johnson and Carrol 1972). Insolation is the same as on Earth with an average of 1367 W m^{-2} but without dampening of an atmosphere it reaches the surface of the Moon unchanged. A feature, which can also be seen by looking at the Moon with the naked eye, is the distinction between bright areas and darker ones on the surface of the Moon, which have the names highland and mare. Their geological composition differs and consequently their thermo-optical properties as well. Whilst their infrared emissivity is quite similar at around 0.95, their albedo differs by a factor of two. Albedo of highlands is about 20 % and of mare about 10 % in average. Local features within those regions can deviate from those values due to different geological composition coming from early volcanism or younger impacts of bodies.

Temperature on the surface of the Moon depends on the latitude because of the nearly perpendicular rotational axis of the Moon on the ecliptic. Highest temperatures occur at equatorial regions with measured values reaching 397 K (Williams et al. 2017) whilst lowest temperature occur at the poles and can drop down to 29 K (Paige et al. 2010b) at spots of permanent shadow but with an average coldest night time temperature of about 50 K (Williams et al. 2017).

The surface of the Moon is mainly influenced by radiation and by impacts of smaller and bigger bodies. With time, a layer formed as the top layer sitting on basaltic rock formation. This layer is usually referred to as regolith. The composition of regolith has only been measured at specific locations and so, many unknowns remain. It is commonly assumed that there is a fluffy top layer of regolith with a thickness of about two millimetres. Below it comes a thicker layer of up to couple of meters with higher density and higher thermal conductivity. This becomes important when dynamic behaviour of the temperatures at the surface is of interest. Then, heat capacity and conduction of regolith and soil dampen temperatures at the surface. In general, regolith thermo-physical properties seem to be uniform across the Moon without a distinction between Mare and Highlands. Deviations from average values occur on smaller scale at impact craters and their vicinity. Here, thermal inertia as well as rock abundance show variations (Hayne et al. 2017). Thermo-physical properties used for simulation in this thesis are described in chapter 3.1.2

2.3.3 Lunar Poles

Illumination conditions at the poles are extreme because of the low solar elevation angle justified by the low inclination of the spin axis of the Moon. Long shadows casted by terrain elevations are the consequence of that. For example, a mountain with an elevation of 2 km casts a shadow with a length of about 77 km with the Sun elevated at 1.5° assuming parallel rays from the Sun. If the real shape of the Sun were factored in, the penumbra length would be about 10.92 km. One can see with that example that the Sun must not be considered as a point source emitting parallel rays as usually done in thermal simulations for spacecraft. Instead, it can be approximated by disc with a diameter of about 0.54°, which is the average field the Sun covers as seen from the Moon. Figure 15 highlights this situation. An observer on the lunar surface can also see the Sun only partially, which creates penumbra at this specific location. Figure 15 also illustrates the movement of the Sun. It covers nearly its diameter every hour, with moving about 0.5° per hour. Hence, a time step for calculating solar heat load on the terrain in a realistic way would be less than one hour. Furthermore, around the poles the movement of the Sun is mainly in a horizontal way as opposed to positions closer to the equator.

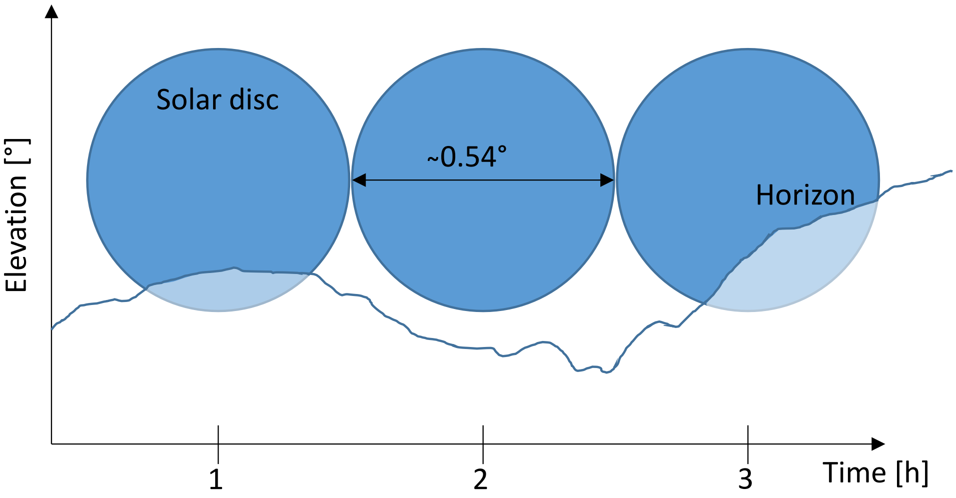

Figure 15: Propagation and size of the solar disc as seen from the Moon. Adapted from (Gläser et al. 2014)

Lunar poles look quite different in their local topography. Figure 16 shows the elevation at north and south polar region above or below the reference sphere of the Moon with a radius of 1734.40 km. It is a 400 km by 400 km DEM derived from co-registration of LOLA tracks resulting in a resolution of 20 m per pixel (Gläser et al. 2018). The region around the north pole is more homogenous in terms of elevation than the region around the south pole. Craters are already filled with material and the terrain seems to be much smoother. In addition, the difference between minimum and maximum elevation is significantly less at the north pole with values ranging from -5 km to 2 km compared to the south pole where values lie between -5.5 km and 7 km. This indicates that craters at the north pole are older and consequently further weathered than craters at the south pole.

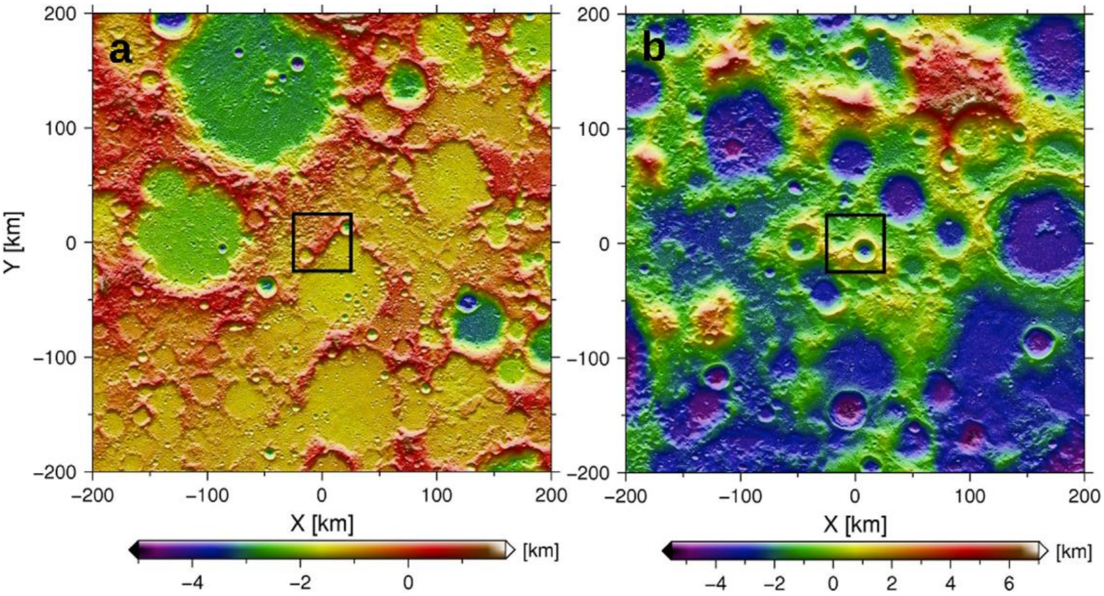

Figure 16: Digital elevation model of lunar north pole (a) and lunar south pole (b). Image source: (Gläser et al. 2018)

The difference in the elevation profile has also a big effect on the size of the terrain that has to be considered for calculation of illumination. In Figure 17, the maximum distance of the local horizon of each pixel is depicted with its colour. The colour scheme ranging from 0 km in blue to 300 km in red clearly shows that for locations around the south pole much longer distances of local horizon occur than around the north pole. For example, if a region of interest around the south pole has to be modelled with a size of about 40 km by 40 km, it is hardly avoidable to use a size of the overall scene with less than 200 km by 200 km. In contrast to that, the same size of ROI at the north pole would require a total scene size of roughly 100 km by 100 km. Both examples show that the overall size of the scene for the simulation has to cover long distances leading to models with a big amount of data and a higher computational demand, also.

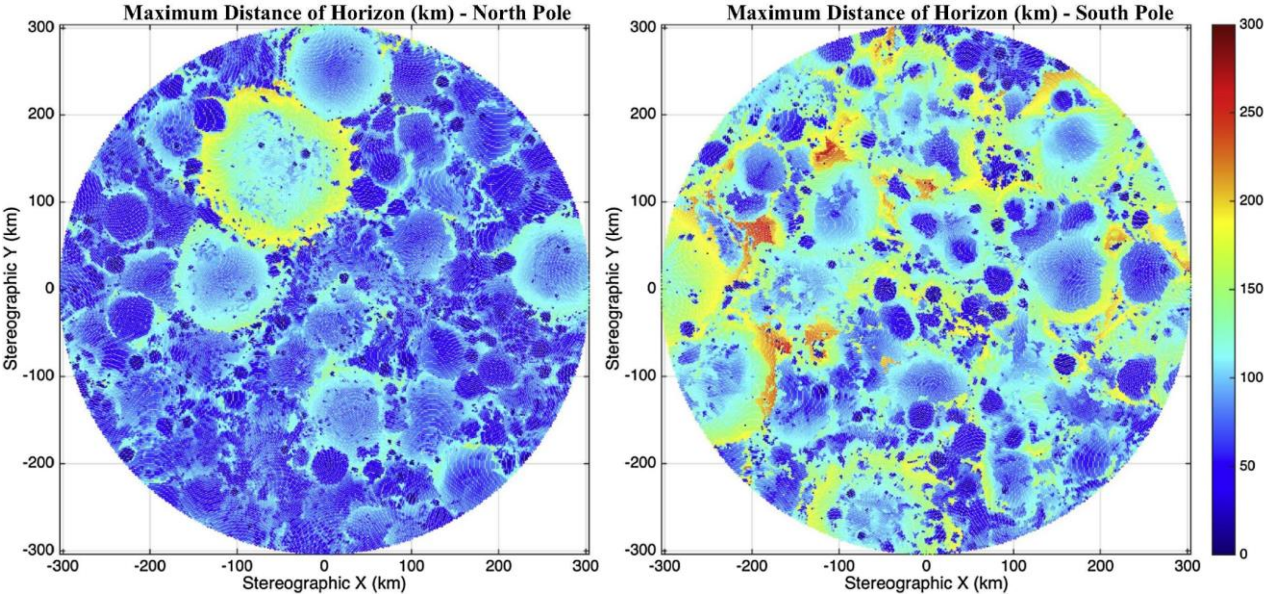

Figure 17: Maximum distance of horizon at north and south pole of the Moon. Image source: (Mazarico et al. 2018)

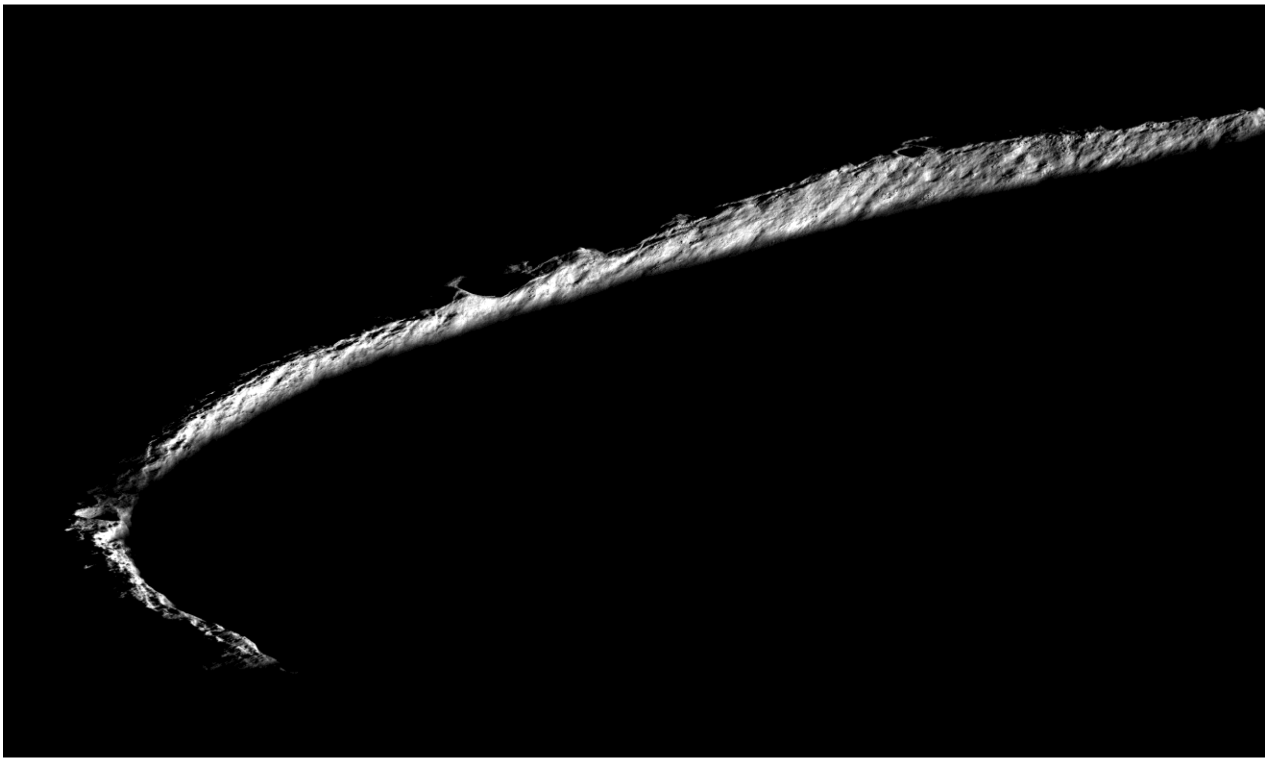

Figure 18: Image M1224655261LR from NAC of LRO showing extreme lighting conditions at lunar south pole at rim of crater Shackleton

Figure 18 depicts extreme lighting conditions at the lunar poles. It is a picture taken by NAC on board of LRO looking down to the south pole of the Moon at the rim of crater Shackleton. In the particular case of illumination depicted in Figure 18, only a part of the rim receives sunlight and regions in front of and behind the crater rim are in darkness. Such illumination conditions can last for several hours at the lunar poles in contrast to equatorial regions where they last only a couple of minutes

3 Models

3.1 Moon

This chapter describes the model of the Moon, which is implemented for simulation of surface temperatures of the Moon at the south pole.

3.1.1 Topography

A DEM is available as gridded mesh from LOLA data on PDS but it covers only latitudes from +-60° called LOLA Digital Elevation Model Coregistered with SELENE Data (SLDEM). It is a combination of LOLA data and data from Kaguya for best accuracy of combining available measurements by laser altimeters. For polar regions, only direct measurements of elevation profiles from LOLA are available on PDS. This comes with the drawback that there are misaligned cross tracks in it as can be seen in Figure 19 a). In order to create the best digital elevation model possible with most recent data one option is to use stereo images from LRO NACs and derive a high resolution DEM from that. This works only for illuminated regions in that pair of stereo images and only for the region captured in those images. Resulting DEMs are of high precision and have a high resolution as well, but they might have local spots without any height data in it due to being in shadow while the picture was taken. An even more sophisticated approach can be used called co-registration of LOLA tracks. The basis is again a DEM derived from NAC stereo image pair. This DEM is then used to derive the offset of LOLA data tracks. As the offset is constant along an orbit, this co-registration is valid for other regions outside of the captured one in the NAC image pair creating a high resolution DEM for the entire polar region. This is what Gläser et al. (2014) did and a DEM with a resolution of 50 m per pixel derived by the same technique is used in this work as the baseline for all other resolutions used in scenes (Gläser et al. 2010; Gläser et al. 2013; Gläser et al. 2014).

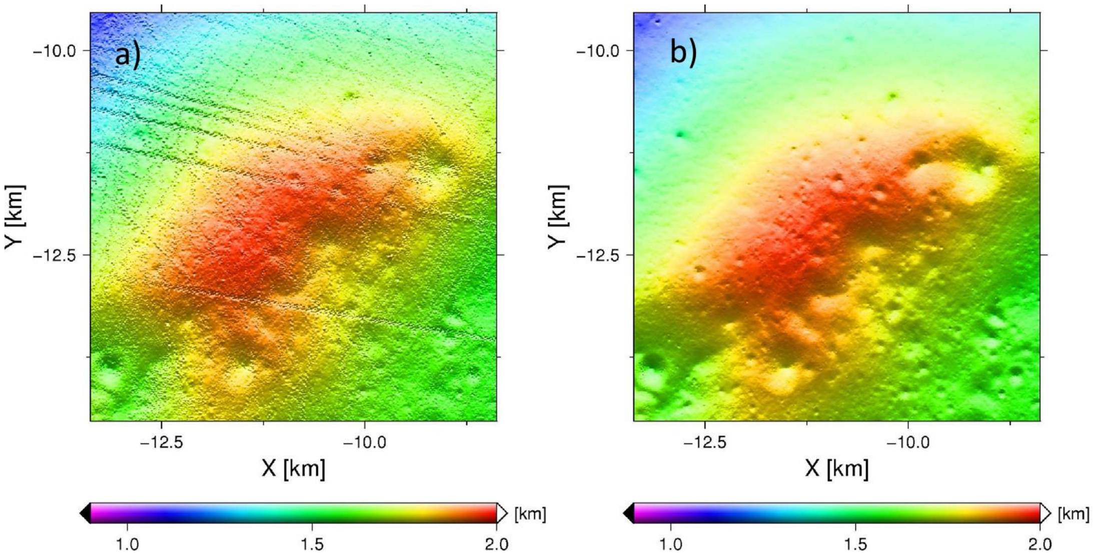

Figure 19: DEM with resolution of 5 m derived from original LOLA data (a). Final co-registered and filtered DEM (b). Both plotted in stereographic projection. Image source: (Gläser et al. 2014)

Figure 20 shows the DEM scaled down to 160 m per pixel that is provided by Technische Universität Berlin (TUB) with a resolution of 50 m per pixel. It consists of the south pole in a 400 km by 400 km stereographic projection. It is the basis for all terrain models that are used in simulations in this thesis and that have different resolutions. Using the full resolution of 50 m per pixel over the entire scene for thermal simulations is computational expansive and often not necessary because mission profiles focus on smaller areas than the polar DEM covers. Hence, a reduction of the resolution as well as the scene size becomes necessary in order to reduce computational time of simulations. Specific locations at the poles require vast scenes for properly simulating illumination conditions at the lunar poles as described in chapter 2.3.3. In order to reduce computational costs, the scene can be split in a centre part where the region of interest (ROI) is modelled with higher resolution and an outer part where the resolution is decreased and surfaces are only present in ray tracing for shading and reflection effects. TherMoS-X calculates only temperatures for the ROI. Figure 21 depicts this situation exemplarily. The centre part of the terrain in green has a resolution of ~160 m per pixel and the outer part in blue has a resolution of ~800 m per pixel. The size of this scene is not representative for study cases in this thesis but is adjusted in size in order to show how scenes look like in general.

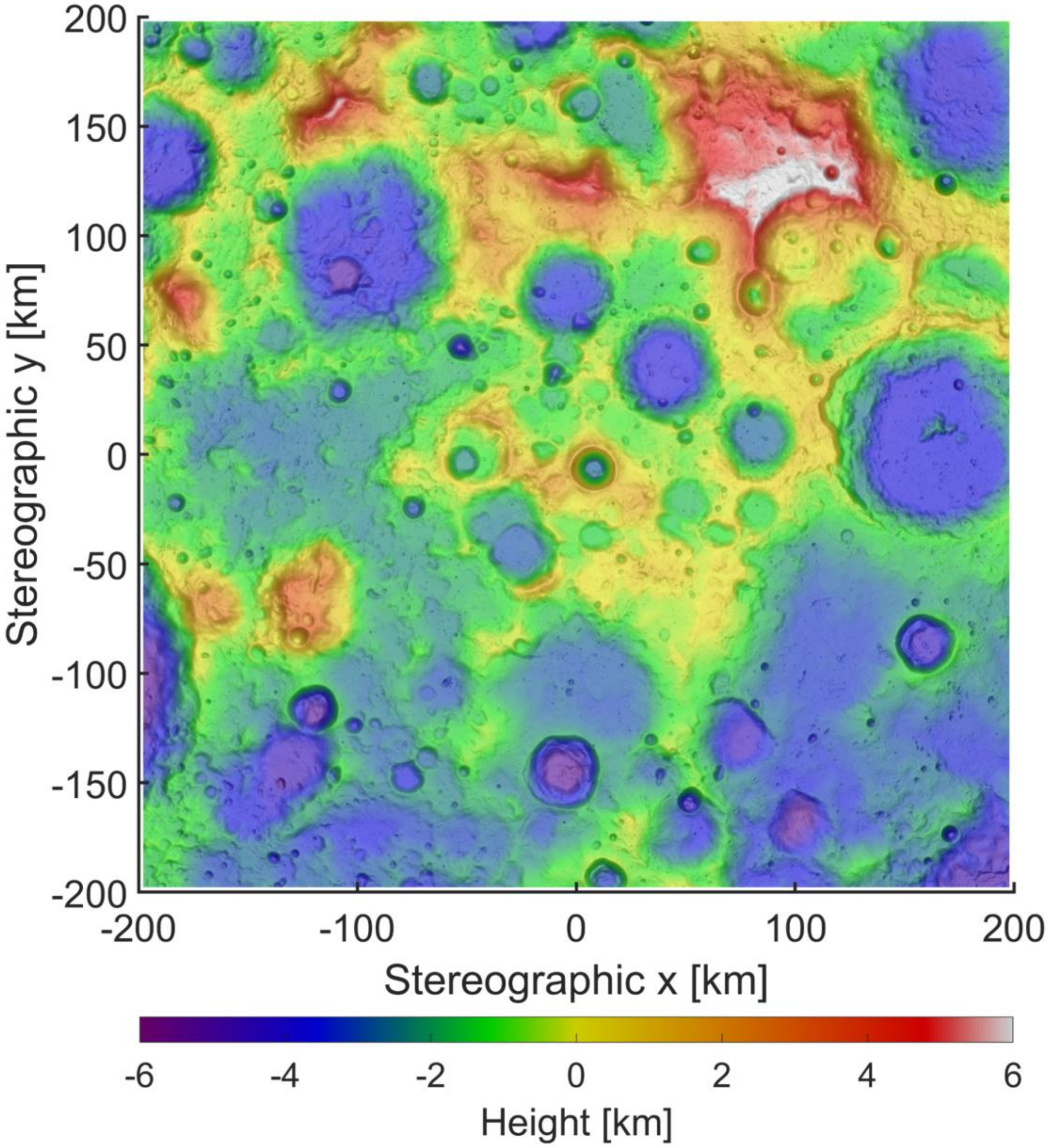

Figure 20: DEM of south pole scaled down to 160 m per pixel. DEM is provided by TUB with resolution of 50 m per pixel.

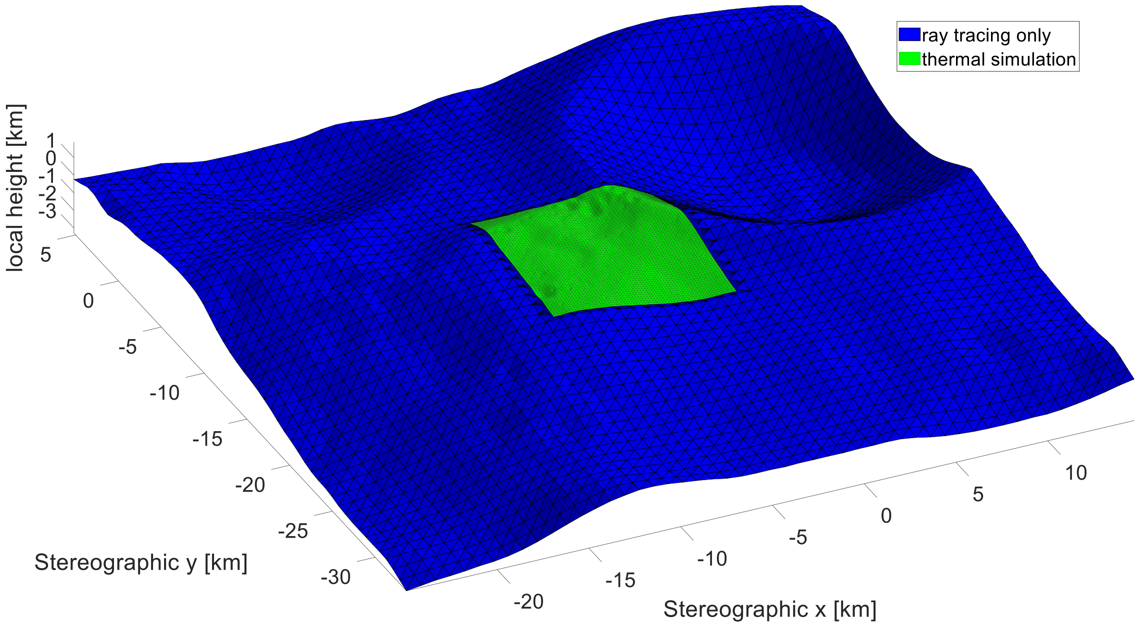

Figure 21: Example scene for thermal simulation. Blue triangles consider solar radiation including reflections and shading of green triangles for infrared radiation. Green triangles are fully simulated and later the basis for traverse optimisation.

3.1.2 Thermal Model

In order to simulate temperatures on the surface of the Moon, the most recent thermal model with the two-layer approach from Hayne et al. (2017) is implemented. The model requires implementation of lunar regolith to a depth of two meters where constant thermal conditions occur. The terrain is meshed with triangles and for each triangle a one-dimensional differential equation is solved numerically. Cross coupling between surface triangles can occur by heat transfer by radiation and reflected solar rays of terrain triangles. Additionally, a triangle can emit heat by radiation to space and receive direct solar heat load. All heat transferred by radiation is calculated with a dedicated ray tracer on Nvidia® GPUs. The implementation of ray tracing is explained in chapter 4.1.4.

In total, ten nodes are allocated to each surface triangle. The distribution into depth is non-linear as depicted in Figure 22. Highest gradients in temperature occur to a depth of about 0.3 m as described in chapter 3.2.5. Hence, nine of those ten nodes are located between 0.005 m and 0.375 m. The cross sectional area of all nodes is the same as the surface area of the uppermost node. All nodes of one surface triangle are connected by conduction and the uppermost as well as the bottom node receive additional heat loads. Whilst the heat load for the uppermost node comes from radiation, the bottom node at 2 m receives heat coming from the lunar core of 0.018 W m^{-2} (Hayne et al. 2017).

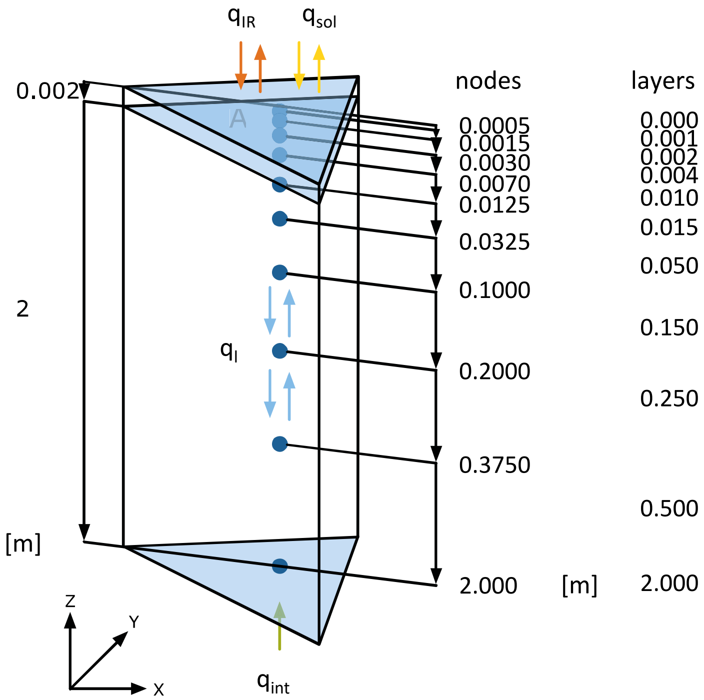

Figure 22: Nodal distribution into depth of surface triangle

The thermal radiation environment for each triangle is determined in three steps by ray tracing. In brief, first the view factor of each triangle towards space is calculated. This value is then used in the one-dimensional differential equation. Second, the heat exchange by radiation between triangles is determined by launching a predefined amount of rays per triangle randomly distributed over a hemisphere. When a ray hits another triangle, it absorbs the heat power of that ray and eventually all hits are summed up. Reflections in infrared range are neglected due to high infrared emissivity of regolith close to unity. Finally, the solar heat load is simulated at each triangle by shooting rays towards the Sun in a cone with a half cone angle of 0.27 degrees. Reflections of solar heat load are considered with one bounce realised as an additional launch of rays distributed over the hemisphere of each triangle.

Thermo-optical properties: Albedo and infrared emissivity are the main characteristics needed for proper simulation because radiation is the dominant heat transfer mechanism on the Moon. Regolith material at the poles is of highland type, which has an average albedo of 0.2. The value for albedo in TherMoS-X is the only one within the entire model which differs from the model of Hayne et al. (2017). They implemented an albedo dependent on the angle towards Sun with a minimum value of 0.2. This value is implemented as a constant value in TherMoS-X as proposed by Paige et al. (2010b). They state that temperatures from their model are in good agreement with measurements and this is the only publication verifying a thermal model at the poles of the Moon with measurements. Infrared emissivity is a constant value in all publications. In this thesis infrared emissivity set to 0.95.

Specific heat: Specific heat c_p is calculated by a polynomial function resulting from curve fitting to measurements (Hayne et al. 2017). The equation is based on Hemingway et al. (1981) and Ledlow et al. (1992) with measurements from Apollo samples by Robie et al. (1970). Its calculation is given in equation (12).

$$c_p(T) = c_0 + c_1 T + c_2 T^2 + c_3 T^3 + c_4 T^4 \tag{12}$$

The constants for equation (12) are c_0 = -3.6125 J kg^{-1} K^{-1}, c_1 = +2.7431 J kg^{-1} K^{-2}, c_2 = 2.3616e-03 J kg^{-1} K^{-2}, c_3 = -1.234e-05 J kg^{-1} K^{-3}, and c_4 = 8.9093e-09 J kg^{-1} K^{-4} (Hayne et al. 2017)..

Density: Equation (13) represents the density of regolith dependent on the depth z and the scale factor H (Hayne et al. 2017). In this thesis H is always set to H = 0.06 m. Values for ρ_s = 1100 kg m^{-3} and ρ_d = 1800 kg m^{-3} are taken from Hayne et al. (2017) where ρ_s is slightly altered from Vasavada et al. (2012b).

$$\rho(z) = \rho_d - (\rho_d - \rho_s) \cdot exp(-z/H) \tag{13}$$

Thermal conductivity: Equation (14) describes the thermal conductivity of regolith and it depends on depth and temperature. Again, values for constants differ slightly between publications. In this thesis, k_s = 0.00074 W m^{-1} K^{-1} and k_d = 0.0034 W m^{-1} K^{-1} and χ = 2.7 is the radiative conductivity parameter (Hayne et al. 2017).

$$k(z,T) = k_d - (k_d - k_s) \cdot exp\left(-\frac{z}{H}\right) + \chi \cdot k_s \cdot (T/350)^3 \tag{14}$$

The implementation of equation (14) is not straightforward in modelling code because it is not obvious which temperature shall be used for two regolith nodes in conductive contact. In TherMoS-X, temperature of the lower node of the conductive link is applied to equation above. This leads to proper temperature profile into depth.

Equations (12) to (14) form the basis for an implementation of a lumped parameter model in TherMoS-X. The simulation approach changes to previous version of TherMoS (Hager 2013) as describe in chapter 4.1. All equations depending on temperature of a thermal node are now part of the solver and are solved numerically instead of an explicit calculation for one time step.

Initial temperatures: Temperatures of the model have to be initialised at the beginning of a simulation. The surface node of a triangle is calculated as an equilibrium temperature T_0. Sources for heat exchange are absorbed solar heat load as the single heat source derived by ray tracing and radiation to space with its view factor that is provided by the ray tracer as well. If temperature falls below 85 K it is overwritten with the value of 85 K in order to avoid undercooling of surface nodes. Equation (15) explains the calculation of T_0.

$$T_0 = \sqrt[4]{\frac{\dot{Q}_{solar}}{\sigma \cdot \varepsilon_i \cdot A_i \cdot F_{i,space}}} \tag{15}$$

The temperature of the bottom node of a triangle T_{bottom} is set to the constant value of 255 K. Nodes into depth are initialised with calculation of equation (16) (Hayne et al. 2017) depending on their depth z.

$$T_i = T_{bottom} - (T_{bottom} - T_0) \cdot e^{-z_i/H} \tag{16}$$

After this first initialisation, temperatures within the model are still far off from being at equilibrium. Especially the propagation to nodes into depth is slow within lunar regolith. Best practice for scientific models is to let them run for a full precession cycle of the Moon, which is about 18.6 years. If changes in temperature are still bigger than a threshold value, an additional precession cycle should be simulated. However, this is only possible with fast running models. In addition, temperatures at the surface of the Moon derive an equilibrated state much faster, which renders the implemented approach sufficient for the purpose of this thesis.

3.2 Validation of Moon Model at Poles

Model validation is required in order to gain confidence in the model for upcoming simulations. Hayne et al. (2017) validated their thermal model of the surface of the Moon against measurements from DLRE, but they used a different approach for calculation of heat transferred by radiation and heat load received by the Sun. Their model shows very good agreement with measurements in the investigated range of latitudes between ±70° and it is considered to be verified. Therefore, only the implementation of their model in TherMoS-X is validated in this thesis. The main drivers for temperatures of the surface of the Moon are the solar heat load and heat transferred by radiation beside the regolith material properties. Consequently, insolation is verified first with a comparison of visual light sampled in photographs, followed by a comparison with a simulation tool from literature. Finally, the comparison of simulated temperatures with measured temperatures highlights the quality of the thermal mode implemented in TherMoS-X. As models describe reality only in a simplified version, there is always the question how accurate is accurate enough in order to achieve the desired results. This is discussed in the last part of this chapter.

3.2.1 Visual Illumination

A physically correct simulation of solar insolation is mandatory in order to derive meaningful results from temperature simulation on the surface of the Moon. For validation, results from TherMoS-X runs have to prove two things. First, illumination of the surface of the Moon has to be the same as in reality, which can be proven by comparing results with pictures from the surface of the Moon. Second, direct insolation on the scene has to match realistic values, which can only be compared with other simulations.

On board of LRO there are also two cameras taking pictures of the surface of the Moon at visual wavelength. One of them is the WAC, which covers wide distances with one shot and is best suited to compare simulation results with pictures from it due to the lower resolution of about 75 m per pixel.

Figure 23 a) shows a crop from image M1105682983ME taken at 24th of October in 2012 at roughly 01:55 am. The region is centred at roughly 87° S and 62° E between craters Faustini and Shoemaker. For comparison, Figure 23 b) is a visualisation of simulation results with the same solar angles as occurred during the WAC photography. The grey scale values of pixels in that picture represent the absorbed solar heat load of thermal nodes assuming that pixel in the WAC image are brightest, when they receive highest heat loads. One can clearly see a nearly perfect match of illumination conditions at visible light spectrum. Shapes of crater look identical with peaks in brightness at the same locations and the shape of shadows is similar in both pictures. Grey values seem to differ at some locations but that comes from the fact that results of TherMoS-X are not rendered with real optical properties of the surface of the Moon. As stated before, grey values here are a direct result of absorbed solar heat load. For simulation of illumination conditions, the terrain consisted of an inner part with a resolution of 160 m per pixel and an outer part with a resolution of 800 m per pixel. Only the high-resolution inner part is shown in Figure 23 b).

This comparison proves that TherMoS-X represents illumination conditions properly and in a realistic way.

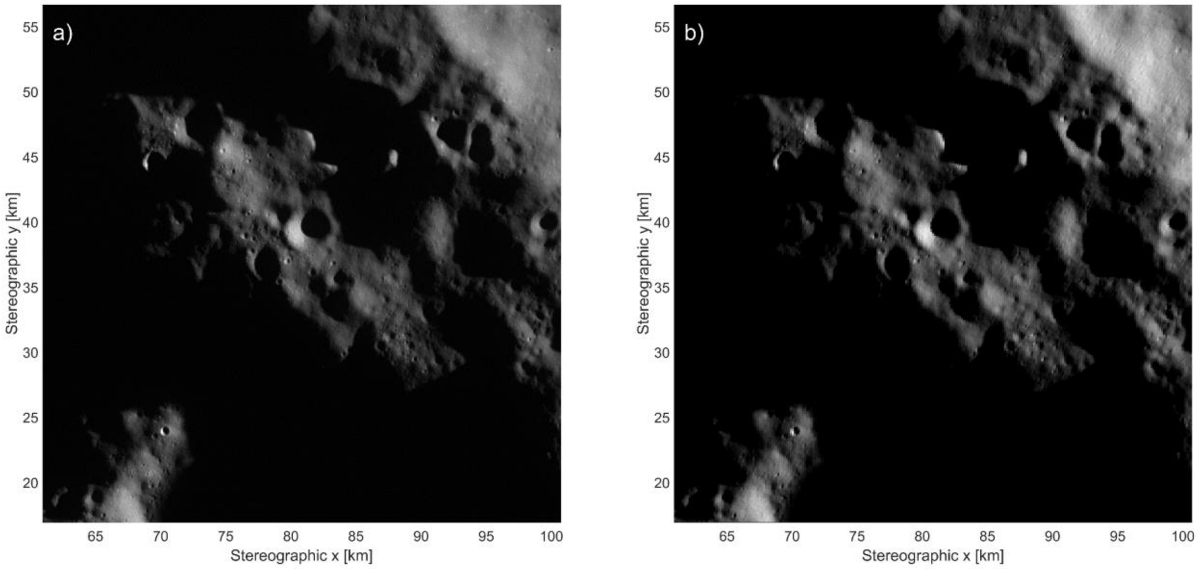

Figure 23: WAC picture M1105682983ME taken on 2012-10-24 at 01:55:15 from LRO a) and simulation results of TherMoS-X with resolution of 160 m per pixel. Colour is the absorbed solar heat load plotted in grey scale with same Sun position b)

3.2.2 Insolation

Visual comparison of illumination conditions in the previous chapter already proves that a realistic implementation of sun light is part of TherMoS-X. However, visual comparison alone is only a part of model validation because models require calculation of direct insolation on the surface of the Moon in order to get the heat flux density of thermal nodes as an input to the thermal solver. In this case, TherMoS-X can only be compared to other modelling tools, as there is no measured data available for insolation. Mazarico et al. (2018) developed a tool for simulation of optical remote sensing instruments which can improve the accuracy of the instrument by understanding sensitive behaviour of critical elements within. Their tool allows them to calculate the insolation of all bodies in our solar system at any time. One example in their publication is the Moon. Figure 24 shows the incident solar heat flux in the region of crater Faustini on August 29th 2012 at 02:37 UTC. It ranges from 0 W m^{-2} to a maximum of 700 W m^{-2}. Figure 24 a) is taken from the Mazarico et al. (2018) who used a resolution of the terrain of 240 m per pixel and full modelling of the Moon with decreasing resolution with higher distance from the centre of the scene. Figure 24 b) shows results of ray tracing performed by TherMoS-X with a resolution of the terrain of 160 m per pixel and a 400 km by 400 km model of the south pole. It was not possible to match the colour scheme exactly between both plots as no source data but only the picture itself was available from Mazarico et al. (2018). Because of that, colours look slightly different between both pictures. Neglecting the slight difference in colour reproduction, the direct insolation in both pictures looks nearly identical. Peak insolation occurs at the same locations with the same values. In addition, areas with no sun light at all seem to have similar shapes leading to the conclusion that the direction of the Sun is properly implemented in the model and the resolution of 160 meters per pixel is sufficient as well.

The effect of solar limb darkening, where the intensity of solar light decreases from its centre to its limb, is neglected in the frame of this thesis. Furthermore, the effect of a changing solar constant due to the orbit of the Earth-Moon system around the Sun is not implemented. Instead, a constant value is used.

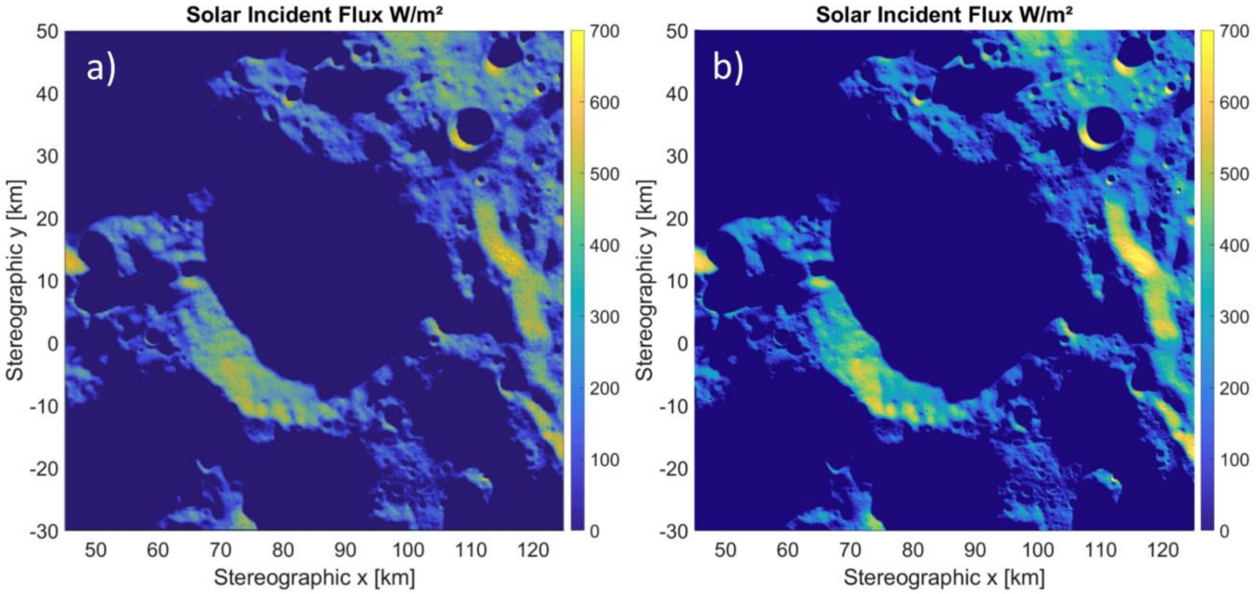

Figure 24: Direct insolation at crater Faustini on August 29th, 2012 at 02:37 UTC from Mazarico et al. (2018) in (a) and from simulation in TherMoS-X in (b)

3.2.3 Reflections of Solar Light

The total absorbed heat load from solar rays is the parameter, which is used as an input to the solver of the thermal model. For lunar regolith, it consists of the absorbed portion of incident solar heat load and the absorbed portion coming from diffuse reflection of it. Chapter 3.2.2 validates the incident solar heat flux density against another simulation tool. The remaining question is how reflections of solar light should be addressed in a thermal model because in lunar highland around the south pole the albedo is about 0.2. However, one can assume that most of the reflected sun light is sent back to space due to the surface slope of the terrain. In TherMoS-X, all surface triangles are regarded as Lambertian radiators, which is typical for basaltic geology.

A comparison between incident solar heat flux and absorbed solar heat flux with one generation of diffuse reflection shall quantify the impact of reflections on the solar heat flux. The scene is centred nearly at the south pole and the ROI has a size of roughly 100 km by 100 km at a resolution of 160 m per pixel resulting in a total number of 793,800 triangles. The outer region has a reduced resolution of 320 m per pixel and an outer frame of 300 km by 300 km and is only implemented for a realistic implementation of shading effects. Solar reflections as well as incident solar heat flux is calculated exclusively for the ROI. Absorbed solar heat flux at each triangle is computed by shooting 100 rays towards the Sun as described in chapter 4.1.4. Solar constant is set to 1367 W m^{-2}. In order to assess the effect of reflected rays, 1000 rays are shot randomly distributed around the hemisphere of each triangle that received direct sun light. Only one generation of reflection is considered in this study.

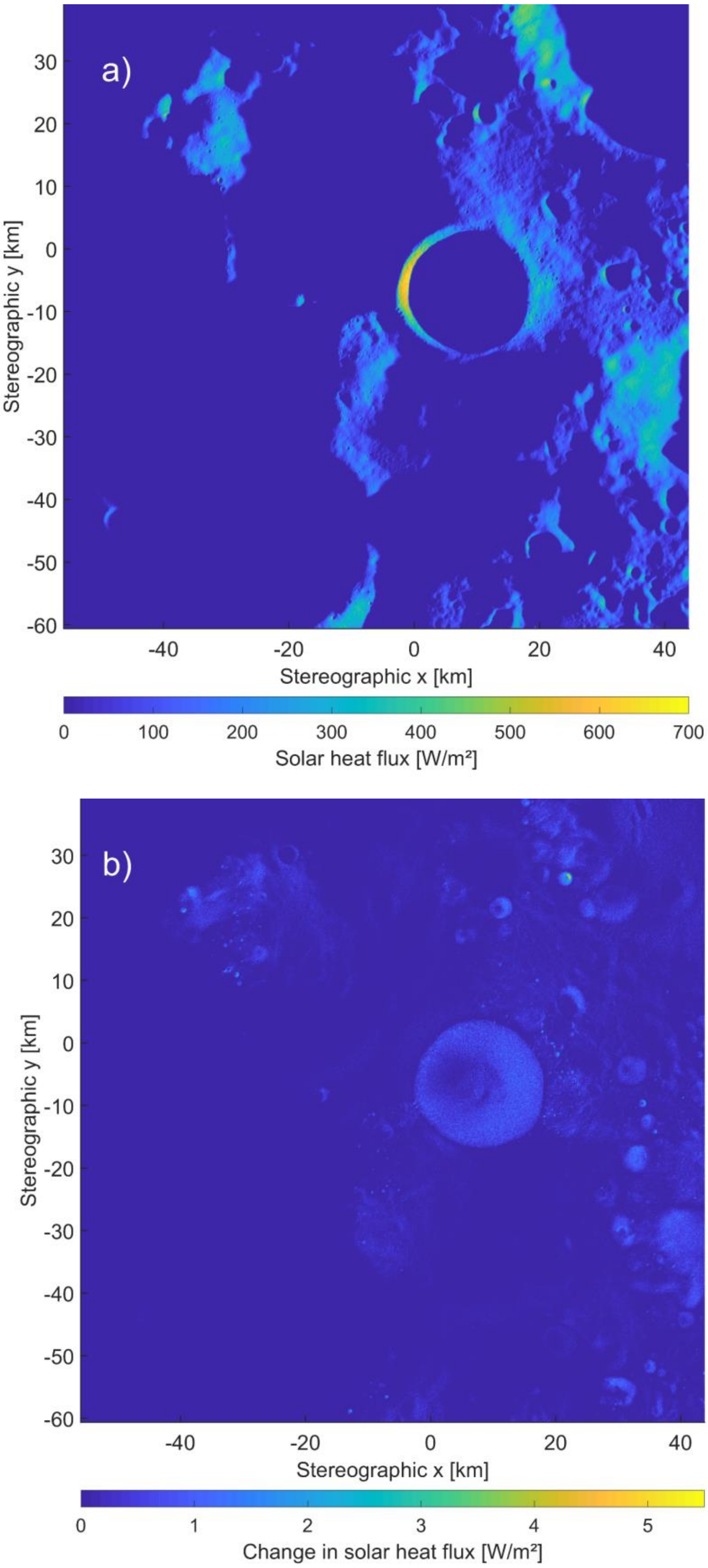

Figure 25: Absorbed solar heat flux without reflections (a) and difference with one generation of reflection (b)

Figure 25 a) shows the absorbed solar heat flux of the scene. The sun comes nearly exactly from the right side of the plot with an azimuth angle of 97.746° and an elevation of 1.194°, both with regard to the south pole and they would occur on 9th of January 2022 at 16:00. Absorbed heat fluxes range from 0 W m^{-2} to 695 W m^{-2}. Highest values occur on the western region of the rim of Shackleton crater due to steepest slopes of the scene. This plot shows again the strange looking illumination conditions at the poles of the Moon. There are some local features on the left side, which elevate out of the shadow and receive sun light in an area where the surrounding is in complete shadow.

Figure 25 b) highlights changes in total absorbed solar heat flux if one generation of reflected sun light is simulated. Values range from 0 W m^{-2} to 5.4 W m^{-2} and in total 420,626 triangles of 793,800 triangles are affected by it. This represents nearly 53 % of all. However, the mean change of those triangles is small with only 0.1571 W m^{-2}: The median of changes of affected triangles is as low as 0.085 W m^{-2}. Results underline that mainly craters are affected by reflections. For example, this can be seen at crater Shackleton in the centre. Nearly the entire interior of the crater does not see the Sun directly but reflected solar rays reach those triangle. Especially the crater wall opposite to the directly lit wall receives reflected solar light. This is also true for the many small craters within areas of higher direct sun light at the right side of the figure.

The comparison shows that the change in absorbed solar heat flux is small if first order reflection is considered. Implementation of even more generations of reflections seems to be only important if most accurate temperatures at cold spots should be simulated. Small changes at those locations could already increase the temperature by a couple of K if there has not been any sunlight simulated before. This is not required for simulations within this thesis and one generation of reflection is deemed accurate enough for calculations within this thesis.

A brief review of literature reveals that reflections are handled differently. Paige et al. (2010b) for example considered three generations of reflections. Their main interest lied in finding cold spots where volatiles could be trapped and this number of reflections seems to be sufficient. The model from Gläser and Gläser (2019) is even more precise as they trace scattering of solar radiation until an abort criterion is reached but at least three generations of scattering are considered in any case. In contrast to the topic of this thesis, the focus in those publication lies in finding cold spots where volatiles can be trapped.

3.2.4 Earth as Heat Source

The Sun shines directly on the surface of the Moon, but also reflected solar light from Earth reaches the Moon. Mazarico et al. (2018) implemented Earth as a three-dimensional sphere consisting of 671 surface elements. In their model, Earth reflects sunlight with varying albedo and the incoming heat flux was simulated. At a region around crater Faustini, it reached only 1 mW m^{-2}. This low amount of heat flux has to be considered in some cases, for instances if sensitive optics were to be simulated, but for the thermal simulation of the surface it plays only a minor role. It is neglected within this thesis because on areas receiving sunlight, the direct heat flux is by order of magnitudes bigger and for areas in shadow Earthshine would only influence long-term equilibrium temperatures within PSRs. This is of scientific interest but can be ignored for engineering purposes with regard to topics in this thesis.

Additionally, Earth represents a heat source in terms of infrared radiation. The infrared heat flux in an Earth orbit has an average value of about 230 W m^{-2} (Gilmore 2002-©2003) which decreases at the distance of the Moon (R_{Moon} = 384.400 km) to about 0.063 W m^{-2}. This is one order of magnitude more than the reflected solar light of Earth, but still only 0.00463 % of the solar constant. In addition, this value is only true for surfaces, which are perpendicular to the incoming radiation. It decreases further with the high angle of incidence on surfaces at lunar poles. With the same reason for neglecting Earthshine, infrared radiation from Earth is also not considered in simulations in this thesis.

3.2.5 Temperatures

Model comparison

In order to judge whether the model is properly realised within TherMoS-X, temperatures are compared against plots from the original model of Hayne et al. (2017). An idealised location at the lunar equator on the reference sphere of the Moon is simulated in TherMoS-X. Figure 26 shows two comparisons. In Figure 26 a), temperature of one lunation of one thermal node at the surface for each model is plotted whilst Figure 26 b) shows temperature into depth of the same thermal surface node at different times. Hot stands for hottest temperatures occurring shortly after midday and cold stands for coldest temperatures, which are reached just prior to sunrise.

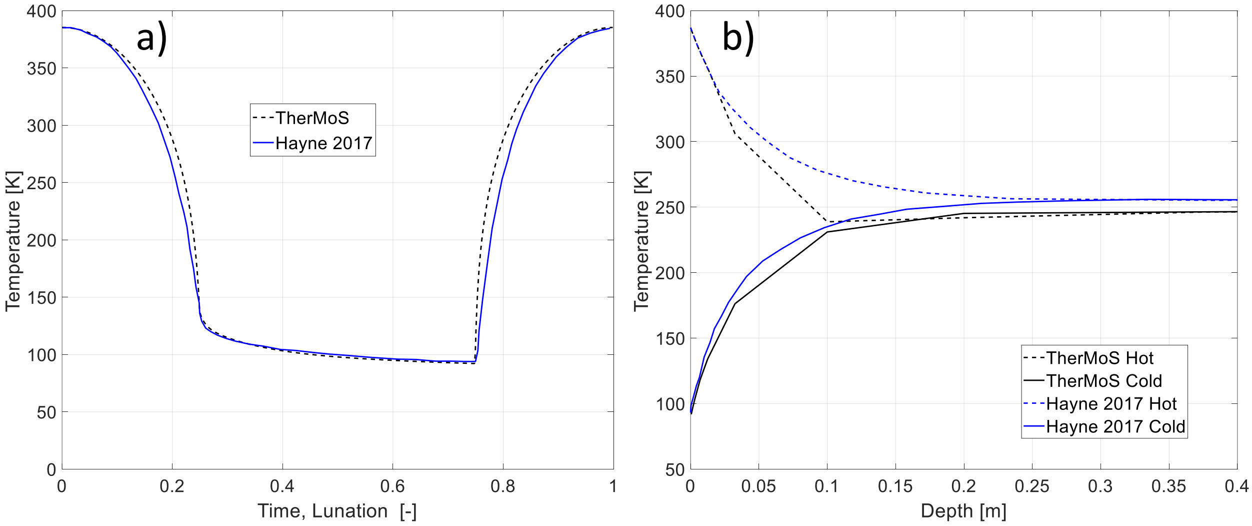

Figure 26: Temperature comparison between TherMoS-X and the original model from (Hayne et al. 2017). a) shows one lunation and b) temperature into depth at noon and seconds prior to sunrise

Temperatures over one lunation are close together between the original model and its implementation in TherMoS-X. Temperatures during night are a nearly perfect match, which makes sense, as there is actually hardly any difference in both implementations. Temperatures at midday are also nearly similar, again, because here both implementations match. However, in the time between midday and sundown as well as between sunrise and midday, temperatures deviate. The main reason for that is the aforementioned angle dependency of albedo which is present in the model from Hayne et al. (2017) but is not implemented in TherMoS-X. This will be addressed in the future.

Temperatures into depth of regolith, which are shown in Figure 26 b), are also in good agreement for hot conditions at midday and cold conditions just prior to sunrise. The difference of temperature in the depth profile is mainly driven by the amount of nodes of the model. Hayne et al. (2017) state they use 15 to 20 whilst the implementation of TherMoS-X has only 10 nodes spread into depth. A higher amount of nodes would lead to more accurate temperature profiles. For example, Gläser and Gläser (2019) use 39 nodes into depth resulting in a smoothly curved temperature distribution into depth.

Temperature measurements

The most important parameter for validation of a thermal model is temperature. In this chapter, temperatures of simulation runs are compared with measured temperatures from the surface of the Moon. One of the instruments of LRO with the name DLRE provides those measurements. It is a telescope measuring radiance at different wavelength in nine channels. From those, the four channels numbered six to nine are useful for measuring thermal radiation. The measured value of radiance can be transferred into temperature values assuming an infrared emissivity of unity. The field of view of one sensor of DLRE is roughly about 200 m in diameter at ground level on the Moon, which smoothens features on the surface. All channels are also most sensitive in only a small waveband. More information is given in Appendix B and also in (Paige et al. 2010a).

For temperature comparison in this chapter, only channels six to nine of DLRE are used and the data is filtered additionally by comparing centre coordinates of the measurements with coordinates of thermal nodes. A maximum deviation between both coordinates of 40 m is allowed. Measurements are ditched if no matching thermal node could be found. Further filtering is applied if measured temperatures fall outside the regime where the sensor is most sensitive. Orbit numbers 15243 to 15249 from LRO are used, passing over the ROI at nearly every 2 h starting at 1:50 on 24th of October 2012.

The terrain size of simulation is roughly 267 km by 300 km with a high resolution inner part of about 40 km by 40 km. Resolution of the high-resolution part is ~250 m per pixel while the surrounding outer area is modelled with ~800 m per pixel. Its centre is located at -87.069544° N 65.511749° E.

In order to compute initial temperatures for the simulated scene an approach with two steps is conducted. First, the simulation runs for two years with solar angles from 1st of October 2010 at 17:30 to 1st of October 2012 23:30 with a time step of the solver of 12 h. Only sun light and first order reflections of the entire terrain are used for heat transfer by radiation together with proper view factors to space. Heat transfer between triangle surfaces is neglected to speed up calculation time. Second, the simulation is continued to 23rd of October 2012 23:30 with a solver time step of 30 min and the full radiation model running. After that, at 24:00 on 23rd of October 2012, the solver time step is decreased to 5 min with logging temperatures every 10 min. Figure 27 b) illustrate the simulated ROI and Figure 27 a) measurements from DLRE instrument.

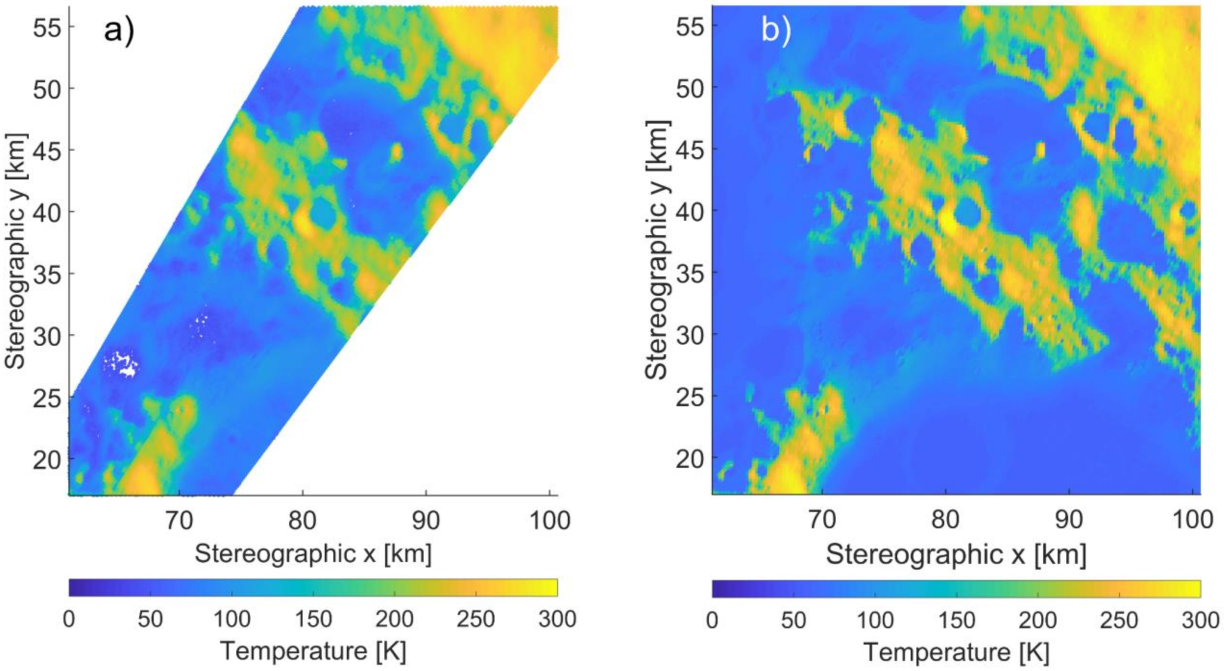

Figure 27: Measured brightness temperatures by DLRE orbit number 15243 to 15249 (a) and simulated temperatures in ROI at same conditions as in orbit number 15243 (b)

Figure 27 shows measured brightness temperatures and simulated temperatures for visual comparison. Measured temperatures are depicted for orbits with number 15243 to 15249 spanning a period of about 12 h. Simulated temperatures match conditions that occur during measurements of orbit number 15243. In Figure 27, simulated temperatures cannot be compared directly to the plot of measured values because of the discrepancy in time. Still, one can already draw conclusions as the thermal inertia of the Moon is high and changes in temperature progress slowly. At a first glance, the temperature distribution looks similar, but temperatures on the simulated scene seem to be warmer than measured values because of brighter yellow colours in the warm areas.

For a better comparison, Figure 28 plots measured temperatures from DLRE against simulated temperatures in a density plot. Temperatures of the model have the same time stamp as measured values, which makes a direct comparison possible. Ideally, all points lie on the diagonal line in the plot meaning both temperatures are equal. Points on the left side of the diagonal line mean that modelled temperatures are warmer than measured temperatures and vice versa. In general, temperatures between the model and measurements match quite well with Pearson’s correlation coefficient of 95.5 %, especially at the cold and warm end of the temperatures range. There, temperatures are dominated by radiative equilibrium. However, the plot in Figure 28 shows that at lower temperatures the model gets colder than the measured values while at warmer temperatures, the model leans towards hotter temperatures than measurements. Additionally, the dynamic behaviour of the terrain with temperature between 120 K and 200 K where temperatures are not close to thermal equilibrium seems to be harder to match by the model. The cause for that can be manifold. Illumination conditions might be slightly off in the simulation or thermo-physical properties might vary locally. Future research has also to focus on those specific temperature deviations in order to improve the model. For the purpose of this paper, simulated temperatures and illumination conditions are considered adequate as the high correlation coefficient proves.

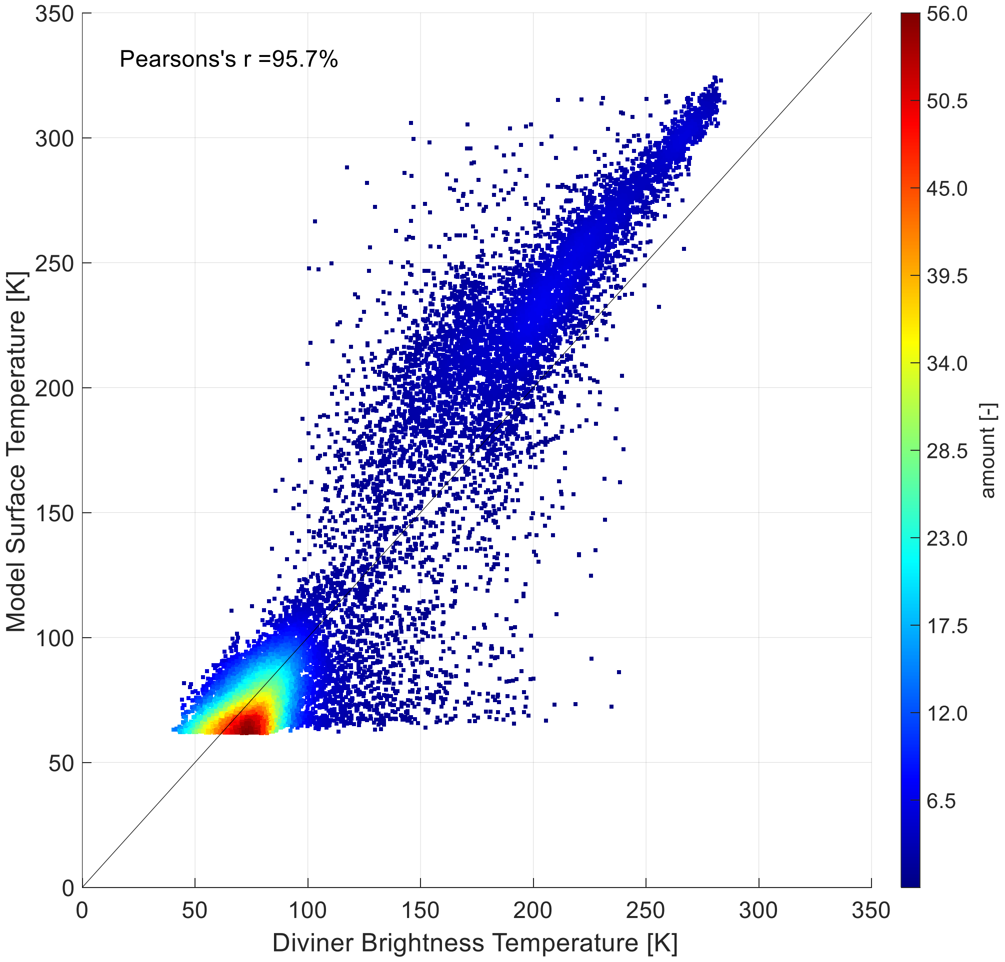

Figure 28: Temperature comparison of TherMoS-X (2 year simulation time for initialisation, 250 m per pixel) with DLRE measurement of orbits 15243 to 15249 all from 24th of October 2012

Two conclusion can be drawn from temperature comparison. The first one is that the time for swing in of two years for temperatures is not enough because at lower temperatures, results from the model did not reach minimum values from measurements. This comes from initial conditions of the model and the required time for regolith to cool down. Measured temperatures reach even below 50 K whilst modelled temperatures only cooled down to 58 K within the simulation run time of about two years. Longer simulation times are not yet possible due to the high computational demand. Models from Hayne et al. (2017) and Paige et al. (2010b) do several years, Gläser and Gläser (2019) even consider several lunar precession cycle of 18.6 years prior to their required date of simulation. The second conclusion is that an angle dependent solar absorptivity might have to be implemented in the future for ray tracing of solar light. In the current implementation this modelling is neglected because other publications also use a constant value (Gläser and Gläser 2019; Paige et al. 2010b). However, Hayne et al. (2017) have an angle dependency of albedo on the solar angle implemented resulting in lower heat load in the range between minimum and maximum insolation whilst the ray tracer matches extreme values only. Another deviation in temperatures might come from the amount of nodes into depth. TherMoS-X uses only 10 nodes while Gläser and Gläser (2019) uses 39 node and also Hayne et al. (2017) state they use 15 to 20 nodes. Still, these deviations are considered to be of minor influence on the traverse planning process. They will be addressed in future work.

There might also exist an angle dependency on both, infrared emissivity and solar absorptivity, but no direct measurements of thermal properties of regolith from polar regions are available. There is also a general uncertainty on the thermos-physical properties of regolith at polar regions, again due to lacking measurements. Only data from Apollo landing sites is available and these are all in equatorial regions. This can also explain some part of the differences in modelling of last publications. Finally, a model is a simplified representation of reality and can never exactly match the real world. It has to be evaluated when a model is accurate enough in order to produce results that are asked from it. For the purpose of this thesis, the current implementation of the thermal model of the Moon is deemed a well-fitting model that allows a proper assessment of traverse planning with thermal interactions of the rover and its environment

3.3 Rover

A model of a rover shall represent its real behaviour in an accurate way, which is still manageable computational wise. For this thesis, no explicit rover system of a dedicated mission is implemented and because of that, assumptions are necessary. The rover implementation shall consider capabilities of a realistic rover system in a modular way. This allows for a more detailed implementation later on if real missions or rover systems shall be simulated. Main characteristics of a rover are its mobility system, its power system and its thermal behaviour. Hence, these domains are modelled and typical values assumed. It is important to bear in mind that within this thesis only concepts for rovers powered by solar energy are considered. This includes solar cells for converting solar energy to electricity and rechargeable batteries for storing energy with a certain capacity.

The thermal model of the rover and the way values from optimisation maps are incorporated to it are described in chapter 3.3.1. A description of the power model of the rover in chapter 3.3.2 completes the overall rover model needed to simulate its energy state at any time.

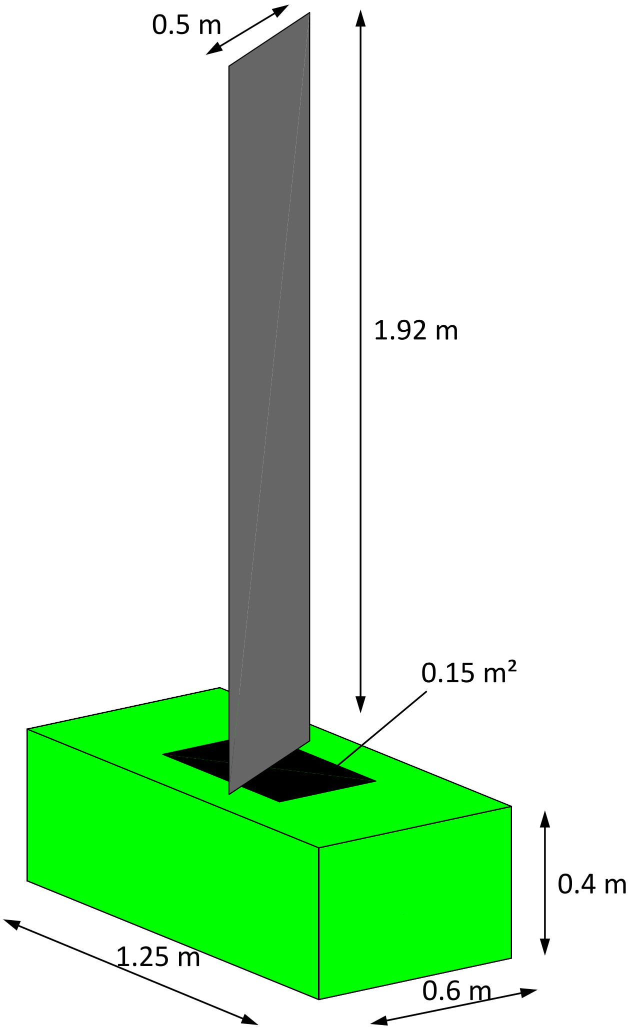

Figure 29: Rover model as a box and its dimensions

Figure 29 depicts the geometry of the modelled roved. It is a box shaped geometry with dimensions of 1.25 m in length, 0.4 m in height, and 0.6 m in width. These dimensions resemble those of MER. An additional radiator is mounted on top of the box with a size of 0.15 m² determined by the thermal model of the rover. Solar cells with a total area of 0.96 m² are mounted perpendicular on the top of the rover for provision of energy to all systems. The total weight is set to 200 kg, again being close to the system of MER. The rover system of ExoMars has a weight of about 240 kg while the Mars Science Laboratory (MSL) and its successor twin Mars2020 weigh about 900 kg (Grotzinger et al. 2012; van Winnendael et al. 2005).

Table 4 gives an overview of rover speed used in some publications with the topic of traverse planning and traverse optimisation on the Moon. A wide range of speeds is used starting as low as 0.06 km h^{-1} and reaching 3.6 km h^{-1} as fastest value. In TherMoS-X, the default rover model has a speed of 0.5 km h^{-1} that is in the middle of values within publications. Overall speed of successful missions Chang'e 3, Chang'e 4, MER, MSL, Mars2020, and ExoMars is usually less. For example, MER has a top speed of 0.165 km h^{-1} (Lindemann R. A. et al. 2006) and MSL is in the same range, but with hazard avoidance turned on, the average speed decreases to 0.054 km h^{-1} (Grotzinger et al. 2012).

Table 4: Speed of rovers in other publications with traverse planning

Name	TherMoS-X	Otten (2018)	Potts et al. (2015)	Speyerer et al. (2016)	Steenstra et al. (2016)	Allender et al. (2019)
Rover speed [km h^{-1}]	0.5	3.6	1.7	0.06	0.36	0.36

3.3.1 Thermal Model

The thermal model of the rover consist of three nodes in order to sustain a flexible representation of a rover system, which is easy to handle at the same time. Its main aim is to calculate the power demand needed for heating the interior of the rover. The outer shape of the rover is assumed as a box and the thermal model represents this box only. Multi-layer insulation (MLI) covers the entire box in order to decouple its interior from the external environment. A radiator is mounted on the top surface of the box for emitting internal heat to space. Additional external elements such as wheels, suspension mechanism, antennas, cameras, and so on are not considered as it is assumed they are operational in the lunar environment at any time. Furthermore, an implementation of additional external elements in the thermal model imposes to account for the orientation of the rover during optimisation, which is only possible with a high increase in computational demand.

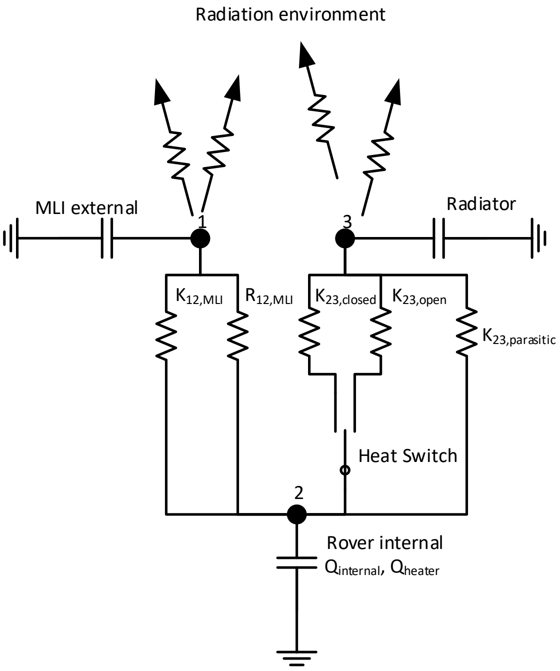

Figure 30: Thermal network of rover model.

Figure 30 shows all nodes and the connection between them. One node represents the external shell of the box and it is called "MLI external". It receives heat fluxes as prepared by optimisation maps and emits heat by radiation. As one node represents the entire surface area of the box, it has to factor in incoming radiation from the sides of the rover box only partially. Figure 31 shows that solar heat load as stored in optimisation maps is applied directly on the top face of the box by considering the angle between this surface and the direction towards Sun. Side panels also absorb solar heat, but with only 35 % of their total surface as an assumption to factor in orientation of the rover. For Infrared radiation from the optimisation map, it is assumed that it reaches all surfaces of the box except for the top one. In order to derive physically correct temperatures, the total surface of the external MLI emits heat by radiation. The external MLI node is connected to the internal node of the rover by conduction and radiation. This allows to account for temperature dependant insulating efficiency of MLI. The implemented MLI has 20 layers with a conductivity of 0.031 W m^{-2} K^{-1} and an emissivity of 0.0067 [-]. The conductivity can be used as described in equation (5) by multiplying in with the MLI area. The emissivity of the MLI represents the coupling by radiation R_{ij} of equation (9) if it is multiplied with the Stefan Boltzmann and the area of the MLI.

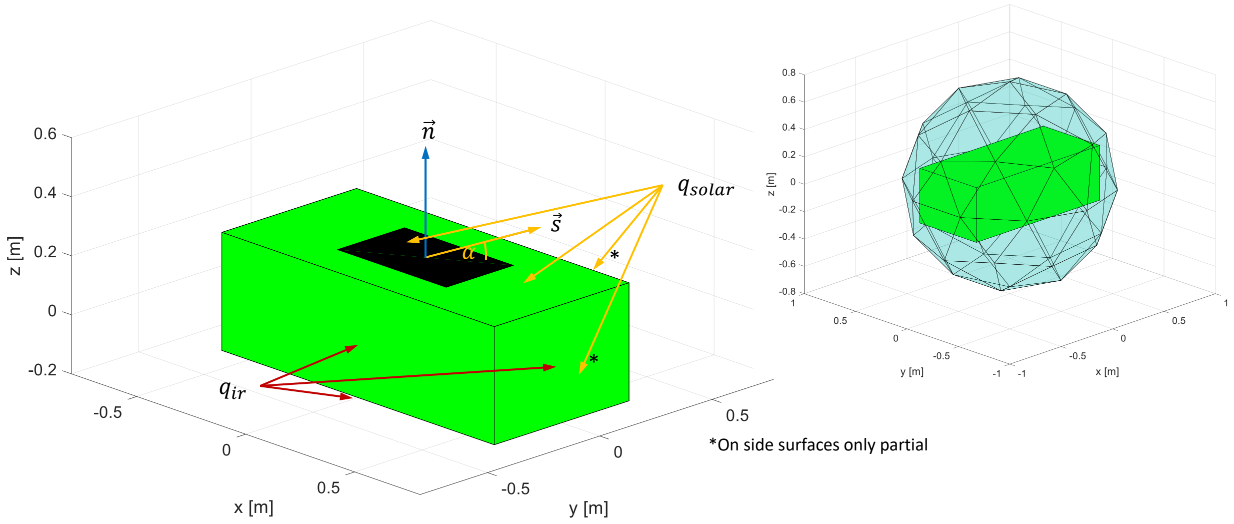

*On side surfaces only partial

Figure 31: Application of heat fluxes from optimisation maps onto thermal model of rover

The node “Rover internal” represents the frame of the rover and all its internal components. In this thesis, the assumption is that 80 % of the total mass of the rover system are located inside the rover. This assumption is based on the common design for rovers of having a warm electronic box (WEB) where most of the mass is kept at benign temperatures and is placed in a well-insulated compartment. For example, this is the case for the design of MER; MSL; Mars2020 and ExoMars (Alary and Lapensée 2010; Bhandari et al. 2005; Novak et al. 2003; Novak et al. 2014). However, the mass distribution of these rovers could not be established due to unpublished documentation and the assumption that 80 % of the rovers total mass are located within a WEB is an engineering guess. The heat capacity of this node is defined by assuming heat capacitance of Aluminium with 890 J kg^{-1} K^{-1} (Gilmore 2002-©2003). Excessive heat production can occur within such volume. Hence, a conductive path to an external radiator is necessary. Hot temperatures can then be controlled by sizing the radiator properly. As a drawback, temperatures of the internal node would drop quickly under cold conditions. It is possible to reduce heat transfer during cold conditions and increase heat transfer during hot conditions with an implementation of a heat switch. The conductive link between radiator and the internal node is assumed with 0.05 W K^{-1} in open position and with 3.33 W K^{-1} in closed position. Values are adjusted to match a heat transfer of 20 W through the heat switch from values of MER which was designed to transfer 6 W of heat (Sierra Nevada Corporation 2018). Set point of the heat switch is 245 K. The value of 20 W comes from the constantly running on-board computer as presented in chapter 3.3.2. A parasitic conductive heat loss to the radiator of 0.2 W K^{-1} is also present in the model at any time. It accounts for all heat losses of the internal node due to simplification of reality. Such heat losses can come from mounting structures together by screws, attaching MLI on the structure, simplifying geometrical shapes and dimension and many more. Hence, this value is purely estimated by engineering guess and has to be adjusted for real systems after testing.

A heater is implemented at the internal node of the rover. It is a bang-bang heater switching on if temperature falls below a lower threshold temperature and switches off after reaching the threshold temperature again. It is chosen due to its simple implementation even though it comes with the drawback of using small time steps for solving of the thermal model for a realistic representation of the energy consumption. Default set point for the heater is the same as for the heat switch at 245 K and a power of 20 W.

A radiator is placed on the top plane of the box, as this is an ideal location for rovers operating at lunar poles. It mainly sees deep space with best conditions to emit heat. The radiator is made out of aluminium with a thickness of 1 mm and a homogenous temperature distribution due to its modelling approach of only one node. The real size of it would be bigger due to this simplifying assumption. The radiator also receives solar heat load as stored in the optimisation maps but the angle between sun and the plane of its surface is factored in by the sine of that angle. Furthermore, the surface slope underneath the rover is considered for definition of the normal of the radiator plane. It is assumed that no infrared heat radiation from the terrain reaches the radiator. Heat load on the radiator is given in equation (17).

$$\dot{Q}_{solar} = q_{solar} \cdot sin\alpha \cdot A \cdot \alpha_{solar} \tag{17}$$

Q_{solar} is the absorbed heat load from the Sun, q_{solar} the heat flux from the optimisation map, α the angle between the plane of the radiator and the Sun, A the area of the surface, and α_{solar} the absorptivity of the radiator in the solar spectrum.

Table 5 lists all connections between the thermal nodes of the rover. Heat exchange with the environment is not included. Values are already describe in this chapter.

Table 5: Conductance values within the thermal model of the rover

Conductor Name	Conductor Type	Index first node	Index second node	Value
$K_{l,MLI}$	Conduction	1	2	0.031 [W m^{-2} K^{-1}]
$R_{r,MLI}$	Radiation	1	2	0.0067 [-]
$K_{l,closed}$	Conduction	2	3	3.33 [W K^{-1}]
$K_{l,open}$	Conduction	2	3	0.05 [W K^{-1}]
$K_{l,parasitic}$	Conduction	2	3	0.2 [W K^{-1}]

3.3.2 Power Model

A realistic model of the power consumption of the entire rover system is crucial for meaningful results of traverse optimisation. This is especially true for a solar powered rover system because it can only charge batteries in sun light and relies purely on batteries in darkness. In this thesis, the implementation of the power subsystem is basic by modelling power needed for communication, for on-board computer, and for driving. An implementation of more detailed power models is straightforward and it might become necessary during the evolution technical details of a mission are known. The basic implementation in this thesis is suitable to account for the most important power parameters because the ones with highest power demands are considered in the model and are handled dynamically where this is essential.

On-board Computer

This power figure represents all active electronics, including CPU, sensor electronics, data storage electronic etc. The value used in this thesis can be replaced with real numbers as soon as a certain design of a rover matures. This is a number that could not be established for successful missions such as MER and MSL by investigation of literature. For MSL one source states that it needs at least 45 W to 70 W while asleep, at least 150 W when awake, and up to roughly 500 W when driving. (Gross and Cardell 2011). How the power is distributed across all systems is not detailed. For MER, a peak load of 140 W can be produced by the solar cells in combination with the battery (Stella et al. 2005) but again, no power distribution is given.

For the purpose of thesis, it is deemed adequate to assume a constant power value for electronics used during driving. A different power figure would only influence the size of the battery because solar cells should be sized such that they always can deliver enough power for full operation as long as they are fully illuminated. For the standard rover of this thesis it the on-boar power is set to 20 W constantly and it is applied to the thermal node inside the rover.

Communication power

Power demand for communication depends on the mission architecture and on the amount of data that needs to be transferred. The model in this thesis assumes a relay satellite in lunar orbit, just as is the case for MSL operating on Mars. A relay satellite at an altitude of 200 km would return roughly every 2 hours for a time slot for communication of close to 4 minutes. Hence, it is assumed that the rover consumes 40 W every 2 h for communication. The power is justified by the transceiver on board of MSL, which consumes 60.2 W at maximum, but it is a much bigger rover system. For the smaller size of the default rover model, less data might have to be transmitted resulting in a lower power demand. This power is not distributed on any thermal node because of its short-live nature and with the assumption that the thermal capacity of the communication electronics would buffer that heat load.

Driving power

During the Apollo program, there was an extensive test campaign in order to develop a mobility system for a lunar roving vehicle. Numerous design options were created, evaluated, and eventually tested. Empirical equations derived by that time (Bekker 1962, 1964) are still valid and have been enhanced further for utilisation in traverse planning (Ding et al. 2011; Leader et al. 2014; Potts et al. 2015; Speyerer et al. 2016). Also, the model for wheels of ExoMars is based on Bekker (1964) but has been enhanced further to predict tractive performance with flexible wheels (Favaedi et al. 2011). Other improvements in aforementioned publications also focussed on improving specific aspects of the original equations. For a general prediction of the power need for driving, the original equations provide reasonable numbers without the need of a manifold of input parameters. A sensitivity study on the influence of the implemented equation on the optimisation algorithm is provided in chapter 5.3, in order to assess the effect of a different power demand. In this thesis, the power demand for driving of the rover system is calculated dependent on the rover speed, the rover weight, and the current slope (Bekker 1964). Equation (18) gives the total power P_{drive} in W.

$$P_{drive} = P_{horiz,wheel} \cdot n_{wheels} + P_{slope} \tag{18}$$

It is the sum of the power needed for driving on a non-planar surface P_{slope} and the power necessary to drive which is composed of the power need of a single wheel $P_{horiz.wheel}$ which is calculated with equation (19) (Bekker 1964) and of the amount of wheels n_{wheels}.

$$P_{horiz,wheel} = \frac{v}{550 \cdot \eta(3-n)^{(2n+2)/(2n+1)}(n+1)\left(k_c + bk_\varphi\right)^{1/(2n+1)}} \cdot \left[\frac{3W_{wheel}}{\sqrt{D}}\right]^{\frac{(2n+2)}{(2n+1)}} \cdot 745.7 \tag{19}$$

Values of η, k_c, and k_φ define the pressure-sinkage characteristics of lunar soil under a wheel load. k_c represents the cohesive modulus of soil deformation, k_φ is the frictional modulus of soil deformation, and η is the exponent of sinkage. Values for them are k_c = 0.14 N cm^{-2}, k_φ = 0.82 N cm^{-3}, n = 1 (Heiken 1995). In equation (19), v is the velocity of the rover, b is the smaller dimension of loading area of a deformable wheel, D is the diameter of the wheel, and W_{wheel} the load on wheel as defined in equation (20).

$$W_{wheel} = \frac{m}{n_{wheel}} \cdot g_{Moon} \tag{20}$$

The load on one wheel is calculated by dividing the mass of the rover m with the amount of wheels n_{wheel} and multiplying the result with the gravity acceleration on the Moon, $g_{Moon} = 1.62$ m s^{-2}.

$$W = m \cdot g_{Moon} \tag{21}$$

The total weight of the rover W can be derived by multiplying the mass of the rover with the gravity acceleration on the Moon as equation (21) highlights.

Equation (22) describes the power demand for roving over a non-planar surface with a slope of α.

$$P_{slope} = W \cdot sin\alpha \cdot v \tag{22}$$

With equation (18) to (22) presented it is possible to calculate the power demand for driving on any point of the terrain and with different rover mobility concepts.

Solar Cells

Solar cells power the rover in this thesis. It is assumed that an array of solar cells sits rectangular on top of the rover and that it can track the Sun in a way that it is always perfectly aligned with the Sun. For a rover operating at the poles this is a valid assumption, as only one degree of freedom for a pointing mechanism would be needed. Considering a slope of the terrain of about 15° at a position around -87° N and the maximum solar elevation possible there (i.e. 4.54°), it is still possible to receive nearly 94 % of the solar heat flux with a mechanism with one degree of freedom due to the dependency on the cosine. The incoming solar radiation as produced by the optimisation maps described in chapter 4.2.3 is multiplied with the area of the solar cells.

Total size of the solar cells for the standard rover in this thesis is set to 0.96 m². This seems to be a feasible size with the given dimension of the rover and foldable solar array. For example, the total area of solar cells mounted on the foldable array on MER are about 1.3 m² (Novak et al. 2005) with an output of up to 460 W and efficiency of about 27 % (Stella et al. 2005). For comparison, ExoMars rover have a total of 1.5 m² area of solar cells with an efficiency of 30 % (Ferrando et al. 2017; van Winnendael et al. 2005). The total efficiency of converting solar energy in the default model of the rover is set to 20 %. Multiple junction solar cells provide efficiencies in the range of 30 % (Ley et al. 2019) but in order to account for line losses and also lunar regolith sticking onto solar cells over the time which reduces their efficiency, a lower value is chosen. For planning of a mission scenario or traverse optimisation of a rover in a later design stage, values that are more realistic can be incorporated in the model.

Battery

The power model considers the capacity of a rechargeable battery and the maximum charge rate of it. A default value for capacity is not set. Individual settings for traverse are set later in mission scenarios. During illumination of solar cells along the traverse, batteries can be recharged with the remaining power delivered by solar cells after subtracting all power that the rover currently consumes. A maximum charge rate can be considered and it is assumed with 1 C, meaning that the battery can be fully charged within one hour if enough power is provided by solar cells. This is a characteristic common to Lithium based batteries often used in space applications where a guideline suggest a charge rate of less than 0.8 C (Ley et al. 2019). For batteries with large capacities high currents might occur if a charge rate of 1 C is assumed, it might happen that the charger is not able to handle high power values needed to charge with 1 C. If this has to be considered in the model, the charge rate has to be adapted accordingly. In the current implementation, no temperature dependent behaviour of the battery is implemented. In addition, the current implementation of a pure linear charge/discharge behaviour is deemed accurate enough for the purpose of this thesis. Table 6 provides battery capacities of MER, MSL, ExoMars, and RP.

Table 6: Battery capacity of rovers

Name	MER	MSL	ExoMars	Resource Prospector
Battery capacity [W h]	400	1600	1140	5500
Source	(Crisp et al. 2003)	(Welch et al. 2013)	(Amos et al. 2017)	(Andrews 2015)

3.3.3 Level of Detail

The description of the model of the rover in chapters 3.3.1 and 3.3.2 reveals that a most simple but yet sufficient modelling approach is chosen, Advantages of a simple model are obvious. It is easy to understand because there are no complex interactions between different components or within a single component. Because of that, it is also less prone to errors as erroneous values and faulty behaviour have a big influence on the system, which can be identified quickly. Furthermore, refining the model and implementing a higher level of detail to components is connected with little expenditure. On the downside, the accuracy of the model suffers with lower depth of detail with the consequence of higher uncertainties. Finally, it all boils down to the decision when is the model accurate enough in order to represent the behaviour of the real system for fulfilling the purpose of the modelling approach. Literature covers this topic in various publications. One example of trying to give guidelines on modelling and simulation in general and in particular with respect to life support systems is given by Jones (2017). He states that for successful modelling and simulation three tasks are crucial: “Identify the right problem, apply the correct expertise, and plan the effort accordingly” (Jones 2017). The topic of this thesis mainly relates to applying the right expertise on how to model the overall subject in order to achieve meaningful results and answer the question if the consideration of the total energy state of the rover provides benefits to traverse planning. Hence, the chosen model represents the behaviour of a potential rover system accurate enough in order to answer this question. A thorough literature review in combination with experience in the field of engineering lead to assumptions resulting in the model described in chapters 3.3.1 and 3.3.2. The following paragraphs discuss why a higher level of detail in the model is not required in this thesis.

In the context of a model that shall represent the energy state of a rover with a higher level of detail than used in this thesis, a model would have to consider parameters of all components that influence the overall performance of the energy state. For many components, this is a temperature dependency but it can also be a dependency on the load of the component and other values. For example, the discharge capacity of a certain type of battery changes with temperature (Smart et al. 2018). Figure 32 depicts discharge capacities for rechargeable Li-ion batteries used on MER, MSL, and the Mars lander InSight. MER and MSL share the same chemical composition of meso-carbon microbeads (MCMB) anodes and $LiNi_xCo_{1-x}O_2$ (NCO) cathodes whilst the chemistry of the battery of InSight is upgraded to graphite anodes and $LiNiCoAlO_2$ (NCA) cathodes. Results in Figure 32 also include NCO based battery with a substitute electrolyte that can withstand lower temperatures. The term cycling refers to 197 charge/discharge cycles at the specified temperature range. This example of discharge capacity, which depends on temperature, shows that for a specific chemistry its dependency on temperature can be implemented in the model by testing the system thoroughly and derive look-up tables or use curve-fits. This would lead to the fact that statements on the energy state can only be drawn with respect to this specific chemistry only. Additionally, Figure 32 proves that technological progress can render certain performance dependencies obsolete. In this specific case, the newly developed chemistry (NCA with low temperature electrolyte) reduced the decrease in performance from 32 % with the heritage chemistry to 5.2 %.

In the case described above, one can state that the current implementation of the battery model with a fully available capacity and a discharge rate that does not affect the performance of the battery seems to be accurate enough. The loss of 5 % of the capacity after 197 cycles is probably less than the total uncertainty in the optimisation approach developed in this thesis. Of course, this is only true for the temperature dependency. Other dependencies on the performance of a Li-ion battery exist such as on the discharge current, number of charge-discharge cycles, ageing, and so on. They are not discussed further here, as this would exceed the topic of this thesis.

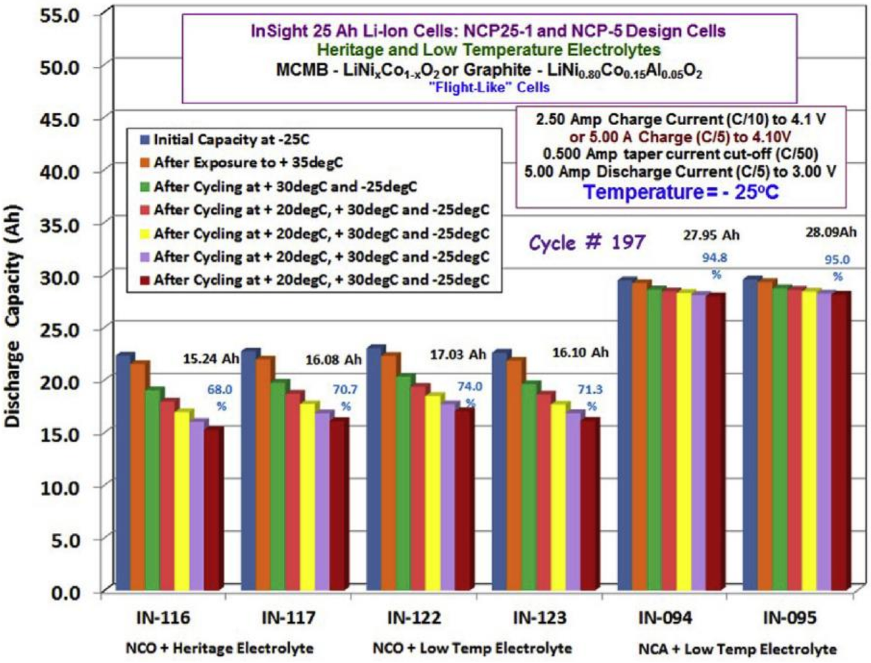

Figure 32: Discharge capacity of different Li-Ion cells. Image source: (Smart et al. 2018)

This is one example that already outlines the complexity of different parameters having an influence on performance characteristics. In the case of a solar powered rover, performance of many more components depends on specific parameters. For example, the efficiency of solar cells depends on the temperature and the efficiency of a power supply depends on the drain current. There are many more interactions within a real system but due to the aforementioned reasons, they are not present in the current model.

It is the main intention of this thesis to evaluate the benefits of a consideration of the overall energy state on traverse optimisation. The implemented model can already achieve this in a general way by identifying trends and important parameters, which have an effect on the optimal traverse.

A more detailed model can then answer different questions such as “is a more stringent temperature control of solar cells improving the overall performance or efficiency of the energy state” and “can heating of the battery guarantee longer distance”. However, those questions are subject to the chosen technological solution. This consequence might be welcome to the engineer but it is not required in order to derive general statements about traverses of a solar powered rover.

4 Traverse Planning

The traverse planning process derived in this thesis incorporates tools, scripts, and flow charts described within this chapter. They are all summed up under the name of TherMoS-X, a further evolution of TherMoS (Hager 2013).

4.1 TherMoS-X

TherMoS was first developed by Hager (2013) at the chair of astronautics at TUM with the intention in mind to prove that dynamic thermal modelling can provide benefits for the thermal design of a system compared to the classical approach of designing against static worst cases for hot and cold conditions. He took the lunar environment during surface operation as an example to demonstrate that point.

Figure 33 depicts the architecture of TherMoS as developed and describe in Hager (2013). Most components run within MATLAB® except the ray tracing algorithm and data exchange between MATLAB® and the ray tracer. Main functionalities include the creation of a spacecraft, which could also be a rover or an astronaut. Furthermore, TherMoS facilitates the creation of an environment for the spacecraft on the Moon's surface, which could be either derived from measured elevation profiles with the choice of data from KAGUYA or LOLA or an artificial setup including rocks, boulders and craters. It also incorporates the creation of orbit and position data at the chosen site with Sun and Earth position relative to the current position of the scene. The entire scene can then be simulated by calling a ray tracing routine outside of MATLAB® and solving the regolith model in MATLAB® with results prepared by the ray tracer.

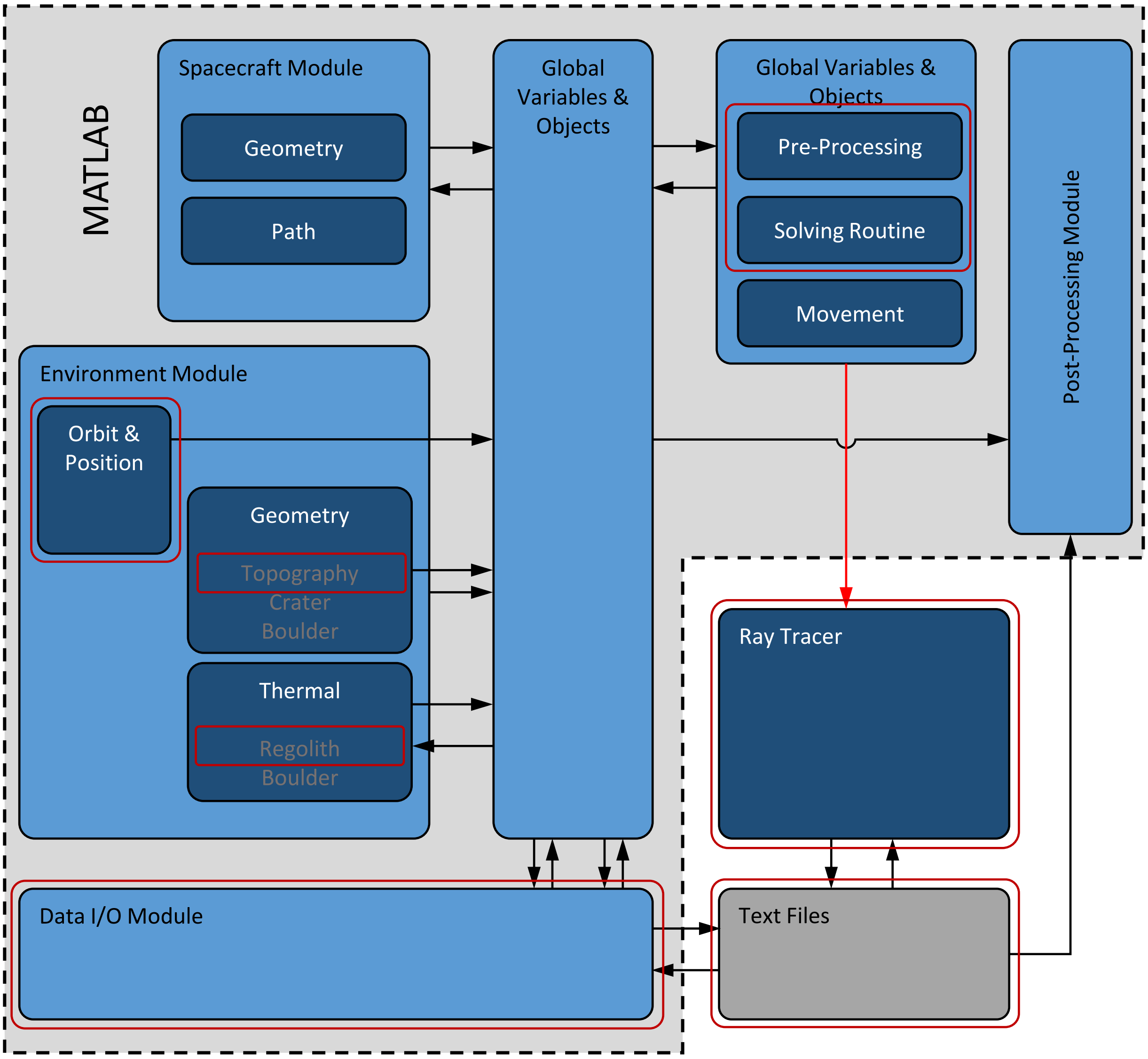

Figure 33: Overview of TherMoS Modules and Components including interactions. Black arrow stands for data flow, red arrow for function call. Necessary changes are framed red. Adapted from (Hager 2013).

Several improvements were necessary in order to use results from simulation of the lunar surface for traverse optimisation. This affects the environment module, the pre-processing routine, the solving routine, the ray tracer, and the data input/output (I/O) module. A brief summary of them is presented in the following paragraphs. Chapter 4.1.4 gives more details about updates concerning ray tracing.

Orbit & Position: It is now also possible to import the position of the Sun relative to the centre of the scene from an external file. For example, the Systems Tool Kit (STK) also provides the capability of sophisticated orbit propagation with the ability to export Sun angles at specific locations for specific dates. This becomes necessary for calculating position of the Sun in polar regions because the orbit propagator of TherMoS has uncertainties in the range of 1°, which causes faulty illumination conditions.

Topography: Another improvement is achieved for the topography part of the environment module. It is now possible to import external digital elevation models. This is required if most accurate digital elevation model should be used. Measurements provided by LOLA are prone to offsets in tracks of repeated ground coverage. In order to achieve best resolution out of LOLA data, Gläser et al. (2013) described a process of co-registration of LOLA tracks resulting in higher positional accuracy than raw data from LOLA alone. Chapter 3.1.1 outlines details about the available DEM at the south pole.

Regolith model: The thermal model of regolith evolved since the first release of TherMoS which mainly based on Vasavada et al. (1999). Consequently, the most recent values from Hayne et al. (2017) are the basis for the updated implementation in TherMoS-X. Properties of regolith affected by that are thermal conductivity, specific heat, and density. Values can be found in chapter 3.1.2.

Pre-processing: The calculation of initial temperatures at begin of the simulation is also improved. After the first call of the ray tracer, temperature of the surface of the Moon are derived by thermal equilibrium calculation with the absorbed solar flux. Nodes into depth are then distributed with an exponential equation as describe by Hayne et al. (2017).

Solving routine: Applied changes in solving of the regolith model can only work with updates of the ray tracer. Previously, at each time step temperature dependent values of regolith are calculated explicitly based on the temperature of nodes from the previous time step and transferred as constant values to the solver. In addition, the total net infrared heat flux of each surface triangle is an output from the ray tracer with an explicit value and is calculated with temperatures from the previous time step. This approach works only with small time steps of up to 20 s with the implemented solver of MATLAB®. The implementation in TherMoS-X minimises dependence on explicit values to only one occurrence within the equation to be solved. Furthermore, an additional solver can be used in order to calculate temperatures of a modelled sample body, which is a rover in the frame of this thesis. More details on the solver can be found in chapter 4.1.2

In TherMoS-X, two major changes enable much longer time steps of the solver up to 1800 s. On the one hand, values for thermal conductivity and thermal capacity are now part of the equation in the solver instead of being calculated as explicit values at each time step. On the other hand, calculation of the infrared heat flux is spit into the total net heat flux of a surface triangle to all other triangles which is calculate with temperature values from the previous time step and a radiation exchange factor from the surface triangle to space. Both changes allow the mentioned increase in time step size.

Ray tracer: It is also necessary to develop the ray tracer further in two domains. First, the solver needs different input from the ray tracer in order to solve temperatures of the Moon. Second, illumination conditions at the lunar poles have to be simulated as accurate as possible. Rays for calculation of the received solar heat flux are now launched from the triangles towards the Sun, which is represented by a disc. This enables realistic lighting conditions including regions on the surface with penumbra. The ray tracer can now distinct between heat transfer by radiation between surface triangles and heat transfer by radiation towards free space. Solving the model requires input from the ray tracer at each time step for calculation of heat transfer between surface triangles whilst the heat transfer to space is based on a constant radiation exchange factor determined once at initialisation. A major increase in performance is achieved by changing the way the solver calls ray tracing. Now, the ray tracer program starts only at the beginning of simulation and stays open throughout the entire duration of the simulation. This is much faster than the previous approach where the ray tracer was started and closed at every solving time step. Lastly, the ray tracer is now able to use multiple GPUs in order to boost performance using Message Passing Interface (MPI).

Data I/O: Data exchange by writing to text files is one of the slowest options for that purpose. Hence, TherMoS-X uses mapped memory for fast exchange of information. This includes update of solar angles, surface temperatures, transformation matrix of the sample, infrared heat fluxes, and solar absorbed fluxes.

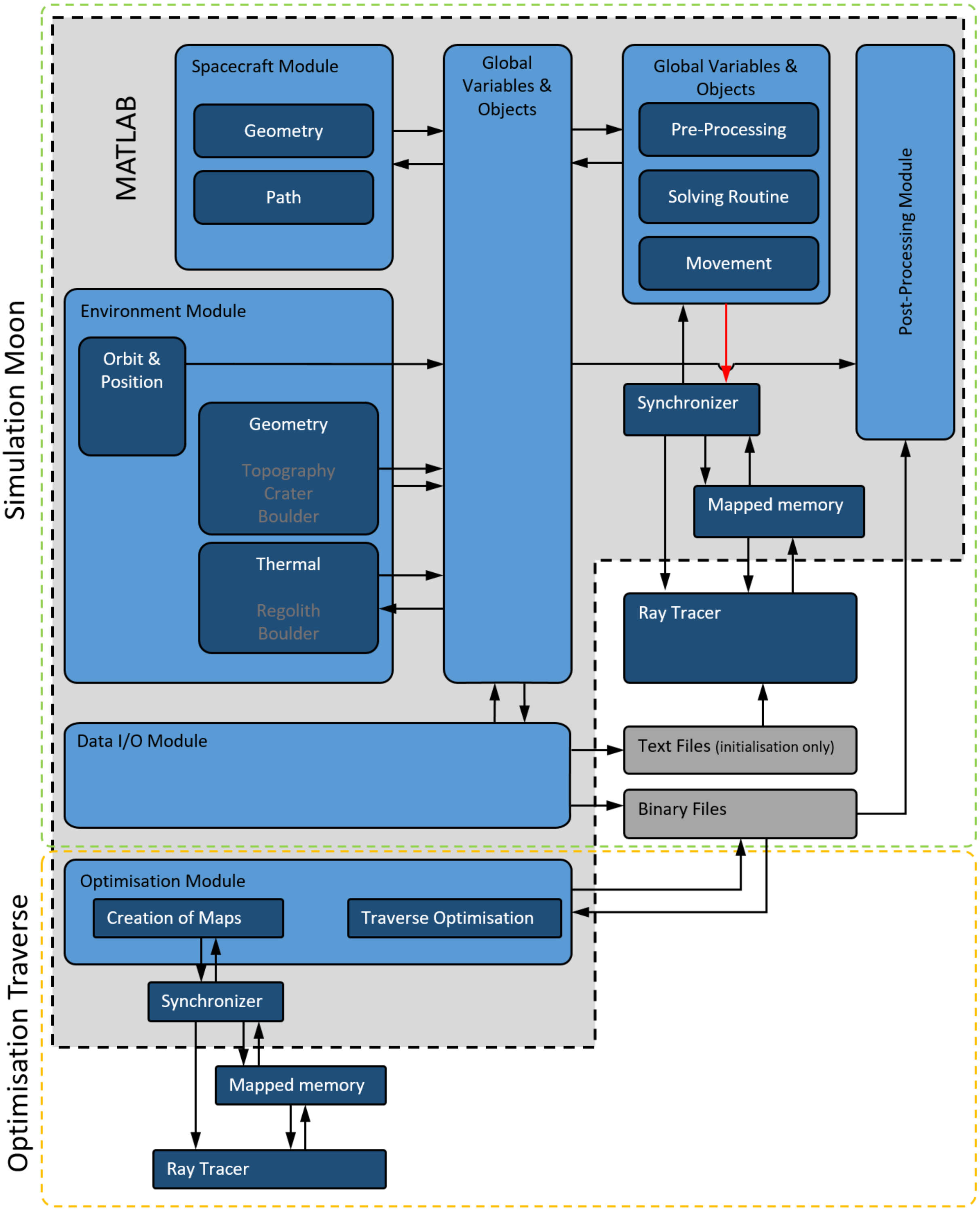

Figure 34: TherMos-X schematic

Figure 34 shows the updated functionality of TherMoS-X. Simulation of the temperature of the surface of the Moon as well as simulation of a moving body on the surface is still possible but the code of the tool is updated with changes as described above. This functionality is framed with a dashed green line in this schematic and is named simulation Moon. It is required to have temperature results from a simulation run in order to start optimisation of a traverse.

The main topic of this thesis is the optimisation module. With this extension, it becomes possible to optimise a traverse between two waypoints for a rover system. This feature is only available if temperatures of the region of interest have already been simulated because the optimisation module needs them as a boundary condition for creation of thermal maps. Maps are created at a defined time interval (1800 s as default) storing information about direct solar heat load and received infrared heat load of a sphere at the centroid of each triangle of the surface of the Moon. It is also possible to reduce the amount of triangles that are considered for those maps if waypoints are already known and engineering guesses reveal triangles, which never could be visited. For example, one can also draw a circle around the centre between start and goal point and only consider triangles of the surface of the Moon, which lie within a certain radius. Furthermore, technological limits reduce the amount of nodes in the map to be considered during optimisation. One example is the maximum slope a rover can overcome. Chapter 4.2.3 gives detailed description of optimisation maps and possibilities to reduce the amount of nodes.

4.1.1 TherMoS-X User Interface and workflow

The user interface of TherMoS-X consists of a graphical user interface (GUI) for running thermal simulations and plain text in scripts for the optimisation part. Figure 35 is a snapshot of the GUI. The workflow to derive optimised traverses is a sequential procedure just as is the case to simulate temperatures on the Moon. The overall functionality of original version of TherMoS remains unchanged but more input sources are now accepted and optimisation of traverses is added.

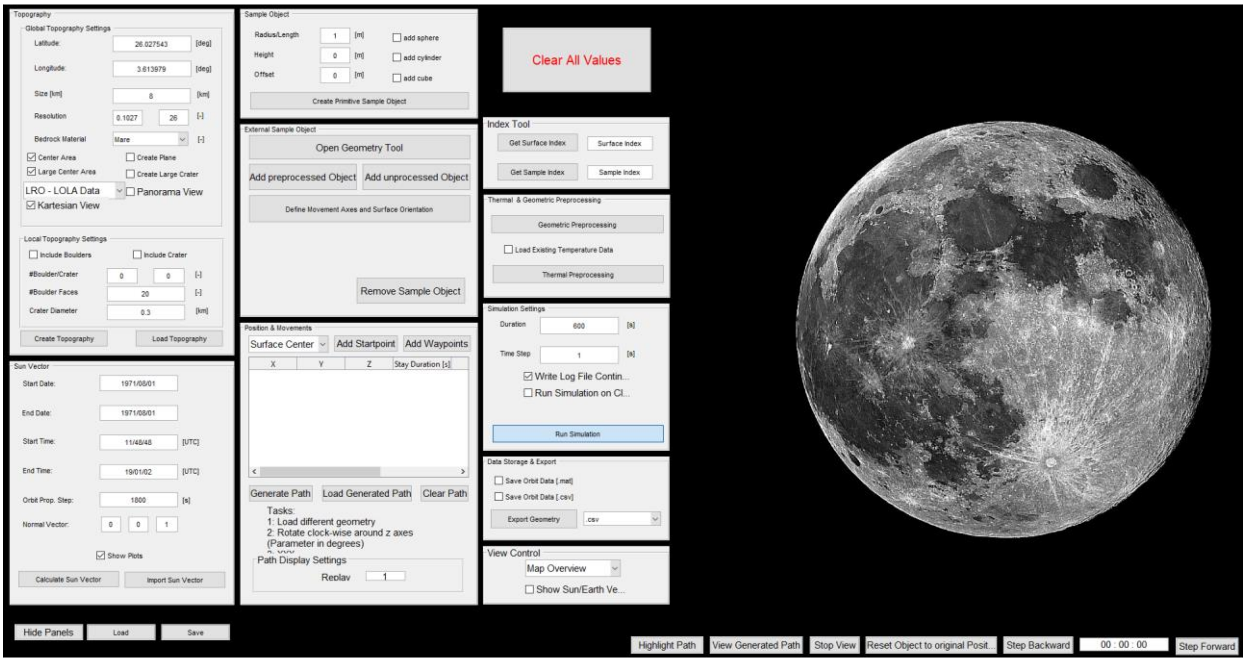

Latitude: 26.027543 [deg]
Longitude: 3.613979 [deg]
Size [km] 8 [km]
Resolution 0.1027 26 [-]
Bedrock Material Mare [-]
☑ Center Area ☐ Create Plane
☑ Large Center Area ☐ Create Large Crater
LRO - LOLA Data ☐ Panorama View
☑ Kartesian View
☐ Include Boulders ☐ Include Crater
#Boulder/Crater 0 0 [-]
#Boulder Faces 20 [-]
Crater Diameter 0.3 [km]
Start Date: 1971/08/01
End Date: 1971/08/01
Start Time: 11/48/48 [UTC]
End Time: 19/01/02 [UTC]
Orbit Prop. Step: 1800 [s]
Normal Vector: 0 0 1
☑ Show Plots
Radius/Length 1 [m] ☐ add sphere
Height 0 [m] ☐ add cylinder
Offset 0 [m] ☐ add cube
Surface Center

X	Y	Z	Stay Duration [s]

Tasks:
1: Load different geometry
2: Rotate clock-wise around z axes
(Parameter in degrees)
Replay 1
Surface Index
Sample Index
☐ Load Existing Temperature Data
Duration 600 [s]
Time Step 1 [s]
☑ Write Log File Contin...
☐ Run Simulation on Cl...
☐ Save Orbit Data [.mat]
☐ Save Orbit Data [.csv]
.csv
Map Overview
☐ Show Sun/Earth Ve...
00 : 00 : 00

Figure 35: Picture of the TherMoS-X GUI for running thermal simulations on the Moon

At the beginning, the location to be simulated has to be defined together with the size of the scene and its resolution. Additional to the usage of direct measurements of data from LRO and Kaguya, it is possible to import the topography from external data source, which is pre-processed automatically in order to match data structure of TherMoS-X. Chapter 3.1.1 explains this process in detail.

After that, the position of the Sun with respect to the local scene has to be calculated. Again, it is now also possible to import solar angles from other tools in plain text files. This allows quickly using different propagators of our solar system.

Environmental settings are now accomplished and one can decide whether a moving object should be used during a thermal simulation. This is not required for traverse optimisation as the rover model and its parameters are set later on in the optimisation module. Hence, this part of TherMoS-X is not described here and the reader is referred to Hager (2013).

The software has now everything available in order to run thermal simulations of the Moon, which is the same as previously in TherMoS. One has to select the time step size of the solver and the duration of the simulation. Also how and if results are stored can be set here. As an additional option, temperature results from a previous run can be used as initial condition for the current simulation run. With that, it is possible to conduct an initialisation run with much larger time steps of the solver and without wasting memory, as results do not have to be stored.

After completion of thermal simulation of the surface of the Moon, the optimisation module can be started. Main control of optimisation is done by running scripts manually and adjust variables within them instead of pressing buttons on the main GUI. This option will be implemented in the future for an easier interaction with the user. Currently, one has to define a model of the rover with parameters described in chapter 3.3. The main function of the optimisation module loads those parameters and starts the iterative optimisation as described in chapter 4.3

4.1.2 Thermal Solver

Temperatures of the Moon are derived by applying equation (11) to each single node in the model. It is important to note that specific heat and thermal conductivity of lunar regolith depend on temperature as described in chapter 3.1.2. The solver in the original version of TherMoS calculated explicit values for entries in these equations, which depended on temperature from the previous time step. This is also true for heat exchange by radiation of nodes on the surface of the Moon where values for absorbed heat are derived by ray tracing and are handed over to the solver. This implementation is a valid modelling approach with the drawback of requiring small time steps. Maximum time step lies between 20 s to 30 s, which is too short for simulation runs spanning more than a couple of hours. Hence, the solver implementation in TherMoS-X diminishes calculation of explicit values that depend on temperature to only one component in the ordinary differential equation as equation (23) shows.

$$C_i(T)\frac{dT_i}{dt} = \sum_{j\neq i} K_{ij}(T)\left(T_j - T_i\right) + \sum_{j\neq i} R_{i-space}\left(T_{space}^4 - T_i^4\right) + \dot{Q}_{ir,net}(T) + \dot{Q}_i + \dot{Q}_S \tag{23}$$

Specific heat c_p needed for thermal capacity C and thermal conductivity k in order to derive the value of conductive coupling K are implemented as a temperature dependent equation in the solving routine as described in chapter 3.1.2. Heat exchange by radiation is split into two parts. One part represents radiation to space with a radiation exchange factor $R_{i\text{-space}}$ that is determined by ray tracing once for a simulation prior to the first time step and stored in memory for ongoing usage in simulation. The other part is the net heat radiation $\dot{Q}_{\mathrm{ir,net}}$ received by that surface node from all others nodes, which is also determined by ray tracing. This is the only explicit value of temperature dependent variables remaining in the updated solver. For nodes at the bottom of the one-dimensional nodal distribution of a triangle, there is also heat $\dot{Q}_{\mathrm{i}}$ coming from the internal of the Moon. Surface nodes also receive heat from the Sun $\dot{Q}_S$. With this implementation, it is possible to increase the time step up to 1800 s, which is in good agreement with the time step required for determination of solar heat load as described in chapter 2.3.3. MATLAB® provides different solvers for ordinary differential equations. For solving of equation (23) the built-in solver ode23 is chosen as it has already proven its capability in the predecessor TherMoS (Hager 2013).

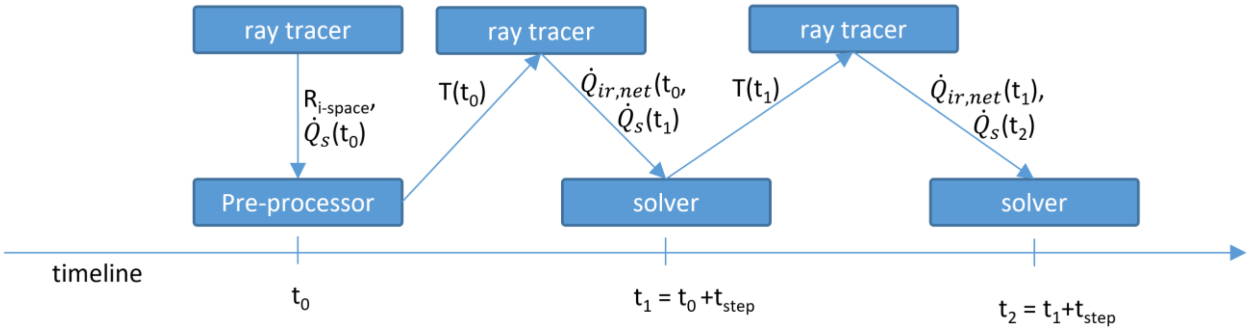

Figure 36: Process of solving during simulation of the lunar surface

Figure 36 shows a flowchart of thermal simulation method within TherMoS-X. It outlines when calls to the ray tracer occur and when calls to the solver. At the start of a simulation, initial temperatures have to be set. The approach is already described in chapter 3.1.2: in brief, the ray tracer determines view factors of the surface triangles to deep space together with the absorbed heat load from Sun. With them, equilibrium temperatures of the isolated surface triangles are derived. Nodes into depth are afterwards initialised after equation (16). With the initialisation done, the simulation can now start by iteratively calling the ray tracer and the solver. At each time step, the ray tracer computes the net heat radiation $\dot{Q}_{\mathrm{ir,net}}$ with temperatures from the previous step and the absorbed solar heat flux $\dot{Q}_{\mathrm{S}}$ of the triangles at the current time step. The solver puts these values in equation (23) and determines the temperature of all thermal nodes.

4.1.3 Optimisation Module

Optimisation executes in two steps. After simulation of the lunar surface is completed, creation of optimisation maps can start. Here, a dedicated ray tracer computes the information for those maps. As soon as they exist, the actual optimisation with an adapted version of A* takes place as described in chapter 4.3.

The optimisation module can run independently from other modules in TherMoS-X but it relies on input of other modules. It does not matter whether this input comes from a current simulation or from a previous run. All necessary information is stored in a simulation object and in additional binary files. The simulation object contains all data about the terrain, solar angles, solver time steps, and so on. Additional binary files store, among others, the temperature of the surface of the Moon at specified logging time steps. The required input for creation of thermal maps is the geometry of the terrain, the solar angles and the simulated temperatures of the surface of the Moon. Optimisation maps are then created as described in chapter 4.2.3. A synchronising script calls the ray tracer and the algorithm for moving the sphere through the centroids of the scene alternatingly. Results are then stored in maps at a given time step.

The final step is the optimisation itself with the approach as described in chapter 4.3. It relies on optimisation maps and the rover model as described in chapter 3.3. Again, both can be provided by a current simulation setting or be loaded from previously stored binary files. The adapted A* algorithm runs purely in MATLAB® and stores the optimised traverse together with information about the rover states along its traverse.

4.1.4 Ray tracer

In order to derive optimised traverse, calls to a ray tracer are needed during simulation of the surface of the Moon and the creation of optimisation maps. Even though TherMoS-X comprises of three different ray tracing programs, they share a common way of calculating information necessary for heat transfer by radiation. However, the results required from ray tracing by the solver differ and this leads to slightly different programs. Figure 37 gives an overview of the ray tracer programs and their calls during simulation and optimisation.

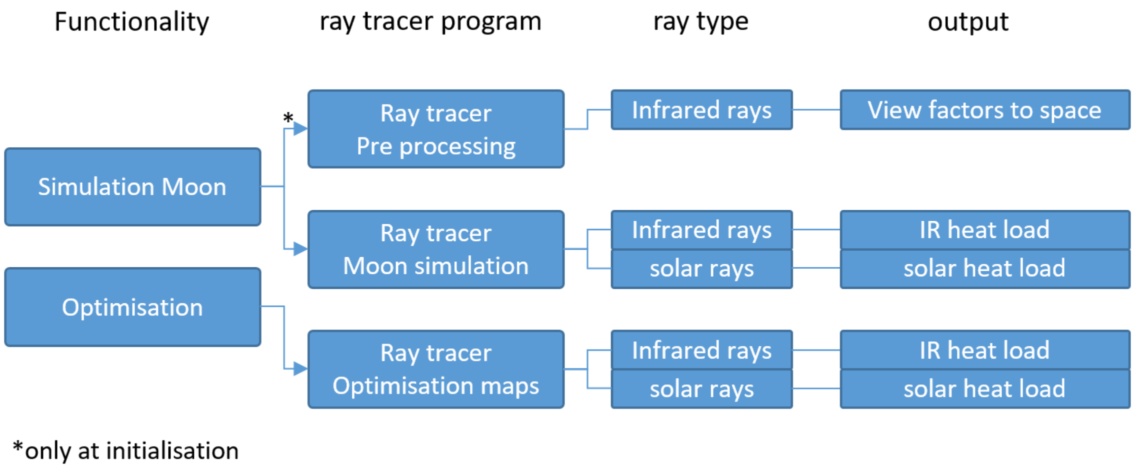

Figure 37: Ray tracer programs in TherMoS-X

The first call during a simulation run in TherMoS-X asks for view factors from surface triangles to space because they are necessary in order to calculate heat losses to space. They are constant values in the case of terrain triangles because they are fixed in their position and triangles are orders of magnitudes bigger than triangles of a moving object on the lunar surface. Hence, they are only calculated once prior to the simulation run with launches of only infrared rays. TherMoS-X stores the resulting view factors for the simulation run within the simulation object.

After that, at each time step of the solver, a call to another ray tracer is needed as it creates the required input for the solver by means of net heat fluxes of each triangle. Infrared rays determine the net infrared heat flux that each triangle receives from other surface triangles and solar rays are launched, considering first order reflections in a diffuse way in order to compute the absorbed solar heat flux on each triangle.

The third call of the ray tracer is needed for building of optimisation maps but here, rays have to be launched from triangles of a body placed on the lunar surface only. A sphere approximated with triangles is chosen as chapter 4.2.3 describes. The sphere is placed above each centre position of the triangles in the high-resolution part of the terrain. With the help of infrared rays, the program identifies the total heat flux received by the sphere. Rays are launched from triangles and as soon as they hit a triangle of the surface of the Moon, the heat load emitted from the triangle of the terrain is calculated and the absorbed portion added to the total heat flux of the triangle of the sphere. The absorbed portion is the ratio of rays hitting this surface and the total amount of rays shot from the triangle of the sphere. Solar rays are launched in the same way as for the terrain in order to determine the solar heat load. This time, only incident solar heat load is considered.

The two types of rays are depicted in Figure 39. A predefined amount of infrared rays is launched at each triangle. They are randomly distributed around a hemisphere sampling enclosing the triangle by cosine-weighted sampling based on Lambert's cosine law. Figure 38 shows a schematic sketch of cosine-weighting rays over a hemisphere on the left while the right side gives an example of rays shot from the centre of a triangle by the ray tracer program. Only rays which hit another triangle of the terrain contribute to calculation of incoming heat flux. The surface of the Moon has a high emissivity of about 0.95, which makes reflections of infrared rays redundant in the frame of this thesis.

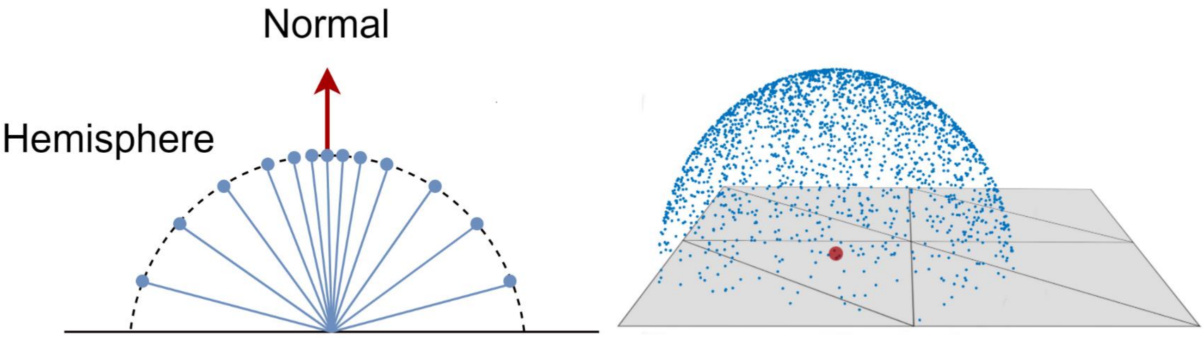

Figure 38: Cosine hemisphere sampling for representing a Lambertian radiator. More points are sampled perpendicular to the surface than parallel to it. Image source: (Alhasni 2018)

Solar rays are shot towards the Sun within an encapsulating cone. The absolute position of the Sun with respect to the centre of the scene is known as well as the size of the Sun seen from the Moon. This is about 0.54°, which is also twice the half cone angle. The ray tracer determines the absorbed solar heat flux of direct illumination by shooting a defined amount of rays towards the Sun randomly distributed within the aforementioned cone. Reflection of solar light is implemented by an additional launch of rays from each triangle. The surface of the Moon is considered to reflect solar rays in diffuse manner only as a Lambertian diffusor. At the poles, albedo is about 20 % and reflected solar light can contribute a meaningful portion of the total absorbed heat load as shown in chapter 3.2.3. Additional rays are shot to factor in diffuse solar radiation. Launching of rays follows the same approach as for infrared rays. The ray tracer considers only one reflection in the current implementation. Most of the solar energy is already absorbed after tracing where first order reflections hit the terrain and all following reflections are neglected in order to reduce computational time.

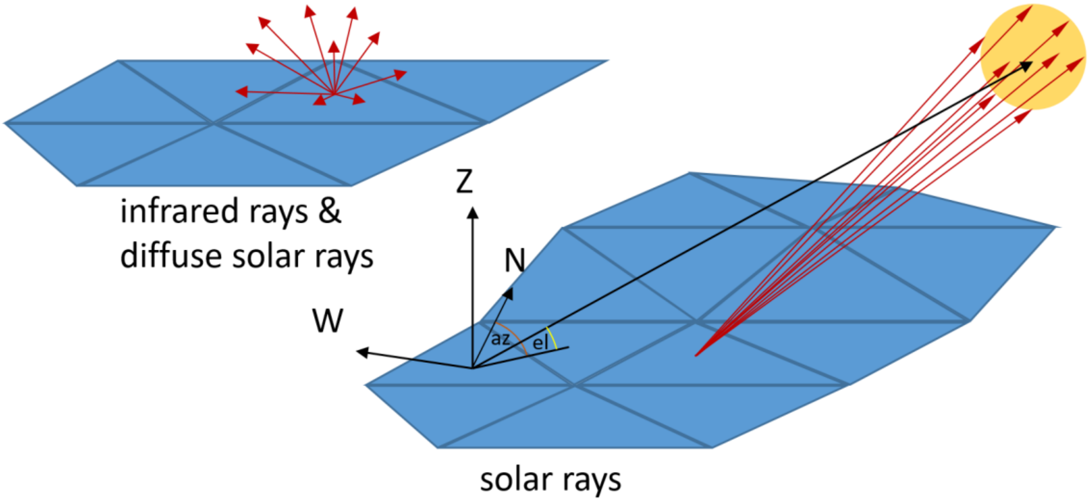

Figure 39: Schematic of ray launches for infrared and solar rays from ray tracer of TherMoS-X

Data exchange between the ray tracer and TherMoS is realised by mapped memory. A script with the name heat synchroniser calls the thermal solver within MATLAB® alternating with the ray tracer and handles communication between both. It is also possible to use multiple GPUs for an increase in ray tracing performance (Alhasni 2018).

Table 7 list the default settings for the ray tracer programs.

Table 7: Default setting of ray tracer programs

Output of ray tracer	Number rays per triangle	Number rays reflection per triangle	Solar constant
View factor to space	8000	Na	Na
Solar heat load Moon simulation	100	100	1367 W m^{-2}
Infrared heat load Moon simulation	8000	Na	Na
Solar heat load optimisation map	100	Na	1367 W m^{-2}
Infrared heat load optimisation map	1000	Na	Na

4.2 Preparatory Steps

Some preparatory steps are necessary before the optimisation of a traverse can start. This is common to complex problems where many different aspects have to be considered. This chapter shall give an overview of the most important steps.

In general, the required steps in pre-processing can be summed up as follows:

1. Determine the required size of the scene in order to capture proper illumination conditions within the ROI
2. Reduce the resolution of the ROI to an acceptable minimum which still provides accurate results with reasonable computational time
3. Reduce amount of nodes to be considered in the optimisation map due to violating boundary conditions or physical limits of the rover system
4. Pre assess illumination conditions if start date of driving is not defined and can be chosen within a given period
5. Run thermal simulation of the Moon for the chosen period
6. Create thermal maps for the optimisation algorithm
7. Run traverse optimisation

Points 1 to 3 are addressed in chapter 4.2.1. Selecting a fitting period from point 4 is presented in chapter 4.2.2. Point 5, running the thermal model of the Moon, is already described in chapter 3.1.2. Creation of thermal maps from point 6 is described in chapter 4.2.3. Chapter 4.3 explains how the optimisation itself is realised.

4.2.1 Required Size of Scene and Resolution

The approach in this thesis foresees a distinction between the region of interest, which is represented as a high-resolution part in the centre of the scene and an outer terrain model with lower resolution. The lower resolution part is only needed for ray tracing of solar insolation and reflected solar light as well as for shading effects in the infrared emission of elements of the high-resolution part to space. TherMoS-X simulates temperatures of the surface of the Moon only for the high-resolution part.

At the lunar poles, the size of the scene, which has to be considered in the model, depends on the location and size of the region of interest. If it is located within a crater, for example in crater Shoemaker, the surrounding crater rim mainly determines the visibility of the Sun within that region. A look at Figure 17 shows that the farthest features that have an influence on insolation are located about 50 km away. In contrast to that, features over 200 km away have to be considered if the region of interest includes the rim of a crater as well, for example the rim of Shackleton crater, only inches away from the south pole. In TherMoS-X, the user can define a maximum distance from a dedicated location at which terrain is still modelled. An algorithm searches for all values in x-direction with distance less than the defined maximum. It filters those afterwards in the same way with distances in y-direction having to be lower than the defined value. The result is a square-shaped scene as Figure 21 shows.

In the same way, the user defines the size of the high-resolution part. The location of the centre to which distance is calculated to is the same as for the low-resolution part. The tool searches triangles of the low-resolution terrain and removes them from the scene. They get replaced with triangles from the higher resolution DEM. Remaining gaps between the high and low resolution part are then filled with triangles which will belong to the low resolution part for later calculations. Regarding the size of the high-resolution part, it is important to ensure that the border of it is far enough away from waypoints for two reasons. On the one side, one does not want to exclude triangles, which might become part of the optimized traverse. On the other side, temperatures are only simulated for the high-resolution part of the scene. If a mountain is nearby a waypoint one has to ensure to include it in the high-resolution part for a realistic calculation of heat transfer by radiation. Rana et al. (2017) discuss the influence of the size of the scene on the heat transfer by radiation on a lander located at 82.7° S and 33.5° E. They found out, that features under certain circumstances could have an influence on infrared radiation. However, they made only a crude distinction of features being either 1 km away or 30 km away. They conclude that effects of mountains located 20 km to 30 km away are negligible (Rana et al. 2017). Hence, the border should be at least a couple of km away from any waypoint.

Comparative runs revealed that a resolution of about 160 m per pixel is the highest resolution possible with the given size of the region of interest in terms of acceptable computational time to simulate temperature of the surface of the Moon. Also, Gläser and Gläser (2019) used a similar resolution of 180 m per pixel with good agreement between measured and simulated temperatures. The outer part of the scene has a resolution of 800 m per pixel.

The implementation of a fixed resolution and size of the low-resolution part of the scene is a simple but effective solution. Temperatures show good agreement to measurements as described in chapter 3.2.5 but computational demand for ray tracing is much less than for solving the thermal model of the Moon. Hence, a more sophisticated approach of determination of required size and resolution might not increase quality of results in a meaningful way. In the future, a preparatory step is foreseen where the resolution and size of the low-resolution part is determined prior to simulation. This will quantify potential improvements on temperature simulation.

4.2.2 Select Time Period

The next step is to define the time of simulation. For a mission with a dedicated timeline this can be straightforward come from that timeline. Then, only the covered time span of the simulation has to be defined within which optimisation of the traverse takes place.

For other missions, the date might not be specified but a time frame instead. If this is the case, it is possible to simulate only illumination on the region of interest within that time frame. An assessment of illumination conditions within an expected time span for driving of the rover from the start point to the goal point can guide the mission planner to promising dates. This can be done by creating a video of the illumination conditions as Figure 40 highlights some time steps of a simulation of illumination conditions of crater de Gerlach located at -88.5° N 272.9° E. It shows again how strange looking illumination conditions at different times of a year can be and that the terrain itself looks completely different.

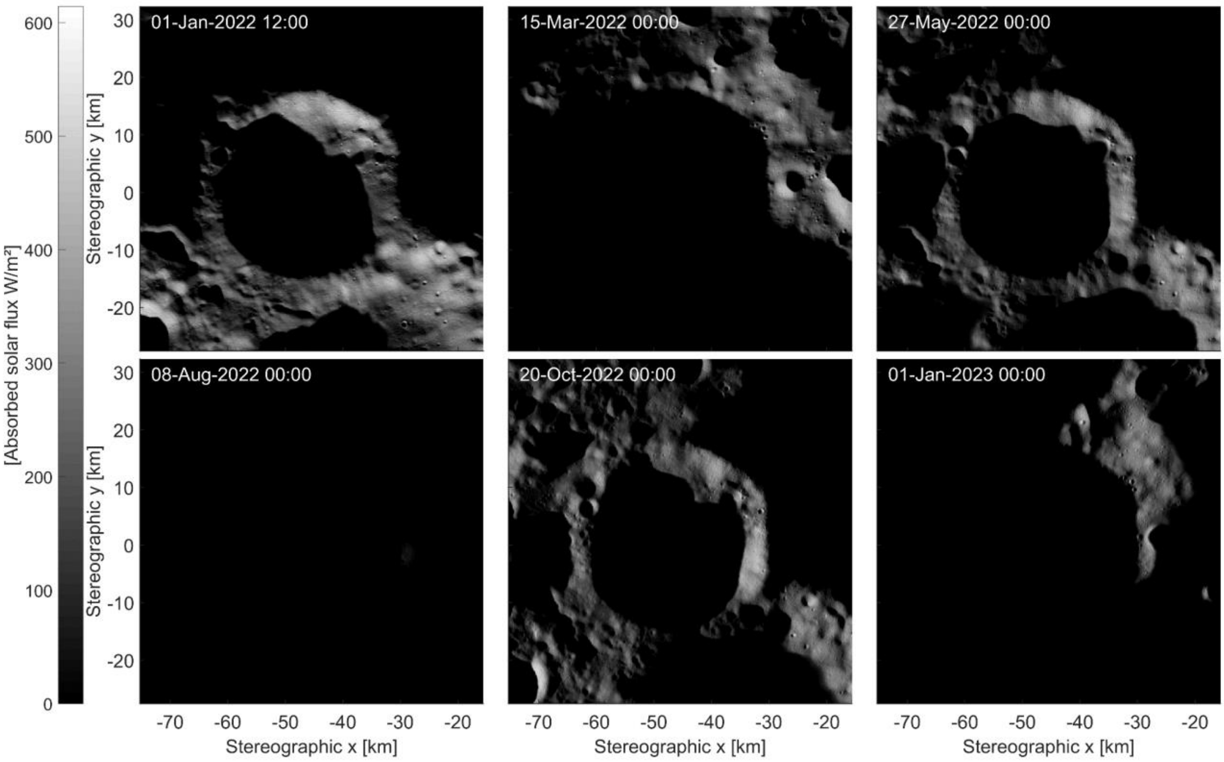

Figure 40: Illumination series of crater de Gerlach at six different points in time through the year 2022, simulated with TherMoS-X

After establishing the time, TherMoS-X can now simulate temperatures of the surface of the Moon during this period. Results have to be stored because the optimisation modules makes use of them later on for the creation of maps with incident heat load on the rover by infrared radiation.

Simulation of surface of the Moon takes place in two consecutive steps. Temperatures of the surface of the Moon need quite a long time (couple of years) to reach realistic values even with sophisticated initial values for them. Consequently, an initialisation run is needed which is set to two month prior to the start date of driving on the Moon. A longer time would be beneficial in order to match lower temperatures of the surface of the Moon more accurately, but computational limits prevent this. Results after this run are deemed well enough for optimisation, because usually rover systems are insulated to a high degree and heat transfer by radiation depends on the fourth power of temperature. Hence, the error is quite small if the rover moves in an environment of 70 K compared to 50 K. Radiated infrared flux can be calculated with equation (9). If a temperature of 100 K for the outside of the rover is assumed and emissivity is set to one, then difference in received heat flux is about 23.4 %. However, this is only on the surface of the rover resulting in even much less influence on the internal components because of the high insulating efficiency of MLI.

4.2.3 Create Required Maps

The last preparatory step prior to optimisation is the creation of maps later used by the optimisation algorithm. It requires two maps, one with the incident solar heat flux density and one with the incident heat flux density from infrared radiation received from the lunar surface. In order to derive those, a sphere consisting of 80 faces as depicted in Figure 41 representing the outer hull of the rover is placed in the high-resolution part of the scene. It has a radius of 0.75 m.

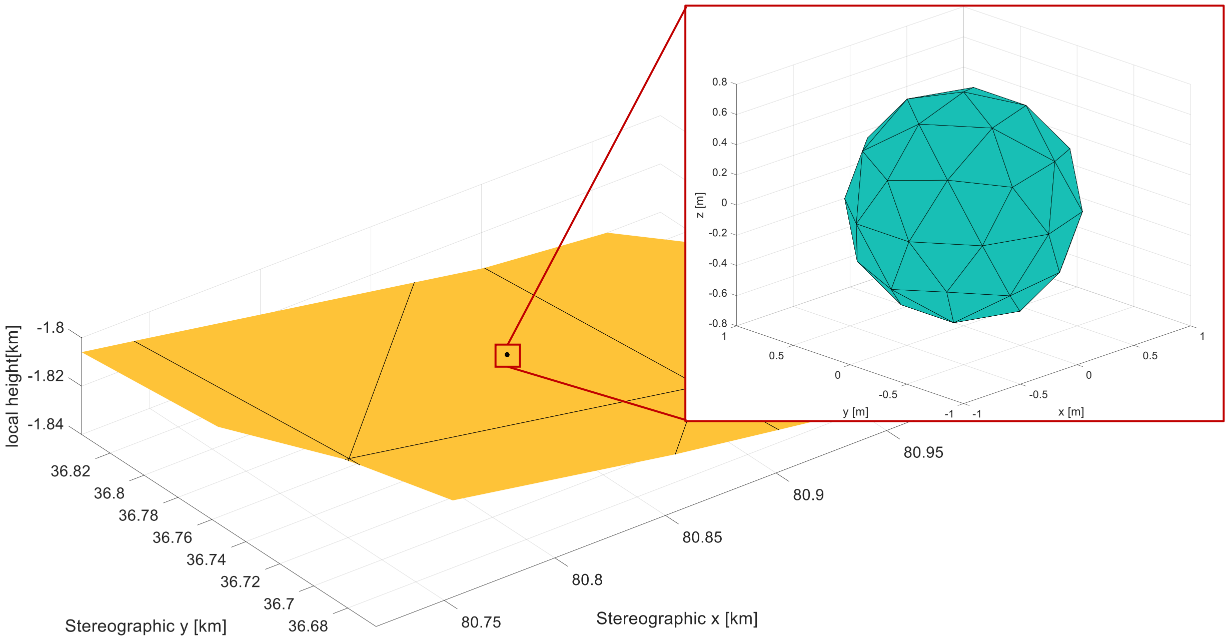

Figure 41: Sphere representing outer hull of rover displayed on terrain with resolution of 160 m per pixel

TherMoS-X calculates maps for every time step of the results from the simulation. The centre of the sphere is placed at the centre of each triangle in the scene at the same time step sequentially at a height of 0.75 m and values for both types of maps are calculated.

For solar heat load, 100 rays per face are shot towards the Sun in the same way as for simulation of solar heat load on the terrain but reflections of solar light from the surface of the Moon are neglected in contrast to ray tracing for simulation of the model of the Moon. The sum of the received solar heat flux over all surfaces of the sphere is then multiplied by four in order to calculate the heat flux on a disc oriented perpendicular to the Sun. The projected area of a sphere is four times less than the area of the sphere, which justifies the multiplication of the heat flux by four. A correction factor due to the discretisation of a sphere by triangles has to be considered as well. The solar heat flux q_i in equation (24) on this disc is then stored within the map at the specific location i. Chapter 3.3.1 explains how this information is used in the model of the rover.

$$q_i = \sum q_{n,ray-tracing} \cdot 4 \cdot c_{Area} \tag{24}$$

In equation (24), q_i is the solar heat flux reaching the sphere at a specific location in the scene. $q_{n,ray-tracing}$ is the solar heat flux reaching triangle n of the sphere, c_{Area} a correction factor to account approximation a sphere with triangles, here $c_{Area} = 0.99$. The solar constant is set to 1367 W m^{-2} as the default value and is assumed to be constant throughout the entire period of map creation.

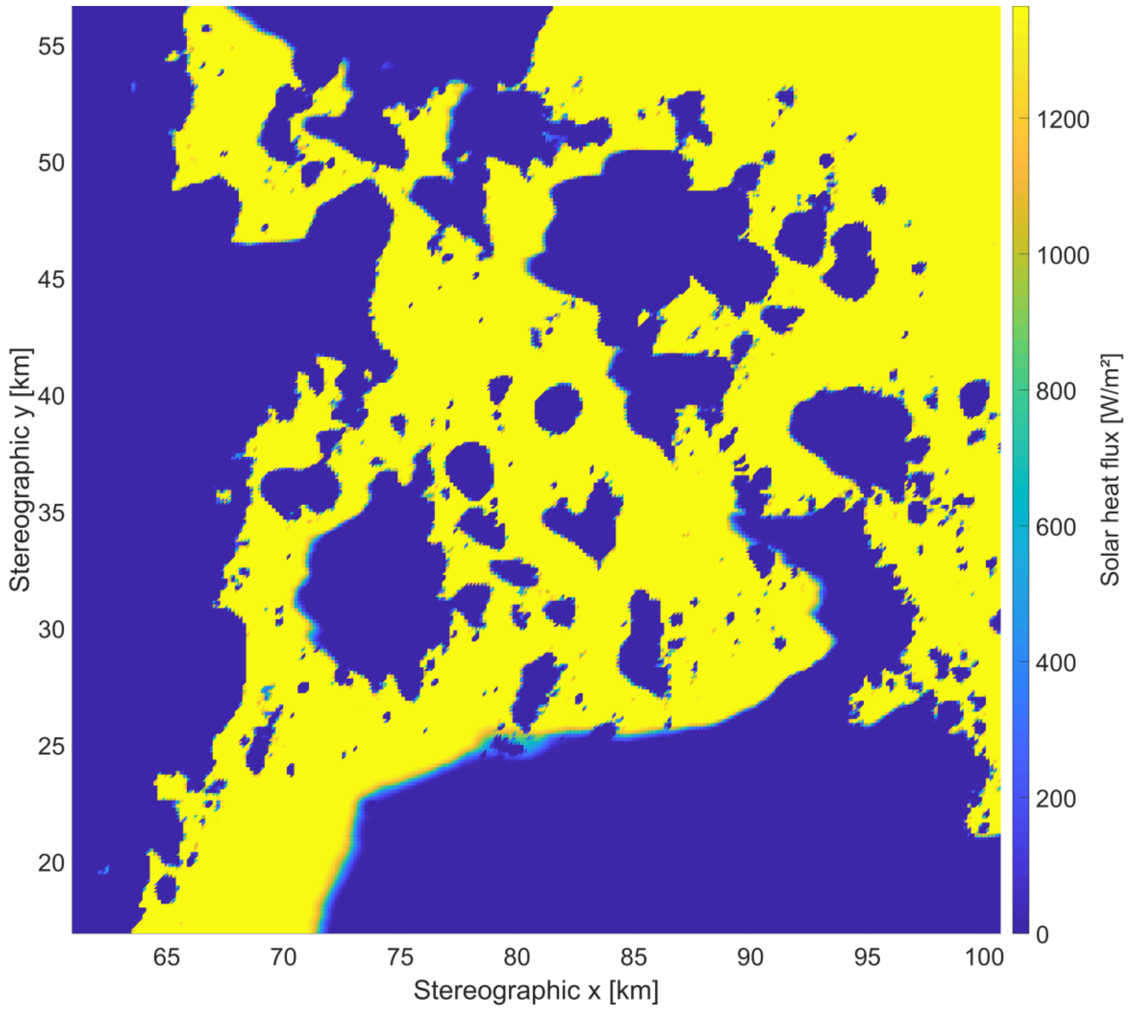

Figure 42: Example map for solar heat flux on rover at one time step

Figure 42 shows an example of an optimisation map for solar heat load at a given time. In most parts of that map, the full solar radiation reaches either the rover or no solar radiation at all. However, regions with penumbra can also be clearly identified. For example, there is extensive penumbra at the left border of the big shadowed part at the bottom. This shows the importance of implementing the Sun with its real shape instead of a points source. Regions with penumbra might still provide enough solar energy in order to power the rover or even charge the battery.

The received heat load by infrared radiation from the surface of the Moon is also calculated at the centre of all triangles. The ray tracer fires 1000 rays from each face of the assuming a Lambertian radiators. Rays hitting a triangle on the surface of the Moon contribute to the calculation of heat transfer by radiation as defined by equation (20). Heat loads of all faces of the sphere are summed up in order to derive the overall heat flux on the sphere.

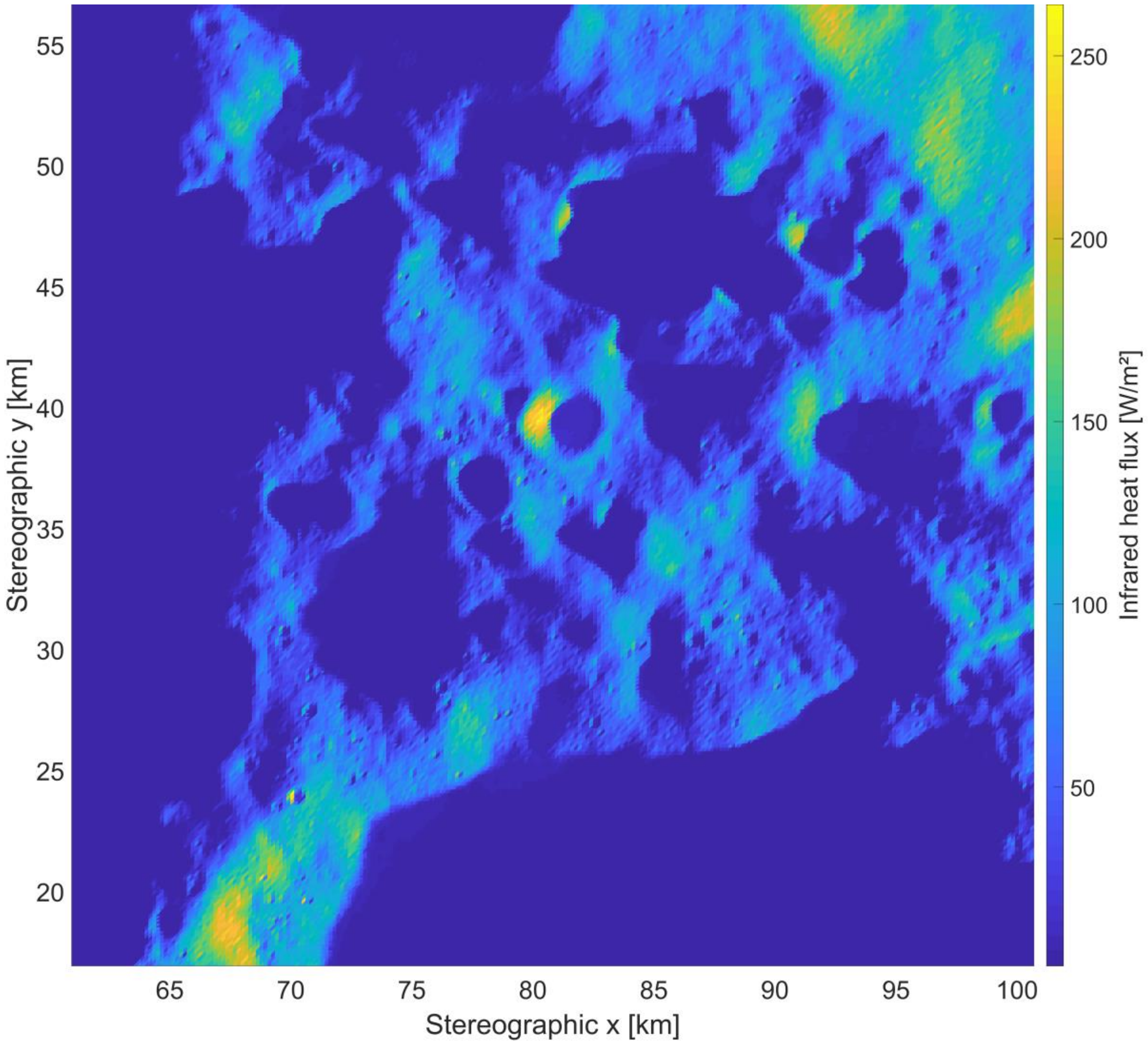

Figure 43: Example map for infrared heat flux on rover at one time step

Figure 43 shows an optimisation map at a specific time step of the incoming heat flux by infrared radiation from the surface of the Moon. The heat flux depends on the temperature on the surface of the Moon. It is mainly dominated by the triangle the sphere is placed on due to the differences in size between the sphere and the triangles of the Moon. As mentioned before, this map is needed for a proper simulation of the thermal state of the rover, which includes heating power of the thermal control system.

Both maps are stored for later use in the optimisation process. They are the basis for simulation of the rover system during optimisation. Values for time steps between stored values in the map are interpolated during optimisation as explained in chapter 4.3.

Computational time is high for the creation of thermal maps. In order to speed it up, it is also possible to exclude triangles from map creation. This might be due to a steep slope, a distance to far from start and goal points and triangles, which are highly unlikely to be part of the optimised traverse after engineering judgement. Those triangles are stored in a list and no ray tracing will be conducted at those locations. The value in the map for these triangles is set to infinity, which is defined in the optimisation algorithm as an unpassable node chapter 4.3.

Figure 44 shows two examples for such a reduction of optimisation maps. Figure 44 a) colours triangles black that have a slope steeper than 20°, which would be the limit of a potential rover mobility system. In Figure 44 b) triangles that are further out from the centre between both points are coloured black, additionally. The result is a reduction of the amount of triangles to be considered in the optimisation algorithm by nearly 65 %.

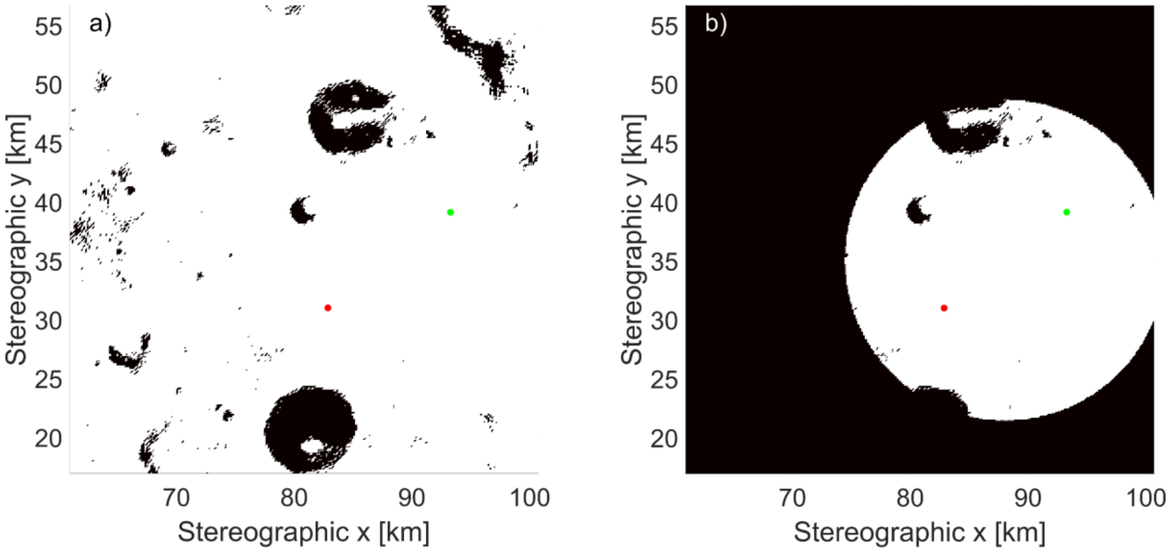

Figure 44: Reduction of optimisation maps due to slope limit of 20° in a) and additionally due to distance from waypoints in b)

4.3 Optimisation

The most common approach in traverse optimisation is the A* approach as described in chapter 2.1. It is also the approach chosen as basis for an implementation in this thesis for finding near-optimal traverses in a dynamic environment. Cunningham et al. (2014) also adapted A* in order to optimise through spatiotemporal problems. In this thesis an even simpler adaption of A* is developed because the main topic is to judge if an implementation of the thermal state of the rover is reasonable. This can already be achieved with a simpler implementation of A* which swaps the feature of finding the optimal solution under high computational costs with finding a near-optimal solution under lower computational costs and an easier implementation. Especially solving the thermal state of the rover with built-in solvers of MATLAB® is slow in computation, which is the main reason for the chosen approach.

At first, it is necessary to define the parameter, which shall be optimised. For all cases in this thesis, it is the distance, which is minimised, and at the same time, the traverse has to ensure that all technical boundary conditions are satisfied. As mentioned already, specific mission needs might render other optimisation parameters to be more important. It is then feasible to adjust the evaluation function and the heuristic in the code due to its modular implementation. The baseline A* algorithm (Hart et al. 1968) is extended in the implementation in TherMoS-X in order to handle a dynamic environment and dynamic behaviour of the rover system. This allows the algorithm to find a short traverse with compliance to requirements of the rover system but as a drawback, it loses its capability to find the optimal solution. In its current implementation, it is also restricted to rovers driving with constant speed. Furthermore, an iterative approach is required calling the adapted A* implementation repeatedly with varying battery capacities in order to find the shortest traverse of all. This is necessary because it can happen that the optimisation algorithm finds shorter traverses with lower battery capacity. Of course, those traverses are also useable with higher battery capacities but as stated above, the algorithm only finds good solutions and not necessarily the best traverse. Figure 46 outlines the pseudocode of the optimisation approach in TherMoS-X.

The optimisation approach developed in this thesis is just one option of many. Other approaches for finding a near optimal traverse are possible as well. For example, it might be the case that a faster traverse exists if the rover is allowed to stop and wait. This would be the case if it encounters a shadowed area on the direct way to its goal, which would drain its battery completely. The rover would continue its way after the shadow becomes short enough to pass through. Under certain circumstances, the time for waiting could be less than the detour the rover has to take if it is constantly driving. However, after intensely investigating illumination conditions at the poles, those conditions seem to occur rarely and such an implementation adds complexity and computational time to the code. Therefore, this kind of approach is currently not foreseen in TherMoS-X.

An optimisation algorithm has the need for an evaluation function that it minimises or maximises. In the frame of this thesis, it is the real distance, which is needed to drive from the start node to the goal node. The heuristic, which guides the algorithm to converge faster, uses the Euclidian distance from any investigated node to the goal node. It is always less than the real distance due to local elevations and the shape of the grid, which forbids a movement along a straight connection from any node to the goal node. Hence, the heuristic fulfils requirements of A* as described in chapter 2.1.

A* as well as the adapted implementation used in this thesis operate with a list of nodes which can be examined next. This list is continuously updated with neighbouring nodes of the currently investigated one. A definition of movements allowed to travel from one node to its neighbours is mandatory. In a regular grid, a rover could move from one node either to four neighbour nodes or to eight, depending on whether diagonal movement is allowed as Figure 11 shows. In a mesh created from centroids of triangles, the implemented A* approach allows only four movements per node because this movement has to fulfil two criteria: one is that no additional triangle shall be crossed and the other one is that the distance between both nodes has to be less than the resolution of the grid. Hence, only the movements depicted in Figure 45 are allowed. They look different depending on the type of triangle. The blue arrows show movements allowed from triangles with odd numbers to its four neighbouring nodes. The red arrows depict permitted movements from a triangle with an even number. The way nodes are sorted in TherMoS-X renders this distinction necessary. Figure 45 also shows that the distance to travel to each neighbour differs and in the case of a resolution of 160 m per pixel is in a range between ~ 75 m and ~ 152 m

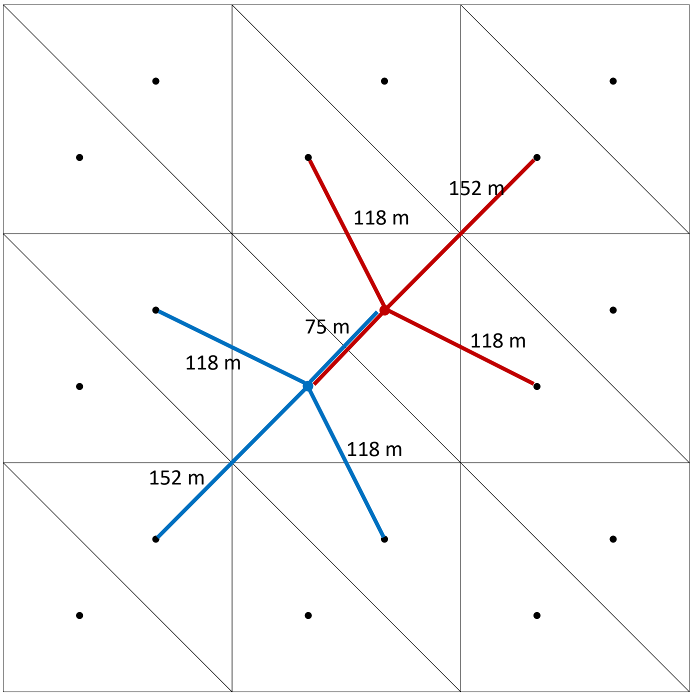

Figure 45: Allowed movements within the grid for the optimisation algorithm. Resolution is 160 m per pixel

As described in chapter 2.1, the implemented A* algorithm minimises the evaluation function f(N) as declared in equation (1). It does that while fulfilling boundary conditions on a static map and considering the energy state of the rover by running its model in parallel.

In TherMoS-X, one map containing all static boundary is created in a preparatory step as outlined in chapter 4.2.3. In brief, in the frame of this thesis, a node is unpassable if its slope exceeds the capability of the rover. Furthermore, many nodes are set to unpassable in order to reduce the amount of nodes if engineering judgement reveals that they are highly unlikely part of the optimal traverse. Values of unpassable nodes are marked in this map and the algorithm checks whether the node to be simulated is marked as can be seen in line 12 of the pseudocode given in Figure 46. Static boundary conditions are implemented straight forward into A* and they do not change the behaviour of the algorithm meaning that it is still able to find the optimal traverse. Further static boundary conditions can be implemented if they are needed for a specific mission case. If those additional conditions are based on the same map, an implementation is straightforward. If they rely on a map with a different mesh and resolution, matching and interpolation might be required increasing the effort of implementation.

Other boundary conditions such as a minimum temperature, a maximum temperature, battery capacity, and current power consumption have to be tracked dynamically. The term energy state summarises those specific conditions. In order to track them, a Model of the rover runs in parallel with the optimisation approach and tells the algorithm if a node is unreachable with the current state and traverse due to violation of a boundary condition. In the reference model of this thesis, which is describe in chapter 3.3, all boundary conditions except for traversable slope condense in an impact on the battery capacity eventually. For example, if a heater in the thermal model had to warm up the interior, the battery delivers this energy. If no solar energy reached the solar panel of the rover, this drains capacity from the battery. The result could be an empty battery leading to a termination of the optimisation algorithm at that node. The algorithm would then continue with another node having lowest value of evaluation function in the open list. In contrast to the original version of A* it is allowed to also revisit grid nodes on the closed list if the new cost value is lower than the previous one. This ensures that a near optimal solution can be found within reasonable computational time.

The function “simulate RoverState” in the pseudocode executes the simulation of the energy state of the rover along its way from the currently investigated node to the neighbour node. All aforementioned descriptions of the rover model and the creation of thermal maps are required to understand the implementation of this function. The ultimate goal of this function is to calculate the current battery capacity. This is done in steps of 10 s along the traverse between both nodes. Calculation of power demand for driving and communication is straightforward from the rover model and the slope underneath. The function determines when the rover crosses the border of the start triangle and adjusts slope values accordingly. With that, it can compute the current power need for driving. Power for communication depends only on time and ca be calculated directly as described in chapter 3.3.2. Evaluation of the thermal state is more sophisticated mainly because required values have to be interpolated. A constant time step of 1800 s is used during creation of optimisation maps for direct heat flux from the Sun and for infrared heat fluxes from surface triangles of the Moon. In addition, corresponding solar angles are stored at the same time intervals. The consequence is the necessity to interpolate those values in order to match the solver time step of 10 s to derive the thermal state as described in chapter 3.3.1. The total time at the current node is known from the previous optimisation step and with that, absolute time values for all time steps with a 10 s interval in order to reach the next neighbouring node can be calculated. Heat fluxes and solar angles are then interpolated linearly with values from the node underneath the rover. The function determines when the crossing point between both triangles is reached and it swaps interpolation to heat fluxes of the next node. Hence, after crossing the edge between two triangles, there could be a harsh change in those conditions. By simulating the thermal state of the rover, the algorithm also triggers a resistive heater as defined in the rover model. The required power is taken from the battery and the algorithm updates the state of the battery accordingly. If the battery gets empty, the node cannot be reached by the current state of the rover and the algorithm jumps to the next step.

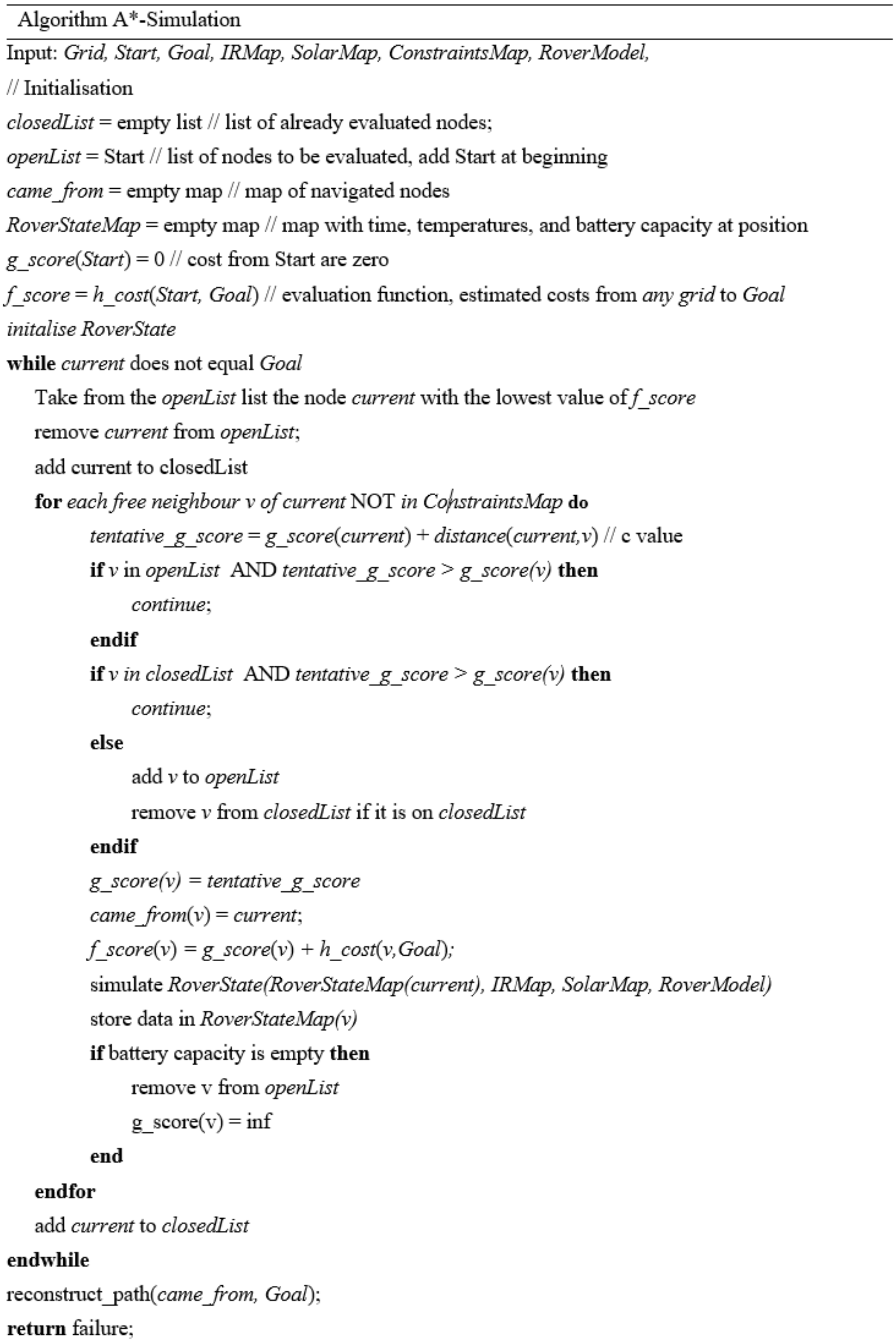

```
Algorithm A*-Simulation
Input: Grid, Start, Goal, IRMap, SolarMap, ConstraintsMap, RoverModel,
// Initialisation
closedList = empty list // list of already evaluated nodes;
openList = Start // list of nodes to be evaluated, add Start at beginning
came_from = empty map // map of navigated nodes
RoverStateMap = empty map // map with time, temperatures, and battery capacity at position
g_score(Start) = 0 // cost from Start are zero
f_score = h_cost(Start, Goal) // evaluation function, estimated costs from any grid to Goal
initalise RoverState
while current does not equal Goal
    Take from the openList list the node current with the lowest value of f_score
    remove current from openList;
    add current to closedList
    for each free neighbour v of current NOT in ConstraintsMap do
        tentative_g_score = g_score(current) + distance(current,v) // c value
        if v in openList  AND tentative_g_score > g_score(v) then
            continue;
        endif
        if v in closedList  AND tentative_g_score > g_score(v) then
            continue;
        else
            add v to openList
            remove v from closedList if it is on closedList
        endif
        g_score(v) = tentative_g_score
        came_from(v) = current;
        f_score(v) = g_score(v) + h_cost(v,Goal);
        simulate RoverState(RoverStateMap(current), IRMap, SolarMap, RoverModel)
        store data in RoverStateMap(v)
        if battery capacity is empty then
            remove v from openList
            g_score(v) = inf
        end
    endfor
    add current to closedList
endwhile
reconstruct_path(came_from, Goal);
return failure;
```

Figure 46: Pseudocode of the adapted A* implementation for optimisation in TherMoS-X

5 Analysis & Results

This chapter presents analysis cases and their results. At first, a sanity check of the adapted A* algorithm is presented in an artificial illumination setting at a location near the south pole. An investigation of the convergence of the optimisation algorithm through follows. After that, sensitivity analyses show the influence of a varying power demand of the rover system on results of the optimisation algorithm. Finally, potential mission cases are analysed at two different site with operation in the first quarter of the year 2022.

5.1 Sanity Check of Optimisation

This chapter gives an example of how the adapted A* optimisation algorithm works and validates it. For that, a reference scene is chosen represented by the same terrain as for validation of the thermal model of the Moon in chapter 3.2.5. Illumination conditions in this reference case are static only. Figure 47 shows the scene and the artificial lighting, which is incorporated in the scene. Colour blue stands for positions where the rover receives no Sun light and at all other positions in yellow it receives full solar heat load. For both, at the start (green) and the goal (red) node, there is a corridor allowing the rover to follow sun light for the entire traverse without using any power from the battery. The corridors are positioned such that they block the shortest traverse, which can be found if the energy state is neglected.

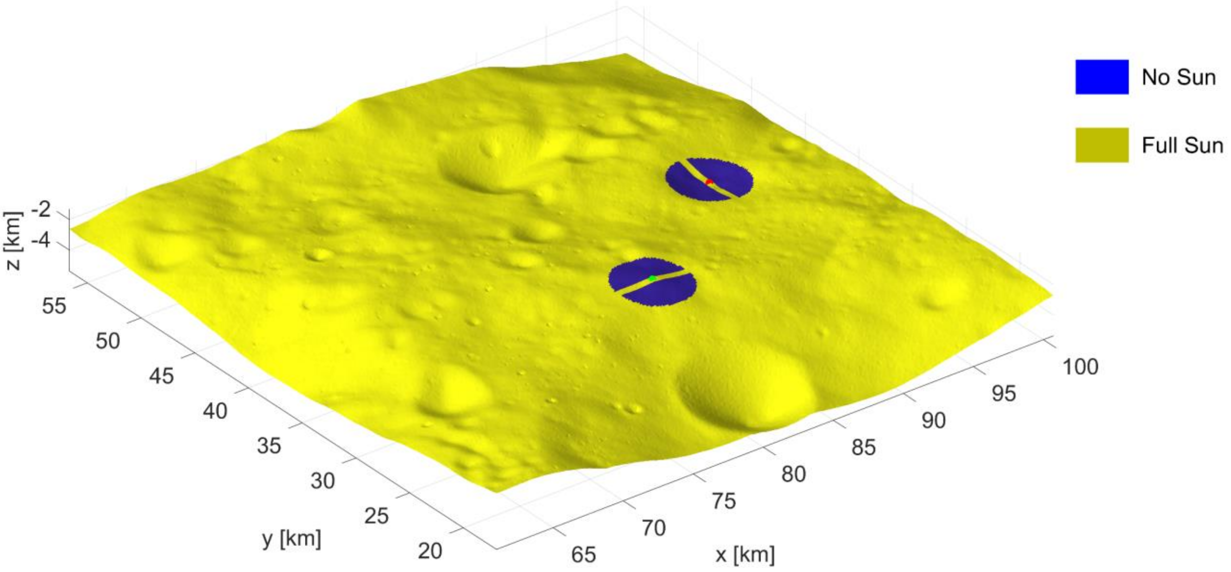

Figure 47: Artificial illumination map for validation of the optimisation algorithm

Figure 48 shows resulting traverses from the adapted A* optimisation algorithm. The green traverse is the shortest traverse possible. It is the same traverse that the classic A* algorithm finds by neglecting the energy state. The yellow traverse is the one where the battery capacity is set to 0 W h and the rover has to follow the Sun along the entire traverse. One can see that the traverse follows the aforementioned corridors in the vicinity of the goal and start point. The red traverse is the shortest traverse found with a battery capacity of 80 W h.

Results of the optimisation prove that the algorithm is capable of finding the shortest traverse matching results from the classic A* approach if the battery capacity is high enough for the rover to drive through all occurring shadows. It also showed that it is able to find short traverses with lower battery capacities. Finally, it can also follow a persistently sun-lit traverse if it exists and if the rover power system lacks a rechargeable battery.

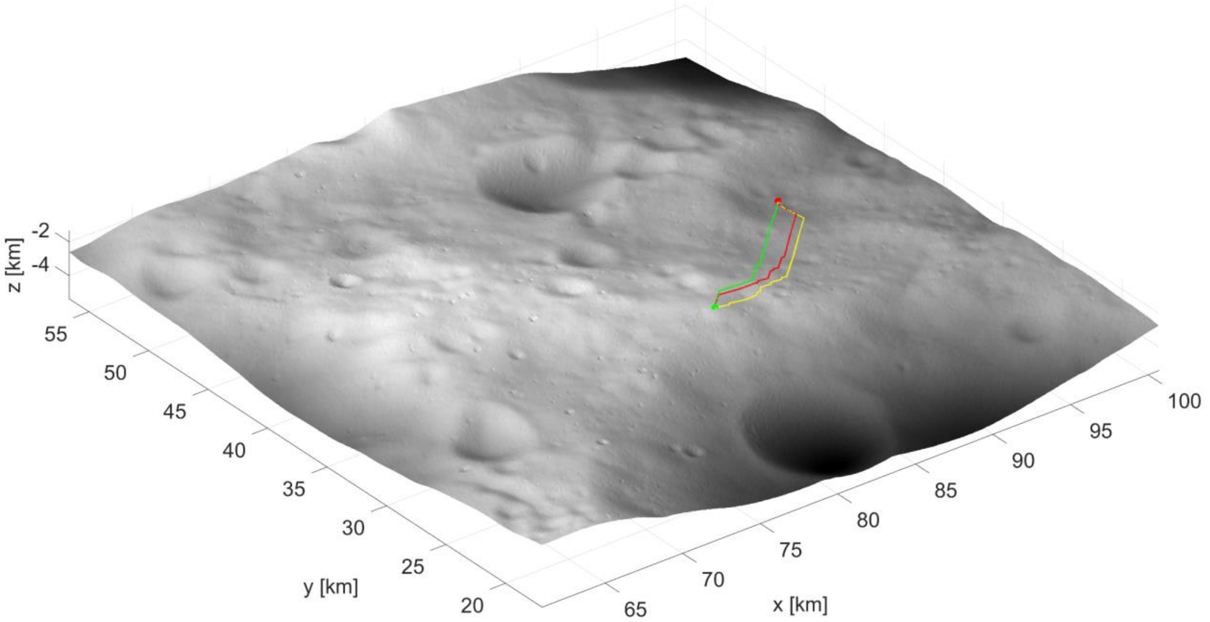

Figure 48: Optimised traverses of reference case. Green line is shortest traverse possible, red line is shortest traverse with energy of battery considered, and yellow line is shortest traverse with constant solar illumination

5.2 Convergence of Optimisation

Choosing the right resolution for traverse planning is a difficult process as described in chapter 4.2.1 because there has to be a balance between computational costs and quality of results. In this chapter, convergence of the optimisation approach through space is presented and discussed. This affects only the high-resolution ROI, as this is also the mesh used by the optimisation algorithm. For investigation of this influence the same location as for the mission case described in chapter 5.4.1 is chosen.

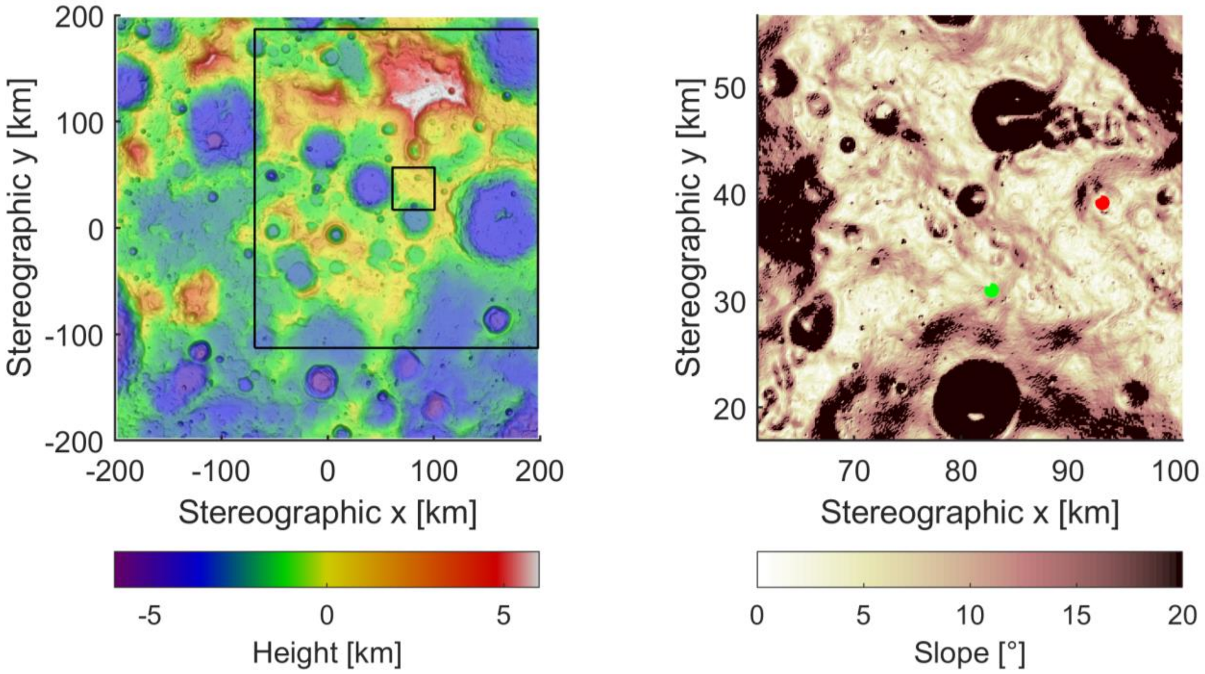

Figure 49: Site location for convergence through space, ROI with respect to the overall DEM of the south pole and ROI with start (green) and goal point (red) at a resolution of 160 m per pixel

Figure 49 shows the location and size of the investigated ROI in the DEM of the south pole by the small black square. The big black square represents the outer region of the scene, which is needed for shading effects on the ROI. The ROI itself with slopes between 0° to 20° is depicted on the right of Figure 49. The resolution of the ROI is set 160 m per pixel, 320 m per pixel, 640 m per pixel, and 800 m per pixel whilst the outer region is fixed at a resolution of 800 m per pixel. Highest resolution is limited by the available computation power and lowest resolution resembles the resolution of the low-resolution part of the scene. For all different resolutions the adapted A* algorithm determines the shortest path for battery capacities between 0 W h and 300 W h in steps of 10 W h. Illumination conditions are chosen from 9th of March 2022 at 16:00 to 12th of March 2022a at 16:00.

Convergence through time is not covered in this chapter, as temperatures on the lunar surface and the solar heat flux are determined every 1800 s. Values are interpolated linearly between the default time step size by the optimisation algorithm. A higher resolution in time would not significantly alter these values. Time step of solving the energy state of the rover is set to 10 s and is not varied because thermal control heaters have to be tracked in order to simulate energy consumption of them. This ensures proper simulation of the current energy state of the rover and especially of the remaining energy in the rechargeable battery.

Table 8 presents results of optimisation runs with different resolutions. Results are based on the Euclidian distance between triangle centroids instead of the real distance. The final approach used in this thesis also factors in the slope of the terrain in order to derive real distances of the traverse. Traverse without simulating the energy state represent classic results produced by A*. The shortest traverse of all occurs in the DEM with a resolution of 320 m per pixel. With a total distance of 14.81 km, it is about 117 m shorter than the shortest traverse if a resolution of 160 m per pixel is used. This comes from the fact that centroids are placed differently in 3d space at different resolutions. The arrangement of centroids with regard to the start and goal point seems to be beneficial at a resolution of 320 m per pixel.

Figure 50 shows that shortest traverses with simulation of the energy state of the rover at all resolutions of the terrain reveal a similar shape from a global perspective. Only the traverse on a terrain with lowest resolution seems to have a slightly different shape mainly close to the goal point. The deviation in total length between shortest traverse with simulation of energy state and without is only marginal except for lowest resolution. Here, the relatively benign ROI in terms of slopes is helpful because it allows brief detours to sun illuminated spots without changing the length of the traverse in a meaningful way. The lowest battery capacity, which still allows driving from the start to the goal node, also stays in the same magnitude for all resolutions of the terrain. Only a resolution of 640 m per pixel requires a 40 % higher battery capacity than if a resolution of 160 m per pixel or 320 m per pixel is used.

A significant difference occurs for the battery capacity at which the optimisation algorithm finds shortest traverse. For a resolution of 160 m per pixel and 320 m per pixel, a battery capacity of around 200 W h leads the algorithm to find the shortest traverse of all. With lower resolution, the algorithm tends to find shortest traverses at lower battery capacities of 70 W h and 40 W h respectively.

Looking at all numbers, a resolution of 160 m per pixel or 320 m per pixel seems to be a good choice because shortest traverses occur at those resolutions under similar battery capacities. In addition, the lowest battery capacity is the same in both cases. In order to stay conservative and because available computational power allows for it, a resolution of 160 m per pixel is chosen for mission cases presented in the following chapter.

Table 8: Traverse comparison at different resolutions of the DEM

Parameter	Resolution of ROI [m per pixel]			
	160	320	640	800
Total length Shortest traverse of all capacities [km]	14.928	14.815	14.967	15.745
Corresponding battery capacity [W h]	210	200	70	40
Lowest battery capacity possible [W h]	50	50	70	40
Shortest traverse without energy state [km]	14.927	14.810	14.963	15.366

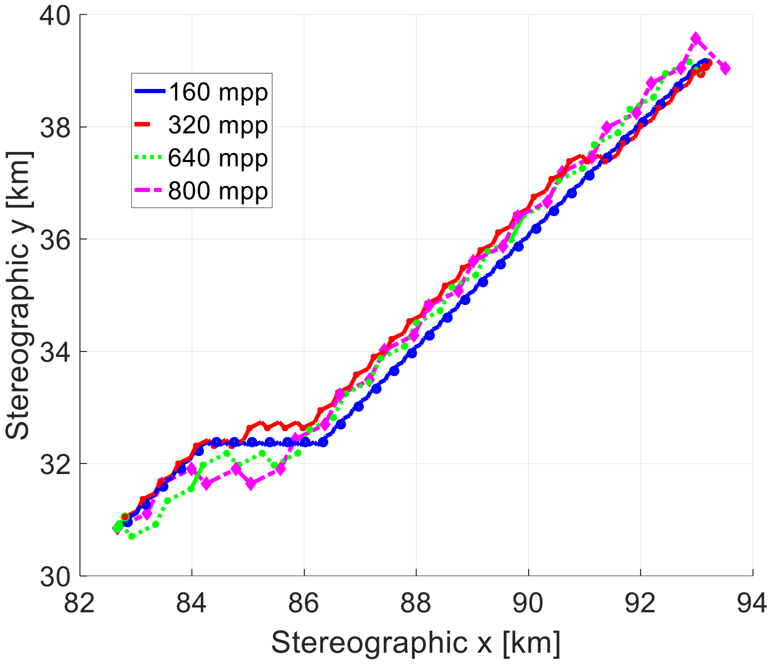

Figure 50: 2-D plot of shortest traverses (reference case) with consideration of energy state at different resolutions of the terrain

5.3 Sensitivity

This chapter covers a sensitivity analysis on model parameters of the rover in order to examine stability of the optimisation algorithm if parameters of the rover model vary. Other parameters such as the implementation of the battery, of the solar cells, accuracy of the terrain model etc. are not investigated, as their influence would lead to similar conclusion because the main driver for the algorithm is always the energy state of the rover. Ultimately, all changes in parameters of the model lead to a change in the energy state and this sensitivity can already be assessed by varying specific parameters of the power model of the rover only.

Sensitivity of the optimisation algorithm is investigated exemplarily by varying the power need P_{drive} of the rover for driving directly as a factor on equation (18) and only partially on the dependency of the power needed for driving on a slope P_{slope} in equation (22). The power need is varied for three different battery capacities at two different sites. Chosen sites are described in chapter 5.4. The battery capacities are chosen accordingly to results from investigated mission cases. The lowest battery capacity is the minimum one that is needed in order to find a traverse between start and goal. The highest battery capacity is close to the capacity which is at least required to drive along the shortest traverse determined by the classic A* approach. In order to see the influence here, 10 W h less are used as input value for the battery capacity. A third case represents the battery capacity of the shortest traverse that the adapted A* algorithm finds for all lower battery capacities than the one needed to follow the shortest traverse of all.

Table 9 presents results at the site with the name LVP. Overall, the highest deviation in total length is 4.7 % and it occurs at a battery capacity of 110 W h by applying a sensitivity factor of 1.2 on P_{drive}. Deviations are small in any case if the total power consumption changes. If the power demand for driving is increase to 150 % of the reference demand, the algorithm does not find a traverse anymore for the lowest battery capacity. For sensitivity on P_{slope}, there is hardly an influence. Only at the extreme values for the sensitivity factor of 0.5, 0.6, 1.4, and 1.5, one can see a difference of only 0.5 % in total length. In this particular case, the algorithm is relatively stable in terms of total length of the traverse with a mean deviation of 2.34 % if sensitivity is applied on P_{drive} and less than 0.1 % if applied on P_{slope}.

Another interesting observation is that the algorithm prefers longer traverses for lower power demand at this site. This can be seen for all sensitivity factors less than 1.0 with a battery capacity of 110 W h and for sensitivity factors of 0.7, 0.8, and 0.9 at a battery capacity of 70 W h. One would expect shorter traverses with lower power demand. There is also one outlier with a battery capacity of 250 W h and a sensitivity factor of 1.4 where the result is a 3 % shorter traverse compared to the reference value. Again, one would expect the opposite behaviour. However, deviations are always below 4.2 % in any case.

Table 9: Deviation in total length for sensitivity applied on power for driving, LVP site

Sensitivity Factor		0.5	0.6	0.7	0.8	0.9	1.0	1.1	1.2	1.3	1.4	1.5
	Battery capacity [W h]											
On P_{drive}	70	0.990	0.990	1.036	1.031	1.031	1.000	1.000	1.031	1.031	1.031	Na
	110	1.010	1.042	1.005	1.005	1.000	1.000	1.000	1.047	1.042	1.042	1.042
	250	0.960	0.960	0.960	0.960	0.960	1.000	1.000	1.000	1.000	0.970	1.000
On P_{slope}	70	1.000	1.000	1.000	1.000	1.000	1.000	1.000	1.000	1.000	1.000	1.000
	110	1.000	1.000	1.000	1.000	1.000	1.000	1.000	1.000	1.000	1.000	1.000
	250	1.005	1.005	1.000	1.000	1.000	1.000	1.000	1.000	1.000	1.005	1.005

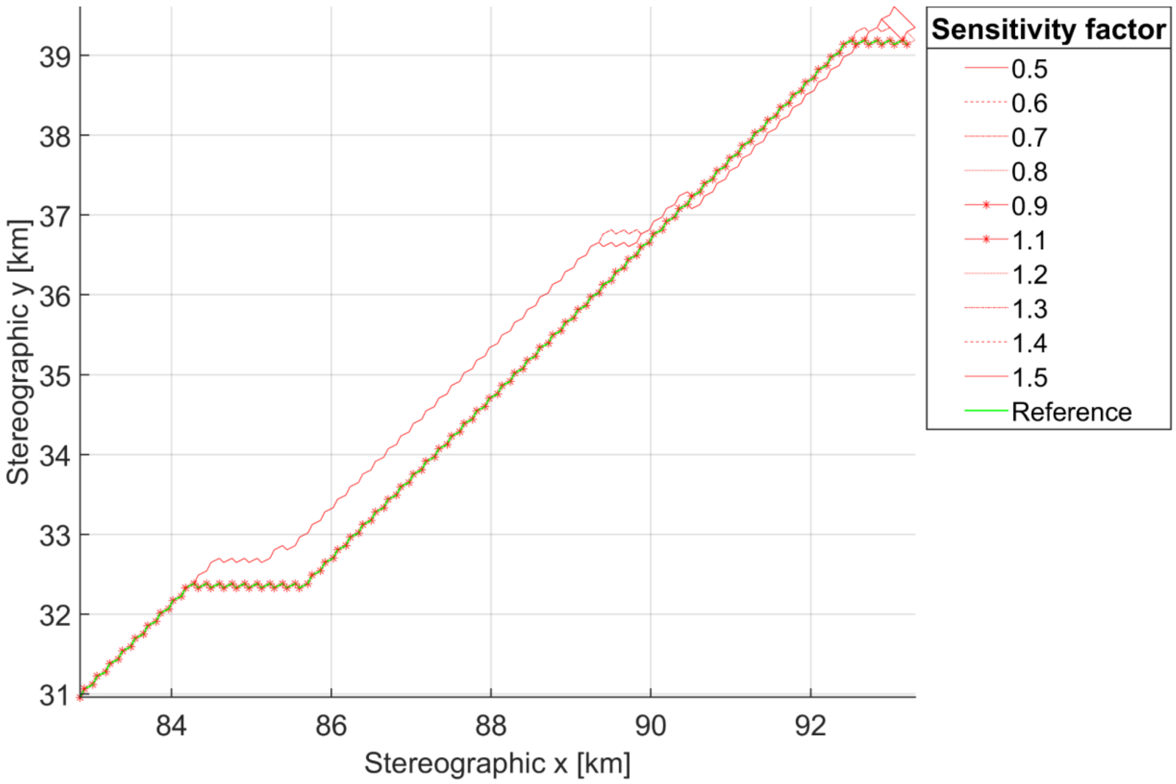

Figure 51: Traverses with different sensitivity factors on total power for driving for battery capacity of 110 W h at LVP site

Figure 51 depicts resulting traverses with a battery capacity of 110 W h and the sensitivity factor applied to the total power demand for driving, P_{drive}. All traversers have similar shapes and differ only slightly in total length. The most obvious variation occurs at the end of the traverse on the top right of the plot, where the goal is approached from different directions because of the shape of the shadow there and the variation in power demand.

Results of the sensitivity runs at the Speyerer site are given in Table 10. They show that the optimisation algorithm is more sensitive at this site than at the LVP site investigated in Table 9. With the lowest battery capacity of 100 W h, there is no traverse possible by increasing P_{drive} above 110 %. For higher battery capacities, the algorithm finds alternative traverses but this comes with high increases in total length. Highest deviations with 36.1 % occur at sensitivity factors of 1.2, 1.3, and 1.4 at a battery capacity of 400 W h and at sensitivity factors of 1.3, 1.4, and 1.5 with a battery capacity of 420 W h. Sensitivity on P_{slope} is nearly negligible. Only for five cases, an increase of 0.6 % in total length can be observed. They all appear at a battery capacity of 400 W h with sensitivity factors higher than 1.0. Overall, the deviation in total length averaged over all cases is about 10.5 % if applied on P_{drive} and less than 0.1 % if applied on P_{slope}.

Table 10: Deviation in total length for sensitivity applied on power for driving, Speyerer site

Sensitivity Factor	Battery capacity [W h]	0.5	0.6	0.7	0.8	0.9	1.0	1.1	1.2	1.3	1.4	1.5
On P_{drive}	70	0.991	0.999	1.000	1.000	1.000	1.000	1.008	Na	Na	Na	Na
	110	0.941	1.000	1.000	1.000	1.000	1.000	1.006	1.361	1.361	1.361	1.349
	250	0.941	0.941	1.000	1.000	1.000	1.000	1.006	1.006	1.361	1.361	1.361
On P_{slope}	70	1.000	1.000	1.000	1.000	1.000	1.000	1.000	1.000	1.000	1.000	1.000
	110	1.000	1.000	1.000	1.000	1.000	1.000	1.006	1.006	1.006	1.006	1.006
	250	1.000	1.000	1.000	1.000	1.000	1.000	1.000	1.000	1.000	1.000	1.000

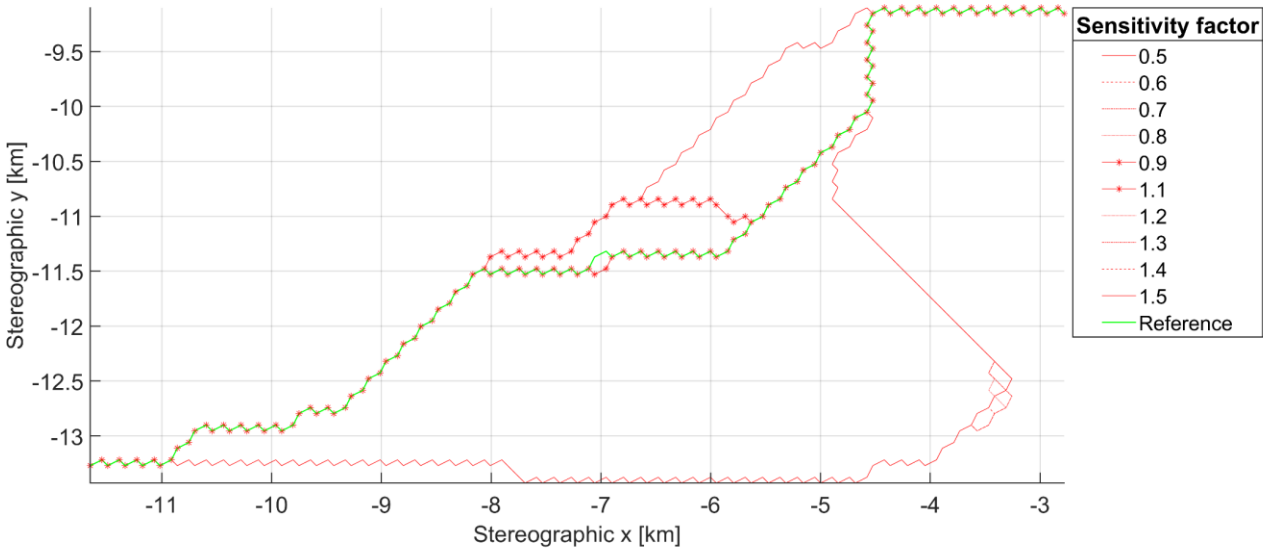

Figure 52: Traverses with different sensitivity factors on total power for driving for battery capacity of 400 W h at Speyerer site

Figure 52 illustrates traverses as an output of the optimisation algorithm. The sensitivity factor is applied to the total power demand of driving, P_{drive} at a rover model with a battery capacity of 400 W h. It can be seen that some resulting traverses look very different from the reference traverse in green. Shorter traverses are the result of lower sensitivity factors and longer traverses the result of higher sensitivity factors. Especially the traverses at higher sensitivity factors are much longer (up to 36.1%) and they take a detour on the right side of the plot. A more direct approach to the goal is not possible due to slopes of the terrain and illumination conditions.

The sensitivity analysis in this chapter shows that the optimisation algorithm is sensitive under certain circumstances. If the total power demand for driving is subject to variation, the influence on the length and shape of the traverse are substantial if the illumination in the scene is peppered with shadows, as is the case for the Speyerer site. Then, a maximum increase of 36.1 % can be noticed compared with a maximum increase of 4.7 % at the LVP site with more persistent illumination conditions throughout the scene.

The more benign environment at the LVP site has another interesting influence on the performance of the optimisation algorithm. With lower power demand, the total length of the traverse should be the same or even less than the reference traverse. However, in some cases the length increases but only with low numbers always below 4.2 %. There is also one case where the optimisation algorithm finds a shorter traverse with higher power demand, which is also unexpected. The reason for this lies in the way the optimisation algorithms works. Non-optimal traverses are the result of adapting the original A* approach in order to decrease the computational time of the algorithm. Consequently, slightly longer traverse than the shortest one are accepted and output as result. This is deemed adequate especially deviations are small with less than 4.2 % and this only happens at the LVP site. The more challenging conditions at the Speyerer site seem to help the algorithm to find better solutions than at the LVP site. No such an occurrence can be found at the Speyerer site.

Sensitivity analysis also revealed that the influence of varying only the power needed additionally to overcome a slopped terrain can be neglected, as the deviation in total length is always less than 0.6 % in any case. However, if a value of the model has a high influence on the total power demand of the rover such as is the case of varying the total power needed for driving, resulting traverses of the algorithm can be much longer and have different shapes. This is already true for an increase of 20 % on the total power needed for driving which is roughly a change of 13 % on the total power of the rover.

5.4 Mission Cases

Simulation of traverses in realistic scenarios shall give insight about the feasibility and potential benefits of optimisation in a dynamic environment with a dynamic rover model. This chapter gives details about two cases close to the lunar south pole taken from literature. For both, the same standard rover model developed in chapter 3.3 is used for optimisation. In addition, the initialisation process for the simulation of the temperature of the Moon is the same. Thermal simulation is started more than two years prior to the start date of driving. Time step of the solver during this period is set to 12 h. This is only possible, because the net infrared heat exchange between surface triangles of the Moon is neglected in this phase. The simulation approach changes again roughly one month prior to the start date of driving by switching the net infrared heat exchange back on and adjust the time step of the solver to 30 min. This setting is retained until the end of the simulation is reached.

5.4.1 LVP site

ESA identified, besides others, a potential region of interest between craters Faustini, Shoemaker, and Nobile (Flahaut et al. 2016) and already waypoints of interest have been identified fulfilling requirements of ESA. Previous analysis focused on thermal simulation of a rover at this site along those waypoints (Killian and Fisackerly 2017). Centre of the ROI is set to -86.8724° N 68.378° E, start point lies at -87.0817° N 69.5037° E and the goal point at -86.6637° N 67.253° E and the ROI has a size of roughly 27.7 km by 27.9 km with a resolution of ~160 m per pixel represented by 61,600 surface triangles. The outer part is 259.4 km by 298.9 km in size at a resolution of 800 m per pixel and a total number of 244,670 surface triangles. Figure 53 depicts the size of the modelled scene with respect to the DEM of the south pole. The big black square represents dimensions and location of the outer part, which is needed for simulation of proper insolation at the ROI. The small black square represent dimensions and location of the ROI with respect to the lunar south pole. The right plot of Figure 53 shows the ROI only with slopes of the triangles coloured from 0° to 20° and higher. The start and goal point are highlighted additionally. Colours indicate that slope conditions seem to be benign for a rover with a maximum slope capability of 15° in the area between start and goal.

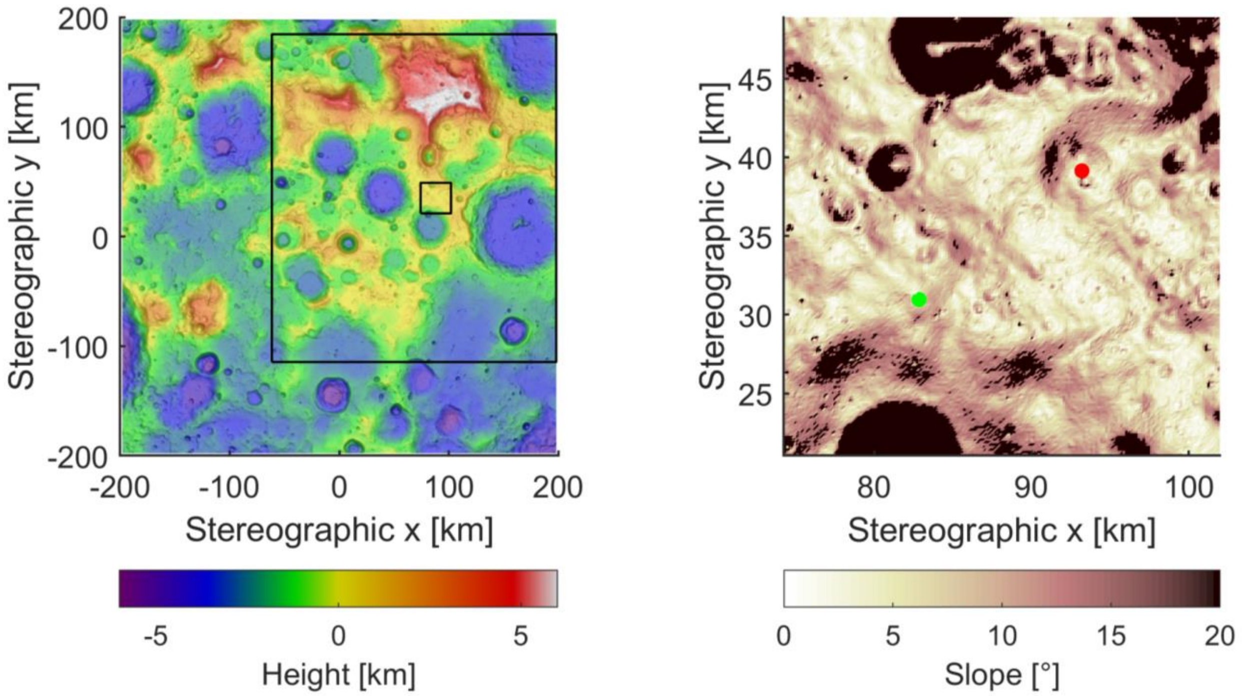

Figure 53: LVP site, ROI with respect to the overall DEM of the south pole and ROI with start (green) and goal point (red)

The date of mission operation actually defines the required size of the terrain at this ROI. If the Sun was behind the big mountain (Malapert massif) at positive y-axis, it is inevitable to include this terrain in the simulation. However, it would also serve as a border behind which remaining terrain could never have an impact on lighting conditions of the ROI. In all other directions, it is harder to find a distinct border after which terrain can be neglected. Figure 17 suggests considering a local horizon this ROI between 100 km and 150 km. In order to meet maximum distance of the local horizon at any case, the terrain considered during ray tracing is set to 150 km in any direction but on the plus x-axis the DEM from TUB already ends after 110 km.

The year 2022 is chosen as an arbitrary date for a mission and operation of the rover on the surface of the Moon. Throughout this year, preferable illumination conditions for an operation period of 3 days are sought. This period ensures that the optimisation algorithm has enough margin in time in order to find an optimal traverse. The minimum time needed to cover the Euclidian distance between start and goal point of about 13.235 km is 26.47 h with the constant speed of the rover of 0.1388 m s^{-1}. Visual inspection reveals that a start date of the traverse at 16 o´clock on 9th of March 2022 seems to be a potentially good fit. Figure 54 shows illumination conditions of this period at the ROI. The start point (green) receives sun light throughout the entire period while illumination conditions at the goal point (red) change over this period. At the beginning, there is no persistent illuminated traverse possible to reach the goal, which changes roughly around 10th of March at 20:30 when the surrounding of the goal point starts to be illuminated at the top left. The Sun continues to move further illuminating the left and finally the bottom left part at the vicinity of the goal point, but it never reaches the goal point within the investigated period. Hence, the optimisation will reveal whether a constantly illuminated traverse exists.

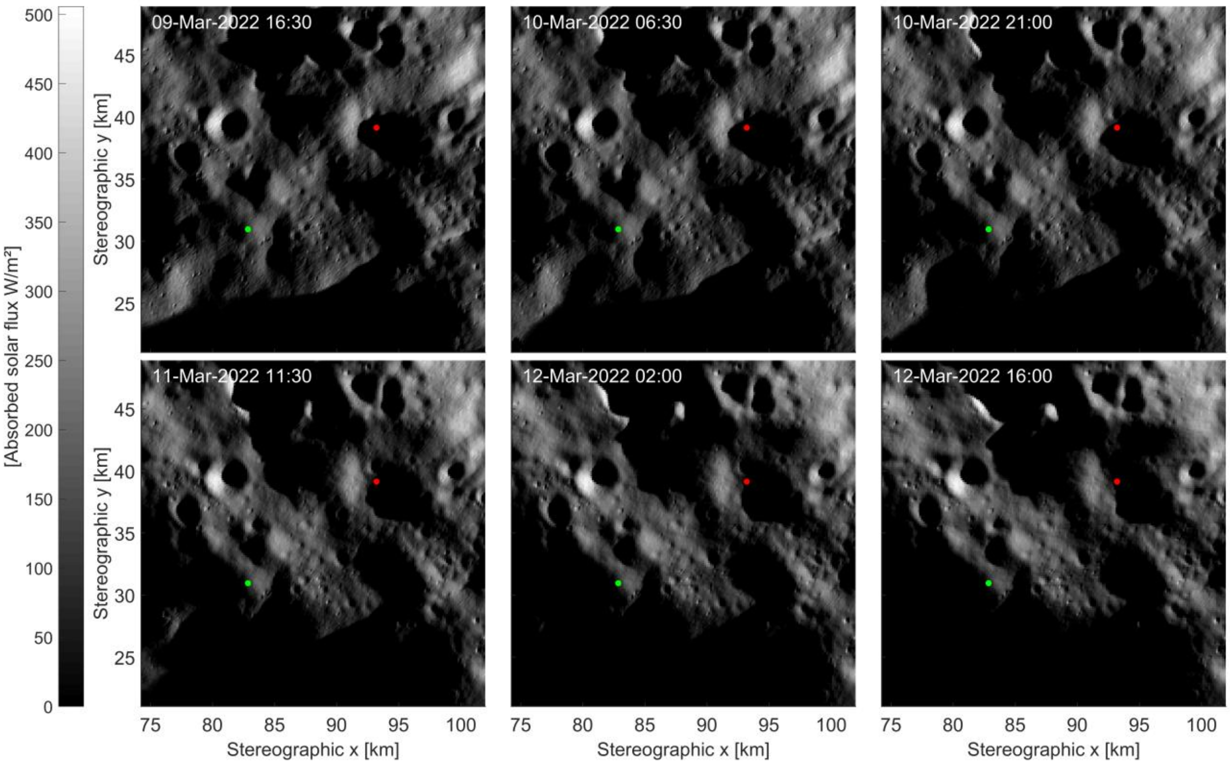

Figure 54: Illumination series of the ROI of LVP site. Grey scale values are absorbed solar heat flux of each triangle

The optimisation algorithm searches for the shortest traverse that is possible with a given battery capacity. This is repeated from a capacity of 0 W h to a capacity of 300 W h in steps of 10 W h. Step size is chosen due to energy required to drive from one node to another with the given rover model which is approximately 10 W h but depends on the slope of terrain. During optimisation, the state of the rover is updated every 10 s at which temperatures are simulated and power outputs are updated. The results of optimised traverses are stored every time the rover reaches a centroid of a triangle. This corresponds to times between 537.7 s and 1077.3 s depending on the distance between adjacent centroids along the traverse.

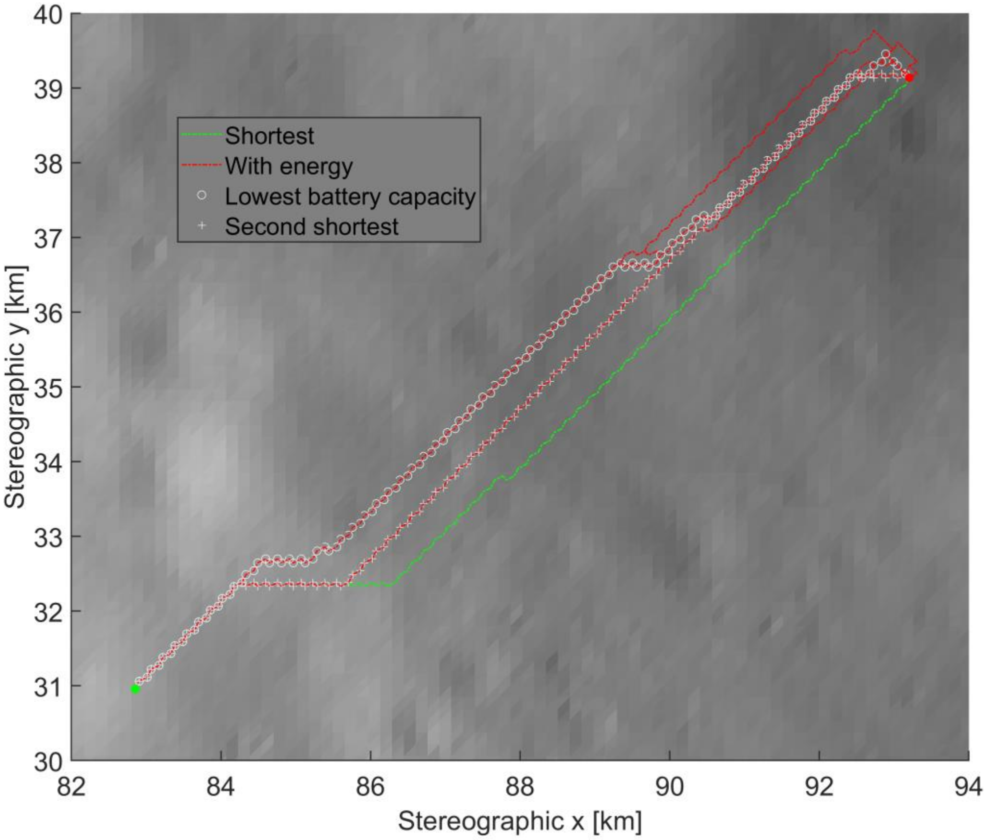

Figure 55: Shortest traverses at LVP site. Green line is traverse without energy state; red lines are traverses at different battery capacities. Markers highlight traverse with lowest battery capacity and second shortest.

Figure 55 shows all traverses that the optimisation algorithm finds. The green line represents the shortest traverse without simulation of the energy state of the rover and it is determined by the classic A* algorithm. It is the shortest option possible with a length of 14.927 km but at least an energy of 260 W h is required in order to follow it with the current rover model and the chosen start date. Red lines represent all traverses the algorithm creates with the energy state of the rover considered and an implemented battery capacity ranging from 0 W h to 300 W h. No traverse exists without a battery. The lowest battery capacity, which is needed to arrive at the goal point, is 70 W h, which is 18.2 % of the capacity needed to complete the shortest traverse, and the total length is about 15.085 km. It is highlighted in Figure 55 with white circles. Under the chosen circumstances, this battery capacity is quite small and demonstrates that only a brief detour resulting in a slightly different traverse makes a traverse between both points possible. The shortest traverse with energy state simulated is 14.9335 km long and occurs at a battery capacity of 110 W h. It is marked with white crosses in Figure 55.

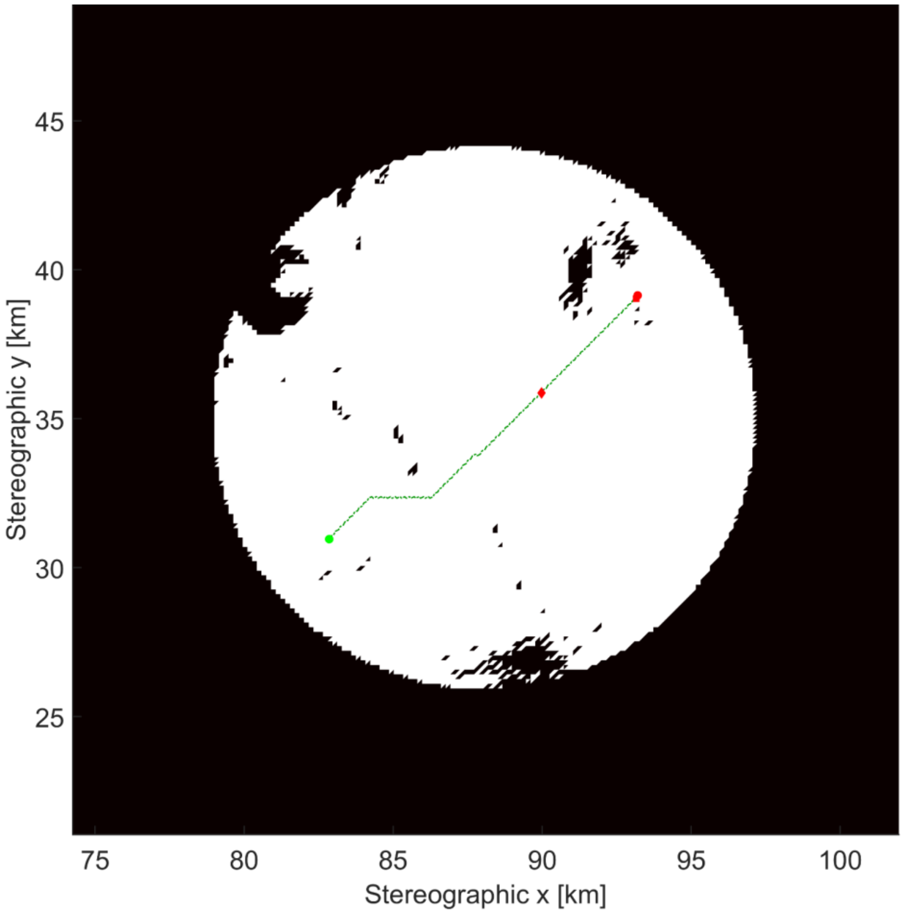

Figure 56: Map of LVP site with unpassable triangles marked black. Green line is shortest traverse without simulation of energy state. Red diamond indicates when battery is empty at lowest possible capacity and the red square with highest battery capacity

Figure 56 is a binary map of unpassable nodes within the investigated ROI. Black triangles are unpassable on the one hand due to slopes being higher than 15° and on the other hand because it is unlikely that they would be part of a potential traverse. This is reasoned by the fact that they are too far away from both, start and goal. In order to define them, all nodes lying outside of a circle with a diameter of 18.2 km with its centre at the midpoint between start and goal, are excluded from optimisation. As Figure 56 shows, only few nodes have a higher slope than the rover can cope with. This gives the optimisation algorithm many options of finding nearly similar looking traverses with total lengths around the same value. Additionally, illumination conditions are benign in the area between start and goal as shown in Figure 54. Only around the goal point illumination conditions can become challenging depending on the time.

The red markers in Figure 56 highlight at which points the rover would stop working if it followed the shortest traverse of A* with a battery capacity of 70 W h (diamond marker) and of 250 W h (square marker). A battery capacity of 70 W h powers the rover along the traverse for 10.063 km and it is the lowest capacity for which the optimisation algorithm could find a different traverse to reach the goal point. With 250 W h, the rover can follow the shortest traverse to one node prior to the goal node resulting in a length of 14.809 km. Shadow seems to play only a role at the end of the shortest traverse which is confirmed by the illumination series in Figure 54.

The shortest traverse which is the traverse by calling A* without simulation of the energy state is about 14.927 km long and a battery capacity of 260 W h is enough in order to follow this track. With less capacity, the algorithm finds slightly different solutions at different capacities. A full overview of all traverses with all investigated battery capacities can be found in Appendix E. Lowest battery capacity that still allows driving between both points is about 70 Wh. There is no traverse with continuous illumination of solar cells.

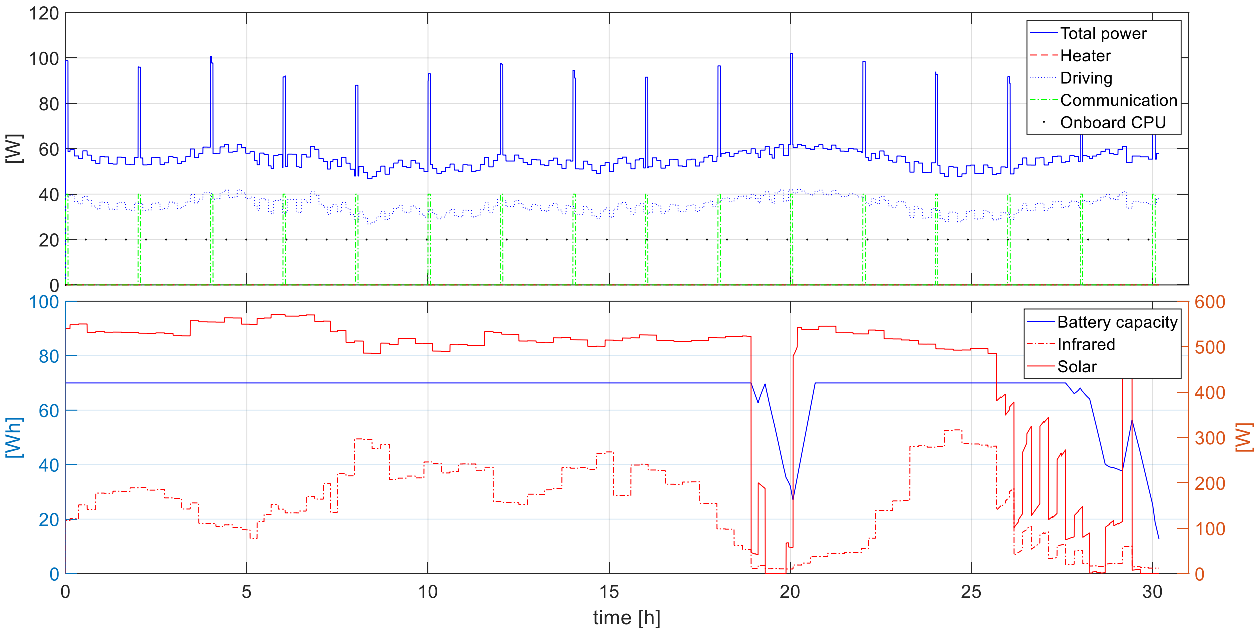

Figure 57: Power consumption and heat loads along the traverse with lowest battery capacity possible (70 W h) at LVP site

Figure 57 shows results along the shortest traverse with a battery capacity of 70 W h. The upper plot shows power consumption of the total rover system with the blue line. It is composed of power for heating in dashed red line, power for driving in dotted blue line, power needed for communication in dash-dot green line and the power of the on board computer in dotted black. The bottom plot displays the capacity of the battery (blue line), the absorbed infrared heat power (dotted red), and the absorbed solar heat load (red) of the rover system. Values are from external MLI surface only (thermal node 1), excluding the radiator.

The total power consumption varies between 46.9 W and 101.8 W with an average of 56.4 W. A peak power demand occurs every 2 h coming from switching communication on. A constant power of 20 W is needed for operation of the on board computer. The power need for driving varies between 26.9 W and 41.9 W with an average of 35 W.

One can see that no power is needed for heating, as it is always zero along the traverse. This is due to the fact that the period of operation falls into a well sun-lit phase with warm temperature of the surface and a lot of direct solar illumination. The first shadow phase occurs after 19 h where roughly 40 W h are sufficient to pass through the shadow. There is also a brief period of penumbra at the beginning of this shaded phase. The next shadow phase appears after 26 h and persist much longer than the previous one. There is also a pronounced phase with penumbra rendering additional heater power unnecessary. During this part of the traverse at least 70 W h are required in order to reach the goal node. A brief peak of direct solar light just prior the goal point recharges the battery slightly before full shadow occurs.

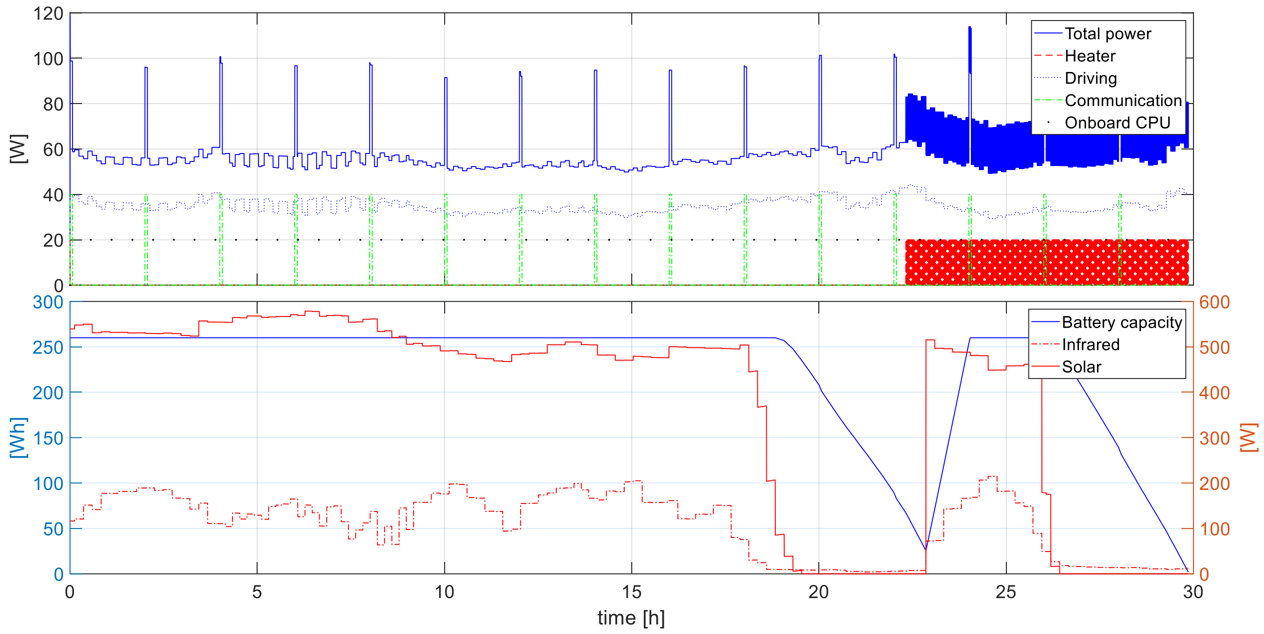

Figure 58: Power consumption and heat loads along the shortest traverse with lowest battery capacity possible (260 W h) at LVP site

Figure 58 highlights power consumption, the state of the battery capacity, and radiation heat loads absorbed by the rover along the shortest traverse with the minimum battery capacity possible. In contrast to the traverse of lowest battery capacity of all, heater power is necessary after 22.5 h in order to keep the internal temperature above its limit. The reason is simply a prolonged segment in shadow along the traverse. Additionally, the lunar surface is colder than for the previously described traverse as the infrared heat transfer from the terrain to the rover is much less. In combination, both facts lead to a faster drop of the internal temperature resulting in the need for heater power. There is also hardly any penumbra in the last phase of shadow. This drains the battery even further than in the previous shadow period. As a consequence, the rover reaches the goal with an empty battery, which is also the case for the traverse outlined in Figure 57.

Table 11 summarises results at the LVP site in terms of battery capacities. The first battery capacity is the one required to follow the shortest traverse possible. The definition of the lowest battery capacity possible in order to reach the goal point follows and the last row gives the shortest traverse that is possible with a battery capacity being less than the one in the first case.

Table 11: Overview of three important traverses at LVP site

traverse	Battery capacity [W h]	Total length [km]	Avg. power demand [W]	Avg. power heater [W]	Avg. power driving [W]
Shortest (= A*)	≥ 260.0	14.93	59.2	2.9	35.0
Lowest capacity	70.0	15.09	56.4	0.0	35.0
Second shortest	110.0	14.93	57.0	0.7	35.0

5.4.2 Speyerer site

Speyerer et al. (2016) investigate a site located almost at the south pole at the rim of crater Shackleton and the ridge connecting it to de Gerlach crater. They identify different station points and present results of their optimisation algorithm connection those points to each other. Appendix D gives more details about their work. In this section, only a traverse between SR-1 (start at -89.685° N, 196.7° E) and CR-3 (goal at -89.418° N, 221.3° E) are investigated. The centre of the ROI lies at -89.592° N and 209.4° E and has a size of 27.9 km by 27.9 km at a resolution of ~160 m per pixel represented by 61,925 surface triangles. The outer part of the terrain has a size of 299.0 km by 299.7 km at a resolution of ~800 m per pixel leading to a number of 283,268 surface triangles.

Figure 59 depicts the size of the modelled scene with respect to the DEM of the south pole. The big black square represents dimension and location of the outer part, which is needed for simulation of proper insolation at the ROI. The small black square represent dimensions and location of the ROI with respect to the lunar south pole. The right plot of Figure 59 shows the ROI only with slopes of the triangles coloured from 0° to 20° and higher. In addition, the start (green) and goal point (red) are highlighted here. Slope conditions within the ROI exclude already many triangles from traverse optimisation for a rover with a maximum slope capability of 15°.

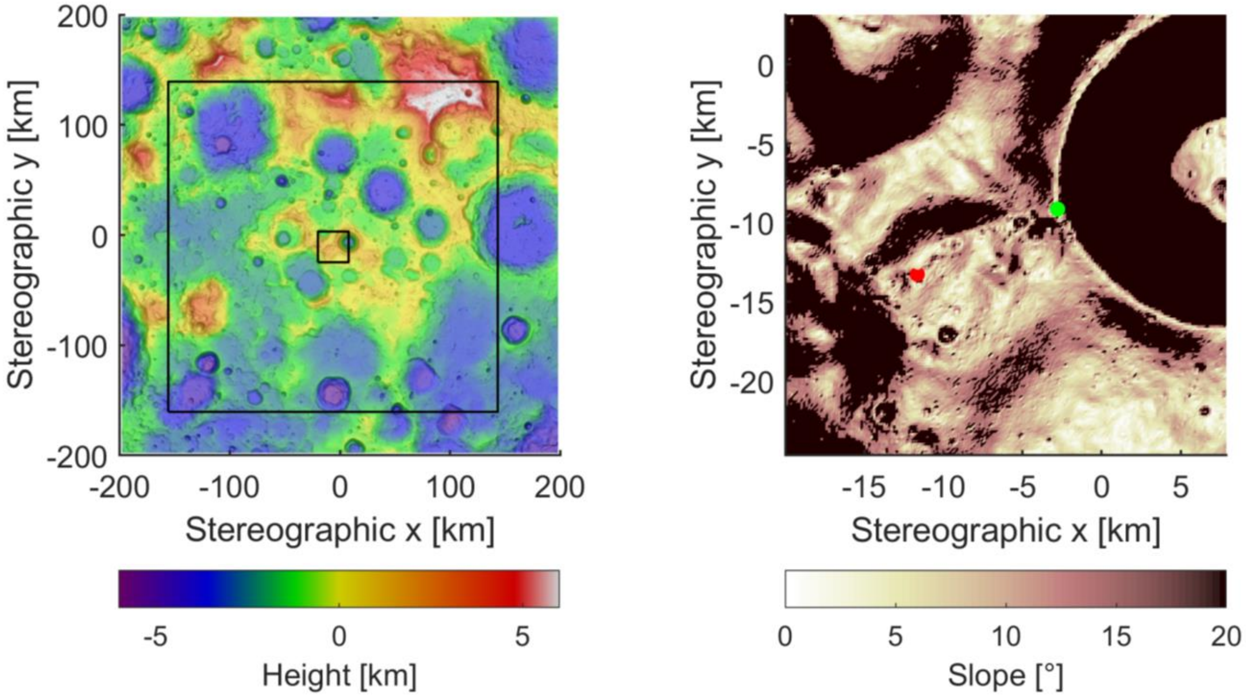

Figure 59: Speyerer site, ROI with respect to the overall DEM of the south pole and ROI with start (green) and goal point (red)

The maximum local horizon of points within the ROI is between 150 km and 180 km away as Figure 17 indicates. This would require the outer low-resolution part to have a size of 360 km by 360 km in order to meet maximum distance of the local horizon at any case. Due to limited computational power available, the size is reduce to roughly 300 km by 300 km.

Illumination conditions are investigated through the entire year 2022 and the most favourable conditions for an operation time of 3 days are identified by visual inspection. A period of 3 days is chosen because the Euclidian distance between start and end point is about 9.78 km, which requires the rover to drive for roughly 19.56 h with its constant speed of 0.1388 m s^{-1}. In order to maintain some margin in time, the period of potential operation is extended to 3 days. Looking closely, starting the traverses on 1st of March 2022 at 16:00 o'clock provides beneficial illumination conditions. It is mainly looked for illumination of the scene in minus y-direction of the start point because it is expected that the rover is going to driver there. The slope map in Figure 59 seems to prohibit a traverse along the upper region of the connecting ridge, as the rover cannot reach the goal point coming from the left behind the ridge. Figure 60 depicts this period while also highlighting the start point and goal point investigated in this chapter. At the beginning, the start and goal point seem to be illuminated but there is a shadowed part in between which receives Sun light about 1.5 days later. At the end, illumination along a direct line between both points seems to reach even more parts of the terrain.

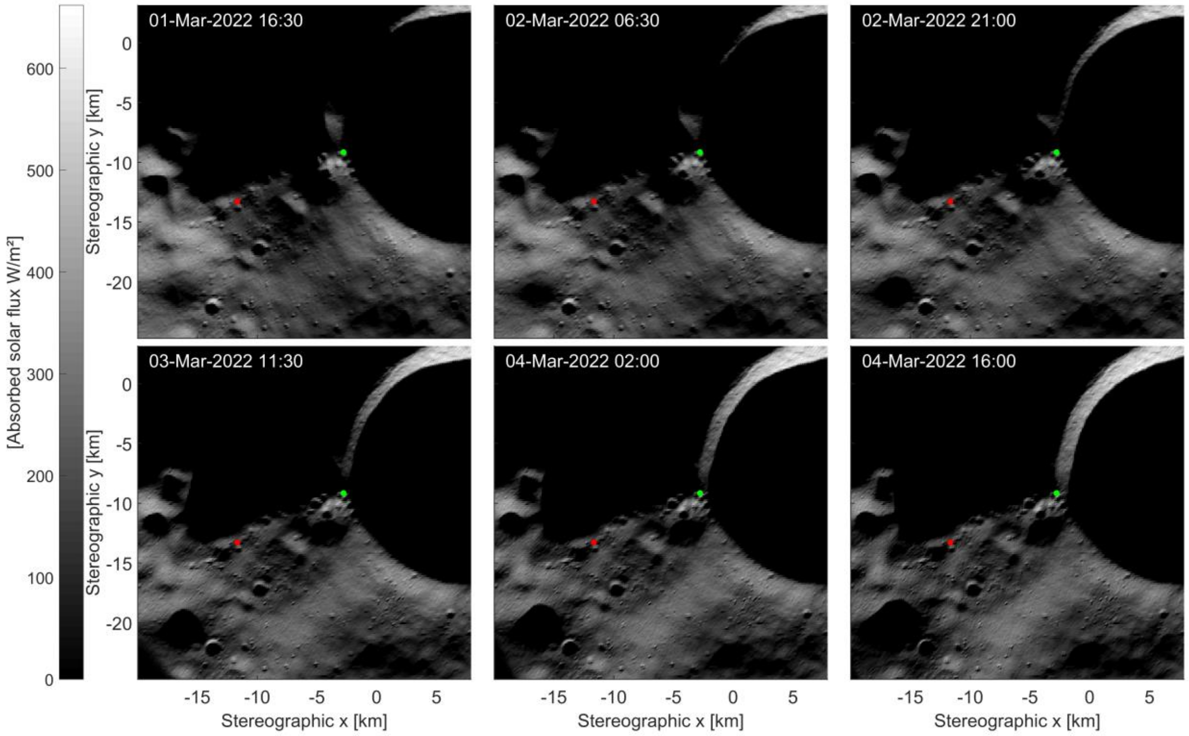

Figure 60: Illumination series of the ROI of Speyerer site. Grey scale values are absorbed solar heat flux of each triangle

In the case of the ROI close to the south pole, the optimisation algorithm searches for optimal traverses for battery capacities ranging from 0 W h to 500 W h in steps of 10 W h. This step size factors in the minimum energy required to drive the shortest path from one node to all other neighbours in the grid. The energy state is simulated every 10 s in order to get a precise prediction of the battery capacity.

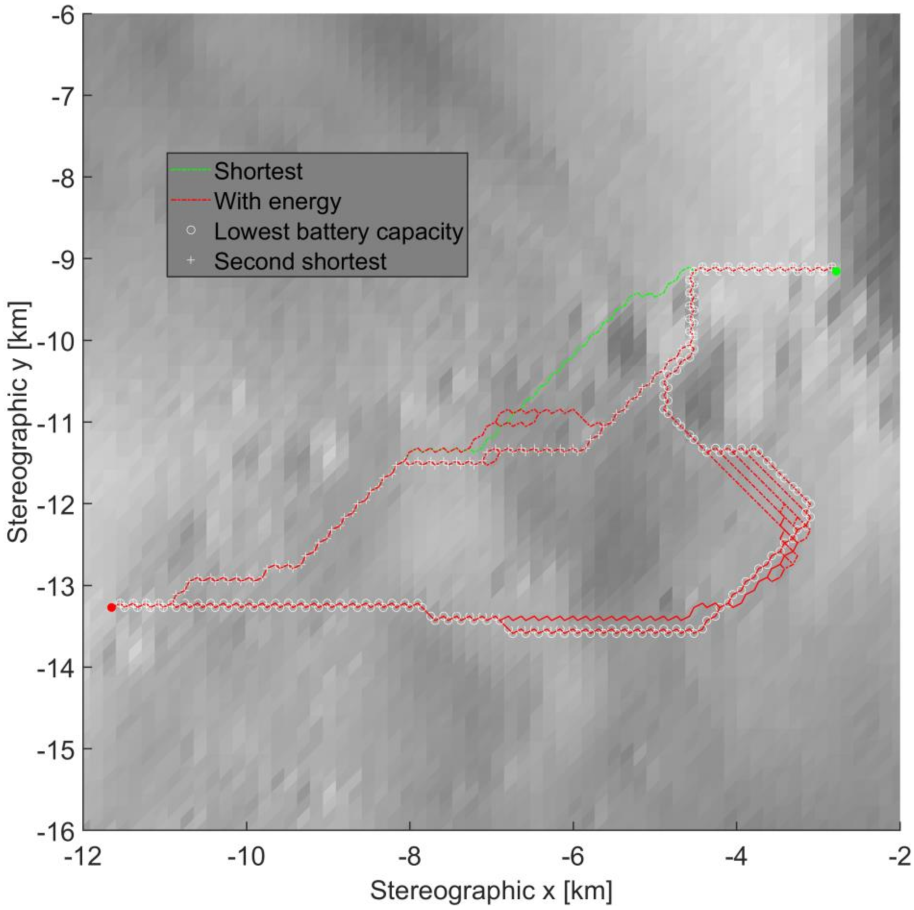

Figure 61: Shortest traverses at Speyerer site. Green line is traverse without energy state; red lines are traverses at different battery capacities. Markers highlight traverse with lowest battery capacity and second shortest.

Figure 61 shows all traverses that the optimisation algorithm finds. The green line represents the shortest traverse without simulation of the energy state of the rover and it is determined by the classic A* algorithm. The result is the shortest traverse of all with a length of 12.7304 km. A battery with a capacity of 430 W h is sufficient to reach the goal point along this traverse with the standard rover model under the selected circumstances. Red lines represent all traverses that the adapted algorithm creates with the energy state of the rover considered and an implemented battery ranging from 0 W h to 500 W h. The algorithm could not find a traverse with constant solar illumination, which equals a capacity of 0 W h. The minimum battery capacity for a traverse is 100 W h leading to a total distance of 17.811 km. This capacity is only 23.3 % of the capacity needed to travel along the shortest traverse. The traverse is marked with white circles in Figure 61 . The shortest traverse with simulation of the energy state occurs with a battery capacity of 400 W h which is ~7 % less than the required capacity to follow the shortest traverse without simulation of energy state and with 12.3705 km total length, it is only marginally longer than that traverse. It is highlighted with white crosses in Figure 61.

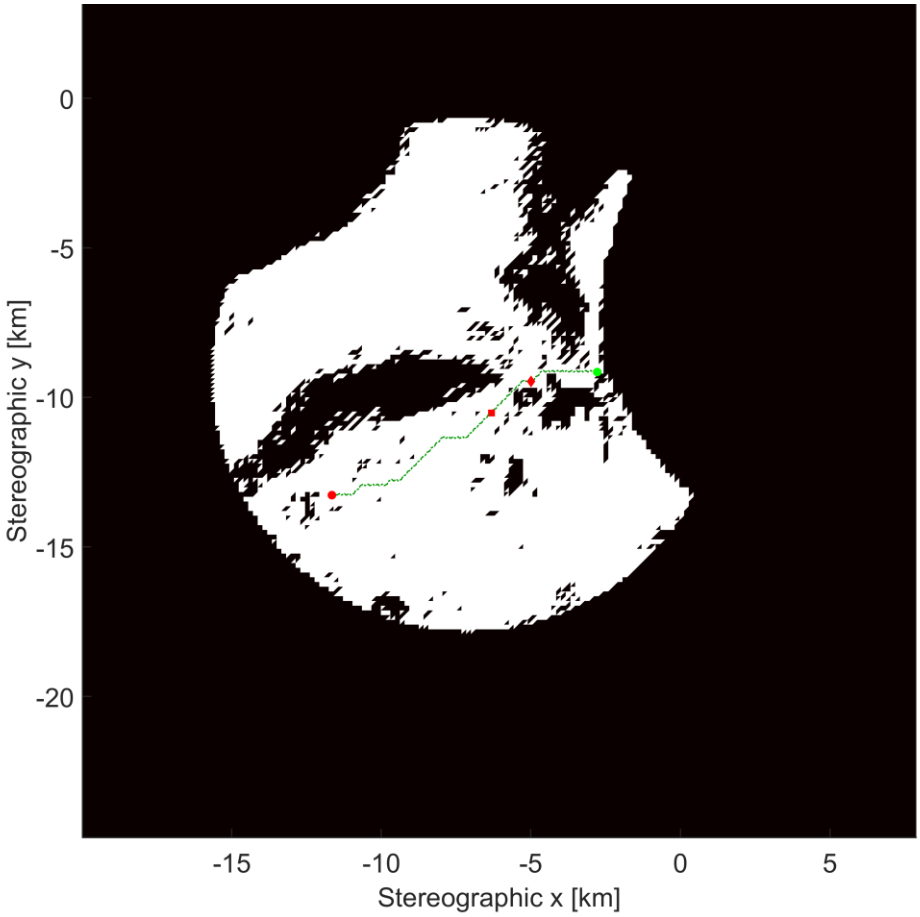

Figure 62: Map of Speyerer site with unpassable triangles marked black. Green line is shortest traverse without simulation of energy state. Red diamond indicates when battery is empty at lowest possible capacity and the red square with highest battery capacity

As for the LVP site, a binary map of unpassable nodes within the investigated ROI is shown in Figure 62. The slope limit is set to 15° and all nodes lying outside of a circle with a diameter of 17.13 km with its centre at the midpoint between start and goal are excluded from optimisation.

One can see in Figure 62 that nodes violating the slope limit of the rover build a kind of a corridor through which the rover has to drive if it wants to reach the goal node. It occurs at the first third of the shortest traverse shown in green in Figure 62, which is optimised without simulation of the energy state. The upper left part of the ROI would never be visited because it is isolated from the rest by a rim with slopes higher than 15°. It might be the case that the reduction of nodes to be considered for optimisation is too harsh, as traverses might exist that take a detour around that rim on the left side. However, nodes in that area are excluded from optimisation by engineering judgement prior to optimisation. This example emphasises how carefully the reduction of node has to be done. The red markers in Figure 62 highlight at which points the rover would stop working if it followed the shortest traverse of A* with a battery capacity of 100 W h (diamond marker) and of 420 W h (square marker).

A battery capacity of 100 W h delivers power to drive 2.813 km along the shortest traverse. With 420 W h, the rover could follow this traverse for 4.738 km. As already mentioned, with 430 W h it could complete the shortest traverse. The bottleneck seems to be the first third of the traverse in Figure 62 where the rover is in shadow. If it can traverse through this part, conditions along the rest of the traverse are more benign.

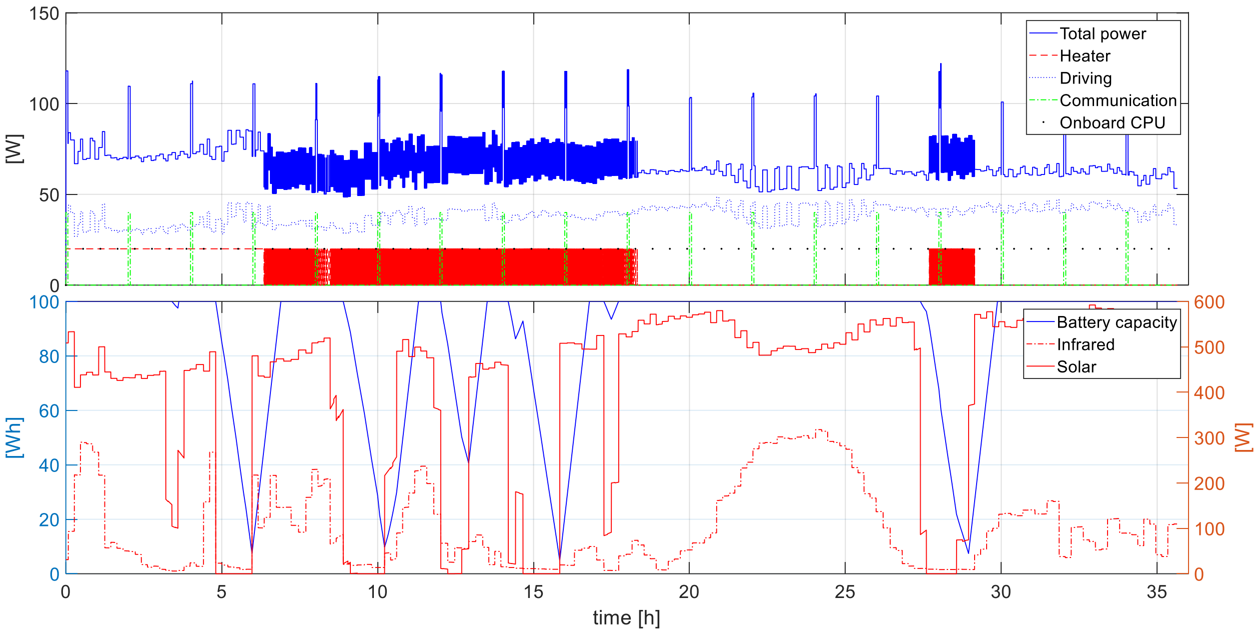

Figure 63: Power consumption and heat loads along the traverse with lowest battery capacity possible (100 W h) at Speyerer site

Figure 63 highlights results along the shortest traverse with a battery capacity of 100 W h because this is the lowest capacity, which still allows driving from start point to the goal point. The upper plot shows power consumption of the total rover system with the blue line. It is composed of power for heating in dashed red line, power for driving in dotted blue line, power needed for communication in dash-dot green line, and the power of the on board computer in dotted black. The bottom plot displays the capacity of the battery (blue line), the absorbed infrared heat power (dotted red), and the absorbed solar heat load (red) of the rover system Values are from external MLI surface only, excluding the radiator.

The total power consumption varies between 48.1 W and 122.1 W with an average of 67.1 W. A peak power demand occurs every 2 h coming from switching communication on with additional power of 40 W. A constant power of 20 W is needed for operation of the on board computer. The power need for driving varies between 26.9 W and 48.4 W with an average of 38.5 W. During operation, the heater is on for longer parts and the average heater power is 7.2 W.

Illumination conditions vary often along the traverse as can be seen in the lower plot of Figure 63. At least seven phases can be identified where the rover drives through penumbra or full shadow. Consequently, the absorbed solar heat load as well as the absorbed infrared heat change often. Conditions at the start point result in an initial temperature of the rover system below the required minimum temperature of the internal rover node. Hence, the heater is switched on until a temperature of 245 K is reached after 6 h. Between 6 h and 18 h, there is a period where the heater is switched on and off alternately because its nature of a bang-bang control and the varying thermal environment. Relatively benign conditions follow to about 27 h during which no heating is required. At the last shaded part, heater switch on again in order to ensure the required temperature. Along this traverse, there is hardly penumbra, only during the very first part with lower solar heat load, the rover drives through pronounced penumbra. Steep drops in battery capacity occur in shadowed phases and if heating is required, this drop gets even steeper.

Another fact to highlight is that charging of the battery occurs in a short time because the charge rate is set to 1 C meaning its full capacity can be charged within one hour. If the charge rate was less, the rover might have to take another traverse or even more capacity might be needed. In Figure 63 the traverse might not be possible with given values but a different charge rate because of the two consecutive shadow phases at 8.5 h to 10 hand 12 h to 12.5 h. In addition, the following shadow part starting at 14 h seems to be critical then.

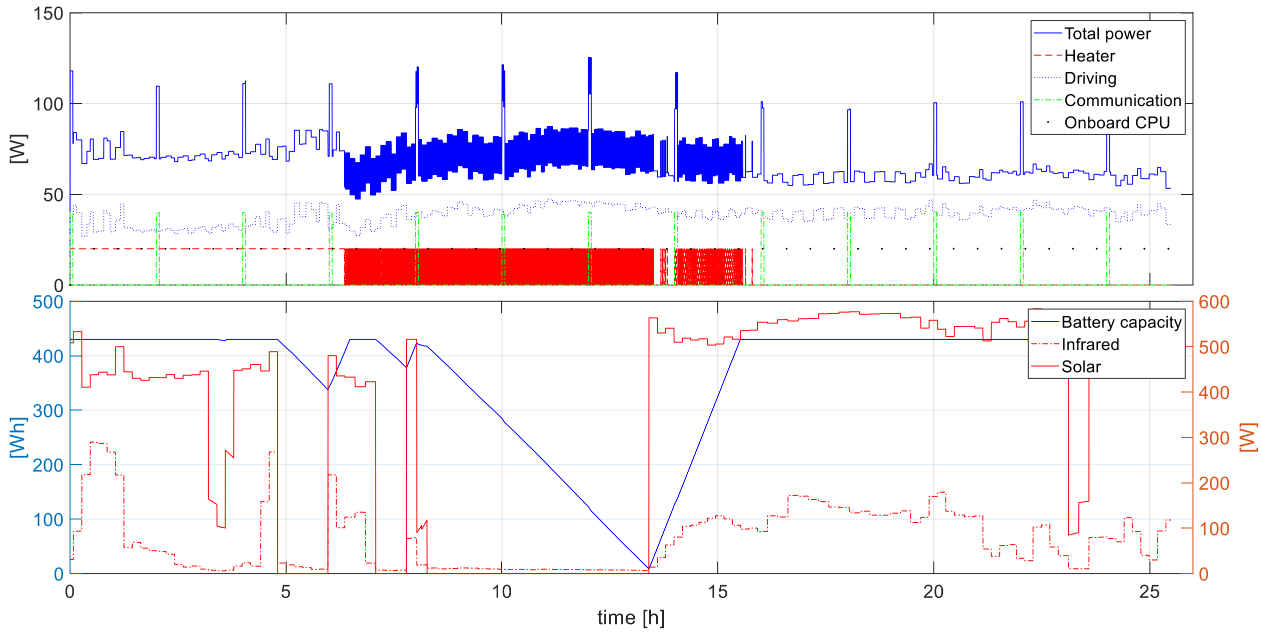

Figure 64: Power consumption and heat loads along the shortest traverse with lowest battery capacity possible (430 W h) at Speyerer site

Figure 64 highlights power consumption, the state of the battery capacity and radiation heat loads absorbed by the rover along the shortest traverse with the minimum battery capacity possible. Instead of many brief shadow periods, there is a prolonged phase in shadow between 8 h and 14 h. This phase is the critical one along the shortest traverse and it alone defines the required size of the battery. The average demand in heat power is with 2.9 W less than half of that of the traverses presented before. The total power consumption varies between 49.3 W and 118.8 W with an average of 59.3 W. A peak power demand occurs every 2 h coming from switching communication on with additional power of 40 W. A constant power of 20 W is needed for operation of the on board computer. The power need for driving varies between 29.3 W and 44.2 W with an average of 35 W. This means that the average power demand is less than during the traverse with lowest capacity presented before.

Table 12 summarises results at the Speyerer site in terms of battery capacities. The first battery capacity is the one required to follow the shortest traverse possible. The definition of the lowest battery capacity possible in order to reach the goal point follows and the last row gives the shortest traverse that is possible with a battery capacity being less than the one in the first case.

Table 12: Overview of three important traverses at Speyerer site

traverse	Battery capacity [W h]	Total length [km]	Avg. power demand [W]	Avg. power heater [W]	Avg. power driving [W]
Shortest	≥ 430	12.73	69.4	9.4	38.7
Lowest capacity	100	17.81	67.2	7.2	38.5
Second shortest	400	12.73	69.2	9.2	38.7

6 Applicability for Missions to Mars

Mars represent another celestial body with high scientific interest and unknown scientific questions to be solved. Numerous exploration missions were conducted including orbiters, landers, and roving vehicles on the ground. Currently, NASA's Mars Science Laboratory (MSL) travels along the surface of Mars sending back scientific data from drilling experiments, measurements as well as high-resolution images of geographical features. A rover with the name ExoMars, which is developed by ESA, is supposed to reach Mars by 2020, just about the same time as the successor of MSL named Mars2020 is scheduled for arrival on Mars, too. For exploration rovers of such type traverse planning is mandatory but in case of MSL, it involves a lot of manual operation. This chapter examines whether the introduced approach is also applicable for operation on Mars.

6.1 Environment on Mars

Mars is the next neighbour to Earth in our solar system in outward directions. In terms of orbit specifications, Mars resembles Earth with a time for a full revolution around its axis of about 24.6 h. The tilt of the rotational axis with 25.5° is also in a similar range as the one of Earth. However, it takes Mars about 1.88 Earth years to complete one orbital revolution around the Sun. The eccentricity of the orbit ($e = 0.0934$) is higher than for Earth ($e = 0.0167$) and the semi major axis is about 1.52 AU. This leads to lower solar insolation with a higher variation throughout one year compared to Earth. Consequently, conditions are completely different during an exploration mission that involves a rover operating on Mars than on the Moon.

Figure 65 depicts average temperatures on the surface of Mars depending on latitude and longitude (Kieffer 2013). They are the result of simulation run with a tool called KRC at a resolution of 0.05° per pixel. The terrain data is provided by the instrument Mars orbiter laser altimeter (MOLA) on board the Mars reconnaissance orbiter (MRO) at resolution of 0.03125° per pixel. Polar regions are coldest locations on Mars with temperatures as low as 160 K whilst warmest regions lie at equatorial latitudes with temperatures exceeding 232 K.

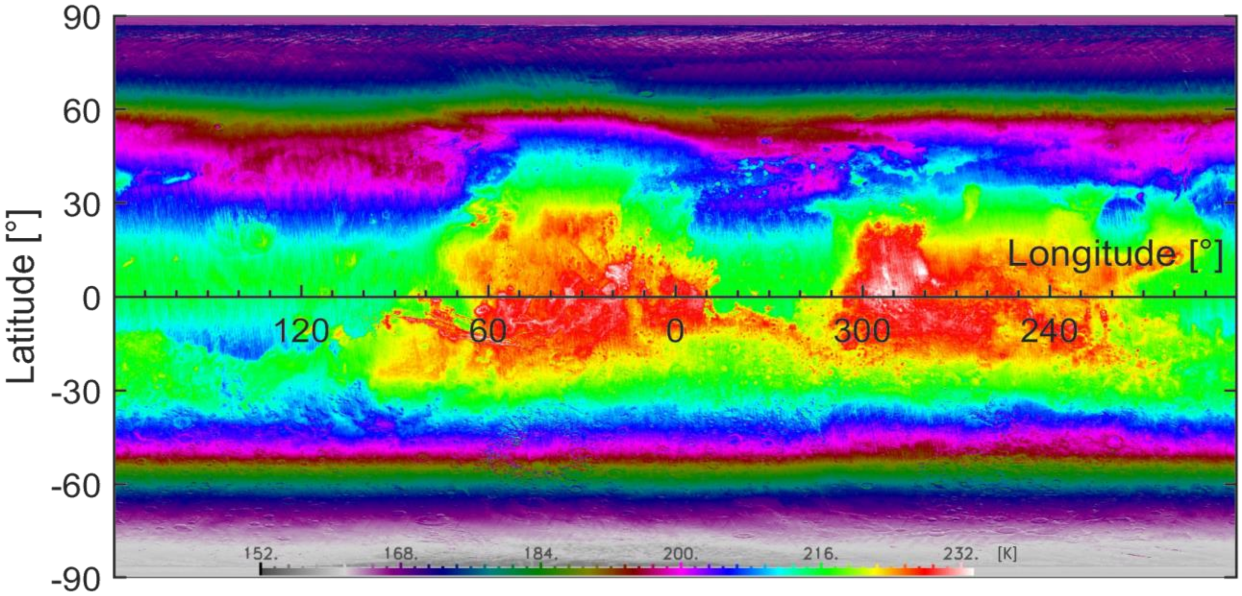

Figure 65: Average temperatures on the surface of Mars as simulated with KRC. Adapted from: (Kieffer 2013)

The environment on Mars differs from that of the Moon drastically due to the different orbital parameters and because of the presence of a low-pressure atmosphere mainly composed of CO_2 (~95 %) on Mars. Even though the pressure is low at about 700 Pa in average with variation of 20 % (Leovy 2001), convection can be the dominant type of heat transport due to high wind speeds and the high thermal conductivity of CO_2 (Gscheidle and Killian 2017). The presence of an atmosphere poses different challenges for a thermal subsystem of a rover. For example, insulation is not as efficient as in an ultra-high vacuum environment with radiation as the main heat transfer process. Additional convection adds heat flow between two components, which should be insulated. In addition, the fact, that either radiation or convection can become the main type of heat transfer during a mission due to varying wind speeds on Mars, lead to more complex thermal design solutions for rovers. At selected landing sites of previous missions on Mars including rovers, the wind speed is usually between 5 m s^{-1} to 10 m s^{-1}. For example, thermal design of the rover Mars2020 can withstand wind speeds up to 15 m s^{-1} (Novak et al. 2014), which is also the value used for MSL (Novak et al. 2013). Climate models suggest even higher wind speeds on surface depending on location, even 25 m s^{-1} (Vasavada et al. 2012a). Up to now, measurements of wind speed on the surface of Mars rely on three mission only, namely Phoenix, Viking 1, and Viking 2. An investigation shows high variations throughout the day with 7 m s^{-1} and maximum wind speeds of up to 9 m s^{-1} at a height of 1.61 m above ground with minimum wind speeds slightly below 2 m s^{-1} (Murdoch et al. 2017). Direct measurements from Phoenix at 2 m above ground show a maximum of 16 m s^{-1} (Holstein-Rathlou et al. 2010).

Solar heat flux reaching the surface of Mars depends on time and latitude. In general, the solar heat flux is much lower than on Earth due to the bigger distance to the Sun and dust in the atmosphere. Mars2020 for example use 669 W m^{-2} for hot conditions at summer solstice at a latitude of 27.5° S and 258 W m^{-2} for cold conditions during winter solstice at a latitude of 30° N (Novak et al. 2014). Those values are derived by simulation with the Mars General Circulation Model (MGCM) for calculation of conditions (Vasavada et al. 2012a). Furthermore, the eccentricity of the orbit of Mars leads to a shorter summer and to longer winter on Mars.

The environment on Mars has huge impact on latitudes, which have suitable conditions for landing sites of rover operation. The case of MSL landing site selection demonstrates that. Mainly temperature limits of external components such as actuators of MSL restricted latitudes to lie between 5° S and 15° N for full operation over an entire year on Mars without losing performance (Watkins and Steltzner. A 2007). Latitudes between 5° S and 10° S as well as between 15° N and 25° S would result in minor degradation of performance. At all other latitudes, the potential operational time decreases as drastically because conditions are too cold and operational temperatures can rarely be reached. This is another drawback for operation on Mars because cold conditions are usually the limiting factor of a mission due to the higher heat transfer by forced convection. Finally, the decision was made to land at Gale crate located at 4.50° S, 137.35° E (Golombek et al. 2012) even though the final design of MSL allowed for operation between 30° S and 30° N.

6.2 Thermal Control for Rovers on Mars

Successful missions to Mars, which landed a rover, stayed within a narrow band of latitudes close to the equator stretching out to 20° N and 15° S due to more benign temperature range compared to higher latitudes. All rovers until now rely on radioactive decay, which is used at least partially for heating in order to cope with low temperatures occurring during night in combination with heat losses by forced convection. Especially the locomotion system with moving parts is sensitive to low temperatures excluding operation at higher latitudes. Smaller rovers such as Sojourner, the Mars Exploration Rovers, and ExoMars have a radioisotope heating unit (RHU) implemented in a dedicated warm compartment where electronics are located. Energy for operation is supplied by solar generators and stored in secondary batteries. A part of that energy might also be used for additional heaters.

In general, thermal control is more challenging than for conditions on the Moon because the dominant heat transfer mechanism can be forced convection at higher wind speeds and radiation at calm conditions. As stated above insulation is less efficient in the CO_2 rich atmosphere of Mars. Therefore, heat losses during night in cold environment are high and the current thermal solution to cope with that is the usage of radioisotope heating units. An interesting fact about MSL and Mars2020 is that their thermal control system allows the rover to survive cold conditions eternally but then hardly any power is left for operation of science instruments because nearly all power goes directly into heating.

The smaller rovers MER and ExoMars have a constant heat source in form of a RHU implemented in their compartments that consist of temperature sensitive components. However, their thermal architecture differs.

MER has one dedicated warm compartment, which is insulated by aerogel, and heat losses to the environment are kept to a minimum. In total eight RHUs with about 1 W each provide the WEB with heating power in order to survive cold conditions. Additional resistive heaters switch on if the power from RHUs is not sufficient for heating. Additionally, the pair of rechargeable batteries is connected to two radiators by two thermal switches. They react on temperature only as the set point of the paraffin within the thermal switches is chosen accordingly. Excessive heat can only egress trough that heat path (Novak 2003).

Thermal control for the ExoMars rover is based on the same principles as used for MER with housing sensitive parts in insulated boxes (Alary and Lapensée 2010). Insulation is realised by a gas gap filled with CO_2 from the atmosphere of Mars but the gas may not be in motion because forced convection destroys the insulating effect of the low conductivity of CO_2. Each insulated box has its own RHU and own radiators. Loop heat pipes (LHP) in combination with a heat switch define a variable and controllable link to the radiators.

Energy for the big rovers MSL and the evolutionary version Mars2020 comes from an RTG storing energy in secondary batteries. The power provided by converting heat into electricity amounts to 110 W (Welch et al. 2013), and it is not enough in order to power the rover. MSL needs at least 45 to 70 watts while asleep, at least 150 W when awake, and up to roughly 500 W when driving. (Gross and Cardell 2011). Waste heat of RTG can heat up internal components by fluid loops in combination with heat exchangers, and additional resistive heaters can be switched on for survival and for thermal control of external parts of the rover (Novak et al. 2014). However, it is important to consider the orientation of the rover with respect to the direction of wind. Simulation of wind conditions and the performance of the heat rejection reveal differences of up to 61 K with different orientations (Bhandari and Anderson 2013). Telemetry data from MSL indicates that wind speed is of importance as well as local shadowing where both can lead to unpredicted temperature variation over roughly 1 h (Cucullu III G. C. et al. 2014).

6.3 Evaluation of Applicability

In theory, the approach developed in this thesis would also work for rovers operating on Mars. However, this requires a much more sophisticated model of the atmosphere of Mars than currently available. Basically, a daily weather forecast is needed comparable to the ones on Earth in order to calculate heat transfer precise enough for estimation of the heating demand of the rover. Advanced models of the atmosphere on Mars are an ongoing research and up to now only forecasts can be made on a big scale, mainly because of seasons on Mars and visual reconnaissance. Beside a proper forecast on a local scale, also the orientation of the rover with respect to the direction of wind is significant for calculation of heat transfer by forced convection. This is not possible in the current implementation of traverse optimisation. However, the code of TherMoS-X allows for an integration of it within the optimisation process but at the cost of increasing computational time and memory demand. For example, an option could be to create optimisation maps in such way that at each position, the rover rotates in steps of 90° and the algorithm later on uses a proper orientation for traveling to the next node. A higher memory demand of eight times is the consequence and the duration for optimisation would increase exponentially. Other options might exist as well to overcome the higher uncertainties of thermal control during operation on Mars. It is assumed that they require a change in the overall approach of the optimisation strategy that is developed in this thesis and because of that, they are not discussed further.

To sum it up, in general adjustments of the approach presented in this thesis are necessary in order to handle higher uncertainties of heat transfer occurring for a rover operating on Mars. This affects mainly the operational aspect of a mission. If more accurate prediction of wind speeds, the dust coverage, and opacity of the atmosphere were available, an updated approach would provide meaningful results in the future.

7 Conclusion and Outlook

7.1 Summary

This thesis describes a process of implementing automatic traverse planning for solar-powered rovers operating at the lunar poles with sophisticated consideration of the overall energy state of the rover. This implies a power model for the rover, which depends on the thermal state, the locomotion system, and power for communication to an orbiter. The model also simulates active thermal control via an internal heat source ensuring required minimum temperatures of sensitive internal parts. Electric heaters are a common choice for thermal control additionally to passive options. Furthermore, MLI protects the inner parts from the harsh environment and a heat switch between a radiator and the interior allows for controlling the maximum temperature of the internal parts. Driving on the lunar surface requires power, which is calculated depending on the respective slope of the terrain and variable parameters of the overall rover system such as amount of wheels, total mass, deformation of wheels, and others as described in chapter 3.3.2. Communication is estimated to occur every two hours for ten minutes for exchange of data with a relay satellite in lunar orbit. A constant power of 20 W is additionally assumed to factor in power consumption of internal electronics, all combined in the on-board computer. Solar cells with an area of 0.96 m² provide the total rover system with power, stored in a rechargeable battery of varying capacity.

For a most accurate simulation of the environment of the rover, the simulation method has to be as precise as possible. Solar insolation is calculated with the real size of the Sun as seen from the lunar surface and the terrain model has to be as precise as possible. This was implemented based on a DEM with a resolution of 50 m per pixel derived from co-registered LRO tracks. The available computational power required the reduction of this resolution so that the final model had a resolution of 160 m per pixel in the region where optimisation takes place and 800 m per pixel for the surrounding region that is required for realistic calculation of illumination. Validation of the simulation method is presented in different steps and finalised with a comparison to temperature profiles of different orbits measured by LRO DLRE. Results proved a Pearson's correlation coefficient of 0.955.

The validated simulation method provides the required input to the optimisation approach with pre-computed temperature maps of the terrain and corresponding solar angles. Prior to optimisation, maps of incoming infrared heat flux and solar heat flux are prepared by placing a sphere with a diameter of 1.5 m on each centroid in the scene at a given time step. The optimisation algorithm, which is an adapted version of A*, finds nearly optimal solutions for this scenario. It is possible to derive the optimal solution with slight adjustments on the optimisation algorithm but at the price of high computational costs. They render it impossible to calculate the optimal traverse with the given implementation of the rover model and the resolution of the terrain. However, resulting traverses are always close to the optimum and provide sufficient information in order to assess the proposed approach of traverse optimisation.

Sensitivity analyses on the power demand for driving of the rover showed that the optimisation algorithm is sensitive in regions with difficult illumination conditions and high slopes of the terrain. Even moderate changes in the range of 15 % to 20 % of the total power demand can lead to much longer traverses because the capacity of the battery is drained faster in shadowed phases along the traverse and alternative traverses are sparse due to a high number of nodes that are too steep. In a more benign region with flat terrain and more even distribution of illumination, the algorithm is less sensitive to changes in power demand in terms of total length of the traverse.

Two different sites at the vicinity of the lunar south pole represent mission cases for an application of the approach. Here, the optimisation approach showed its potential for improving the understanding of environmental conditions along a traverse as well as its capabilities to provide additional information for mission planners. At both sites, there exists no traverse during the investigated periods, which could be completed without a rechargeable battery. However, even small batteries already allow the rover to drive from start to goal even though a long detour is needed at one site. Consideration of the thermal state provided additional information only at one site, because at the other site the environment was benign enough for the rover to stay within required temperature range without additional heating power.

The optimisation approach developed in this thesis might also be of interest for application on missions to Mars. However, it is anticipated that thermal simulation plays a bigger role for realistic calculation of the energy state than on the Moon. This can only work with a precise model of the environment because wind speed and direction are crucial in thermal control of rovers. Current models of the surface of the Mars are not accurate enough in order to produce information for dynamic simulation at a given time. Hence, the currently implemented approach would not benefit missions to Mars.

7.2 Conclusion

The presented approach allows assessing how useful consideration of the energy state with a thermal model of the rover can be. The simulation and optimisation methods were implemented in an updated simulation framework with the name TherMoS-X.

The most recent thermal model of the surface of the Moon has been implemented and validated at the lunar south pole in contrast to the original publication of the model, where only regions with latitudes between ±70° are incorporated (Hayne et al. 2017). Different parameters have to be considered by the simulation method for a successful implementation of this model. Due to the low solar elevation angles at the poles, a proper representation of illumination is essential as well as a realistic landscape implementation. Illumination has to factor in that the Sun cannot be modelled as point source but one has to consider its real shape. The terrain has to cover all features, which have an influence on the illumination of the region of interest that has to be simulated. In this thesis, a self-written ray tracer determines illumination and heat transfer by radiation. The result of all modelling effort was a realistic simulation of the temperatures on the surface of the Moon that produced results nearly as accurate as results found in literature. However, the accuracy of the model could still be improved, especially in periods with dynamically changing insolation. Increasing the number of ten nodes into depth of a surface triangles to about 15 or 20 as proposed by Hayne et al. (2017) might help as well as angle dependant thermo-optical properties. Still, for an assessment of the optimisation approach, which has been developed in this thesis, the model was considered to be accurate enough.

A classical optimisation approach was adapted in order to incorporate a dynamic energy state of the rover including all domains in the optimisation algorithm. This led to an algorithm that cannot find the real optimum anymore in favour of computational speed. Still, the algorithm is able to find nearly optimal solutions under consideration of the energy state and optimal solution if the energy state is neglected or the stored energy is big enough to cope with all conditions.

The implemented optimisation approach produced meaningful results at two different ROIs. It proved that it can find nearly optimal traverses with any given battery capacity. In general, higher battery capacity correlates with a decrease in the total length of traverses. In the more benign ROI (LVP site) with only few unpassable nodes and high solar visibility at many nodes, the algorithm might have skipped shorter traverse options because it already converged. Those traverses are between 0.5 % and 4.66 % longer than the shortest traverse that the algorithm finds with lower batter capacities. In the more rugged ROI (Speyerer site) with difficult illumination conditions, these deviations in length are even less and lie between 0.001 % and 0.87 %.

Furthermore, the algorithm provides sizing capabilities for the battery capacity for different cases if optimisation is repeated with a stepwise variation of battery capacities. With that, one can determine the lowest battery capacity that is needed in order to follow the shortest traverse that is determined by the classic optimisation algorithm A*. It is important to notice that the required battery capacity strongly depends on the simulated period, on the terrain, and on the model of the rover. At LVP site, at least 260 W h are required and at Speyerer site, it is at least 430 W h. This is about 165 % of the capacity at LVP site even though the Euclidian distance between start and goal is only 73.9 % compared to the one at LVP site.

Another case is the lowest battery capacity, which still allows the rover to drive from start to goal. This capacity is only 18.2 % at one site and 23.3 % at the other site of the one needed to follow the shortest traverse. Obviously, the total length of the traverse increases as the algorithm tries to minimise periods in shadows. At the LVP site, it increases only about 1 % whilst the traverse at the Speyerer site is 39.9 % longer than shortest traverse This proves that alternative traverses exist compared to the classic optimisation approach where the thermal model or even the battery capacity are neglected.

At both sites, implementing thermal simulation for a full representation of the energy state of the rover proved to be superior to previous approaches in publications that neglect at least a sophisticated thermal simulation along the traverse. Results at both sites showed that heating is required for the given rover model in most cases. Neglecting the thermal model of it would presumably result in a different traverse, which could not be driven in reality. However, the implementation of a thermal model comes with high computational costs. Consequently, it has to be assessed by views of mission operation and of the rover design philosophy including engineering margins whether such a detailed optimisation approach is beneficial to the success of the mission. Adding a substantial margin to the battery capacity might render consideration of the thermal state of the rover unnecessary but it would also add mass to the system.

An interesting conclusion can be drawn from the results. The state of the battery capacity correlates well with the incoming solar heat load. As expected, this comes from the power supply of the rover, which is prepared by solar cells and a rechargeable battery. The battery is drained as soon as the incoming solar radiation falls below a threshold value where it cannot meet the current power demand anymore. Additional heating amplifies discharging of the battery. By looking at the power curves along a traverse, it becomes apparent that the heater power represents a small fraction of the entire power consumption of up to 10 % for the implemented model. The main consumer is locomotion, followed by the on-board computer (where in the model all auxiliary electronic components are combined), power consumption for communication and for heating. Of course, this depends on the design of the rover and conclusion drawn here are valid for the used model of the rover. Therefore, the optimisation approach proves that even if only a small fraction of the total power budget is dedicated to thermal control, the rover is able to explore otherwise challenging traverses while relying only on solar power.

Another fact to consider is the charge rate of the battery. In the implemented power system, the battery can be fully charged within one hour if enough solar radiation reaches the solar cells. The steep charging curves in plots of the results (for example Figure 63) show that this is helpful along a traverse with many shaded segments. In the particular case of Figure 63, a reduction of the charge rate by three renders it impossible for the rover to reach the target location.

7.3 Future Work

During creation of this thesis, many new ideas and alternative ways to the chosen implementation could be identified. For some of them an investigation in the near future seems profitable. Future work focuses on aspects considering the thermal model of the Moon at lunar poles and those considering the optimisation process. Mainly all points focus either on accuracy or on accelerating the optimisation process.

Improving calculation time of thermal model

Model validation has proven that the thermal model of the Moon is already at a high level of accuracy. Still, the accuracy can be improved with longer pre-run time before simulation of the actual simulation period. This requires a tremendous speed up of solving of the thermal model because currently this is the bottleneck for long time simulations. Consequently, the obvious next step in improving the overall accuracy of the thermal model is an improvement in computational time. This could be realised by moving the solver to the GPU and make us of the high amount of parallel cores. Furthermore, a self-written solver in another programming language such as C++ might accelerate solving of the model.

Accuracy of thermal model of the Moon

Parameters of the thermal model are chosen in order to realise an efficient implementation with adequate accuracy. Hence, several parameters can be modelled in more detail in order to improve the accuracy of the model. The angle dependency of solar absorptivity of lunar regolith is probably the most obvious and straightforward possibility to adjust the model. The ray tracer program already knows the angle towards the Sun from the surface triangle and only the equation for solar absorptivity has to be implemented. Additionally, the solar constant should be changed from a constant value at any time to the real value defined by the current position of the Moon with respect to the Sun. Another promising change is to increase the number of nodes into depth. An increase to 15 nodes or even to 20 nodes per triangle should increase accuracy in a noticeable way but at the same time, a performance increase in computational time is needed because this high number of nodes calls for a faster solver as discussed in the previous paragraph. Other options with minor effect on improving the accuracy are the implementation of solar limb darkening effect, the number of bounces of reflected solar rays, the implementation of reflections of infra-red rays, and the rock abundance on the surface triangle as they change the thermal inertia at those locations.

Faster computational time of optimisation

As for the thermal model of the Moon, a faster computation of the optimisation should be an aim in the near future. Again, the solver of the thermal model is the slowest component. Two options are available. Either the number of simulation steps has to be decreased or the solver itself has to operate faster. However, a decrease in the number of simulation steps means an increase of the step size, which can reduce accuracy of the results and additional investigations have to show which maximum time step can still be used. In terms of acceleration of the solver, it might be promising to look into switching over to other programming languages such as C++ or python.

Implement real optimisation

The current optimisation approach finds near-optimal solutions but with a slight change in the code it is possible to find the real optimum as proposed by Cunningham et al. (2014). Energy states of the rover should be created and tracked dynamically. This would lead to a high number of states that the algorithm has to track. In order to handle this issue, a way of pruning the number has to be established. Then, only the most promising states are simulated from start to the goal and the optimal solution can be found. This kind of optimisation requires a faster implementation of the simulation of the rover state in order to converge within a reasonable time. The current version within TherMoS-X is too slow for usage of this approach.

Accuracy of simulation during optimisation

The current implementation of heat exchange by radiation for the rover is adequate in order to assess the topic of this thesis. For real mission with a sophisticated design of the rover, a more precise simulation might be needed. In this case, one could change the approach of using a sphere for creation of thermal maps and correlating fluxes to parts of the rover by using the real geometry of the rover. In addition, the optimisation approach could be adjusted from pre-computed maps towards ray tracing only when a centroid is reached during the optimisation algorithm. As a drawback, computational time might increase. Another option could be to place the rover at each centroid in various positions with heading towards all possible subsequent centroids for creation of maps. However, this increases the memory demand.

Rover model

With respect to the power model of the rover, a physically correct charging behaviour of batteries could be implemented in the near future. This would include a model of the internal resistance of the battery depending on the state of discharge. Furthermore, the behaviour of solar cells can be modelled in more detail. Their efficiency depends on their temperature, which could be implemented as well.

8 References

8.1 References

Acierno, Kyle (2017): Mining the Moon with ispace, a Lunar Exploration Company. In : Space Resources Roundtable XVIII / Planetary & Terrestrial Mining Sciences Symposium,

Alary, Coralie; Lapensée, Stéphane (2010): Thermal Design of the ExoMars Rover Module. In : 40th International Conference on Environmental Systems. Barcelona, Spain.

Alhasni, Mohammad (2018): Multi-GPU parallelization of a dynamic heat transfer model on the Moon. Master's Thesis. Technical University of Munich. Available online at http://www5.in.tum.de/pub/2018_Alhasni_thesis.pdf.

Allender, Elyse J.; Orgel, Csilla; Almeida, Natasha V.; Cook, John; Ende, Jessica J.; Kamps, Oscar et al. (2019): Traverses for the ISECG-GER design reference mission for humans on the lunar surface. In *Advances in Space Research* 63 (1), pp. 692–727. DOI: 10.1016/j.asr.2018.08.032.

Amos, Steve; Brochard, Paul; Fernandez, A. (2017): Battery for Extended Temperature Range Exomars Rover Mission. In *E3S Web Conf.* 16, p. 6001. DOI: 10.1051/e3sconf/20171606001.

Andrews, Daniel R.; Colaprete, Anthony; Quinn, Jacqueline; Chavers, Donald; Picard, Martin (2014): Introducing the Resource Prospector (RP) Mission. In : AIAA SPACE 2014 Conference and Exposition. San Diego, CA.

Andrews, Daniel R. (2015): Resource Prospector (RP) - Early Prototyping and Development. In : AIAA SPACE 2015 Conference and Exposition.

Astrobotic Technology (2019a): Peregrine Lunar Lander Payload User Guide. Available online at https://www.astrobotic.com/payload-user-guide, checked on 11/3/2019.

Astrobotic Technology (2019b): Astrobotic Awarded $79.5 Million Contract to Deliver 14 NASA Payloads to the Moon.

Bandfield, J. L.; Edwards, C. S.; Poston, M. J.; Klima, R. L. (2016): Lunar H2O/OH- Distributions: Revised Infrared Spectra From Improved Thermal Corrections. In : 47th Lunar and Planetary Science Conference. The Woodlands, Texas, USA, 21-25 March.

Bandfield, Joshua L.; Hayne, Paul O.; Williams, Jean-Pierre; Greenhagen, Benjamin T.; Paige, David A. (2015): Lunar surface roughness derived from LRO Diviner Radiometer observations. In *Icarus* 248, pp. 357–372. DOI: 10.1016/j.icarus.2014.11.009.

Bekker, M. G. (1962): Land Locomotion on the Surface of Planets. In *ARS Journal* 32 (11), pp. 1651–1659. DOI: 10.2514/8.6357.

Bekker, M. G. (1964): Mechanics of Locomotion and Lunar Surface Vehicle Concepts. In *SAE Transactions* 72, pp. 549–569.

Bhandari, Pradeep; Birur, Gajanana; Pauken, Michael; Paris, Anthony; Novak, Keith; Prina, Mauro et al. (2005): Mars Science Laboratory Thermal Control Architecture. In : 35th International Conference on Environmental Systems.

Bhandari, Pradeep; Anderson, Kevin R. (2013): CFD Analysis For Assessing The Effect Of Wind On The Thermal Control Of The Mars Science Laboratory Curiosity Rover. In : 43rd International Conference on Environmental Systems. Vail, CO.

Bresina, John L.; Morris, Paul H.; Deans, Matthew C.; Cohen, Tamar E.; Lees, David S. (2017): Traverse Planning with Temporal-Spatial Constraints. In : 27th International Conference on Automated Planning and Scheduling (ICAPS 2017). Pittsburgh, PA; United States, 18-23 Jun. 2017.

Carsten, Joseph; Rankin, Arturo; Ferguson, Dave; Stentz, Anthony (2007): Global Path Planning on Board the Mars Exploration Rovers. Big Sky, Montana, March 3-10, 2007. [Piscataway, N.J.]: IEEE.

Cremers, C. J.; Birkebak, R. C.; White, J. E. (1971): Lunar surface temperatures from apollo 12. In *The Moon* 3 (3), pp. 346–351. DOI: 10.1007/BF00561846.

Cremers, C. J.; Birkebak, R. C. (1971): Thermal conductivity of fines from Apollo 12. In : Proceedings of the Lunar Science Conference, vol. 3 (Lunar Science Conference), pp. 2311–2315.

Crisp, Joy A.; Adler, Mark; Matijevic, Jacob R.; Squyres, Steven W.; Arvidson, Raymond E.; Kass, David M. (2003): Mars Exploration Rover mission. In *J.-Geophys.-Res.* 108 (E12), p. 1855. DOI: 10.1029/2002JE002038.

Cucullu III G. C.; Zayas D.; Novak K.; Wu P. (2014): A Curious Year on Mars—Long-Term Thermal Trends for Mars Science Laboratory Rover’s First Martian Year. In : 44th International Conference on Environmental Systems. Tucson, Wa.

Cunningham, Chris; Jones, Heather L.; Kay, Jacqueline; Peterson, Kevin M.; Whittaker, William L. (2014): Time-Dependent Planning for Resource Prospecting. In : The International Symposium on Artificial Intelligence, Robotics and Automation in Space (i-SAIRAS).

Cunningham, Chris; Amato, Joseph; Jones, Heather L.; Whittaker, William L. (2017): Accelerating energy-aware spatiotemporal path planning for the lunar poles. In : 2017 IEEE International Conference on Robotics and Automation (ICRA). 2017 IEEE International Conference on Robotics and Automation (ICRA). Singapore, Singapore, 29.05.2017 - 03.06.2017: IEEE, pp. 4399–4406.

Dijkstra, E. W. (1959): A note on two problems in connexion with graphs. In *Numer. Math.* 1 (1), pp. 269–271. DOI: 10.1007/BF01386390.

Di, K.; Liu, Z.; Liu, B.; Wan, W.; Peng, M.; Li, J. et al. (2019): TOPOGRAPHIC ANALYSIS OF CHANG’E-4 LANDING SITE USING ORBITAL, DESCENT AND GROUND DATA. In *Int. Arch. Photogramm. Remote Sens. Spatial Inf. Sci.* XLII-2/W13, pp. 1383–1387. DOI: 10.5194/isprs-archives-XLII-2-W13-1383-2019.

Ding, Liang; Gao, Haibo; Deng, Zongquan; Nagatani, Keiji; Yoshida, Kazuya (2011): Experimental study and analysis on driving wheels’ performance for planetary exploration rovers moving in deformable soil. In *Journal of Terramechanics* 48 (1), pp. 27–45. DOI: 10.1016/j.jterra.2010.08.001.

Elphic, R. C.; Colaprete, Anthony; Shirley, A.; McGovern A.; Beyer, R.; Siegler, Matthew A. (2017): Landing Site and Traverse Plan Development for Resource Prospector. In : Lunar and Planetary Science Conference 2017. The Woodlands, Texas, USA, 20-24 March 2017.

ESA (2019): Exploration of the Moon - Lunar Mission Campaign. Available online at https://exploration.esa.int/web/moon/-/60922-lunar-mission-campaign, checked on 10/15/2019.

Favaedi, Yalda; Pechev, Alexandre; Scharringhausen, Marco; Richter, Lutz (2011): Prediction of tractive response for flexible wheels with application to planetary rovers. In *Journal of Terramechanics* 48 (3), pp. 199–213. DOI: 10.1016/j.jterra.2011.02.003.

Ferguson, Dave; Stentz, Anthony (2006): Using interpolation to improve path planning. The Field D* algorithm. In *J. Field Robotics* 23 (2), pp. 79–101. DOI: 10.1002/rob.20109.

Ferrando, Emanuele; Zanella, Pietro; Riva, Stefano; Damonte, Giulia; Romani, Romano; Ferrante, Luigi; Fernandez, A. (2017): Photovoltaic Assemblies for the Power Generation of the Exomars Missions. In *E3S Web Conf.* 16, p. 4002. DOI: 10.1051/e3sconf/20171604002.

Fink, W.; Baker, V. R.; Flammia, M.; Tarbell M. A. (2015): Rover Traverse-Optimizing Planner For Multi-Objective Deployment Scenarios. In : IEEE Aerospace Conference. Big Sky, MT.

Fink, Wolfgang (2008): Stochastic optimization framework (SOF) for computer-optimized design, engineering, and performance of multi-dimensional systems and processes. In Wolfgang Fink (Ed.): SPIE Defense and Security Symposium. Orlando, FL, Sunday 16 March 2008: SPIE (SPIE Proceedings), 69600N.

Flahaut, J.; Carpenter, J.; Anand, M.; van Westrenen, Wim; Fisackerly, R.; Williams, J.-P. et al. (2016): Candidate Landing Sites Near the Lunar Poles: A European Perspective. In : European Lunar Symsposium. Amsterdam.

Gilmore, David G. (2002-©2003): Spacecraft thermal control handbook. 2nd ed. El Segundo, Calif.: Aerospace Press.

Gläser, P.; Haase, I.; Scholten, F.; Oberst, J. (2010): Precision Registration of LRO Altimeter Tracks and Stereo Terrain Models – Implications for Surface Slopes and Roughness. In : European Planetary Science Congress.

Gläser, P.; Haase, I.; Oberst, J.; Neumann, G. A. (2013): Co-registration of laser altimeter tracks with digital terrain models and applications in planetary science. In *Planetary and Space Science* 89, pp. 111–117. DOI: 10.1016/j.pss.2013.09.012.

Gläser, P.; Scholten, F.; Rosa, D. de; Marco Figuera, R.; Oberst, J.; Mazarico, E. et al. (2014): Illumination conditions at the lunar south pole using high resolution Digital Terrain Models from LOLA. In *Icarus* 243, pp. 78–90. DOI: 10.1016/j.icarus.2014.08.013.

Gläser, P.; Oberst, J.; Neumann, G. A.; Mazarico, E.; Speyerer, E. J.; Robinson, M. S. (2018): Illumination conditions at the lunar poles. Implications for future exploration. In *Planetary and Space Science* 162, pp. 170–178. DOI: 10.1016/j.pss.2017.07.006.

Gläser, P.; Gläser, D. (2019): Modeling near-surface temperatures of airless bodies with application to the Moon. In *A&A. DOI:* 10.1051/0004-6361/201935514.

Golombek, M.; Grant, J.; Kipp, D.; Vasavada, A.; Kirk, R.; Fergason, R. et al. (2012): Selection of the Mars Science Laboratory Landing Site. In *Space Sci Rev* 170 (1-4), pp. 641–737. DOI: 10.1007/s11214-012-9916-y.

Gross, Michael A.; Cardell, Greg (2011): An Overview of NASA'sMars Science Laboratory. In : Proceedings of the 9th European Space Power Conference.

Grotzinger, John P.; Crisp, Joy; Vasavada, Ashwin R.; Anderson, Robert C.; Baker, Charles J.; Barry, Robert et al. (2012): Mars Science Laboratory Mission and Science Investigation. In *Space Sci Rev* 170 (1-4), pp. 5–56. DOI: 10.1007/s11214-012-9892-2.

Gscheidle, C.; Killian, M. (2017): Mars Rover - Limits of Passiver Thermal Design. In : 47th International Conference on Environmental Systems.

Hager, P. B.; Klaus, D. M.; Walter, U. (2014): Characterizing transient thermal interactions between lunar regolith and surface spacecraft. In *Planetary and Space Science* 92, pp. 101–116. DOI: 10.1016/j.pss.2014.01.011.

Hager, P. B.; Parzinger, S.; Haarmann, R.; Walter, U. (2015a): Transient thermal envelope for rovers and sample collecting devices on the Moon. In *Advances in Space Research* 55 (5), pp. 1477–1494. DOI: 10.1016/j.asr.2014.12.012.

Hager, Philipp B. (2013): Dynamic thermal modeling for moving objects on the Moon. (Dissertation at the Institute of Astronautics at the Technical University of Munich), Dr.-Hut Verlag, München, ISBN 978-3-8439-1224-2. München: Universitätsbibliothek der TU München.

Hager, Philipp B.; Walter, Ulrich; Massina, Christopher J.; Klaus, David M. (2015b): Characterizing a Transient Heat Flux Envelope for Lunar-Surface Spacesuit Thermal Control Applications. In *Journal of Spacecraft and Rockets* 52 (4), pp. 1193–1202. DOI: 10.2514/1.A33182.

Hart, Peter; Nilsson, Nils; Raphael, Bertram (1968): A Formal Basis for the Heuristic Determination of Minimum Cost Paths. In *IEEE Trans. Syst. Sci. Cyber.* 4 (2), pp. 100–107. DOI: 10.1109/TSSC.1968.300136.

Hayne, Paul O.; Hendrix, Amanda; Sefton-Nash, Elliot; Siegler, Matthew A.; Lucey, Paul G.; Retherford, Kurt D. et al. (2015): Evidence for exposed water ice in the Moon’s south polar regions from Lunar Reconnaissance Orbiter ultraviolet albedo and temperature measurements. In *Icarus* 255, pp. 58–69. DOI: 10.1016/j.icarus.2015.03.032.

Hayne, Paul O.; Bandfield, Joshua L.; Siegler, Matthew A.; Vasavada, Ashwin R.; Ghent, Rebecca R.; Williams, Jean-Pierre et al. (2017): Global Regolith Thermophysical Properties of the Moon From the Diviner Lunar Radiometer Experiment. In *J. Geophys. Res. Planets* 122 (12), pp. 2371–2400. DOI: 10.1002/2017JE005387.

Heiken, Grant (1995): Lunar sourcebook. A user's guide to the moon. Reprinted. Cambridge [u.a.]: Cambridge Univ. Press.

Heldmann, Jennifer L.; Colaprete, Anthony; Elphic, Richard C.; Bussey, Ben; McGovern, Andrew; Beyer, Ross et al. (2016): Site selection and traverse planning to support a lunar polar rover mission. A case study at Haworth Crater. In *Acta Astronautica* 127, pp. 308–320. DOI: 10.1016/j.actaastro.2016.06.014.

Hemingway, B. S.; Krupka, K. M.; Robie, R. A. (1981): Heat capacities of the alkali feldspars between 350 and 1000 K from differential scanning calorimetry, the thermodynamic functions of the alkali feldspars from 298.15 to 1400 K, and the reaction quartz + jadeite = analbite. In *American Mineralogist* 66, pp. 1202–1215.

Holstein-Rathlou, C.; Gunnlaugsson, H. P.; Merrison, J. P.; Bean, K. M.; Cantor, B. A.; Davis, J. A. et al. (2010): Winds at the Phoenix landing site. In *J. Geophys. Res.* 115 (12), E00A03. DOI: 10.1029/2009JE003411.

Horai, K.; Simmons, G.; Kanamori, H.; Wones, D. (1970): Thermal diffusivity, conductivity and thermal inertia of Apollo 11 lunar material. In : Proceedings of the Apollo 11 Lunar Science Conference, p. 2243.

Horai, Ki-Iti; Fujii, Naoyuki (1972): Thermophysical properties of lunar material returned by Apollo missions. In *The Moon* 4 (3-4), pp. 447–475. DOI: 10.1007/BF00562011.

Hoshino, Takeshi; Hashimoto, Tatsuaki; Wakabayashi, Sachiko; Ohtake, Makiko; Otake, Hisashi; Morimoto, Hitoshi et al. (2017): Japanese Lunar Polar Exploration Mission—SELENE-R. In : 68th International Astronautical Congress.

Incropera, Frank P. (2007): Fundamentals of Heat and Mass Transfer. WITH IHT/FEHT 3.0 CD-ROM with User Guide. 6 Aufl. [Erscheinungsort nicht ermittelbar]: John Wiley & Sons Ltd.

ISECG (2018): The Global Exploration Roadmap. Available online at https://www.globalspaceexploration.org/wordpress/wp-content/isecg/GER_2018_small_mobile.pdf.

ISRO (2019): Chandrayaan2 Spacecraft - ISRO. Available online at https://www.isro.gov.in/chandrayaan2-spacecraft#spacecraft-pg, checked on 10/15/2019.

Jaeger, J. C.; Harper, A. F. A. (1950): Nature of the Surface of the Moon. In *Nature* 166 (4233), p. 1026. DOI: 10.1038/1661026a0.

Jaeger, J. C. (1953): The Surface Temperature of the Moon. In *Aust. J. Phys.* 6 (1), p. 10. DOI: 10.1071/PH530010.

Johnson, A. W.; Newman, D. J.; Waldie, J. M.; Hoffman, Jeffrey (2009): An EVA Mission Planning Tool based on Metabolic Cost Optimization. DOI: 10.4271/2009-01-2562.

Johnson, Francis S.; Carrol, James M. (1972): Lunar atmosphere measurements. In : Proceedings of the Third Lunar Science Conference.

Jones, Harry W. (2017): How Should Life Support Be Modeled and Simulated? In : 47th International Conference on Environmental Systems.

Kieffer, Hugh H. (2013): Thermal model for analysis of Mars infrared mapping. In *J. Geophys. Res. Planets* 118 (3), pp. 451–470. DOI: 10.1029/2012JE004164.

Killian, M.; Fisackerly, R. (2017): Thermal Environment for the Lunar Volatile Prospector Mission. In : 47th International Conference on Environmental Systems.

Koenig, S.; Likhachev, M. (2002a): D* Lite. In : Proceedings of the National Conference on Artificial Intelligence.

Koenig, S.; Likhachev, M. (2002b): Improved fast replanning for robot navigation in unknown terrain. In : Proceedings of the 2002 IEEE International Conference on Robotics & Automation. Washington, DC, pp. 968–975.

Koenig, S.; Likhachev, M. (2002c): Incremental A*. In : Advances in Neural Information Processing Systems 14: MIT Press, pp. 1539–1546. Available online at http://papers.nips.cc/paper/2003-incremental-a.pdf.

Koubaa, Anis; Bennaceur, Hachemi; Chaari, Imen; Trigui, Sahar; Ammar, Adel; Sriti, Mohamed-Foued et al. (2018): Robot Path Planning and Cooperation. Foundations, Algorithms and Experimentations. 1st edition 2018. Cham: Springer International Publishing (Studies in Computational Intelligence, 772).

Krotikov, V. D., and Shchuko, O. B. (1963): The Heat Balance of the Lunar Surface Layer During a Lunation. In *Soviet Astronomy* 7, pp. 228–232.

Leader, Mark K.; Rege, Rushal N.; Potts, Nicola J.; Gullikson, Amber L.; Curran, Natalie M.; Dhaliwal, Jasmeet K.; Kring, David A. (2014): Velocity of a Rover as a function of Slope of Lunar Terrrain. In : 45th Lunar and Planetary Science Conference.

Ledlow, Michael J.; Zeilik, Michael; Burns, Jack O.; Gisler, Galen R.; Zhao, Jun-Hui; Baker, Daniel N. (1992): Subsurface emissions from Mercury - VLA radio observations at 2 and 6 centimeters. In *ApJ* 384, p. 640. DOI: 10.1086/170906.

Leovy, C. (2001): Weather and climate on Mars. In *Nature* 412, pp. 245–249.

Ley, Wilfried; Wittmann, Klaus; Hallmann, Willi (Eds.) (2019): Handbuch der Raumfahrttechnik. 5., aktualisierte und erweiterte Auflage. München: Hanser (Aerospace Series, v.22).

Li, Chunlai; Liu, Jianjun; Ren, Xin; Zuo, Wei; Tan, Xu; Wen, Weibin et al. (2015): The Chang'e 3 Mission Overview. In *Space Sci Rev* 190 (1-4), pp. 85–101. DOI: 10.1007/s11214-014-0134-7.

Li, Chunlai; Wang, Chi; Wei, Yong; Lin, Yangting (2019): China's present and future lunar exploration program. In *Science (New York, N.Y.)* 365 (6450), pp. 238–239. DOI: 10.1126/science.aax9908.

Lindemann R. A.; Bickler D. B.; Harrington B.D.; Ortiz G. M.; Voorhees C. J. (2006): Mars Exploration Rover Mobility Development. In *IEEE Robotics & Automation Magazine*.

Linsky, Jeffrey L. (1966): Models of the lunar surface including temperature-dependent thermal properties. In *Icarus* 5 (1-6), pp. 606–634. DOI: 10.1016/0019-1035(66)90075-3.

Li, Shuai; Lucey, Paul G.; Milliken, Ralph E.; Hayne, Paul O.; Fisher, Elizabeth; Williams, Jean-Pierre et al. (2018): Direct evidence of surface exposed water ice in the lunar polar regions. In *Proceedings of the*

National Academy of Sciences of the United States of America 115 (36), pp. 8907–8912. DOI: 10.1073/pnas.1802345115.

Litvak, Maxim (2016): The vision of the Russian Space Agency on the robotic settlements in the Moon. Roscosmos.

Mazarico, Erwan; Barker, Michael K.; Nicholas, Joseph B. (2018): Advanced Illumination Modeling for Data Analysis and Calibration. Application to the Moon. In *Advances in Space Research. DOI:* 10.1016/j.asr.2018.08.022.

Menzel, D. H. (1969): Temperature Distribution of the Moon. In : Discussion on Infrared Astronomy, pp. 141–144.

Mitchell, J. K.; Scott, R. F.; Houston, W. N.; Costes, N. C.; Carrier, W. D., III; Bromwell, L. G. (1972): Mechanical properties of lunar soil - Density, porosity, cohesion, and angle of internal friction. In : Proceedings of the Third Lunar Science Conference, pp. 3235–3253.

Murdoch, Naomi; Mimoun, David; Garcia, Raphael F.; Rapin, William; Kawamura, Taichi; Lognonné, Philippe et al. (2017): Evaluating the Wind-Induced Mechanical Noise on the InSight Seismometers. In *Space Sci Rev* 211 (1-4), pp. 429–455. DOI: 10.1007/s11214-016-0311-y.

Mutch, Thomas A. (1972): Geology of the moon. A stratigraphic view. Princeton: Princeton University Press.

NASA (2019a): Artemis Moon Program Advances -The Story So Far. Available online at https://www.nasa.gov/artemis-moon-program-advances, checked on 10/31/2019.

NASA (2019b): New VIPER Lunar Rover to Map Water Ice on the Moon. Available online at https://www.nasa.gov/feature/new-viper-lunar-rover-to-map-water-ice-on-the-moon, checked on 10/29/2019.

Novak, Keith S.; Phillips, Charles J.; Birur, Gajanana C.; Sunada, Eric T.; Pauken, Michael T. (2003): Development of a Thermal Control Architecture for the Mars Exploration Rovers. In : Space Technology Applications International Forum. Albuquerque, New Mexico (USA), 2-6 February 2003.

Novak, Keith S. (2003): Development of a Thermal Control Architecture for the Mars Exploration Rovers. In : SPACE TECHNOLOGY AND APPLICATIONS INT.FORUM-STAIF 2003: Conf.on Thermophysics in Microgravity; Commercial/Civil Next Generation Space Transportation; Human Space Exploration; Symps.on Space Nuclear Power and Propulsion (20th); Space Colonization (1st). Albuquerque, New Mexico (USA), 2-5 February 2003, pp. 194–205.

Novak, Keith S.; Phillips, Charles J.; Sunada, Eric T.; Kinsella, Gary M. (2005): Mars Exploration Rover Surface Mission Flight Thermal Performance. In : International Conference On Environmental Systems, JUL. 11, 2005: SAE International400 Commonwealth Drive, Warrendale, PA, United States (SAE Technical Paper Series).

Novak, Keith S.; Kempenaar, Joshua; Liu, Yuanming; Bhandari, Pradeep; Lee, Chern-Jiin (2013): Thermal Performance of the Mars Science Laboratory Rover During Mars Surface Operations. In : 43rd International Conference on Environmental Systems. Vail, CO.

Novak, Keith S.; Kempenaar, Joshua; Redmon, M.; Bhandari, Pradeep (2014): Preliminary Surface Thermal Design of the Mars 2020 Rover. In : 44th International Conference on Environmental Systems. Tucson, Wa.

Otten, Nathan D.; Jones, Heather L.; Wettergreen, David S.; Whittaker, William L. (2015): Planning routes of continuous illumination and traversable slope using connected component analysis. In : 2015 IEEE International Conference on Robotics and Automation (ICRA). 2015 IEEE International Conference on Robotics and Automation (ICRA). Seattle, WA, USA, 26.05.2015 - 30.05.2015: IEEE, pp. 3953–3958.

Otten, Nathan D. (2018): Planning for Sun-Synchronous Lunar Polar Roving. PhD Thesis. Carnegie Mellon University, Pittsburgh, PA.

Padma, T. V. (2019): India's Chandrayaan-2 mission to the Moon set for launch. In *Physics World* 32 (7), p. 8. DOI: 10.1088/2058-7058/32/7/11.

Paige, D. A.; Foote, M. C.; Greenhagen, B. T.; Schofield, J. T.; Calcutt, S.; Vasavada, A. R. et al. (2010a): The Lunar Reconnaissance Orbiter Diviner Lunar Radiometer Experiment. In *Space Sci Rev* 150 (1-4), pp. 125–160. DOI: 10.1007/s11214-009-9529-2.

Paige, David A.; Siegler, Matthew A.; Zhang, Jo Ann; Hayne, Paul O.; Foote, Emily J.; Bennett, Kristen A. et al. (2010b): Diviner Lunar Radiometer observations of cold traps in the Moon's south polar region. In *Science (New York, N.Y.)* 330 (6003), pp. 479–482. DOI: 10.1126/science.1187726.

Pettit, E.; Nicholson, S. B. (1930): Lunar radiation and temperatures. In *ApJ* 71, p. 102. DOI: 10.1086/143236.

Piddington, J. H.; Minnett, H. C. (1949): Microwave Thermal Radiation from the Moon. In *Australian Journal of Scientific Research A* (vol. 2), p.63.

Polifke, Wolfgang (2009): Wärmeübertragung. Grundlagen, analytische und numerische Methoden. 2., aktualisierte Aufl., [Nachdr.]. München [u.a.]: Pearson Deutschland GmbH (Ing).

Potts, Nicola J.; Gullikson, Amber L.; Curran, Natalie M.; Dhaliwal, Jasmeet K.; Leader, Mark K.; Rege, Rushal N. et al. (2015): Robotic traverse and sample return strategies for a lunar farside mission to the Schrödinger basin. In *Advances in Space Research* 55 (4), pp. 1241–1254. DOI: 10.1016/j.asr.2014.11.028.

Ramalingam, G.; Reps, Thomas (1996): An Incremental Algorithm for a Generalization of the Shortest-Path Problem. In *Journal of Algorithms* 21 (2), pp. 267–305. DOI: 10.1006/jagm.1996.0046.

Rana, Hannah; Laneve, Vito; Hager, Philipp; Tirolien, Thierry (2017): Thermal Modelling of Luna 27 Landing Site. In : 31st European Space Thermal Analysis Workshop, 24–25 October.

Robie, R. A.; Hemingway, B. S.; Wilson, W. H. (1970): Specific heats of lunar surface materials from 90 to 350 degrees Kelvin. In *Science (New York, N.Y.)* 167 (3918), pp. 749–750. DOI: 10.1126/science.167.3918.749.

Šeda, Miloš (2007): Roadmap Methods vs. Cell Decomposition in Robot Motion Planning. In : Proceedings of the 6th WSEAS International Conference on Signal Processing, Robotics and Automation. Corfu Island, February 16 - 19.

Sefton-Nash, E.; Williams, J.-P.; Greenhagen, B. T.; Aye, K.-M.; Paige, D. A. (2017): Diviner lunar radiometer gridded brightness temperatures from geodesic binning of modeled fields of view. In *Icarus* 298, pp. 98–110. DOI: 10.1016/j.icarus.2017.04.007.

Sierra Nevada Corporation (2018): Space Technologies Product Catalog. Available online at https://www.sncorp.com/media/2725/snc-space-technologies-catalog-2019.pdf, checked on 9/25/2019.

Smart, Marshall C.; Ratnakumar, Bugga V.; Ewell, Richard C.; Surampudi, Subbarao; Puglia, Frank J.; Gitzendanner, Rob (2018): The use of lithium-ion batteries for JPL's Mars missions. In *Electrochimica Acta* 268, pp. 27–40. DOI: 10.1016/j.electacta.2018.02.020.

Speyerer, E. J.; Lawrence, S. J.; Stopar, J. D.; Gläser, P.; Robinson, M. S.; Jolliff, B. L. (2016): Optimized traverse planning for future polar prospectors based on lunar topography. In *Icarus* 273, pp. 337–345. DOI: 10.1016/j.icarus.2016.03.011.

Steenstra, Edgar S.; Martin, Dayl J.P.; McDonald, Francesca E.; Paisarnsombat, Sarinya; Venturino, Christian; O'Hara, Sean et al. (2016): Analyses of robotic traverses and sample sites in the Schrödinger basin for the HERACLES human-assisted sample return mission concept. In *Advances in Space Research* 58 (6), pp. 1050–1065. DOI: 10.1016/j.asr.2016.05.041.

Stella, P. M.; Ewell, R. C.; Hoskin, J. J. (2005): Design and performance of the MER (Mars Exploration Rovers) solar arrays. Coronado Springs Resort, Lake Buena Vista, FL, January 3-7, 2005. In :

Conference Record of the Thirty-first IEEE Photovoltaic Specialists Conference, pp. 626–630. Available online at http://ieeexplore.ieee.org/servlet/opac?punumber=9889.

Stentz; Anthony (2002): CD*: A Real-Time Resolution Optimal Re-Planner for Globally Constrained Problems. In : Proceedings of the Eighteenth National Conference on Artfi- cial Intelligence (AAAI-02).

Stentz, A. (1994): Optimal and Efficient Path Planning for Partially-Known Environments. In : Proceedings IEEE International Conference on Robotics and Automation. 94th ed., pp. 3310–3317.

The Planetary Society (2019): Beresheet Comes Close before Crashing on the Moon | The Planetary Society. Available online at http://www.planetary.org/blogs/jason-davis/beresheet-comes-close-crashes.html, checked on 10/15/2019.

The Times of India (2019): India's next Moon shot will be bigger, in pact with Japan - Times of India. Available online at https://timesofindia.indiatimes.com/india/indias-next-moon-shot-will-be-bigger-in-pact-with-japan/articleshow/71030437.cms, updated on 9/8/2019, checked on 10/15/2019.

Tompkins, P. (2005): Mission-Directed Path Planning for Planetary Rover Exploration. Carnegie Mellon University, Pittsburgh, PA. The Robotics Institute.

Trautner, R.; Barber, S. J.; Carpenter, J.; Fisackerly, R.; Houdou, B.; Leese, M. et al. (2018): PROSPECT: A Novel Package for Subsurface Sample Acquisition and Analysis of Lunar Volatiles. In : 69th International Astronautical Congress.

van Winnendael, M.; Baglioni, P.; Vago, J. (2005): Development of the ESA ExoMars rover. In : Proc. of 'The 8th International Symposium on Artifical Intelligence, Robotics and Automation in Space - iSAIRAS’.

Vasavada, A.; Paige, David A.; Wood, Stephen, E. (1999): Near-Surface Temperatures on Mercury and the Moon and the Stability of Polar Ice Deposits. In *Icarus* 141 (2), pp. 179–193. DOI: 10.1006/icar.1999.6175.

Vasavada, Ashwin R.; Chen, Allen; Barnes, Jeffrey R.; Burkhart, P. Daniel; Cantor, Bruce A.; Dwyer-Cianciolo, Alicia M. et al. (2012a): Assessment of Environments for Mars Science Laboratory Entry, Descent, and Surface Operations. In *Space Sci Rev* 170 (1-4), pp. 793–835. DOI: 10.1007/s11214-012-9911-3.

Vasavada, Ashwin R.; Bandfield, Joshua L.; Greenhagen, Benjamin T.; Hayne, Paul O.; Siegler, Matthew A.; Williams, Jean-Pierre; Paige, David A. (2012b): Lunar equatorial surface temperatures and regolith properties from the Diviner Lunar Radiometer Experiment. In *J. Geophys. Res.* 117 (E12), n/a-n/a. DOI: 10.1029/2011JE003987.

Walker J. (2017): Final Configuration of the ispace Hakuto Rover for a Google Lunar XPrize Mission. In : 68th International Astronautical Congress.

Warren, T.; King, O.; Bowles, N. E.; Sefton-Nash, E.; Fisackerly, R.; Trautner, R. (2019): The Oxford 3D Thermophysical Model with application to the Lunar PROSPECT Mission. In : 50th Lunar and Planetary Science Conference.

Watkins, M.; Steltzner. A (2007): MSL Landing Site Selection: Status of Engineering Capabilities and Constraints and Plan for Site Selection. In : 2nd MSL Landing Site Selection Workshop. Pasadena, CA, 23 - 25 October.

Welch, Richard; Limonadi, Daniel; Manning, Robert (2013): Systems engineering the Curiosity Rover. A retrospective. In : 2013 8th International Conference on System of Systems Engineering. 2013 8th International Conference on System of Systems Engineering (SoSE). Maui, HI, USA, 02.06.2013 - 06.06.2013: IEEE, pp. 70–75.

Wesselink, A. J. (1948): Heat conductivity and nature of the lunar surface material. In *Bulletin of the Astronomical Institutes of the Netherlands* 10, pp. 351–363.

Williams, J.-P.; Paige, D. A.; Greenhagen, B. T.; Sefton-Nash, E. (2017): The global surface temperatures of the Moon as measured by the Diviner Lunar Radiometer Experiment. In *Icarus* 283, pp. 300–325. DOI: 10.1016/j.icarus.2016.08.012.

Winter, D. F. (1967): Transient radiative heat exchange at the surface of the moon. In *Icarus* 6 (1-3), pp. 229–235. DOI: 10.1016/0019-1035(67)90019-X.

Winter, D. F.; Saari, J. M. (1969): A Particulate Thermophysical Model of the Lunar Soil. In *ApJ* 156, p. 1135. DOI: 10.1086/150041.

Wöhler, Christian; Grumpe, Arne; Berezhnoy, Alexey A.; Feoktistova, Ekaterina A.; Evdokimova, Nadezhda A.; Kapoor, Karan; Shevchenko, Vladislav V. (2017): Temperature regime and water/hydroxyl behavior in the crater Boguslawsky on the Moon. In *Icarus* 285, pp. 118–136. DOI: 10.1016/j.icarus.2016.12.026.

Wu, Peng; Ju, Hehua (2013): Mission-Integrated Path Planning for Planetary Rover Exploration. In *JSW* 8 (10). DOI: 10.4304/jsw.8.10.2620-2627.

8.2 List of Publications

First author publications

Killian, M. and Reiss, P. (2015): Investigating thermal aspects of lunar traverses for scientific exploration. European Lunar Symposium

Killian, M. and Hager, P. B. (2015): Traverse Planning on the Lunar Surface – Benefits from Thermal Modeling. 45th International Conference on Environmental Systems.

Killian, M. and Fisackerly, R. (2017): Thermal Environment for the Lunar Volatile Prospector Mission. 47th International Conference on Environmental Systems.

Killian, M. (2017): Thermal simulation of a rover traverse at the lunar south pole. European Lunar Symposium

Co-author publications

Cusick, A.; Killian, M.; Olthoff, C. (2016): Integrated EVA Thermal Simulations using TherMoS and V SUIT. 46th International Conference on Environmental Systems.

Gscheidle, C. and Killian, M. (2017): Mars Rover – Limits of Thermal Design. 47th International Conference on Environmental Systems.

Janzer, K.; Killian, M.; Langer, M.; Krejcib, D.; Reissner, A. (2018): Thermal Control of Higher Power Applications on CubeSats, 69th International Astronautical Congress.

Volland, D.; Rüth, B.; Killian, M.; Uekermann, B. (2019): Parallel coupling for TherMoS with preCICE. VIII International Conference on Coupled Problems in Science and Engineering.

Urbina, D. A.; Madakashiraa, H. K.M.; Golia, M.; Chailleta, C.; Durnaa, M.; Arnett, C.; Vandevelde, B.; Killian, M.; Trautner, R. (2019): Low Temperature Technologies and Architecture for Extreme Environments. 70th International Astronautical Congress.

8.3 List of Supervised Theses

Lidel, Stephan (2014): Modellierung der Wärmeübertragung durch Multilayer-Insulation (MLI). RT-BA 2014/15, Bachelor Thesis, Technical University of Munich

Steinbacher, Maximilian (2015): Thermo-Opto-Mechanische Testvorhersage für einen geostationären Satelliten. RT-MA 2015/02, Master Thesis, Technical University of Munich

Asen-Hübner, Joshua (2016): Stand-off Design zur Befestigung von Multi-Layer Insulation. RT-BA 2015/20,

Bachelor Thesis, Technical University of Munich

Agabekov, Samir (2015): Design and Layout of Multi-Layer-Insulation. RT-BA 2015/19, Bachelor Thesis, Technical University of Munich

Sievers, Martin (2015): Multi-Layer-Insulation Performance Testbed. RT-MA 2015/07, Master Thesis, Technical University of Munich

Scheurich, Volker (2016): Conceptual Study of the Mobility Systems of Planetary Exploration Vehicles. RT-SA 2016/05, Semester Thesis, Technical University of Munich

Traub, Constantin (2016): Analysis of the influence of scaling factors on the results of ray tracing in ESATAN-TMS. RT-SA 2016/01, Semester Thesis, Technical University of Munich

Steinweg, Dominik (2016): Thermaldesign einer Remote Unit auf dem Mond. RT-SA 2016/08, Semester Thesis, Technical University of Munich

Matz, Maximilian (2016): Adaptives Steady State Simulation Model for Loop Heat Pipes. RT-SA 2016/03, Semester Thesis, Technical University of Munich

Bosch, Colin (2016): Einsatz von LHP und CPL in Raumfahrzeugen. RT-SA 2016/04, Semester Thesis, Technical University of Munich

Uhl, Gregory (2016): Thermal model for local regions on the surface of Mars. RT-BA 2016/09, Bachelor Thesis, Technical University of Munich

Fleck, Andreas (2016): Design, Herstellung und Qualifikation einer neuen Referenzstelle für hochstabile Temperaturmessung mit Thermoelementen in der Weltraumsimulation und Analyse der bestehenden Messkette. RT-MA 2016/07, Master Thesis, Technical University of Munich

Gscheidle, Christian (2017): Limits of passive thermal design on Martian rovers. RT-SA 2016/10, Semester Thesis, Technical University of Munich

Hartmüller, Philipp (2017): Instrumentation for a Loop Heat Pipe Test Bench. RT-SA 2017/18, Semester Thesis, Technical University of Munich

Matz, Maximilian (2018): Solar Illumination Tool. RT-MA 2017/30, Master Thesis, Technical University of Munich

Janzer, Katja (2018): Thermalkontrolle für Cubesats . RT-MA 2017/24, Master Thesis, Technical University of Munich

Junker, Jan (2018): Parametric Analysis of Internal Heat Paths for Variable Emissivity Space Suits. RT-MA 2018/17, Master Thesis, Technical University of Munich

AlHasni, Mohammad (2018): Multi-GPU parallelization of a dynamic heat transfer model on the Moon. Master Thesis, Technical University of Munich

Hartmüller, Philipp (2018): Design and Demonstration of a Miniaturized Lyophilizer Prototype for Spaceflight Science Applications. RT-MA 2018/11, Master Thesis, Technical University of Munich

Volland, Dominik (2019): Coupling TherMoS with preCICE. Master Thesis, Technical University of Munich

Pluhár , Gabór (2019): Thermal Modeling Options in the Frame of FORUM. RT-MA 2019/17, Master Thesis, Technical University of Munich

Appendix A List of Figures and Tables

A.1 List of Figures

A.2 List of Tables

Appendix B LRO DLRE Instrument

The Diviner lunar radiometer experiment on board LRO measures “reflected solar and emitted infrared radiation in nine spectral channels with wavelengths ranging from 0.3 micron to 400 microns” (Paige et al. 2010a). It is a radiometer with “nine 21-element thermopile detector arrays, each with a separate spectral filter. The instrument will predominantly point in the nadir direction, operating as a multi-spectral pushbroom mapper “ (Paige et al. 2010a). Figure 66 shows the wavelength of the nine detector arrays. Figure 67 highlights the focal plane layout of the telescope.

The accuracy of all channels depends the temperature of the radiating surface (Paige et al. 2010a). It lies in a range between less than 1 K and up to 10 K. Average accuracy over all channels measuring temperatures is about 5 K.

Measurements from DLRE are available at NASA’s PDS node. Data can be accessed as their raw measured values up to calibrated and derived products such as gridded maps and special polar products. In the context of temperature comparison in this thesis, the calibrated radiance transferred into brightness temperature of each detector is the required value. This data is available as level 1 reduced data record.

Conversion between radiance and brightness temperature is done with inverse Planck function. However, this is most precise if the wavelength of the measured radiance falls in the vicinity of the peak of the black body radiation for a specific temperature.

It is also possible to derive an, integrated temperature value from DLRE data.

“The bolometric brightness temperature T_{BOL} is the measure of the spectrally integrated flux of infrared radiation emerging from the surface. It is computed from the measured brightness temperatures in Diviner infrared channels as follows:

$$\sigma T_{BOL}^4 = \sum_{i=3}^{9} \sigma T_i^4 f(T_i, \lambda_1, \lambda_2) \tag{25}$$

Where T_i is the average radiance-weighted measured brightness temperature for a region in Diviner channel i, and:

$$f(T_i, \lambda_1, \lambda_2) = \frac{\int_{\lambda_1}^{\lambda_2} B(\lambda, T) d\lambda}{\int_0^{\infty} B(\lambda, T) d\lambda} \tag{26}$$

Where B(λ,T) is the Planck function of wavelength λ and temperature T “(Paige et al. 2010b). With values for λ_1 and λ_2 given in Table 13, T_{BOL} can be computed.

Table 13: Values to be used in Planck function in order to compute T_{BOL}. Adapted from: (Paige et al. 2010b)

Diviner Channel	3	4	5	6	7	8	9
λ_1 [µm]	0.000	8.075	8.40	13	25	50	100
λ_2 [µm]	8.075	8.400	13.00	25	50	100	1000
Λ_{min} [µm]	7.550	8.100	8.38	13	25	50	100
λ_{max} [µm]	8.050	8.400	8.68	23	41	100	400
T_{min} [K]	190	190	180	95	60	40	-

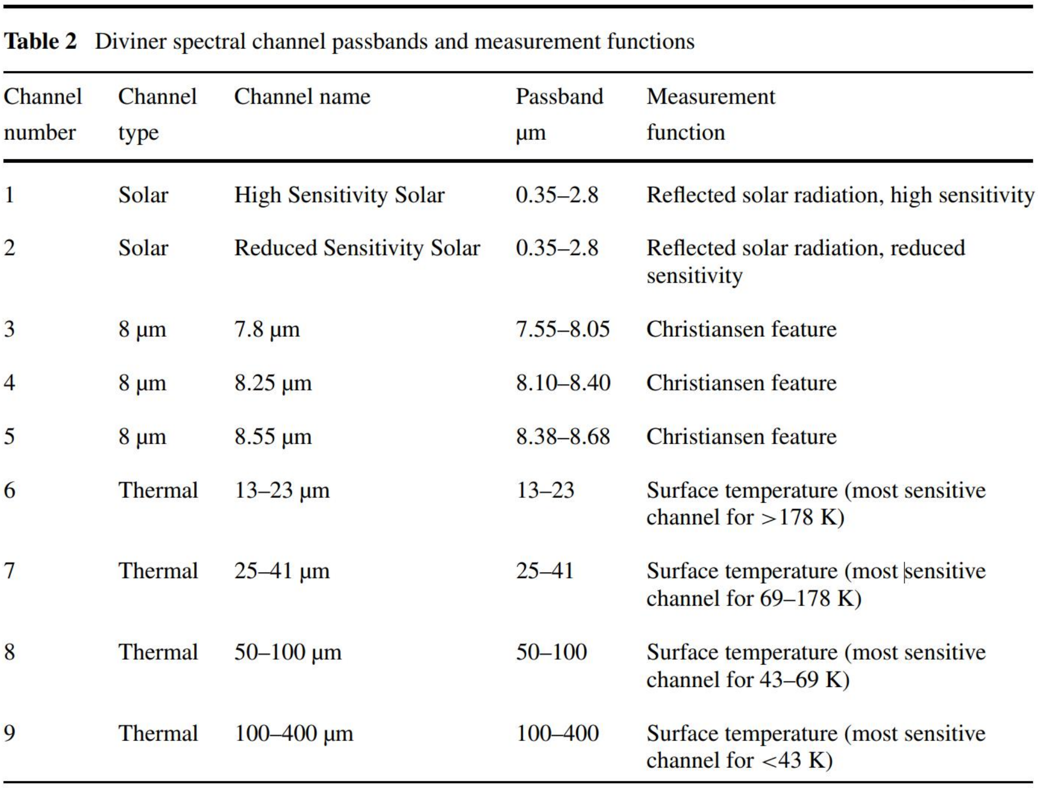

Table 2 Diviner spectral channel passbands and measurement functions

Channel number	Channel type	Channel name	Passband µm	Measurement function
1	Solar	High Sensitivity Solar	0.35–2.8	Reflected solar radiation, high sensitivity
2	Solar	Reduced Sensitivity Solar	0.35–2.8	Reflected solar radiation, reduced sensitivity
3	8 µm	7.8 µm	7.55–8.05	Christiansen feature
4	8 µm	8.25 µm	8.10–8.40	Christiansen feature
5	8 µm	8.55 µm	8.38–8.68	Christiansen feature
6	Thermal	13–23 µm	13–23	Surface temperature (most sensitive channel for >178 K)
7	Thermal	25–41 µm	25–41	Surface temperature (most sensitive channel for 69–178 K)
8	Thermal	50–100 µm	50–100	Surface temperature (most sensitive channel for 43–69 K)
9	Thermal	100–400 µm	100–400	Surface temperature (most sensitive channel for <43 K)

Figure 66: Diviner spectral channel passbands and measurements function. Image source: (Paige et al. 2010a)

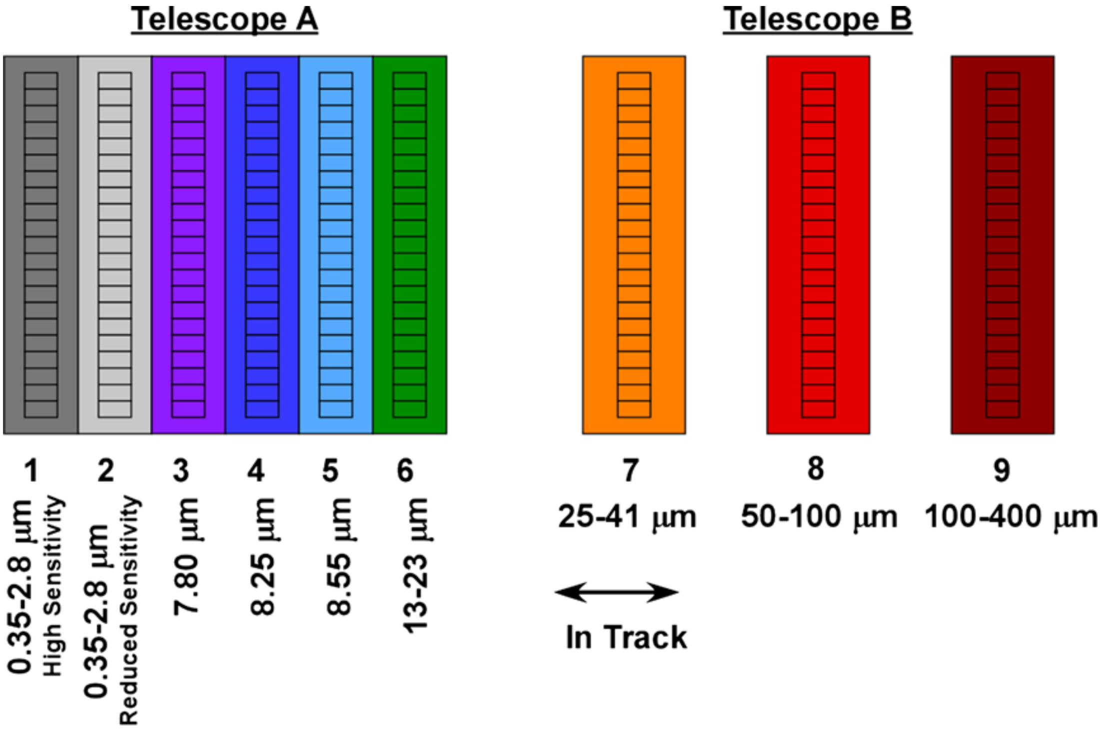

Figure 67: DLRE focal-plane layout. The two telescopes are co-boresighted but are separated in this figure for clarity. Image source: (Paige et al. 2010a)

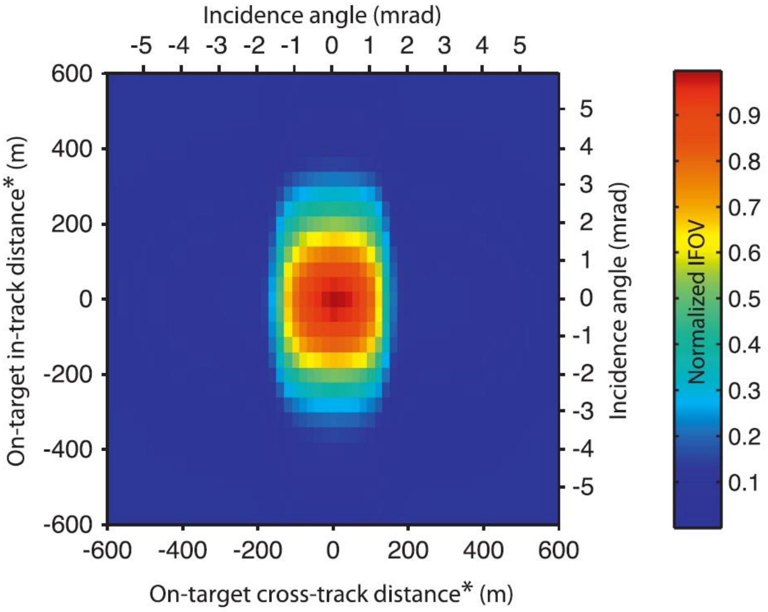

Figure 68: Field of view of one detector of DLRE assuming a height of 100 km and perpendicular view on surface. Image source: (Sefton-Nash et al. 2017)

Appendix C Sensitivity Results

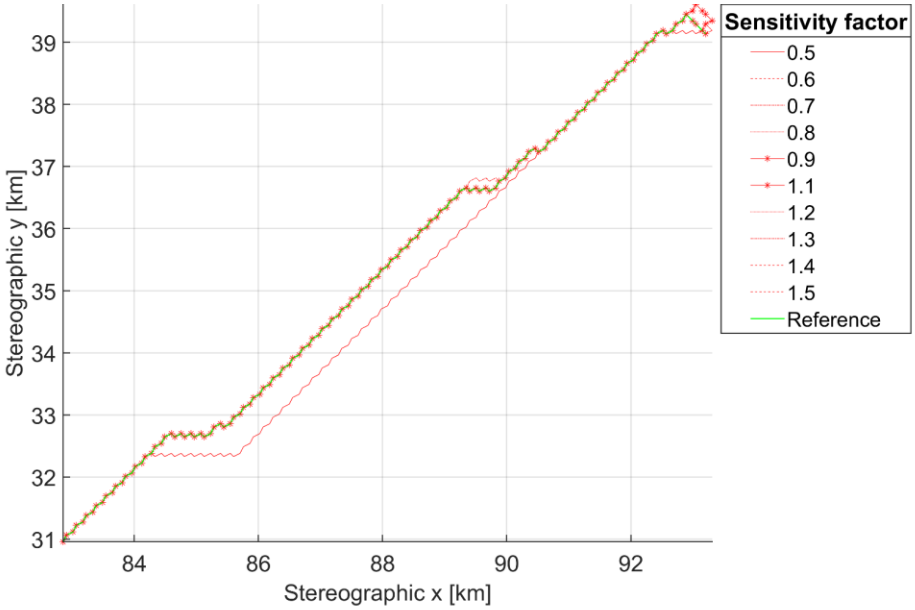

Figure 69: Traverses with different sensitivity factors applied on total power for driving. Battery capacity is 70 W h, LVP site

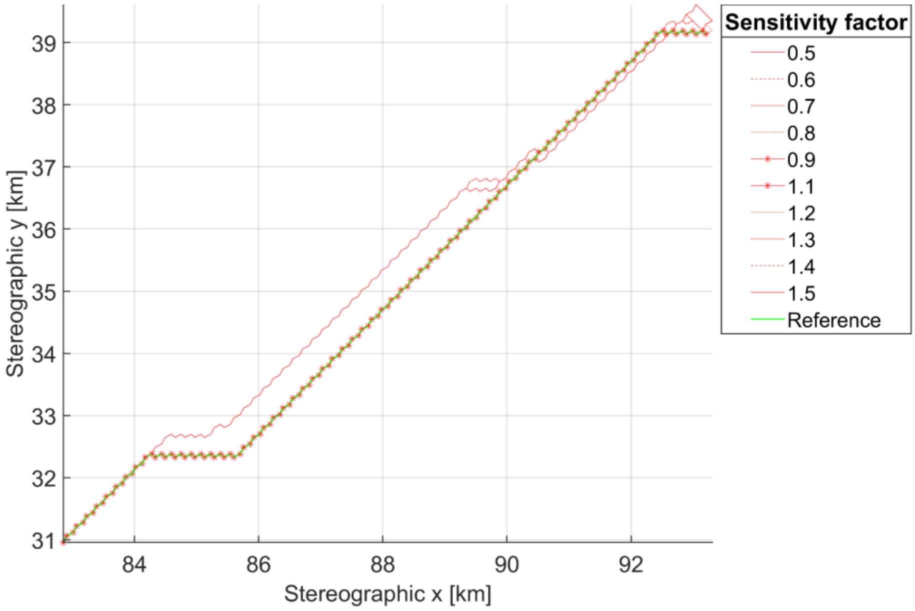

Figure 70: Traverses with different sensitivity factors applied on total power for driving. Battery capacity is 110 W h, LVP site

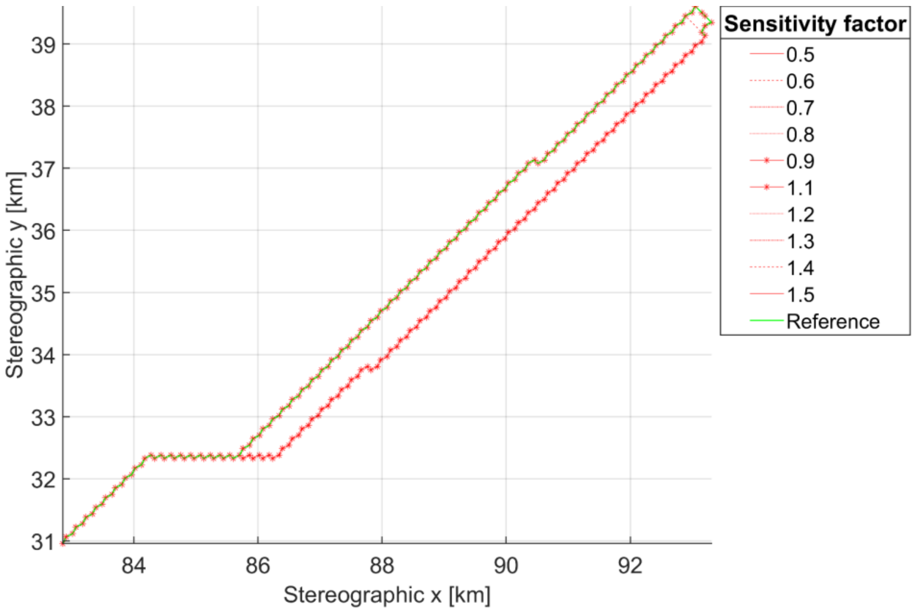

Figure 71: Traverses with different sensitivity factors applied on total power for driving. Battery capacity is 250 W h, LVP site

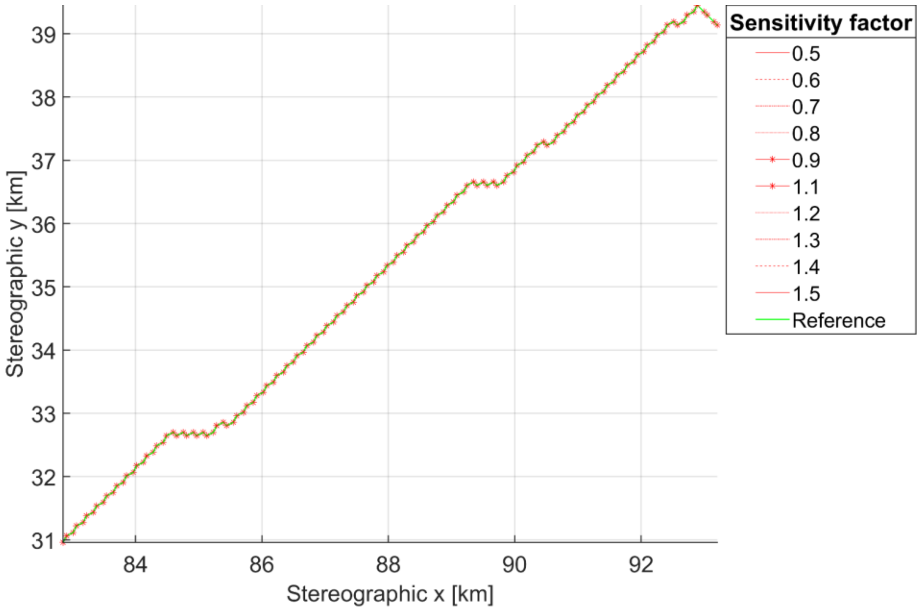

Figure 72: Traverses with different sensitivity factors applied on power for driving on slope. Battery capacity is 70 W h, LVP site

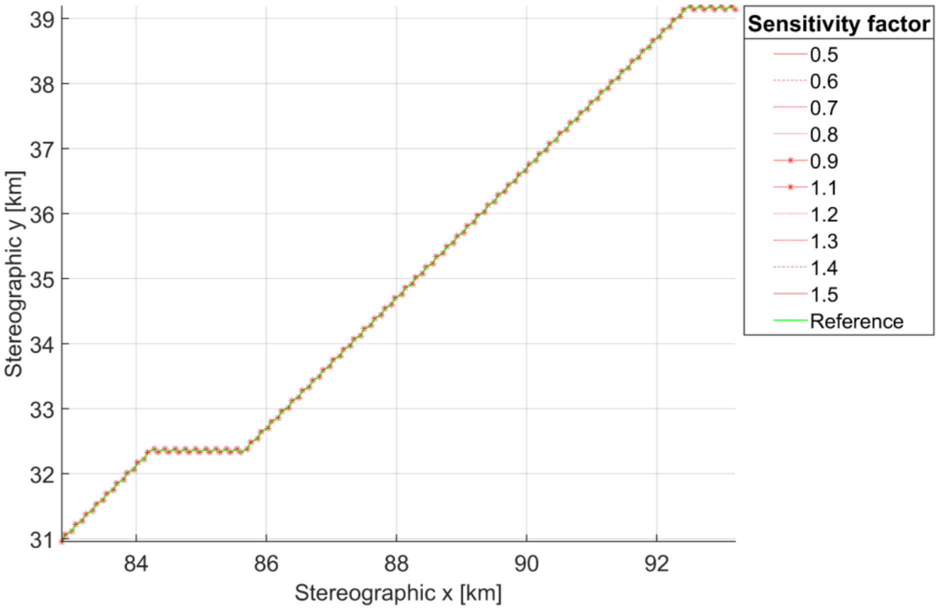

Figure 73: Traverses with different sensitivity factors applied on power for driving on slope. Battery capacity is 110 W h, LVP site

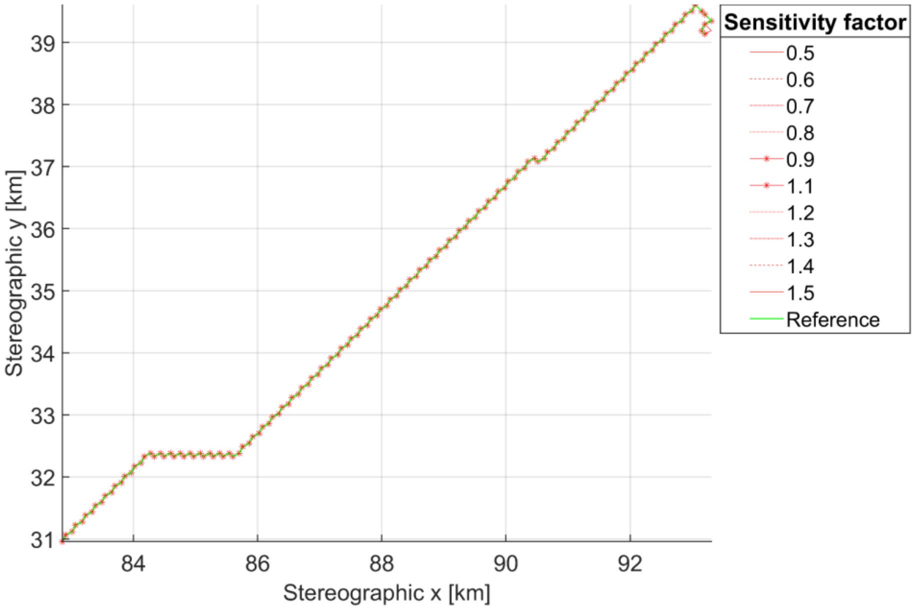

Figure 74: Traverses with different sensitivity factors applied on power for driving on slope. Battery capacity is 250 W h, LVP site

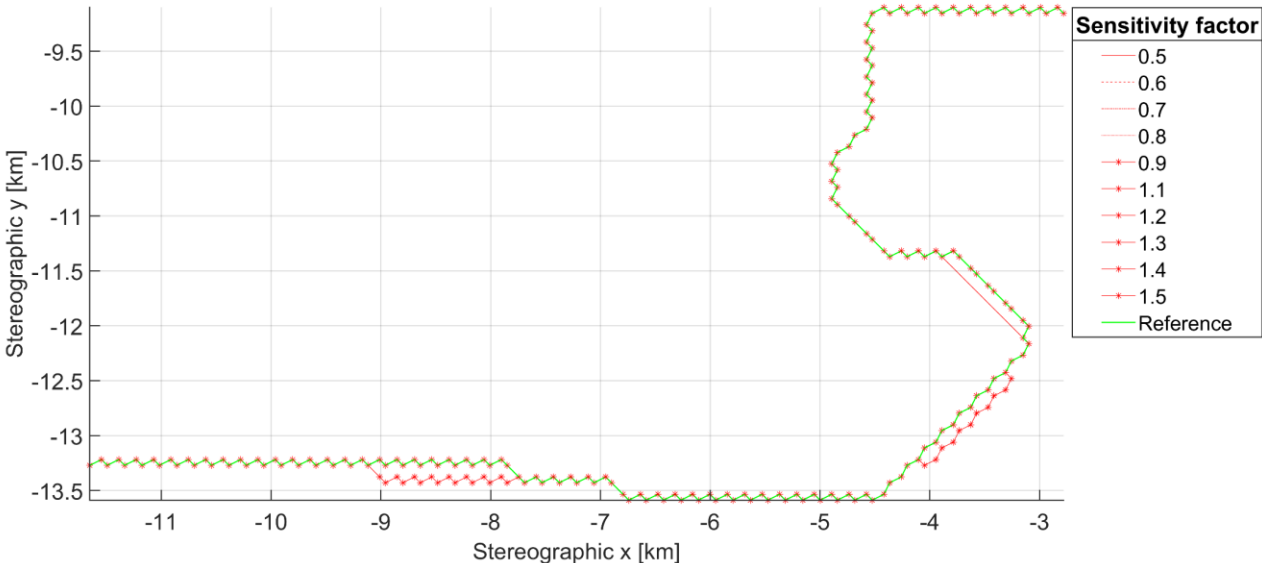

Figure 75: Traverses with different sensitivity factors applied on total power for driving. Battery capacity is 100 W h, Speyerer site

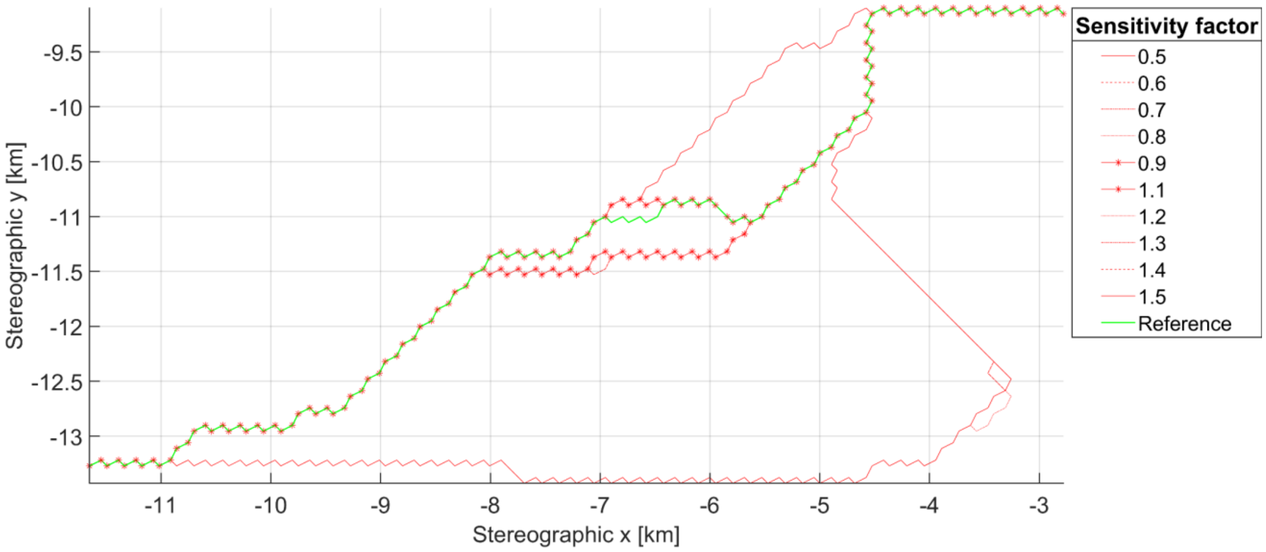

Figure 76: Traverses with different sensitivity factors applied on total power for driving. Battery capacity is 400 W h, Speyerer site

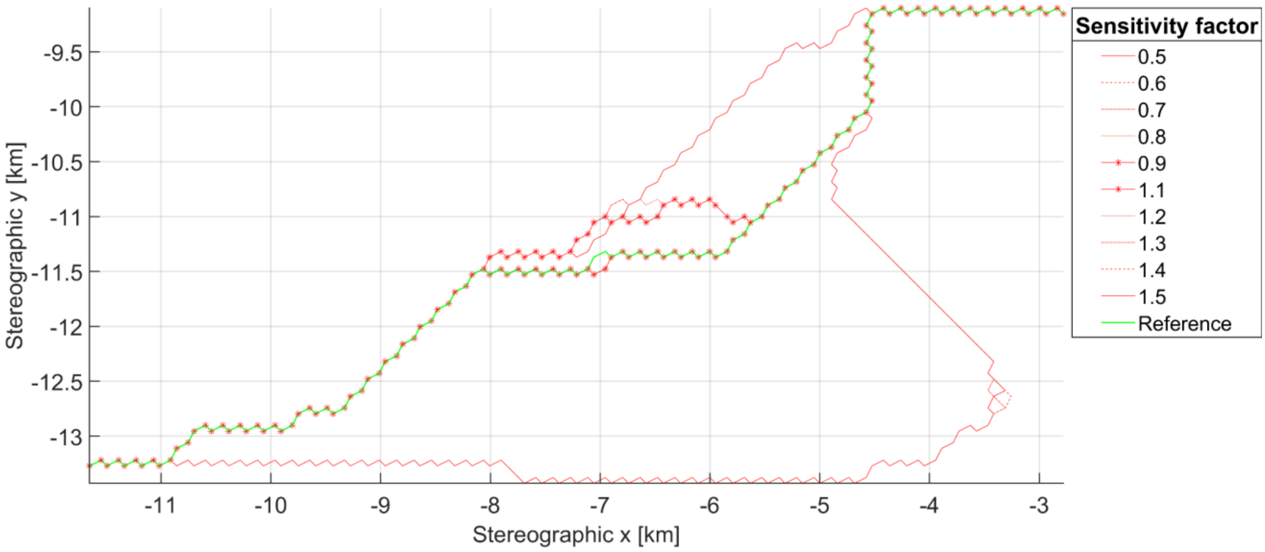

Figure 77: Traverses with different sensitivity factors applied on total power for driving. Battery capacity is 420 W h, Speyerer site

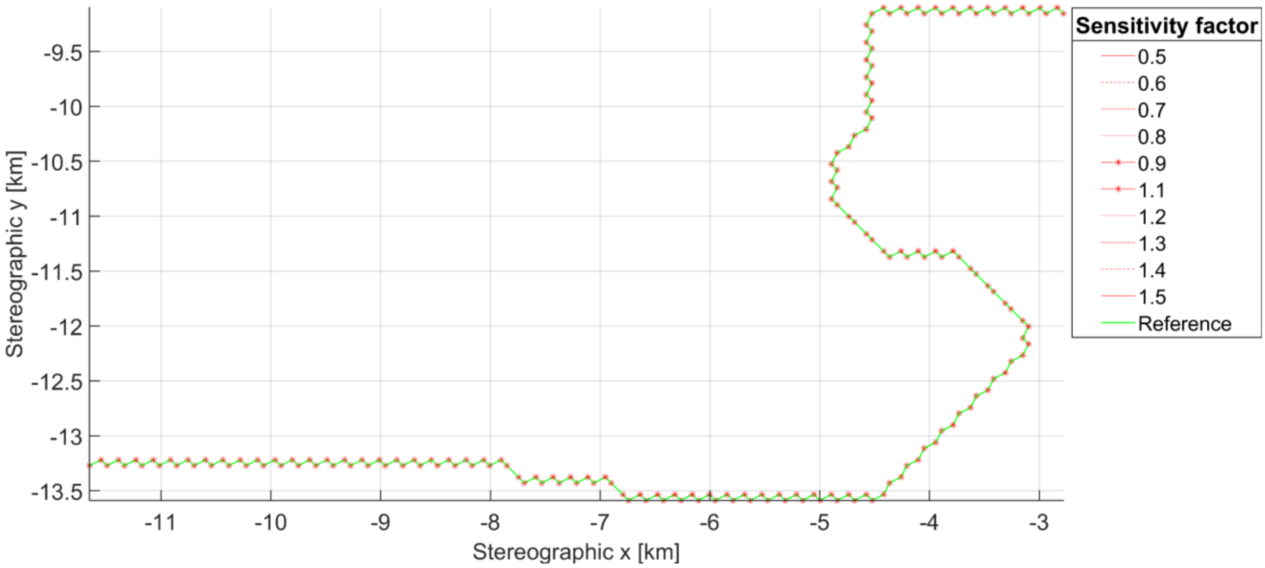

Figure 78: Traverses with different sensitivity factors applied on power for driving on slope. Battery capacity is 100 W h, Speyerer site

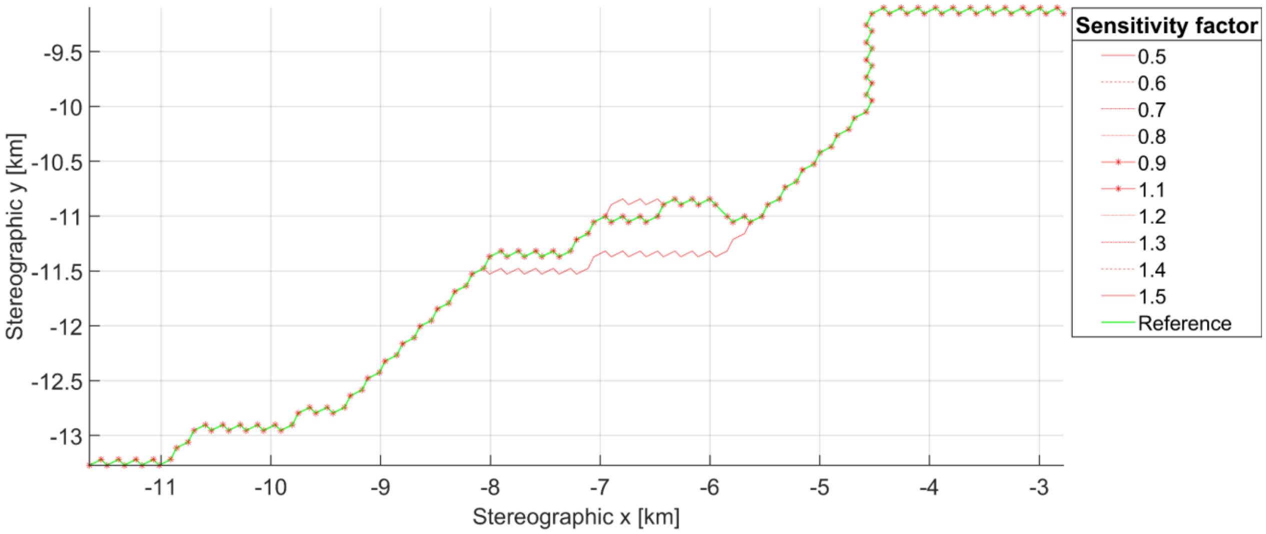

Figure 79: Traverses with different sensitivity factors applied on power for driving on slope. Battery capacity is 400 W h, Speyerer site

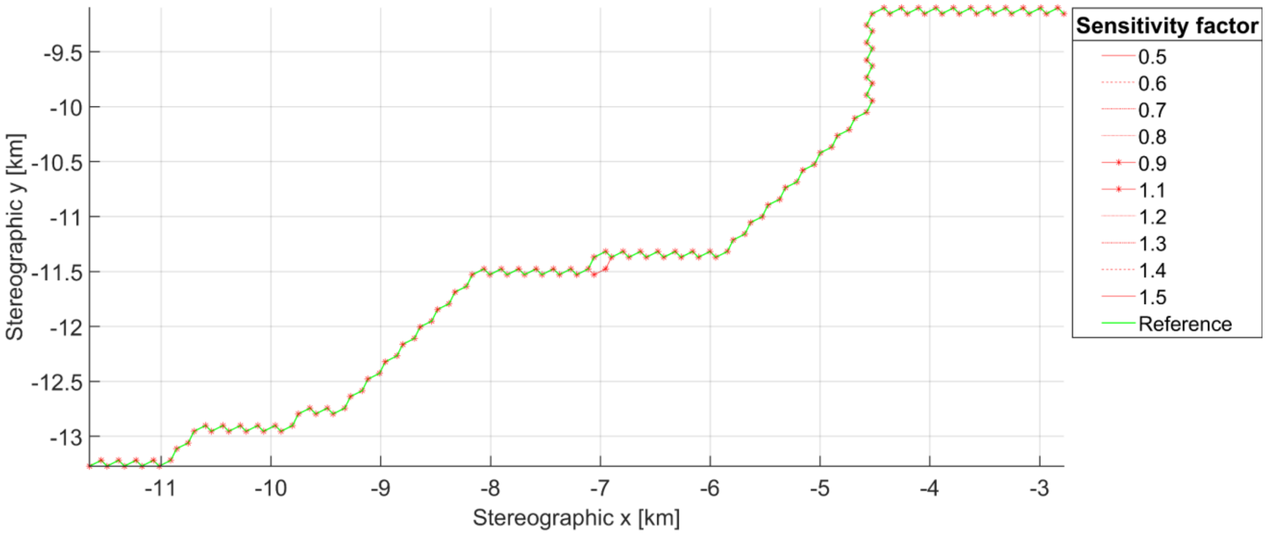

Figure 80: Traverses with different sensitivity factors applied on power for driving on slope. Battery capacity is 420 W h, Speyerer site

Appendix D Information on Speyerer Site and Traverses

Table 14: Station locations and illumination statistics collected over a 1-year period (1 January 2021 to 31 December 2021) using 1-h time intervals. For each location, we calculate the average Sun visibility (mean of the Boolean Sun visible/not visible) and the average Sun illumination (mean of the normalized solar disc area visible). Source: (Speyerer et al. 2016)

Station	Location		Average Sun visibility at the surface, %	Average Sun visibility 2 m above the surface, %	Average Sun illumination 2 m above the surface, %	Longest eclipse period 2 m above surface, h
	Latitude ° N	Longitude ° E				
SR-1	−89.685	196.7	49.25	86.71	82.71	135
SR-2	−89.740	201.2	42.64	79.35	75.04	359
SR-3	−89.808	205.9	43.40	55.50	51.02	1144
CR-1	−89.468	222.6	20.15	46.56	40.67	1421
CR-2	−89.500	222.1	44.44	49.87	46.31	1188
CR-3	−89.418	221.3	50.01	60.41	58.82	891
PSR-1	−89.575	196.7	0	0	0	n/a

Table 15: Optimal traverse statistics based on least-energy usage between the various south pole stations defined in Table 15 . The table provides the distance needed to travel (km) and the mean absolute slope (°) along the optimal traverse. Source: (Speyerer et al. 2016)

Distance (km)/mean(abs(slope))		Ending node						
		SR-1	SR-2	SR-3	CR-1	CR-2	CR-3	PSR-1
Starting node	SR-1	–	1.85/2.9	4.02/3.3	9.36/5.5	8.36/5.8	10.67/5.0	3.63/8.7
	SR-2	1.85/2.9	–	2.25/2.2	10.01/4.9	9.01/5.1	11.31/4.3	5.39/6.6
	SR-3	4.02/3.2	2.25/2.2	–	11.26/7.0	10.26/7.4	12.57/6.7	7.65/5.3
	CR-1	9.36/5.6	10.01/5.7	12.27/5.0	–	1.00/2.8	1.69/2.3	7.47/6.7
	CR-2	8.36/5.9	9.02/6.0	11.27/5.2	1.00/2.9	–	2.62/2.7	6.98/6.8
	CR-3	10.67/5.0	11.33/5.1	13.58/4.6	1.69/2.3	2.62/2.6	–	8.39/5.6
	PSR-1	3.64/8.2	5.40/6.3	7.65/5.1	7.47/6.7	6.98/6.7	8.40/5.7	–

Appendix E Results of Traverse Optimisation

All battery capacities and the total length of the traverse that the algorithm finds are shown in Table 16 for LVP site:

Table 16: Total length of all traverses with investigated battery capacities at LVP site

Battery Capacity [W h]	Total length [km]
0	None found
10	None found
20	None found
30	None found
40	None found
50	None found
60	None found
70	15.08520725
80	15.55776292
90	15.63188558
100	14.93507924
110	14.93347638
120	14.93347638
130	15.00820508
140	15.00820508
150	15.47147044
160	15.62884594
170	15.08157253
180	15.55412820
190	15.55412820
200	15.08157253
210	15.55412820
220	15.55412820
230	15.55412820
240	15.55412820
250	15.55412820
260	14.92731810
270	14.92731810
280	14.92731810
290	14.92731810
300	14.92731810

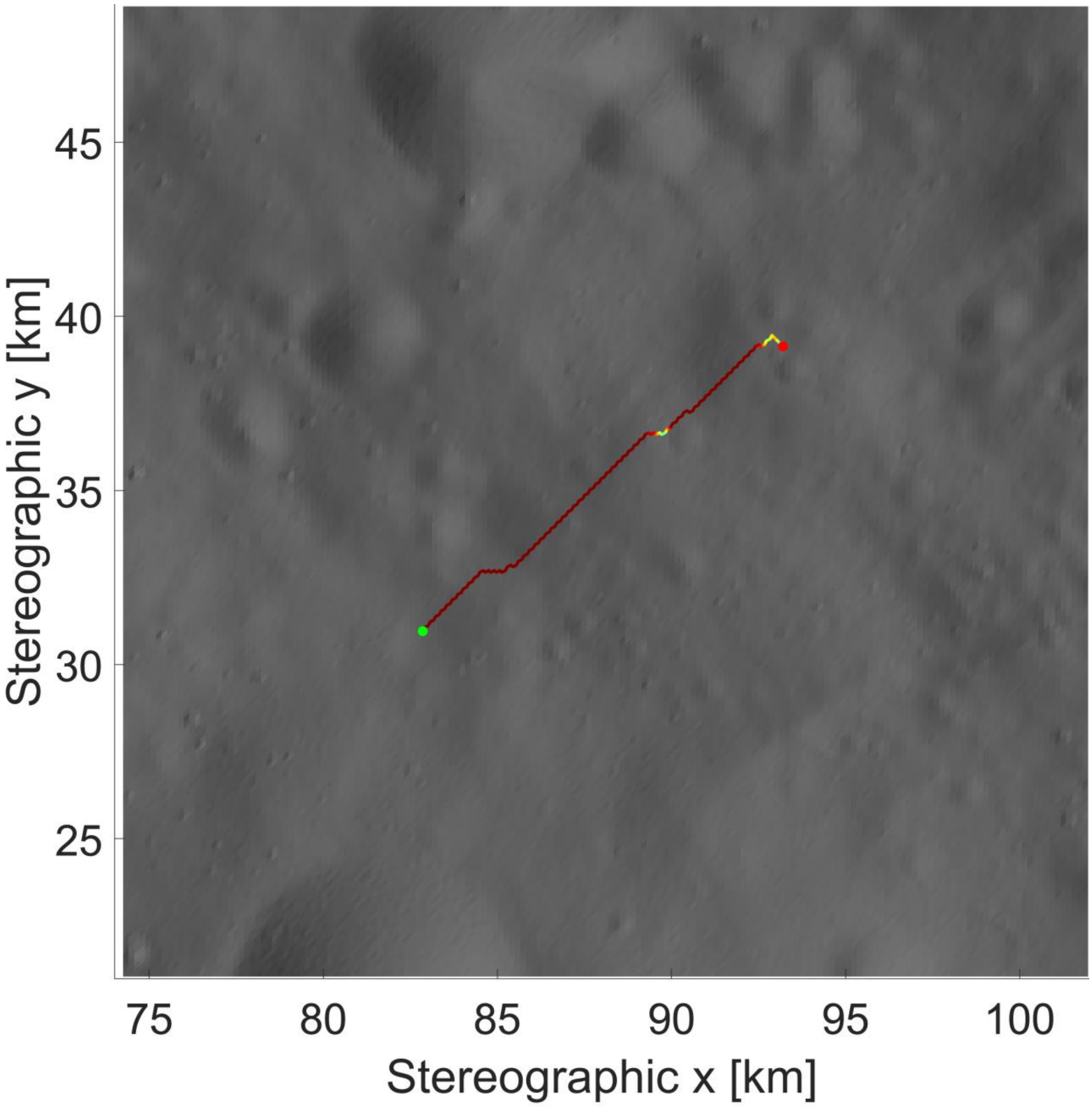

Figure 81: Travers at LVP site e with lowest possible battery capacity of 70 W h. Colours along traverse indicate the state of charge of the battery. Red is full, blue is empty.

All battery capacities and the total length of the traverse that the algorithm finds are shown in Table 17 for Speyerer site:

Table 17: Total length of all traverses with investigated battery capacities at Speyerer site

Battery Capacity [W h]	Total length [km]
0	None found
10	None found
20	None found
30	None found
40	None found
50	None found
60	None found
70	None found
80	None found
90	None found
100	17.81100898
110	17.81100898
120	17.81100898
130	17.79956313
140	17.65036186
150	17.65036186
160	17.63917050
170	17.63917050
180	17.56356671
190	17.56356671
200	17.49255795
210	17.64171369
220	17.49255795
230	17.49255795
240	17.49255795
250	17.41896047
260	17.56839679
270	17.33252984
280	17.33264981
290	17.33264981
300	17.17274319
310	17.17274319
320	17.17274319
330	17.17246815
340	17.17246815
350	17.32191808
360	17.32169353
370	12.80552353
380	12.80552353
390	12.80519422
400	12.73052493
410	12.73052493
420	12.73052493
430	12.73035902
440	12.73035902
450	12.73035902
460	12.73035902
470	12.73035902
480	12.73035902
490	12.73035902
500	12.73035902

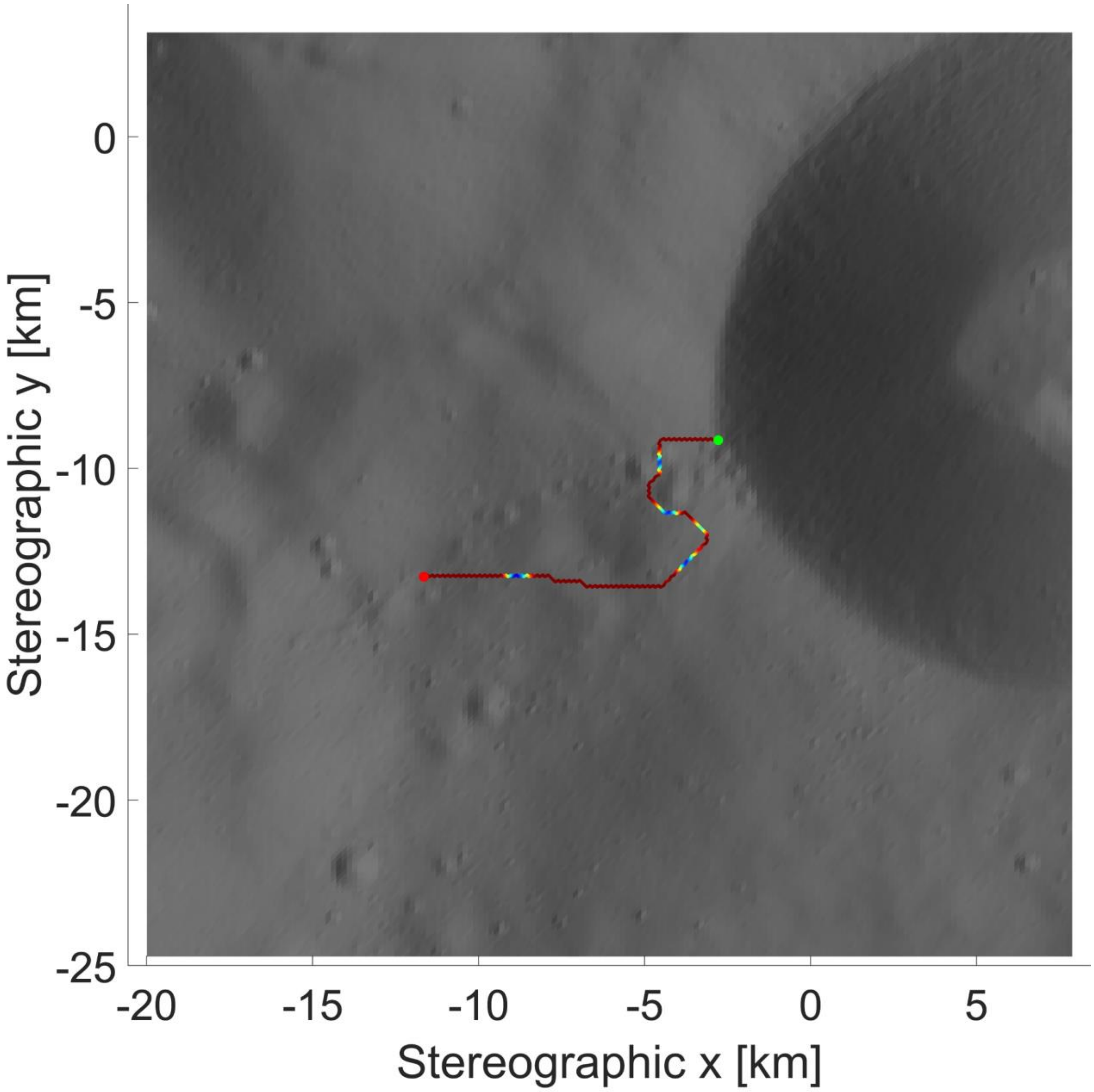

Figure 82: Travers at Speyerer site e with lowest possible battery capacity of 70 W h. Colours along traverse indicate the state of charge of the battery. Red is full, blue is empty.